Charge instabilities, Mott transition and transport in Hund metals

Maria Chatzieleftheriou

PSL UNIVERSITÉ PARIS

THÈSE DE DOCTORAT
DE L'UNIVERSITÉ PSL

Préparée à l'ESPCI PARIS

Instabilité de charge, transition de Mott et transport dans les métaux de Hund
Charge instabilities, Mott transition and transport in Hund metals

Soutenue par

Maria CHATZIELEFTHERIOU

Le 13/07/2021

École doctorale n°564

Physique en Île-de-France

Spécialité

Physique

Composition du jury :

Markus AICHHORN Professor, TU Graz	*Rapporteur*
Philipp WERNER Professor, University of Fribourg	*Rapporteur*
Silke BIERMANN Professeure, École Polytechnique	*Présidente, Examinatrice*
Massimo CAPONE Professor, SISSA Trieste	*Examinateur*
Catherine PÉPIN Directrice de Recherche, CEA - Saclay	*Examinateur*
Giorgio SANGIOVANNI Professor, University of Würzburg	*Examinateur*
Luca DE' MEDICI Professeur, ESPCI Paris	*Directeur de thèse*
Antoine GEORGES Professeur, Collége de France	*Invité*

ESPCI PARIS | PSL

Abstract

Strongly correlated electron systems represent one of the most active research fields in condensed matter physics, exhibiting intriguing phenomena like unconventional superconductivity and anomalous transport. In this thesis we theoretically analyze the multi-orbital Hund metals, using Slave Spins Mean-Field (SSMF) and Dynamical Mean-Field Theory (DMFT).

We study the emergence of a charge instability towards phase separation/charge-density wave, signalled by a diverging electronic compressibility, in doped multi-orbital Mott insulators for a finite "Hund's" intra-atomic exchange coupling. The effect is enhanced once the local spin or orbital symmetry is broken by e.g. a crystal field splitting and is understood in terms of energetics. The results are in agreement with realistic studies of iron-based superconductors.

We also connect the first order of the Mott metal-insulator transition found in the Hund metals at half-filling to the coexistence of two metallic solutions away from half-filling, giving rise to the charge instability zone which at zero temperature ends in a quantum critical point (QCP). Using perturbation theory we analytically describe this physics within Landau's theory of phase transitions. We single out a small energy scale (here the Hund's coupling) splitting a degenerate atomic ground state as the ultimate cause of this phenomenology.

We finally adapt the Exact Diagonalization algorithm for solving the DMFT equations to the calculation of transport properties, with an accuracy comparable in some cases to the more precise but numerically heavier Numerical Renormalization Group solver. We then apply our method on different multi-orbital systems and study their resistivity.

Résumé

Les systèmes d'électrons fortement corrélés représentent l'un des domaines de recherche les plus actifs en physique de la matière condensée, présentant des phénomènes intrigants tels que la supraconductivité non conventionnelle ou un transport anormal. Dans cette thèse, nous analysons théoriquement les métaux à plusieurs orbitales de Hund, en utilisant le champ moyen des Spins Esclaves (SSMF) et la Théorie du Champ Moyen Dynamique (DMFT).

Nous étudions l'émergence d'une instabilité de charge vers une séparation de phase/onde de densité de charge, signalée par une compressibilité électronique divergente, dans les isolants de Mott à plusieurs orbitales dopés, en présence d'un échange intra-atomique de "Hund" fini. L'effet augmente quand la symétrie locale de spin ou orbitale est rompue, par exemple par un champ cristallin, et est compris en termes énergétiques. Les résultats sont en accord avec des études réalistes des supraconducteurs à base de fer.

Nous connectons également le premier ordre de la transition métal-isolant de Mott des métaux de Hund au démi-remplissage à la coexistence de deux solutions à dopage fini, donnant lieu à la zone d'instabilité de charge qui, à température nulle, se termine en un point critique quantique (QCP). En utilisant la théorie des perturbations, nous décrivons analytiquement cette physique dans la théorie des transitions de phase de Landau. Nous isolons une petite échelle d'énergie (ici le couplage de Hund) levant la dégénérescence de l'état fondamental atomique comme la cause ultime de cette phénoménologie.

Nous adaptons enfin l'algorithme de Diagonalisation Exacte pour la solution des équations de la DMFT au calcul des propriétés de transport, avec une précision comparable dans certains cas au solveur d'impureté à base de Groupe de Renormalisation Numérique, plus précis mais numériquement plus lourd. Nous appliquons ensuite notre méthode sur différents systèmes multi-orbitales et étudions leur résistivité.

Acknowledgements

First and most of all I would like to thank my advisor Luca de' Medici for these three and a half years of guidance with endless patience. Thank you for insisting on the importance of details and for always creating a scientifically stimulating environment, while sharing your excitement about physics in the most genuine way. Your high sense of responsibility towards the education of your students and young collaborators is to me admirable. Thank you for everything you have taught me while always making sure the fun of doing research is not neglected!

I would also like to thank the members of the StrongCoPhy4Energy group (past and present). Lorenzo Fratino, Tommaso Gorni, Pablo Villar Arribi, Matteo Crispino and Karla Baumann, this experience would not have been the same without you. Thank you for the scientific discussions and collaborations, the huge range of non-physics related conversations, the after work dinners and certain truly memorable conferences spent together! I must also thank all the members of the LPEM lab in ESPCI for nice lunch break conversations and very interesting seminars.

I am very grateful to all the external scientific collaborators who contributed to this thesis. A huge thanks to Adriano Amaricci for being extremely patient with all my questions and constantly available to answer them. Thank you to the other collaborators from SISSA, Massimo Capone and Maja Berović, as well as the ones from the University of Würzburg, Giorgio Sangiovanni and Alexander Kowalski, for very fruitful discussions and excellent collaborations. Lastly to Lorenzo De Leo, thank you for sharing with us your NRG knowledge and impressive white-board painting skills!

A huge thanks to all my beloved friends in Paris for the beautiful moments we have spent together in the city and all across the country. A special thank you to Stavros and the rest of the Couronnes family Maria, Anna and Stelios for making our flat a true home and even the quarantine times the most fun anyone could hope for. You and our home will be forever in my heart!

To my friends from Athens, thank you for being always there for me no matter where, when or how. Finally, I want to thank my mom Dimitra, my dad Kostas and my brother Yannis for their infinite support, for being prouder of me than I am and for trying to put aside the fact that they miss me when giving me life and career advice. I know it is not easy!

Introduction

The *strongly correlated electron systems* have been at the center of active research in condensed matter physics for many years. This thesis focuses on the particular class of the multi-orbital *Hund metals*, which have attracted a lot of attention over the last decade mainly due to their linkage to the iron-based superconductors. The study of the latter under the prism of Hund's physics has given new perspectives to the field.

In chapter 1 of this thesis, we introduce the strongly correlated systems, discuss the paradigmatic example of *Mott insulators* and provide an introduction to the *Fermi liquid theory* and the emergent notion of *quasiparticles* within it. We present the materials motivating this work; the *iron-based superconductors (IBSC)* and the *early transition metal oxides*. In chapter 2 we introduce the *Hubbard model*, one of the most successful models describing correlated systems. We present the two approximate methods we use throughout this work to treat the model: the *Slave Spins Mean-Field (SSMF)* and its perturbative expansion and the *Dynamical Mean-Field Theory (DMFT)*. In chapter 3 we give an introduction to the Hund metals. A number of different studies on the Hund metal phase have been performed and in this work we adopt the approach suggested in [1]. Within this analysis, there are three main properties defining by their rapid increase a frontier in the interaction-doping plane, between a normal metal and a Hund metal: the *strong mass enhancement*, the *large local fluctuating magnetic moments* and the *orbital selectivity*. We discuss experimental evidences of these features on compounds of iron-based superconductors. We moreover show results of previous theoretical works on both simplified models and realistic Hamiltonians of IBSC exhibiting the clear emergence of the Hund metals frontier.

In chapter 4 we discuss a fourth feature appearing at the Hund metals frontier; a *charge instability zone*, due to a diverging/negative electronic compressibility [2]. Such an instability regime can induce *phase separation* or *charge density waves* in the system, in turn possibly linked to superconductivity. In a new research work we use SSMF and *Rotationally Invariant Slave-Bosons (RISB)* to explore the effect of breaking the rotational invariance of the system on the instability zone and we show that it gets enhanced. This trend is found upon introducing a spin asymmetry in the interaction or a crystal field splitting of the orbital energies. The result is in agreement with findings of a very extended zone of strongly enhanced or diverging compressibility in realistic studies of the iron-based superconductors, in which indeed the orbital energies are non-degenerate. Moreover, we provide a description of the mechanism responsible for this instability in terms of energetics. Hund's coupling J reduces the available local

configurations and consequently the available hopping channels and therefore limits the quasiparticle itinerancy. The divergence (or enhancement) of the electronic compressibility is directly linked to a rapid change in the electronic kinetic energy, due to an abrupt unfreezing at the Hund metal frontier of these local degrees of freedom, quenched by Hund's coupling. The main results of this work have been published in [3].

In chapter 5 we link the abruptness of this frontier and the accompanying phase separation zone to the first order of the Mott transition at half-filling and we report the appearance of a *quantum critical point (QCP)* at the end of the zone. We present new DMFT calculations showing a first-order Mott transition at *zero temperature* in a two-orbital system with $J \neq 0$, as opposed to the $T = 0$ results of a second-order transition for a single-orbital model or the multi-orbital case with $J = 0$ [4, 5, 6]. For a range of interactions there is coexistence of a metallic and an insulating solution, with the transition taking place when their energies cross. By continuation, when the system is doped two metallic solutions coexist for a range of electron filling giving rise to a *bistability zone*. Once this zone closes it evolves into a phase separation region, where there are no stable solutions, ending at a QCP. Using the more agile SSMF, we show that the stable solutions are connected through an unstable branch. When the resulting spinodals merge into one continuous solution the QCP emerges. We use the perturbative expansion of the SSMF around the insulating solution, introduced in chapter 2, and express the mechanism within *Landau theory of phase transitions*. We show that the free energy of the system can be written as a polynomial expansion of the quasiparticle weight's square root, identified with the order parameter. At half-filling the free energy landscape indeed exhibits two minima - corresponding to two stable solutions - connected through an unstable maximum. We further show that the partial lifting of the atomic ground state degeneracy by the introduction of a small energy scale (in our case a finite $J \neq 0$) is what gives rise to the first-order transition.

In chapter 6 we present a new method for calculating *electronic transport* properties of correlated systems using the *Exact Diagonalization (ED)* impurity solver in DMFT. We discuss previous results of a single-orbital Hubbard model obtained using DMFT with the *Numerical Renormalization Group (NRG)* solver [7]. There the authors show the resistivity's Fermi liquid character ($\sim T^2$) at small temperatures and for growing T they report the emergence of *resilient quasiparticles* and a linear in T resistivity. At higher temperatures the *Mott-Ioffe-Regel limit* is crossed and coherence is lost. We evaluate the resistivity of a single-orbital model directly from the real axis functions calculated using ED and report results exhibiting very good agreement with the NRG ones. We compare the resistivity with its low-T expanded form and show that the two coincide in the Fermi liquid region and they bifurcate in the zone of resilient quasiparticles.

We furthermore provide a qualitative method of estimating the crossing of the *Mott-Ioffe-Regel limit*. We calculate the resistivity in a two-orbital Hund metal and report a quick departure from the Fermi liquid behavior upon crossing the Hund metal frontier, thus confirming the lowering of the Fermi liquid energy scale in Hund metals. At the last section of the chapter we investigate the early transition metal oxides $SrCrO_3$ and $SrVO_3$ and provide some preliminary results of our on-going research. The first compound having two electrons in its three transition metal t_{2g} orbitals is strongly correlated and considered a Hund metal, while the second with one electron in the three orbitals is moderately correlated. We calculate the low-T expanded resistivity of the two compounds as a function of temperature and observe that there is a big difference between them, in line with experimental measurements.

In Appendix A the particle-hole symmetric form of the Hubbard model is calculated. In Appendix B a technical derivation of the gauge in the SSMF formalism is performed and in Appendix C the perturbative expansion of SSMF is detailed. In Appendix D the relation between the electronic compressibility and the spin symmetric Landau parameter is explicitly shown. In Appendix E the low-T expansion of the resistivity is derived and in Appendix F technical details of the transport calculations within ED in DMFT are presented.

Introduction

Les *systèmes électroniques fortement corrélés* sont au centre de la recherche active en physique de la matière condensée depuis de nombreuses années. Cette thèse se concentre sur la classe particulière des *métaux multi-orbitaux de Hund*, qui ont attiré beaucoup d'attention au cours de la dernière décennie, principalement en raison de leur lien avec les supraconducteurs à base de fer. L'étude de ces derniers sous le prisme de la physique de Hund a donné de nouvelles perspectives au domaine. Les trois premiers chapitres du manuscrit sont des introductions, discutant de la base théorique et de la méthodologie utilisée dans le reste du texte et donnant un aperçu des systèmes étudiés. Les trois chapitres suivants comprennent les principaux résultats originaux de ce travail, organisés en fonction des articles pertinents publiés ou en préparation.

Dans le chapitre 1 de cette thèse, nous présentons les systèmes fortement corrélés et discutons de l'inadéquation de la théorie des bandes conventionnelle pour les décrire. Nous faisons une brève introduction à l'exemple paradigmatique des *isolants de Mott*, la transition métal-isolant pertinente ayant lieu dans un système où il y a en moyenne un nombre entier d'électrons par site. Nous discutons de la *théorie du liquide de Fermi*, dans laquelle un système fortement corrélé est décrit par des *quasi-particules* avec des masses renormalisées et une durée de vie finie. Nous présentons ensuite les matériaux qui motivent les travaux menés dans cette thèse. Nous discutons de la structure cristalline et du diagramme de phase des *supraconducteurs à base de fer (IBSC)*, ainsi que des propriétés de transport des *oxydes des certains métaux de transition* de la partie gauche de la table périodique.

Dans le chapitre 2, nous introduisons *le modèle de Hubbard*, l'un des modèles les plus étudiés décrivant les systèmes fortement corrélés. Nous présentons les deux méthodes d'approximation que nous utilisons dans ce travail pour traiter ce modèle et ses generalisations à plusieurs orbitales: le *champ moyen des Spins Esclaves (SSMF)* et la *Théorie du Champ Moyen Dynamique (DMFT)*. L'idée principale de la première est d'introduire dans le système des degrés de liberté auxiliaires de spin-1/2 et, après avoir effectué deux approximations de champ moyen, de résoudre le problème en utilisant une équation d'auto-cohérence. Nous présentons également l'expansion perturbative du SSMF, un outil qui s'avérera utile dans les chapitres suivants du manuscrit. Nous discutons du formalisme DMFT et décrivons son cycle en précisant les étapes pour le cas de la *Diagonalisation Exacte (ED)* comme solveur d'impuretés. Enfin, nous abordons

brièvement un problème technique que nous avons rencontré lors de l'utilisation de l'algorithme de Lanczos/Arnoldi dans ED dans certains cas spécifiques.

Dans le chapitre 3, nous présentons une introduction aux *métaux de Hund*. Un certain nombre d'études différentes sur la phase des métaux de Hund ont été réalisées et, dans ce travail, nous adoptons l'approche suggérée dans [1]. Dans le cadre de cette analyse, trois propriétés principales définissent par leur augmentation rapide une frontière dans le plan d'interaction-dopage, entre un métal normal et un métal de Hund: *la forte augmentation de la masse, les grands moments magnétiques locaux fluctuants et la sélectivité orbitale*. Nous discutons des preuves expérimentales de ces caractéristiques sur des composés de supraconducteurs à base de fer. Nous présentons également les résultats de travaux théoriques antérieurs sur des modèles simplifiés et des Hamiltoniens réalistes pour les IBSC, qui montrent l'émergence claire de la frontière des métaux de Hund.

Dans le chapitre 4, nous discutons d'une quatrième caractéristique apparaissant à la frontière des métaux Hund; une *zone d'instabilité de charge*, en raison d'une compressibilité électronique divergente/négative [2]. Un tel régime d'instabilité peut induire une *séparation de phase* ou des *ondes de densité de charge* dans le système, à leur tour éventuellement liées à la supraconductivité. Dans un nouveau travail de recherche, nous utilisons le SSMF et les *bosons esclaves rotationnellement invariants (RISB)* pour explorer l'effet de la rupture de l'invariance rotationnelle du système sur la zone d'instabilité et nous montrons qu'elle est renforcée. Cette tendance est trouvée en augmentant le nombre d'orbitales, en introduisant une asymétrie de spin dans l'interaction (en utilisant une forme densité-densité des interactions) et en considérant un clivage des énergies orbitales par un champ cristallin fini. En plus en general l'étendue de la zone de dopage dans laquelle on trouve cette instabilité augmente avec le nombre d'orbitales. Le résultat est en accord avec les découvertes d'une zone très étendue de compressibilité fortement renforcée ou divergente dans des études réalistes des supraconducteurs à base de fer, dans lesquels les énergies orbitales sont non dégénérées. De plus, nous fournissons une description du mécanisme responsable de cette instabilité en termes d'énergétique. Le couplage de Hund J réduit les configurations locales disponibles et par conséquent les canaux de saut disponibles et limite donc l'itinérance des quasiparticules. La divergence (ou l'augmentation) de la compressibilité électronique est directement liée à un changement rapide de l'énergie cinétique électronique, dû à un dégel abrupt à la frontière du métal de Hund de ces degrés de liberté locaux, bloqués par le couplage de Hund. Les principaux résultats de ce travail ont été publiés dans [3].

Dans le chapitre 5, nous établissons un lien entre le caractère abrupt de cette frontière et la zone de séparation de phases qui l'accompagne et le premier ordre de la transition de Mott au demi-remplissage, et nous signalons l'apparition d'un *point critique quantique (QCP)* à l'extrémité de la zone. Nous présentons de nouveaux calculs DMFT montrant une transition de Mott de premier ordre à *température nulle* dans un système à deux orbitales avec $J \neq 0$, par opposition aux résultats $T = 0$ d'une transition de second ordre pour un modèle à une orbitale ou le cas multi-orbitale avec $J = 0$ [4, 5, 6]. Pour une gamme d'interactions, il y a coexistence d'une solution métallique et d'une solution isolante, la transition ayant lieu lorsque leurs énergies se croisent. Par continuation, lorsque le système est dopé, deux solutions métalliques coexistent pour une gamme de remplissage électronique donnant lieu à une *zone de bistabilité*. Une fois que cette zone se ferme, elle évolue vers une région de séparation de phases, où il n'y a pas de solutions stables, et se termine par un QCP. En utilisant le SSMF plus agile, nous montrons que les solutions stables sont connectées par une branche instable. Lorsque les spinodales résultantes fusionnent en une solution continue, le QCP émerge. Nous utilisons l'expansion perturbative de la SSMF autour de la solution isolante, introduite dans le chapitre 2 et évaluons la dépendance du poids des quasiparticules par rapport à la force d'interaction $Z(U)$ à proximité de la solution isolante. Nous montrons que l'ordre de la transition est lié au signe de la pente de $Z(U)$; lorsque la pente est négative, il y a une transition du second ordre et lorsqu'elle est positive, une transition du premier ordre. Nous exprimons le mécanisme dans le cadre de la *théorie des transitions de phase de Landau*. Nous montrons que l'énergie libre du système peut être écrite comme une expansion polynomiale de la racine carrée du poids des quasiparticules, identifiée comme paramètre d'ordre. Au demi-remplissage, le paysage de l'énergie libre présente en effet deux minima - correspondant à deux solutions stables - reliés par un maximum instable. De même, à l'écart du demi-remplissage dans la zone de bistabilité, il existe deux minima et un maximum dans l'énergie libre, correspondant aux solutions stables et instables. Nous montrons en outre que la levée partielle de la dégénérescence de l'état fondamental atomique par l'introduction d'une petite échelle d'énergie (dans notre cas, un $J \neq 0$ fini) est ce qui donne lieu à cette dependance de l'énergie libre et donc à la transition de premier ordre.

Dans le chapitre 6, nous présentons une nouvelle méthode pour calculer les propriétés de *transport électronique* des systèmes corrélés en utilisant le solveur d'impureté *Diagonalisation Exacte (ED)* en DMFT. Nous discutons des résultats précédents sur le modèle Hubbard à une bande obtenus à l'aide de DMFT avec le *Groupe de Renormalisation Numérique (NRG)* en tant que solveur [7]. Les auteurs y montrent le caractère

liquide de Fermi de la résistivité ($\sim T^2$) aux petites températures et pour des T croissantes, ils signalent l'émergence de *quasiparticules résilientes* et une résistivité linéaire en T. A des températures plus élevées, la *limite de Mott-Ioffe-Regel* est franchie et la cohérence est perdue. Notre méthode pour calculer la résistivité directement à partir des fonctions sur l'axe réel en utilisant l'ED consiste en deux étapes. Tout d'abord, nous dissocions la discrétisation de l'axe imaginaire de la température du système et utilisons une grille de fréquence plus fine pour l'equation d'auto-cohérence DMFT, améliorant ainsi la résolution basse fréquence. Nous calculons ensuite la résistivité en fonction d'un paramètre qui mesure la distance des fonctions spectrales de l'axe réel et extrapolons pour obtenir la résistivité sur l'axe réel. De cette façon, nous évaluons la résistivité d'un modèle à une orbitale directement à partir des fonctions sur l'axe réel calculées à l'aide de l'ED et rapportons des résultats présentant un très bon accord avec ceux du NRG. Nous comparons la résistivité avec sa forme approchée de basse T et montrons que les deux coïncident dans la région du liquide de Fermi et qu'elles bifurquent dans la zone des quasi-particules résilientes. Nous fournissons en outre une méthode qualitative d'estimation du franchissement de la limite *Mott-Ioffe-Regel*. Nous calculons la résistivité dans un métal de Hund à deux orbitales et signalons un départ rapide du comportement du liquide de Fermi lors du franchissement de la frontière du métal de Hund, confirmant ainsi l'abaissement de l'échelle d'énergie du liquide de Fermi dans les métaux de Hund. Dans la dernière section du chapitre, nous étudions les oxydes de métaux de transition $SrCrO_3$ et $SrVO_3$ et fournissons quelques résultats préliminaires de nos recherches en cours. Le premier composé ayant deux électrons dans ses trois orbitales de métal de transition t_{2g} est fortement corrélé et considéré comme un métal de Hund, tandis que le second avec un électron dans les trois orbitales est modérément corrélé. Nous calculons la résistivité à basse-T des deux composés en fonction de la température et observons qu'il existe une grande différence entre eux, en accord avec les mesures expérimentales.

À la fin du manuscrit se trouvent les annexes, qui comprennent certaines dérivations techniques et des détails importants complétant le texte principal. Dans l'annexe A, la forme symétrique particule-trou du modèle de Hubbard est calculée pour une ou plusieurs orbitales. L'annexe B présente une dérivation technique de la jauge dans le formalisme SSMF et l'annexe C détaille l'expansion perturbative du SSMF pour différents cas: modèles avec deux orbitales en l'absence ou en présence du couplage de Hund, avec différentes formes d'interaction, avec un champ cristallin fini ainsi qu'en dehors du demi-remplissage. L'annexe D montre explicitement la relation entre la compressibilité électronique et le paramètre de Landau symétrique en spin. Dans l'annexe

E, l'expansion à basse T de la résistivité est dérivée et dans l'annexe F, les détails techniques des calculs de transport dans ED DMFT sont présentés.

Contents

Chapter 1

Strongly correlated electron systems

In this first chapter we give an overview of the properties of *strongly correlated electron systems*. We discuss the paradigmatic example of *Mott insulators* and describe with simple arguments the mechanism behind them. We give a short summary of the properties of *quasiparticles* in *Fermi liquid theory*. In the last two sections we give a brief presentation of materials that have motivated our work. In particular, we introduce the *iron-based superconductors*, discussing their crystal structure and phase diagram and the *early transition metal oxides*, focusing on their transport properties.

1.1 Introduction

In condensed matter physics the electronic properties of a solid are usually portrayed in the context of band theory. The electrons governing the behaviour of each material are those closer to the Fermi level and they can be described in a wave-like picture. In particular, individual wave-functions are calculated from an effective one-electron potential assuming a system of independent particles. That is a successful approximation when the corresponding energy bands are broad, hence the electrons' kinetic energy is large and they are highly delocalized throughout the solid [8].

However, in certain materials these valence electrons appear to have reduced itinerancy. This usually happens in systems with partially filled d or f atomic shells, such as the transition metal ($3d$), the rare earth ($4f$) and the actinide ($5f$) elements. What is common between these atomic shells is their reduced spatial extension. For example in the $3d$ case, none of the wave-functions of smaller principal quantum number ($n = 1$ and $n = 2$) can have the same angular momentum $l = 2$ as the $3d$ ones, hence the latter do not need to have nodes in the radial part and they do not extend far from the nucleus. In these materials the active orbitals, being rather localized around the atomic nucleus, have a smaller overlap with the orbitals of their neighbouring atoms, compared to the typical cases where the atomic shell extension is of the order of the interatomic distance. Therefore, the system exhibits narrow energy bands and the kinetic energy of the electrons is decreased, so that it becomes comparable to the Coulomb

repulsion between two electrons occupying the same atomic orbital. With the energy gain for delocalizing the electrons across the solid limited by their high mutual repulsion, the electrons try to avoid each other with their motion becoming *correlated* [9].

The *strongly correlated systems* provide us with a vast playground of interesting phenomena. Instabilities and phase transitions associated with these materials give rise to complex physical mechanisms to be investigated. The quest for formulating a consistent theory has made the field of strongly correlated materials extremely active for many decades.

1.2 Mott insulators

One the most studied effects of strong correlations is the *Mott transition*, named after N.F. Mott [10]. In a system where the total number of electrons in the conduction bands is such that there is on average an integer number of electrons per site, an insulating phase driven by correlations can take place. This insulator is not related to the formation of a band gap, as expected from conventional band theory. On the contrary, from a band theory point of view the system should be metallic, therefore the description at this level completely breaks down. The mutual repulsion between electrons on the same site is so high compared to the kinetic energy gain of large itinerancy, that in order to minimize the double occupation of orbitals the electrons chose to localize on a site. As a direct result, the solid becomes an insulator.

In order to illustrate the mechanism more clearly we can take as an example the simple case of a single-band system at half-filling, so that on average there is one electron per atomic site. We further simplify the problem by assuming a semi-circular density of states (DOS) with only nearest-neighbour hoping. The bandwidth W is a good approximate measure of the electrons' kinetic energy. As shown schematically in Fig.1.1, at large $U > W$ the system is a Mott insulator with a spectrum showing two bands separated by an energy U corresponding to the atomic excitation in which a double occupancy is formed, and broadened by the electronic kinetic energy $\sim W$. As U is reduced the distance between the bands decreases and to a good approximation when $U = U_c = W$ the Mott transition takes place. Real materials often exhibit a multi-orbital character and more complex DOS. In general the Mott transition can take place when there is on average an integer number of electrons per site.

1.3 Fermi Liquid Theory

In the previous section we discussed the inadequacy of conventional band theory to describe interesting phenomena exhibited in strongly correlated systems. However,

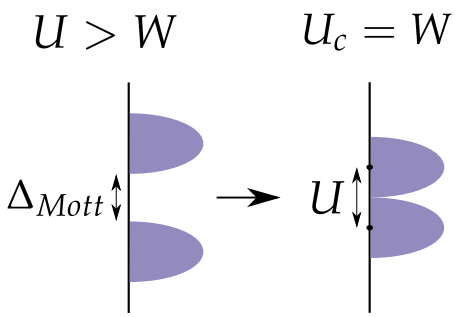

FIGURE 1.1: Schematic representation of the Mott transition by decreasing the interaction strength from the large-U insulating limit.

it very often appears that such systems behave similarly to non-interacting electron gases. Landau in 1957-59 approached this issue by developing the *Fermi Liquid Theory (FLT)*, in the context of which a system of interacting electrons is described by a collection of almost non-interacting *quasiparticles* [11, 12, 13].

The main idea behind the FLT is to analyze the interacting system postulating *adiabatic continuity* with the non-interacting one. This implies that there is a one-to-one correspondence between the excitations in the two cases. In practice, if we start from an excited state of the non-interacting system and we turn on the interactions adiabatically (so that the occupation numbers remain unchanged) we will end up with a corresponding excited state of the interacting system, labelled by the same quantum numbers as the unperturbed one. There are certain limits for the theory to be applicable, namely the system must be at low energy/temperature and it should not be at the verge of a phase transition. The reason for this last condition is that we cannot connect adiabatically an excited state of a metallic system in, for example, the paramagnetic phase to an excited state of a system in a broken symmetry phase.

In the context of FLT, the interacting electron gas exhibits excitations identified as quasiparticle states, which are not the exact eigenstates of the system. They rather have a finite lifetime, long enough to ensure a well-defined energy. FLT is generally valid at very low temperatures and for excitations close to the Fermi level. It can be shown that the inverse lifetime is [14]:

$$\frac{1}{\tau_{FL}} \propto (\epsilon - \epsilon_F)^2 + \pi^2 T^2. \tag{1.1}$$

The core of the FLT idea is that the system is represented by quasiparticles which exhibit residual interactions and effective parameters embodying the original interactions of the strongly correlated electrons. A very important concept emerging from

this approach is the quasiparticle *effective mass* m^*, renormalizing the mass of non-interacting electrons and incorporating the effect of interactions by reducing the electron itinerancy. The interacting system's Green's function is given by:

$$G(\mathbf{k},\omega) = \frac{1}{\omega - \xi_{\mathbf{k}} - \Sigma(\mathbf{k},\omega)}, \tag{1.2}$$

where $\xi_{\mathbf{k}} = \epsilon_{\mathbf{k}} - \epsilon_F$ and $\Sigma(\mathbf{k},\omega)$ is the self-energy reflecting the effect of an electron's interactions with the environment on its energy. As already mentioned, the theory is limited to low frequencies and temperatures. The imaginary part of the self-energy decays as ω^2 for small frequencies [14], hence expanding the self-energy around zero frequency and limiting to linear order in ω, it takes the form:

$$\Sigma(\mathbf{k},\omega) \simeq Re\Sigma(\mathbf{k},0) + \omega \frac{\partial Re\Sigma(\mathbf{k},\omega)}{\partial\omega}\bigg|_{\omega=0} + iIm\Sigma(\mathbf{k},0). \tag{1.3}$$

The Green's function thus becomes:

$$G(\mathbf{k},\omega) = \frac{1}{\Big(\omega\big(1 - \partial_\omega Re\Sigma(\mathbf{k},\omega)\big|_{\omega=0}\big) - \big(\xi_{\mathbf{k}} + Re\Sigma(\mathbf{k},0)\big)\Big) - iIm\Sigma(\mathbf{k},0)}. \tag{1.4}$$

We define $\tilde{\xi}_{\mathbf{k}} = \xi_{\mathbf{k}} + Re\Sigma(\mathbf{k},0)$, $Z_{\mathbf{k}} = \big(1 - \partial_\omega Re\Sigma(\mathbf{k},\omega)\big|_{\omega=0}\big)^{-1}$ and $\Gamma_{\mathbf{k}} = -Z_{\mathbf{k}} Im\Sigma(\mathbf{k},0)$ to obtain:

$$G(\mathbf{k},\omega) = \frac{Z_{\mathbf{k}}}{\omega - Z_{\mathbf{k}}\tilde{\xi}_{\mathbf{k}} + i\Gamma_{\mathbf{k}}}. \tag{1.5}$$

The parameter $Z_{\mathbf{k}}$ is identified with the *quasiparticle weight* and assuming that it is independent of momentum ($Z_{\mathbf{k}} = Z$), it can be shown [14] that the effective mass is given by the expression:

$$\frac{m^*}{m_e} = \frac{1}{Z}. \tag{1.6}$$

$\Gamma_{\mathbf{k}}$ corresponds to the inelastic *scattering rate*[1]. The spectral function:

$$A(\mathbf{k},\omega) = -\frac{1}{\pi} ImG(\mathbf{k},\omega) = \frac{1}{\pi} \frac{Z_{\mathbf{k}}\Gamma_{\mathbf{k}}}{(\omega - Z_{\mathbf{k}}\tilde{\xi}_{\mathbf{k}})^2 + \Gamma_{\mathbf{k}}^2} \tag{1.7}$$

is thus a Lorentzian with a sharp peak related to the quasiparticle. $Z_{\mathbf{k}}$ corresponds to the spectral weight of the quasiparticle peak, while the inverse quasiparticle lifetime $\Gamma_{\mathbf{k}}$ acts as a broadening of the peak. The total integral of the spectral function must always be equal to 1 and since the weight of the quasiparticle peak is determined by

[1] In chapter 6 we are going to define the scattering rate as $\gamma = -Im\Sigma(\mathbf{k},0)$, which is common practice in transport calculations.

$Z_{\mathbf{k}}$, which for an interacting system is < 1, there is some residual weight (related to the neglected part of the expanded self-energy) stemming from other types of excitations.

1.4 Unconventional superconductors

A metal at finite temperature exhibits resistivity against the conduction of electric current. As the temperature is lowered, the resistivity of a conductor decreases gradually down to absolute zero. In 1911, while studying the resistance of solid mercury at small temperatures, Heike Kamerlingh Onnes observed that at around $4.2K$ the resistance vanished completely [15]. This marked the discovery of what was later called *superconductivity*. Each superconductor has a characteristic critical temperature T_c at which the resistivity disappears and remains equal to zero for lower temperatures. Furthermore, those materials have the property of expelling the magnetic field flux, called the *Meissner effect*. In the years following the discovery of superconductivity great effort was made towards the understanding of the underlying mechanisms responsible for it. It turned out that the phenomenon could only be explained in the context of quantum mechanics and it was in 1957 that Bardeen, Cooper and Schrieffer formulated the microscopic *BSC theory* for superconductivity [16][2].

In BSC theory very low temperatures (in practice below $30K$) were thought to be a condition for superconductivity to emerge and liquid helium is needed to access those temperatures. In 1986 Bednorz and Müller discovered that lanthanum barium copper oxide (LBCO) had a superconducting transition temperature of $35K$ [18], with other copper based materials superconducting at even higher temperatures discovered soon after [19, 20, 21, 22], forming the family of *cuprates*. This discovery opened the road to larger access in applications since the expensive liquid helium could be replaced by the cheaper more accessible liquid nitrogen as a coolant.

Another important class of unconventional superconductors was discovered in 2006, when a vanishing resistance was observed in LaFePO at $4K$ and two years later in LaFeAs at up to $43K$ under pressure [23, 24]. Discoveries of more superconducting Fe-based materials were made in the following years and in the next section we will discuss in more detail this family of *iron-based superconductors (IBSC)*.

Fig.1.2 is a combined plot illustrating various superconductors discovered up to 2015 together with their critical temperatures T_c. The highest T_c until 2015 was found in the cuprates, while the compound with the largest T_c from the family of IBSC is

[2]The basis for the understanding of superconductivity was set by the work of Landau and Ginzburg earlier in 1950 and their phenomenological *Ginzburg-Landau theory* [17].

monolayer FeSe [25]. Up to the day that this thesis is being written the highest superconducting T_c ever observed is $287.7 \pm 1.2K$ (in 2020) in a photochemically transformed carbonaceous sulfur hydride system under pressures of around 270 gigapascals [26], which actually constitutes the first claim of room-temperature superconductivity, even if a stable form at ambient pressure is missing.

The pursuit for formulating a microscopic theory explaining this *unconventional superconductivity* has been over the last decades at the centre of active research in condensed matter theory and it remains to this day.

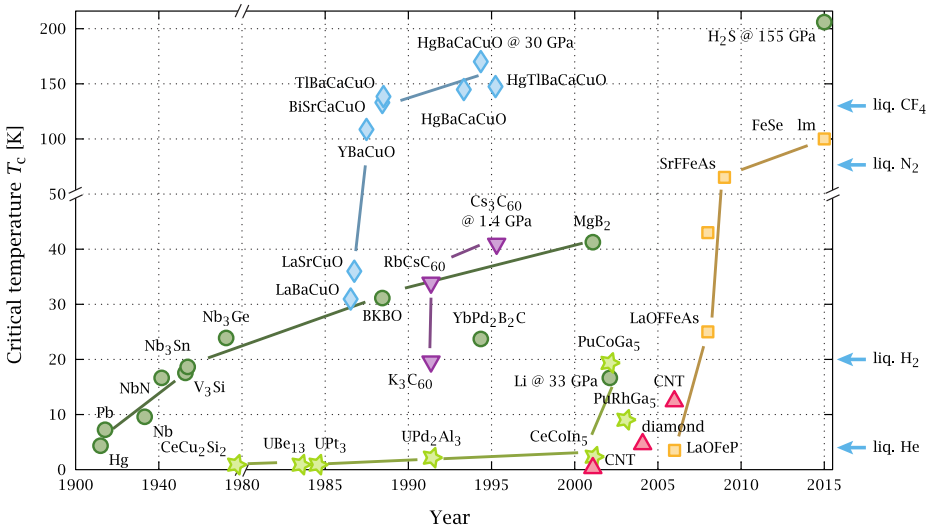

FIGURE 1.2: Year of discovery and critical superconducting temperature of high-T_c compounds discovered up to 2015 [27].

1.4.1 Iron-based superconductors

The compounds constituting the family of iron-based superconductors share a common crystal structure. They all feature a layer of iron, above and below which there are atomic layers of elements within the pnictogen or chalcogen groups -such as As, P, S, Se and Te- in an alternating pattern. The nature of these elements determines wether the system will be in the class of the iron-pnictides or the iron-chalcogenides. Some of these materials also have a "bridging" layer mainly acting as a charge reservoir and depending on their stoichiometry these sub-families are nick-named the '11', '111', '1111', '122' compounds. In Fig.1.3 we see a graphical illustration of the different materials in the family.

Angle-resolved photoemission spectroscopy (ARPES) measurements combined with density functional theory (DFT) calculations have shown that despite their structural differences, the various iron-based superconductors exhibit very similar Fermi surfaces, with an observed roughly two-dimensional character of the electronic structure.

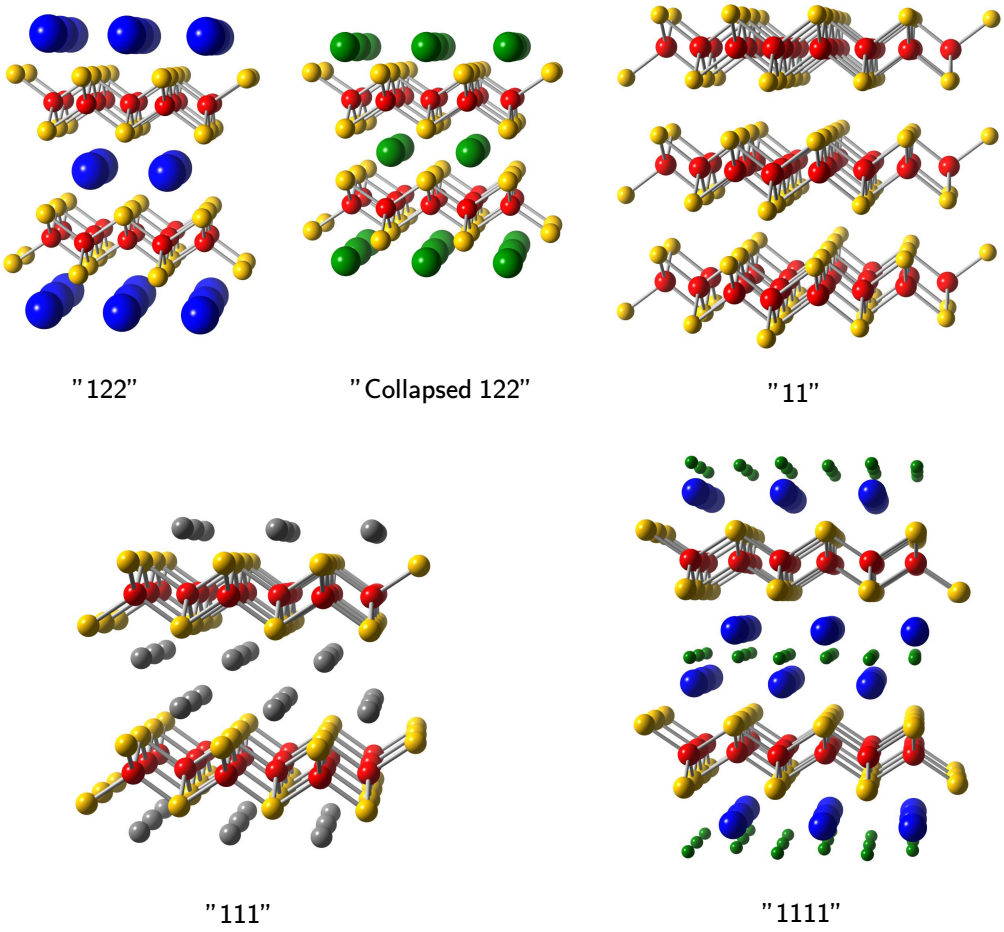

FIGURE 1.3: Schematic representation of the crystal structure in different families of iron-based superconductors [28].

In fact, the electron bands close to the Fermi level are found to be of predominantly iron character and more specifically they have their origin in the $3d$ valence electrons of the Fe atomic plane. DFT calculations have shown that all five d-orbitals of iron have weight around the Fermi level region and they are usually all included in numerical simulations. This multi-orbital character of the compounds plays a crucial role in defining their properties. In a free atom the five orbitals have the same energy but in materials the crystal-field usually lifts this degeneracy. In Fig.1.4 examples of crystal-field splitting are shown for an octahedral and a tetrahedral (which is the case for the IBSC) atomic environment and for a cubic lattice symmetry. When the symmetry instead is tetragonal a further splitting of the orbital energies takes place, as shown at the right-most part of Fig.1.4 for a tetrahedral environment.

The phase diagram of these iron-based materials has certain similarities with that of the more extensively studied cuprates. Upon varying the chemical composition (by electron or hole doping) as well as the temperature different phases emerge. At large

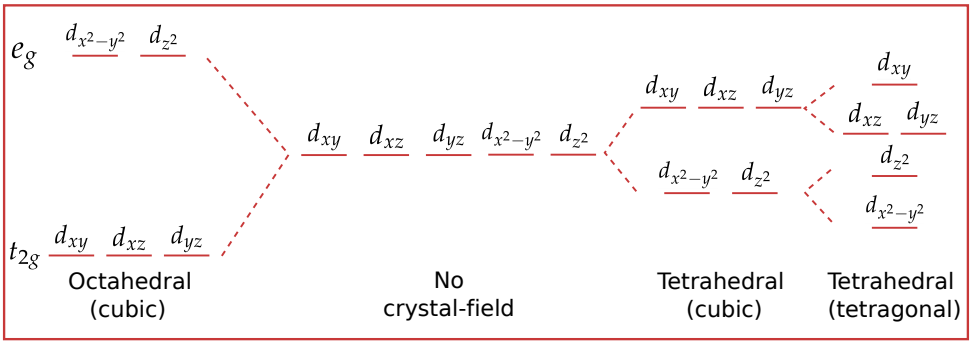

FIGURE 1.4: In the left part: crystal-field splitting of 3*d* orbitals in an octahedral environment under cubic symmetry (early transition metal oxides). In the two right-most parts: crystal-field splitting in a tetrahedral environment under cubic and tetragonal symmetry (IBSC in normal phase).

T there is a paramagnetic phase with tetragonal symmetry (right-most part of Fig.1.4) and the system for a doping range, upon cooling undergoes a structural (tetragonal to orthorhombic) transition into what is called the *nematic phase*. This transition is often accompanied by the formation of long-range antiferromagnetic order and upon further cooling (or doping accordingly) a superconducting transition takes place. A sketch representing a typical phase diagram of iron-based materials is plotted in Fig.1.5.

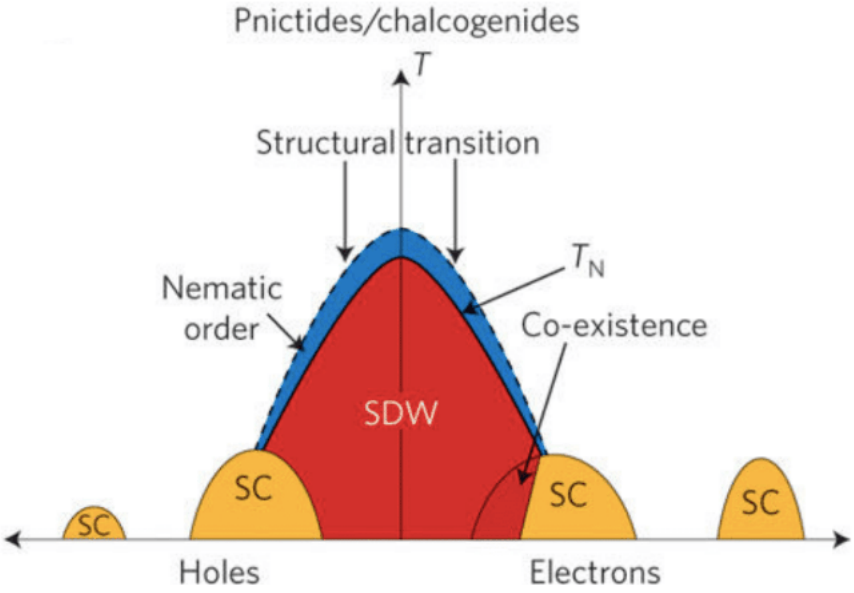

FIGURE 1.5: Sketch of a typical example of phase diagram for the family of iron-based superconductors [29].

1.5 Early transition metal oxides with perovskite structure

In the last chapter of this thesis we will discuss transport properties of another class of compounds, the *early transition metal oxides with perovskite structure*. They have the general form ABX_3, with octahedra of oxygens surrounding the transition metal, as drawn in Fig.1.6. In the left-most part of Fig.1.4 it is shown that the crystal-field in such an octahedral environment in presence of cubic lattice symmetry, largely splits the energy of the two e_g and the three t_{2g} orbitals and only the latter are usually kept in theoretical studies of the systems.

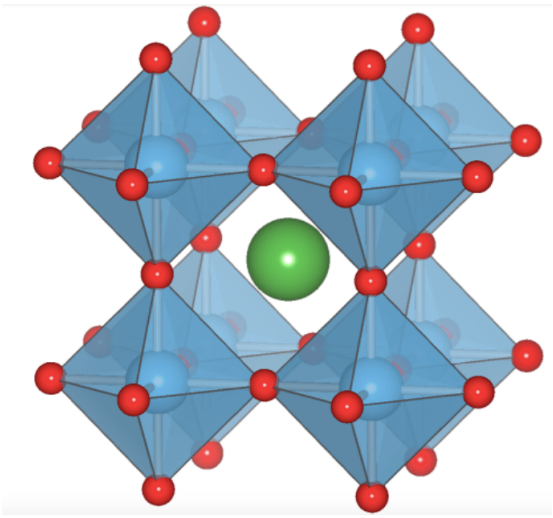

FIGURE 1.6: Perovskite crystal structure of the early transition metal oxides. The green sphere corresponds to the Sr atom, the blue ones to the transition metal V, Cr, Mn and the red ones to the O atoms. Adapted from [30].

In this series the materials $SrVO_3$, $SrCrO_3$ and $SrMnO_3$ are found, with filling of the t_{2g} shell of one, two and three electrons respectively. All three of them are considered to have a common interaction strength value of $U \simeq 3 - 4eV$ and half-bandwidth of $D \simeq 1 - 1.5eV$ [31]. Despite these similarities it is remarkable that, due to Hund's coupling, the difference in electron filling leads to very different properties between these compounds. In fact, $SrMnO_3$ being at half-filling is a Mott insulator at $U/D \simeq 4$. On the other hand $SrVO_3$, having on average only one electron in the three orbitals, is moderately correlated [9]. $SrCrO_3$ having two electrons in the three orbitals and considering that Hund's coupling J highly influences the physics in that regime[3], is

[3]We will discuss extensively the role played by Hund's coupling in the electronic properties of metals in the following chapters.

believed to be a strongly correlated metal. In the next chapter the notion of "Hund metals" will be discussed and it will be suggested, following previous works, that $SrCrO_3$ falls into that category.

A number of different experiments have been performed on this compound but issues have been reported on the purity of the produced samples, due to the high pressure necessary for synthesizing them and in particular in transport measurements, due to the impact of grain boundary scattering [32]. Therefore, the experimental results have been somewhat controversial and often contradicting [33, 34, 35, 36, 37, 38, 39, 40, 34, 41, 42, 32]. Regarding transport measurements, although initially $SrCrO_3$ was considered to be a paramagnetic metal, in later studies there have been observed signatures of insulating behavior. In the recent years the metallic nature of the compound has been a prevalent interpretation following experiments on high-purity samples [37, 32]. In Fig.1.7a the resistivity as a function of temperature is shown as plotted in [32], measured for thin films of $SrCrO_3$[4]. ρ grows with increasing T at $50 - 300K$ showing a resistivity of $1.3m\Omega \cdot cm$ at around room temperature. Below $T = 50K$ there is an observed increase of the resistivity for a diminishing temperature. This is an effect met in other transition metal oxides [43, 44] and it is believed to be the result of enhanced backscattering due to impurities or vacancies [32]. We can estimate the ρ_0 value by extrapolating the curve in Fig.1.7a and obtain $\rho_0 \simeq 0.58m\Omega \cdot cm$, so the shifted room temperature resistivity is $\rho \simeq 0.72m\Omega \cdot cm = 720\mu\Omega \cdot cm$.

The experimental data on $SrVO_3$ regarding transport exhibit an overall better agreement between them -at least qualitatively- and the metallic character of the compound is established [45, 46, 47, 48, 49, 50]. Quantitatively, however, the resistivity at room temperature varies among the different measurements. In Fig.1.7b -adapted from [51]- the resistivity of $SrVO_3$ is measured as a function of temperature. At around room temperature the resistivity is $\rho \simeq 130\mu\Omega \cdot cm$, which subtracting the $\rho_0 \simeq 12\mu\Omega \cdot cm$ gives $\rho \simeq 118\mu\Omega \cdot cm$.

One thing that becomes clear, despite the quantitative disagreements among different experimental data, is that the resistivity of $SrVO_3$ is in general much smaller compared to the one for $SrCrO_3$. In chapter 6 we will study these materials and provide a theoretical calculation of the temperature dependent resistivity. We will interpret the difference in resistivity between the two compounds in terms of Hund's physics, then viewing $SrCrO_3$ as a *Hund metal*. We will discuss these systems in detail in the following chapters.

[4]Clean transport measurements on bulk single crystals are not available in the literature.

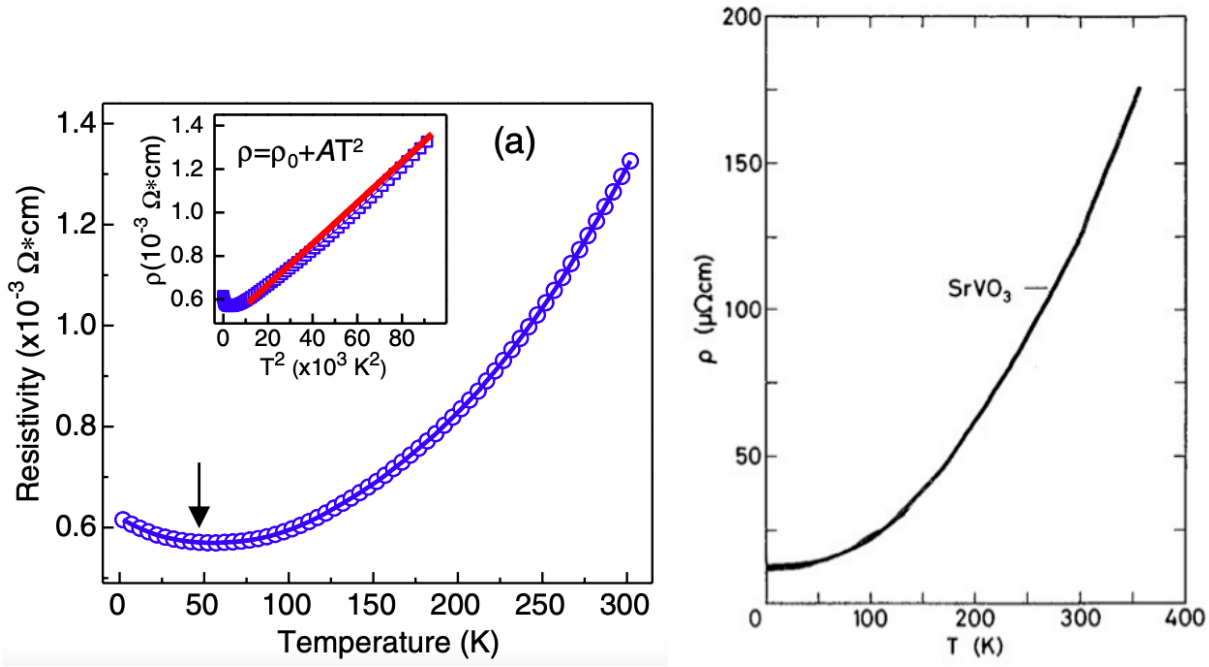

(A) (B)

FIGURE 1.7: Experimental data of resistivity as a function of temperature for **(A)** $SrCrO_3$, adapted from [32] and **(B)** $SrVO_3$ adapted from [51]. Overall $SrCrO_3$ exhibits a much larger resistivity than $SrVO_3$.

Chapter 2

Methods for strongly correlated systems

In this chapter we present the methods used to describe strongly correlated systems throughout this work. We discuss the paradigmatic *Hubbard model* and introduce the two mean-field methods employed to approximate it: the *Slave Spins Mean-Field (SSMF)* and the *Dynamical Mean-Field Theory (DMFT)*. We further perform a perturbative expansion of the SSMF formalism, which will be used extensively in the rest of this thesis. We lastly dedicate a small section to the discussion of a technical issue appearing in certain cases when using the Lanczos/Arnoldi algorithm in the *Exact Diagonalization (ED)* impurity solver of DMFT.

2.1 Hubbard model

As already discussed in the previous chapter, conventional band theory used to describe the electronic properties of solids fails to account for interesting phenomena manifested in the strongly correlated ones. One of the most successful models in studying these systems is the *Hubbard model* [52, 53, 54], with the Hamiltonian:

$$\hat{H} = \sum_{ijmm'\sigma} t_{ij}^{mm'} d_{im\sigma}^{\dagger} d_{jm'\sigma} + \frac{1}{2} \sum_{ijkl} \sum_{mm'nn'} \sum_{\sigma\sigma'} V_{ijkl}^{mm'nn'} d_{im\sigma}^{\dagger} d_{jm'\sigma'}^{\dagger} d_{kn'\sigma'} d_{ln\sigma}. \tag{2.1}$$

The first term of the Hamiltonian is related to the destruction of an electron on site j, orbital m' and the creation of it on site i, orbital m, where the hopping integral is defined as:

$$t_{ij}^{mm'} = \int d\mathbf{r}\, w_m^*(\mathbf{r} - \mathbf{R}_i) \big[-\frac{\hbar^2 \nabla^2}{2m_e} + V(\mathbf{r}) \big] w_{m'}(\mathbf{r} - \mathbf{R}_j). \tag{2.2}$$

The second term in the Hamiltonian corresponding to the electronic interactions involves the interaction parameters:

$$V_{ijkl}^{mm'nn'} = \int d\mathbf{r}\, d\mathbf{r'}\, w_m^*(\mathbf{r} - \mathbf{R}_i) w_{m'}^*(\mathbf{r'} - \mathbf{R}_j) \frac{e^2}{|\mathbf{r} - \mathbf{r'}|} w_n(\mathbf{r'} - \mathbf{R}_k) w_{n'}(\mathbf{r} - \mathbf{R}_l). \tag{2.3}$$

In the above equations we have used Wannier orbitals to express the parameters, as it is customarily done [55, 56]. These can be viewed as Fourier transforms of the standard Bloch waves and are defined (although not uniquely) as:

$$w_m(\mathbf{r}-\mathbf{R}) = \frac{1}{\sqrt{N}}\sum_{\mathbf{k}} e^{-i\mathbf{k}\cdot\mathbf{R}}\phi_{\mathbf{k},m}(\mathbf{r}), \tag{2.4}$$

with $\mathbf{k}$ limited inside the first Brillouin zone.

The big complexity of solving problems for strongly correlated systems stems from the large number of degrees of freedom involved in the Hubbard Hamiltonian. In order to treat this issue one needs to make certain approximations and the first one is to limit the focus on a subset of bands near the Fermi energy. The bands that come from deep shells are completely filled, while the ones of high energy well above the Fermi level are completely empty, so they do not contribute to the electronic properties of our interest, involving states of a few eV around the ϵ_F. They are included in our description through a screened Coulomb interaction, incorporating the effect of these non-valence electrons on the ones around ϵ_F which we treat explicitly. The second approximation made originates from this effective Coulomb interaction (that can be modelled as a *Yukawa potential*) and specifically from its feature of decaying interaction as a function of increasing electronic distance. Treating this Hamiltonian becomes a lot simpler once we restrict ourselves to on-site interactions, keeping in mind that this is an approximation, the validity of which should be verified according to the particular problem at hand.

In the simple case of a single-orbital system, the Hamiltonian obtains the following expression, with U being the on-site Coulomb interaction between the electrons:

$$\hat{H} = \sum_{ij\sigma} t_{ij} d^{\dagger}_{i\sigma} d_{j\sigma} + U n_{\uparrow} n_{\downarrow}. \tag{2.5}$$

When multiple orbitals are active in the system the relevant interaction processes increase. In the case of materials with the valence bands originating from the $3d$ orbitals (in typical models of three t_{2g} or two e_g orbitals) it can be shown that the following independent integrals remain [31]:

$$\begin{aligned}
V^{mmmm}_{iiii} &\equiv U = \int d\mathbf{r}d\mathbf{r'}|w_m(\mathbf{r})|^2 W(\mathbf{r},\mathbf{r'})|w_m(\mathbf{r'})|^2 \\
V^{mm'm'm}_{iiii} &\equiv U' = \int d\mathbf{r}d\mathbf{r'}|w_m(\mathbf{r})|^2 W(\mathbf{r},\mathbf{r'})|w_{m'}(\mathbf{r'})|^2 \\
V^{mm'mm'}_{iiii} &\equiv J = \int d\mathbf{r}d\mathbf{r'} w^*_m(\mathbf{r}) w^*_{m'}(\mathbf{r'}) W(\mathbf{r},\mathbf{r'}) w_m(\mathbf{r'}) w_{m'}(\mathbf{r})
\end{aligned} \tag{2.6}$$

where $W(\mathbf{r}, \mathbf{r'})$ corresponds to the effective Yukawa potential, incorporating the screening effects, given by:

$$W(\mathbf{r}, \mathbf{r'}) = \frac{e^2}{|\mathbf{r} - \mathbf{r'}|} e^{-\lambda|\mathbf{r}-\mathbf{r'}|}. \tag{2.7}$$

In the case of cubic symmetry (present in models and materials we will study in this work) it can be shown that $U' = U - 2J$ [57]. The final form (rigorously for e_g and t_{2g} models, approximately for the full d-shell) of the multi-orbital Hubbard model, the *Kanamori Hamiltonian* [54] is:

$$\begin{aligned}\hat{H} = &\sum_{ijmm'\sigma} t_{ij}^{mm'} d_{im\sigma}^{\dagger} d_{jm'\sigma} + U \sum_{m} n_{m\uparrow} n_{m\downarrow} + U' \sum_{m \neq m'} n_{m\uparrow} n_{m'\downarrow} + \\ &(U' - J) \sum_{m<m',\sigma} n_{m\sigma} n_{m'\sigma} - J \sum_{m \neq m'} d_{m\uparrow}^{\dagger} d_{m\downarrow} d_{m'\downarrow}^{\dagger} d_{m'\uparrow} + J \sum_{m \neq m'} d_{m\uparrow}^{\dagger} d_{m\downarrow}^{\dagger} d_{m'\downarrow} d_{m'\uparrow}.\end{aligned} \tag{2.8}$$

The first term in the Hamiltonian describes the hopping of electrons among different sites and orbitals. The second term is the on-site *intra-orbital* Coulomb repulsion between electrons, which as imposed by the Pauli exclusion principle must possess opposite spin. The third one is the on-site *inter-orbital* Coulomb repulsion between electrons with anti-parallel spins. U' must be smaller than U since the distance separating the interacting electrons is in this case increased, due to the geometry of the orbitals. The fourth term is the on-site *inter-orbital* Coulomb repulsion between electrons with parallel spins and the two last terms in the Hamiltonian correspond to the *spin-flip* and *pair-hopping* processes. The exchange integral J called *Hund's coupling* indicates that in a multi-orbital system the spin alignment among different orbitals is favoured.

In the rest of this work, we will often make use of a simplified version to the above Hamiltonian of Eq.2.8, neglecting the *spin-flip* and *pair-hopping* processes. It has been shown that in systems of our study the inclusion of these terms leads to mostly quantitative changes. Nevertheless, we will address with caution the comparison between the two models in the following chapters. This further approximation gives rise to a non-rotationally invariant form of the multi-orbital Hubbard model, the Hamiltonian with *density-density interaction*:

$$\hat{H} = \sum_{ijmm'\sigma} t_{ij}^{mm'} d_{im\sigma}^{\dagger} d_{jm'\sigma} + U \sum_{m} n_{m\uparrow} n_{m\downarrow} + U' \sum_{m \neq m'} n_{m\uparrow} n_{m'\downarrow} + (U' - J) \sum_{m<m',\sigma} n_{m\sigma} n_{m'\sigma}. \tag{2.9}$$

Over the years various methods have been developed in order to approach and solve these Hamiltonians. In the following sections we give an overview of the two methods applied in our work, the *Slave Spins Mean-Field (SSMF)* and the *Dynamical Mean-Field Theory (DMFT)*.

2.2 Slave Spins Mean-Field method

One of the most widely used classes of methods in addressing strongly correlated systems is that of the *slave-particle techniques*. The main common idea behind these methods is the introduction of auxiliary (*slave*) degrees of freedom in the system and eventually their decoupling through a mean-field approximation. In this process, an effective solvable Hamiltonian emerges including -through renormalization parameters- information related to the problem's correlations. Typical examples of such a technique are the *Slave Rotors* [58, 59] and the *Slave Bosons* [60], with the latter having been largely exploited in the study of strong correlations. In this work we use the computationally agile *Slave Spins Mean-Field (SSMF)* method. In this section we give an overview of the method and more detailed descriptions can be found in [61, 62, 63, 64]. Another version of the SSMF method has been developed in [65], however in this study we work with the formalism demonstrated explicitly in [57].

The principal idea of the SSMF technique is the introduction of spin-1/2 auxiliary variables corresponding to the original fermionic degrees of freedom of the system. The original Fock space of the problem becomes enlarged with one fermionic and one slave-spin degree of freedom associated with each fermionic one of the initial system. The slave-spin variable although is not a physical spin, it obeys the algebra of a spin-1/2 and it is "up" (+1/2) for a present electron and "down" (-1/2) for an absent one. In order to present the SSMF steps in a clear and simple way we focus on the single-orbital model and on a following section we will demonstrate the generalization to the multi-orbital case. The states of this new space are shown below in correspondence with the original ones:

$$\begin{aligned} &| \, n^f_{i\sigma} = 1, S^z_{i\sigma} = +1/2 \rangle \Longleftrightarrow | \, n^d_{i\sigma} = 1 \rangle \\ &| \, n^f_{i\sigma} = 0, S^z_{i\sigma} = -1/2 \rangle \Longleftrightarrow | \, n^d_{i\sigma} = 0 \rangle \\ &| \, n^f_{i\sigma} = 0, S^z_{i\sigma} = +1/2 \rangle \Longleftrightarrow \quad ? \\ &| \, n^f_{i\sigma} = 1, S^z_{i\sigma} = -1/2 \rangle \Longleftrightarrow \quad ? \end{aligned} \tag{2.10}$$

The two last states exist in the enlarged space, they are however unphysical since they do not correspond to any state of the original problem. In order to account for that and exclude the non-physical states, we must incorporate in our description an enforcing constraint. We express this restriction through:

$$f^\dagger_{i\sigma} f_{i\sigma} = S^z_{i\sigma} + \frac{1}{2}. \tag{2.11}$$

One easily notices that the electron number operator can be represented either through the auxiliary fermion's $f^\dagger_{i\sigma} f_{i\sigma} = n^f_{i\sigma}$ or through the z-component of the slave-spin $S^z_{i\sigma} + \frac{1}{2}$. The replacement in the Hamiltonian of $n^d_{i\sigma}$ with $n^f_{i\sigma}$ or $S^z_{i\sigma} + \frac{1}{2}$ is completely equivalent and we will make use of this property in building the SSMF Hamiltonian.

2.2.1 Hamiltonian in the SSMF formalism

Our starting point is the single-orbital Hubbard model Eq.2.5, the interaction term of which can be written in the particle-hole symmetric form (see Appendix A.1 for a detailed derivation):

$$\hat{H}_{int} = U n^d_\uparrow n^d_\downarrow = \frac{U}{2} \sum_i \Big(\sum_\sigma (n^d_{i\sigma} - \frac{1}{2}) \Big)^2. \tag{2.12}$$

Making use of $n^f_{i\sigma} = n^d_{i\sigma}$ and of the constraint Eq.2.11 we can also write the interaction term as:

$$\hat{H}_{int} = \frac{U}{2} \sum_i \Big(\sum_\sigma S^z_{i\sigma} \Big)^2. \tag{2.13}$$

In order to write the system's Hamiltonian in the SSMF formalism we need to map the original fermionic operator onto a new composite one, acting both on the fermionic and the slave-spin degrees of freedom. We define the correspondence $d_{i\sigma} \to f_{i\sigma} O_{i\sigma}$, $d^\dagger_{i\sigma} \to f^\dagger_{i\sigma} O^\dagger_{i\sigma}$, but we naturally notice that there is no unique way to express the slave-spin operator $O^\dagger_{i\sigma}$. For example we can set it to be $S^+_{i\sigma}$ or $2S^x_{i\sigma}$ and the action of both $f^\dagger_{i\sigma} S^+_{i\sigma}$ and $f^\dagger_{i\sigma} 2S^x_{i\sigma}$ on the physical space will be the same. For that reason we define it in the most general way as a complex matrix:

$$O_{i\sigma} = \begin{pmatrix} 0 & c_{i\sigma} \\ 1 & 0 \end{pmatrix} = S^-_{i\sigma} + c_{i\sigma} S^+_{i\sigma}, \tag{2.14}$$

with $c_{i\sigma}$ for now being an arbitrary complex number which will be acting as a gauge for the formalism.

Collecting all the above we write down the SSMF form of the single-orbital Hubbard Hamiltonian:

$$\hat{H} - \mu \hat{N} = \sum_{<ij>\sigma} t_{ij} O^\dagger_{i\sigma} O_{j\sigma} f^\dagger_{i\sigma} f_{j\sigma} + \frac{U}{2} \sum_i \Big(\sum_\sigma S^z_{i\sigma} \Big)^2 - \mu \sum_{i\sigma} n^f_{i\sigma}. \tag{2.15}$$

2.2.2 Mean-field approximations

Up to this stage we have re-expressed the original Hubbard Hamiltonian in terms of auxiliary variables in an enlarged Hilbert space, restricted by a constraint. We further

perform certain approximations which will allow us to treat the system. The first one is to:

- **Decouple the pseudo-fermions $f_{i\sigma}$ and the slave-spin variables $O_{i\sigma}$**

We write:

$$\sum_{<ij>\sigma} t_{ij} O^{\dagger}_{i\sigma} O_{j\sigma} f^{\dagger}_{i\sigma} f_{j\sigma} \simeq \sum_{<ij>\sigma} t_{ij} \langle O^{\dagger}_{i\sigma} O_{j\sigma} \rangle f^{\dagger}_{i\sigma} f_{j\sigma} + \sum_{<ij>\sigma} t_{ij} O^{\dagger}_{i\sigma} O_{j\sigma} \langle f^{\dagger}_{i\sigma} f_{j\sigma} \rangle. \tag{2.16}$$

The hopping term of the Hamiltonian is expressed as a sum of a fermionic part and a slave-spin one and each of them is renormalized by a factor associated with the other term. We can define these average values, which play the role of renormalization factors that couple the fermionic with the slave-spin part of the hopping, as:

$$\begin{aligned} Q_{ij} &= \langle O^{\dagger}_{i\sigma} O_{j\sigma} \rangle_s, \\ J_{ij} &= t_{ij} \langle f^{\dagger}_{i\sigma} f_{j\sigma} \rangle_f. \end{aligned} \tag{2.17}$$

The subscripts s and f refer to an expectation value computed on the slave-spin or the fermionic Hamiltonian respectively, since we can now express the total Hamiltonian as a sum of the two $\hat{H} = \hat{H}_f + \hat{H}_s$ and obtain:

$$\begin{aligned} \hat{H}_f &= \sum_{<ij>,\sigma} t_{ij} \left(Q_{ij} f^{\dagger}_{i\sigma} f_{j\sigma} + h.c. \right) - (\mu + \lambda) \sum_i n^f_i, \\ \hat{H}_s &= \sum_{<ij>,\sigma} \left(J_{ij} O^{\dagger}_{i\sigma} O_{j\sigma} + h.c. \right) + \lambda \sum_{i,\sigma} \left(S^z_{i\sigma} + \frac{1}{2} \right) + \frac{U}{2} \sum_i \left(\sum_{\sigma} S^z_{i\sigma} \right)^2. \end{aligned} \tag{2.18}$$

In the above expression we have introduced a site-independent Lagrange multiplier λ necessary in order to incorporate in the description the constraint as defined in Eq.2.11. In order to calculate the average values of the operators and evaluate Q_{ij} and J_{ij} we introduce the partition function in the enlarged Fock space:

$$Z = Tr \left[e^{-\beta(\hat{H} - \mu \hat{N})} \times \delta \left(S^z_{i\sigma} + \frac{1}{2} - n^f_{i\sigma} \right) \right], \tag{2.19}$$

with the Dirac delta projecting out the unphysical states. This can be enforced using the Lagrange multiplier as defined above and substituting the delta function with an exponential:

$$\delta \left(S^z_{i\sigma} + \frac{1}{2} - n^f_{i\sigma} \right) \rightarrow e^{-\beta\lambda \left(S^z_{i\sigma} + \frac{1}{2} - n^f_{i\sigma} \right)}. \tag{2.20}$$

We should point out that we have assumed working on a uniform phase, so that λ does not carry a spin index. In this previous step the second approximation of SSMF is

hidden, implying that λ can be adjusted in a way that the constraint is satisfied by the expectation values of the operators, namely:

- **The constraint is treated on average**

We define the grand-canonical potential as $\Omega = -\frac{1}{\beta} logZ$ and we adjust λ so that the condition $\frac{\partial \Omega}{\partial \lambda} = 0$ is fulfilled, giving:

$$\begin{aligned} \frac{\partial \Omega}{\partial \lambda} = \frac{\partial(-logZ/\beta)}{\partial \lambda} = -\frac{1}{\beta Z}\frac{\partial Z}{\partial \lambda} = -\frac{1}{\beta Z}\partial Tr\left[e^{-\beta\left(\hat{H}-\mu\hat{N}+\lambda\left(S^z_{i\sigma}+\frac{1}{2}-n^f_{i\sigma}\right)\right)}\right] = \\ \frac{1}{Z}Tr\left\{\left[e^{-\beta\left(\hat{H}-\mu\hat{N}+\lambda\left(S^z_{i\sigma}+\frac{1}{2}-n^f_{i\sigma}\right)\right)}\right]\left(S^z_{i\sigma}+\frac{1}{2}-n^f_{i\sigma}\right)\right\} = \langle S^z_{i\sigma}\rangle + \frac{1}{2} - \langle n^f_{i\sigma}\rangle \end{aligned} \tag{2.21}$$

and indeed the constraint is satisfied on average.
The last approximation of the SSMF formalism is to perform a:

- **Mean-field approximation on the slave-spin Hamiltonian**

We assume that the slave-spin Hamiltonian describes a single-site, coupled to the other sites through average values of their operators. We thus perform a *Weiss mean-field approximation* and obtain an effective single-site Hamiltonian with renormalization factors embodying the influence of the site's surroundings. We further decouple the spin operators as:

$$\langle O^\dagger_{i\sigma} O_{j\sigma}\rangle \simeq \langle O^\dagger_{i\sigma}\rangle O_{j\sigma} + O^\dagger_{i\sigma}\langle O_{j\sigma}\rangle \tag{2.22}$$

and assuming translational invariance we write $< O_{j\sigma} >=< O_{i\sigma} >$. The spin Hamiltonian can thus be written in the following way:

$$H_s = \sum_i H^i_s = \sum_{i,\sigma}\left(h_{i\sigma}O^\dagger_{i\sigma} + h.c.\right) + \lambda\sum_{i,\sigma}\left(S^z_{i\sigma}+\frac{1}{2}\right) + \frac{U}{2}\sum_i\left(\sum_\sigma S^z_{i\sigma}\right)^2, \tag{2.23}$$

where:

$$h_{i\sigma} = h_\sigma = \sum_j J_{ij}\langle O_{j\sigma}\rangle_s = \langle O_{i\sigma}\rangle_s \sum_j \langle f^\dagger_{i\sigma} f_{j\sigma}\rangle_f = \langle O_{i\sigma}\rangle_s \sum_k \epsilon_k \langle f^\dagger_{k\sigma} f_{k\sigma}\rangle_f = \langle O_{i\sigma}\rangle_s \epsilon_0. \tag{2.24}$$

The parameter h_σ - assumed to be independent of i since we work on translationally invariant systems - represents the average kinetic energy per spin for the pseudofermions, defined as the renormalized bare kinetic energy ϵ_0, which is calculated independently through the auxiliary fermions' Hamiltonian. The renormalization of the kinetic energy coincides with the square root of the fermionic quasiparticle weight

yielding $Z = \langle O_{i\sigma} \rangle^2$. The relation between h_σ and Z defines the *self-consistency condition* of the SSMF formalism:

$$h_\sigma =< O_{i\sigma} > \epsilon_0 = \sqrt{Z}\epsilon_0. \tag{2.25}$$

The Weiss mean-field approximation in presence of translational invariance results in:

$$Q_{ij} = \langle O^\dagger_{i\sigma} O_{j\sigma} \rangle_s = \langle O_{i\sigma} \rangle^2_s, \tag{2.26}$$

implying that the electron hopping in the fermionic Hamiltonian is renormalized by the quasiparticle weight Z.

The last piece missing is the determination of the gauge variable $c_{i\sigma}$. We evaluate it by ensuring that the non-interacting limit $Z(U = 0) = 1$ is reproduced in the SSMF formalism and assuming a real $c_{i\sigma} = c_\sigma$ we obtain an expression depending only on the density n_σ (a detailed derivation is performed in Appendix B):

$$c_\sigma = \frac{1}{\sqrt{n_\sigma(1 - n_\sigma)}} - 1. \tag{2.27}$$

2.2.3 The SSMF cycle

The single-orbital Hubbard model has been written in terms of auxiliary degrees of freedom and upon mean-field approximations the resulting Hamiltonian is broken down into the sum of a fermionic and a slave-spin one:

$$\begin{aligned} H_f &= \sum_{<ij>,\sigma} t_{ij} \left(Q_{ij} f^\dagger_{i\sigma} f_{j\sigma} + h.c. \right) - (\mu + \lambda) \sum_i n^f_i, \\ H_s &= \sum_i H^i_s = \sum_{i,\sigma} \left(h_{i\sigma} O^\dagger_{i\sigma} + h.c. \right) + \lambda \sum_{i,\sigma} \left(S^z_{i\sigma} + \frac{1}{2} \right) + \frac{U}{2} \sum_i \left(\sum_\sigma S^z_{i\sigma} \right)^2, \end{aligned} \tag{2.28}$$

including the effective parameters:

$$\begin{aligned} Q_{ij} &= \langle O^\dagger_{i\sigma} O_{j\sigma} \rangle_s = \langle O_{i\sigma} \rangle^2_s = Z_\sigma, \\ J_{ij} &= t_{ij} \langle f^\dagger_{i\sigma} f_{j\sigma} \rangle_f, \\ h_{i\sigma} &= h_\sigma = \langle O_{i\sigma} \rangle_s \epsilon_0. \end{aligned} \tag{2.29}$$

With the addition to the above expressions of the constraint, as treated on average:

$$\langle n^f_{i\sigma} \rangle_f = \langle S^z_{i\sigma} \rangle_s + \frac{1}{2} \tag{2.30}$$

we have gathered the self-consistency equations of the SSMF formalism. Before the SSMF cycle starts (step 1) a seed for Z, λ and μ is provided as well as an input for the interaction parameters U/D, J/D and the total electron density n_{targ} (or the chemical potential μ). In step 2 the fermionic Hamiltonian is diagonalized and h is calculated in order to begin the cycle. This h value is used to construct and diagonalize the slave-spin Hamiltonian (step 3), extract the average value $\langle O \rangle_s$ in order to calculate Z and $< S^z >_s$ (we have assumed a non-magnetic phase). In step 4 the fermionic Hamiltonian is diagonalized and the updated h and $< n^f >_f$ are calculated. The broyden method is used to evaluate λ. In step 5 a check on the constraint is performed and if it is not fulfilled on average the algorithm circles back to step 3. When by adjusting λ the constraint is fulfilled, μ is in turn adjusted (step 6) in order to obtain the desired electron density (if the input was n_{targ}). If two consecutive values of Z (or h) do not differ more than a set tolerance and the desired population n_{targ} (if that was the input) has been reached (step 7) the cycle ends, otherwise the iterations continue from step 3 until convergence is met. This process is shown graphically in Fig.2.1.

2.2.4 Generalization to a multi-orbital system

When multiple orbitals are active in the system, the above equations must obtain a generalized form to account for the multi-orbital character. This process is straightforward, keeping in mind that all the operators and variables now carry an orbital index. The crucial difference with the single-orbital case is related to the slave-spin Hamiltonian. The interactions as shown in Eq.2.9 for the case of a density-density Hamiltonian[1], include three terms, which written in the slave-spin formalism become:

$$\hat{H}_{int}[S] = U \sum_{m} S^z_{m\uparrow} S^z_{m\downarrow} + U' \sum_{m \neq m'} S^z_{m\uparrow} S^z_{m'\downarrow} + (U' - J) \sum_{m<m',\sigma} S^z_{m\sigma} S^z_{m'\sigma}. \tag{2.31}$$

The fermionic and slave-spin Hamiltonians in turn become:

$$\begin{aligned} H_f &= \sum_{i \neq j, mm'\sigma} t^{mm'}_{ij} \sqrt{Z_m Z_{m'}} f^\dagger_{im\sigma} f_{jm'\sigma} + \sum_{im\sigma} (\epsilon_m - \lambda_m - \mu) n^f_{im\sigma}, \\ H_s &= \sum_{m,\sigma} \left[(h_{m\sigma} O^\dagger_{m\sigma} + h.c.) + \lambda_m (S^z_{m\sigma} + \frac{1}{2}) \right] + \hat{H}_{int}[S], \end{aligned} \tag{2.32}$$

where we define:

$$h_{m\sigma} = \sum_{m'} \langle O_{m'\sigma} \rangle_s \sum_{j(\neq i)} t^{mm'}_{ij} \langle f^\dagger_{im\sigma} f_{jm'\sigma} \rangle_f \tag{2.33}$$

[1]The Kanamori interactions within SSMF can only be treated approximately.

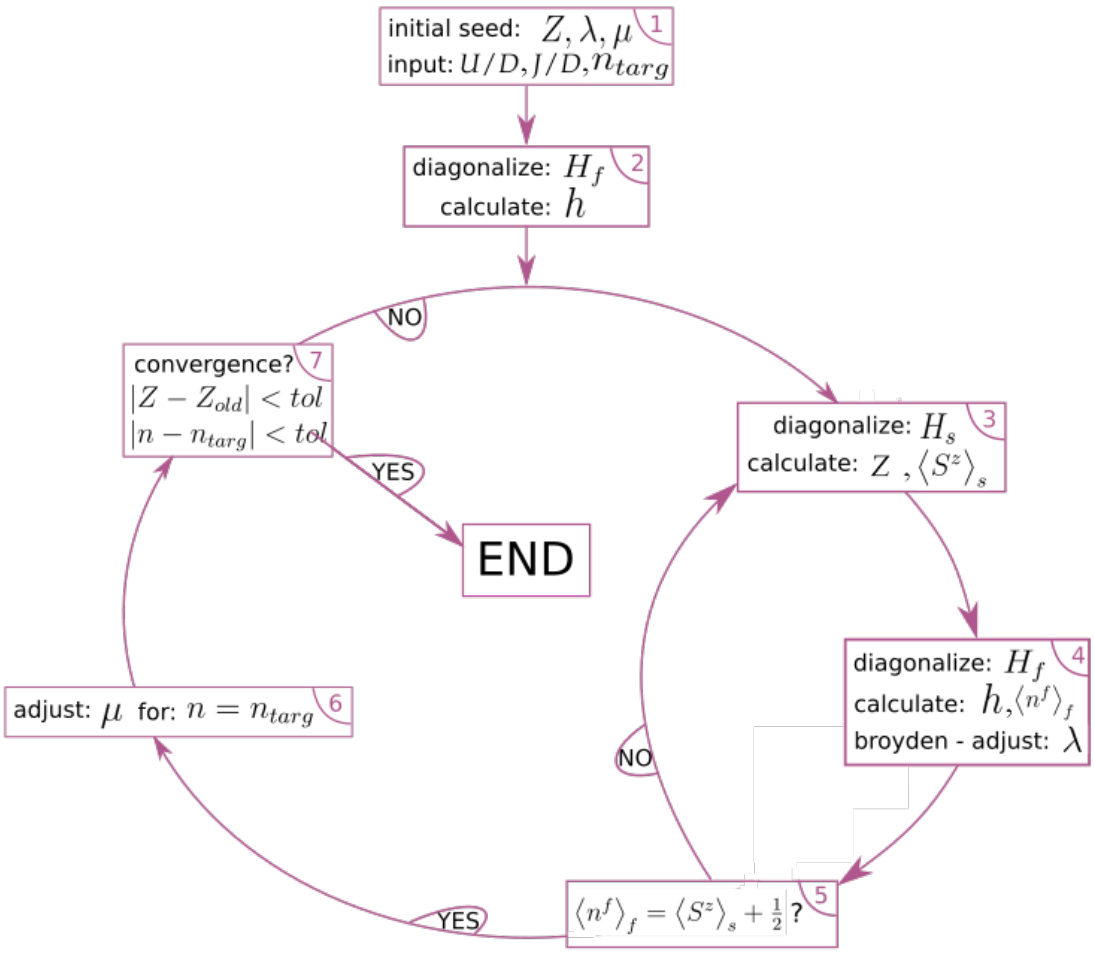

FIGURE 2.1: Schematic representation of the SSMF cycle.

and

$$Z_m = |\langle O_{m\sigma} \rangle_s|^2. \tag{2.34}$$

The constraint as well as the gauge are both also orbitally dependent:

$$\begin{aligned} \langle n^f_{im\sigma} \rangle_f &= \langle S^z_{im\sigma} \rangle_s + \frac{1}{2}, \\ c_{im\sigma} = c_m &= \frac{1}{\sqrt{\langle n^f_{im\sigma} \rangle (1 - \langle n^f_{im\sigma} \rangle)}} - 1. \end{aligned} \tag{2.35}$$

Before presenting the perturbative expansion of the SSMF equations a comment is in order regarding the fermionic Hamiltonian of Eq.2.32. The on-site energy term ϵ_m is *not* renormalized by the quasiparticle weight, its value is instead shifted by the λ_m of

the relevant orbital. In the non-interacting limit the original dispersion of the non-interacting electrons should be recovered and this implies $\lambda_m = 0$. This condition is not fulfilled by the current formulation of the SSMF, since it gives $\lambda_m(U = J = 0) = \frac{2n_{m\sigma}-1}{n_{m\sigma}(1-n_{m\sigma})}h_{m\sigma}$. In order to compensate for this artificial shift and cure the issue we shift the bare orbital energies by adding to the fermionic Hamiltonian a term $+\lambda_m^0 = f_{im\sigma}^\dagger f_{im\sigma}$, where $\lambda_m^0 = \lambda_m(U = J = 0)$. As we said earlier, in [65] a slightly different formulation of SSMF is found and in that case the λ_m^0 shift takes the form $\lambda_m^0 = \sqrt{Z_m}\frac{2n_{m\sigma}-1}{n_{m\sigma}(1-n_{m\sigma})}h_{m\sigma}$. This choice has been found to give improved results, see [66] for a detailed study. In this thesis we will be using the first form (of the present SSMF formulation) but in some parts when aiming to quantitative accuracy we will use the second form of λ_m^0 and specify the choice.

2.2.5 Perturbative expansion of the SSMF formalism

In this section we treat the SSMF equations in a perturbative approach in order to infer some insight from the analysis of the energy spectrum. In the framework of SSMF $h_{m\sigma} = 0$ corresponding to $Z_m = 0$ describes a Mott insulator, so we can develop the system around this solution and analyze the Mott transition. In chapters 4 and 5 this approach will be used to analyze the order of the transition in different models.

We start with the single-orbital Hubbard model at half-filling and calculate the critical interaction strength U_c for the Mott transition by applying first-order perturbation theory. Upon going to higher orders in the perturbation we will be able to also describe the way in which the Mott transition is obtained, through an expression for the quasiparticle weight Z as a function of the interaction U - valid close to the transition. The starting point is the insulating solution, which in the context of the SSMF is actually the atomic limit:

$$H_{at} = \frac{U}{2}\Big(\sum_\sigma S_\sigma^z\Big)^2, \tag{2.36}$$

of which the spectrum is shown in Fig.2.2[2]. The kinetic part of the slave-spin Hamiltonian can be treated as a perturbation on the insulating solution, with h being the parameter of the perturbation, since it is zero at the transition to the insulator and small close by it. The perturbative Hamiltonian will thus be:

$$H_{pert} = h\sum_\sigma 2S_\sigma^x, \tag{2.37}$$

[2]For compactness of notation, the slave-spin states are here indicated with the ket of the physical state they represent.

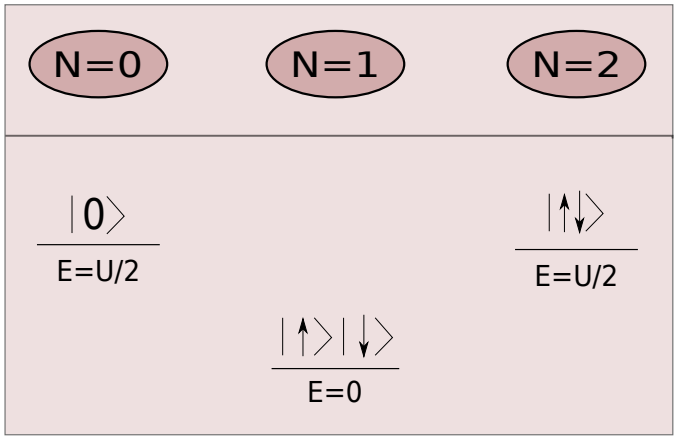

FIGURE 2.2: Atomic spectrum of a single-orbital Hubbard model at half-filling[2].

since at half-filling the gauge is $c = 1$ so $O_\sigma = 2S^x_\sigma$ and we define at this stage $h = h_\sigma + h^*_\sigma$ in order to simplify the formalism. The unperturbed ground state is degenerate, therefore we must apply the degenerate perturbation theory [67]. Moreover, we notice that the perturbation does not have any non-zero elements in the low-energy subspace, so we have to use second-order perturbation theory to calculate the state to which the perturbed one will tend for $h \to 0$. In order to do that we diagonalize in the degenerate subspace the matrix:

$$H^{'} = H_{pert}(E_o - H_{at})^{-1}H_{pert} = -\frac{4h^2}{U}\begin{pmatrix} 1 & 1 \\ 1 & 1 \end{pmatrix} \tag{2.38}$$

and we obtain the ground state:

$$|\phi^0\rangle = \frac{1}{\sqrt{2}}\Big(|\uparrow\rangle + |\downarrow\rangle\Big). \tag{2.39}$$

The perturbative parameter in the expansion is h and the "corrected" ground state is:

$$|\phi\rangle = |\phi^0\rangle + h|\phi^0_{(I)}\rangle + h^2|\phi^0_{(II)}\rangle + h^3|\phi^0_{(III)}\rangle + ... \ . \tag{2.40}$$

We make use of the following compact expressions giving the normalized eigenstates up to third order [68]:

$$
\begin{aligned}
|\phi^0_{(I)}\rangle =& \frac{V_{\kappa_1\phi}}{E_{\phi\kappa_1}}|\kappa^0_1\rangle, \\
|\phi^0_{(II)}\rangle =& \left(\frac{V_{\kappa_1\kappa_2}V_{\kappa_2\phi}}{E_{\phi\kappa_1}E_{\phi\kappa_2}} - \frac{V_{\phi\phi}V_{\kappa_1\phi}}{E^2_{\phi\kappa_1}}\right)|\kappa^0_1\rangle - \frac{1}{2}\frac{V_{\phi\kappa_1}V_{\kappa_1\phi}}{E^2_{\kappa_1\phi}}|\phi^0\rangle, \\
|\phi^0_{(III)}\rangle =& \left[- \frac{V_{\kappa_1\kappa_2}V_{\kappa_2\kappa_3}V_{\kappa_3\phi}}{E_{\kappa_1\phi}E_{\phi\kappa_2}E_{\phi\kappa_3}} + \frac{V_{\phi\phi}V_{\kappa_1\kappa_2}V_{\kappa_2\phi}}{E_{\kappa_1\phi}E_{\phi\kappa_2}}\left(\frac{1}{E_{\phi\kappa_1}} + \frac{1}{E_{\phi\kappa_2}}\right) - \right. \\
& \left. \frac{|V_{\phi\phi}|^2V_{\kappa_1\phi}}{E^3_{\kappa_1\phi}} + \frac{|V_{\phi\kappa_2}|^2V_{\kappa_1\phi}}{E_{\kappa_1\phi}E_{\phi\kappa_2}}\left(\frac{1}{E_{\phi\kappa_1}} + \frac{1}{2E_{\phi\kappa_2}}\right)\right]|\kappa^0_1\rangle + \\
& \left[- \frac{V_{\phi\kappa_2}V_{\kappa_2\kappa_1}V_{\kappa_1\phi} + V_{\kappa_2\phi}V_{\kappa_1\kappa_2}V_{\phi\kappa_1}}{2E^2_{\phi\kappa_2}E_{\phi\kappa_1}}\right]|\phi^0\rangle.
\end{aligned}
\tag{2.41}
$$

In the above formulas we have defined:

$$
V_{\mu\kappa} = \langle\mu^0|V|\kappa^0\rangle, \tag{2.42}
$$

with $V = \sum_\sigma 2S^x_\sigma$ in our case,

$$
E_{\mu\kappa} = E^0_\mu - E^0_\kappa \tag{2.43}
$$

and we are summing over all the states $|\kappa^0_1\rangle \neq |\phi^0\rangle$[3]. In our case $V_{\phi\phi} = 0$ because the basis states are eigenstates of $S^z_{m\sigma}$. Only neighbouring sectors are connected through V, so the terms including $V_{\phi\kappa_3}V_{\kappa_3\kappa_2}V_{\kappa_2\phi}$ vanish as well. The remaining terms are:

$$
\begin{aligned}
|\phi^0_{(I)}\rangle =& \frac{V_{\kappa_1\phi}}{E_{\phi\kappa_1}}|\kappa^0_1\rangle, \\
|\phi^0_{(II)}\rangle =& \frac{V_{\kappa_1\kappa_2}V_{\kappa_2\phi}}{E_{\phi\kappa_1}E_{\phi\kappa_2}}|\kappa^0_1\rangle - \frac{1}{2}\frac{V_{\phi\kappa_1}V_{\kappa_1\phi}}{E^2_{\kappa_1\phi}}|\phi^0\rangle, \\
|\phi^0_{(III)}\rangle =& \left[- \frac{V_{\kappa_1\kappa_2}V_{\kappa_2\kappa_3}V_{\kappa_3\phi}}{E_{\kappa_1\phi}E_{\phi\kappa_2}E_{\phi\kappa_3}} + \frac{|V_{\phi\kappa_2}|^2V_{\kappa_1\phi}}{E_{\kappa_1\phi}E_{\phi\kappa_2}}\left(\frac{1}{E_{\phi\kappa_1}} + \frac{1}{2E_{\phi\kappa_2}}\right)\right]|\kappa^0_1\rangle.
\end{aligned}
\tag{2.44}
$$

From Eq.2.44 the first-order correction to the ground state is:

$$
|\phi^0_{(I)}\rangle = -\frac{4h}{\sqrt{2}U}\Big(|\uparrow\downarrow\rangle + |0\rangle\Big). \tag{2.45}
$$

One fast realises that if we calculate $\langle 2S^x_\sigma\rangle$ we can use the self-consistency condition $h = 2\epsilon_0\langle 2S^x_\sigma\rangle$ - defined earlier in this chapter - to evaluate the critical interaction strength

[3]It is important to notice that the ground state manifold is excluded from the sum.

U_c for the Mott insulator. The calculation of $\langle 2S^x_\sigma \rangle$ up to first order in h gives:

$$\begin{aligned}\langle 2S^x_\sigma \rangle &= \langle 2S^x_\sigma \rangle_{(0)} + \langle 2S^x_\sigma \rangle_{(I)} = \\ &= 2 \cdot \left(\langle \phi^0 | 2S^x_\sigma | \phi^0 \rangle + \langle \phi^0_{(I)} | 2S^x_\sigma | \phi^0_{(I)} \rangle + \langle \phi^0 | 2S^x_\sigma | \phi^0_{(I)} \rangle \right) = \\ &= 2 \cdot \left(0 + 0 - \frac{4h}{U} \right) = -\frac{8h}{U}.\end{aligned} \tag{2.46}$$

Substituting this result in the self-consistency equation $h = 2\epsilon_0 \langle 2S^x_\sigma \rangle$ we obtain the critical interaction for the transition:

$$h = -2\epsilon_0 \frac{8h}{U_c} \Rightarrow U_c = -16\epsilon_0. \tag{2.47}$$

For the infinite coordination Bethe lattice usually used in our calculations, the system has a semi-circular density of states $D(\epsilon) = \frac{2}{\pi D}\sqrt{1 - \left(\frac{\epsilon}{D}\right)^2}$ with half-bandwidth $D = 1$ which gives $\epsilon_0 \simeq -0.2122$, leading to $U_c \simeq 3.39$. This result is in agreement with the numerical one shown in Fig.2.4.

In order to describe the behaviour of the system around U_c close to the Mott transition, the next order in perturbation theory is essential. In a single-orbital system κ_1 could only be equal to ϕ (see Fig.2.2), but the unperturbed ground state is explicitly excluded from the κ sum, so $V_{\kappa_1\kappa_2} V_{\kappa_2\phi} = 0$ as well. The only term left in the expression of the second-order correction is thus proportional to the unperturbed ground state implying that there won't be any non-zero terms in $\langle 2S^x_\sigma \rangle$ to the second order in h. The third order correction to the state is hence required and performing carefully all the necessary summations, keeping the non-zero terms we end up with:

$$|\phi^0_{(III)}\rangle = \frac{96h^3}{\sqrt{2}U^3}(|\uparrow\downarrow\rangle + |0\rangle). \tag{2.48}$$

We calculate $\langle 2S^x_\sigma \rangle$ up to third order and estimate the dependence of the quasiparticle weight Z on the interaction strength U close to the Mott transition.

$$\langle 2S^x_\sigma \rangle_{(II)} = 2 \cdot \langle \phi^0 | 2S^x_\sigma | \phi^0_{(II)} \rangle = 0, \tag{2.49}$$

$$\begin{aligned}\langle 2S^x_\sigma \rangle_{(III)} =& 2 \cdot \left(\langle \phi^0_{(I)} | 2S^x_\sigma | \phi^0_{(II)} \rangle + \langle \phi^0 | 2S^x_\sigma | \phi^0_{(III)} \rangle \right) = \\ =& \frac{64h^3}{U^3} + \frac{192h^3}{U^3} = \frac{256h^3}{U^3}.\end{aligned} \tag{2.50}$$

Summing 2.46, 2.49 and 2.50 making use of the self-consistency equation $h = 2\epsilon_0\langle 2S_\sigma^x\rangle$ we get:

$$\langle 2S_\sigma^x\rangle = -\frac{8h}{U} + \frac{256h^3}{U^3} = \frac{h}{2\epsilon_0}. \tag{2.51}$$

In Fig.2.3 we solve the above equation graphically and show that the linear term in perturbation is enough to calculate U_c, while the cubic term is necessary in order to evaluate the solution at $U < U_c$. The Mott transition $h = \langle 2S_\sigma^x\rangle = 0$ takes place when the tangent of $\langle 2S_\sigma^x\rangle_{pert}$ becomes equal to the linear $\langle 2S_\sigma^x\rangle_{sc}$ curve and in a single-orbital system this happens in a continuous way for U approaching U_c, giving rise to a second-order transition.

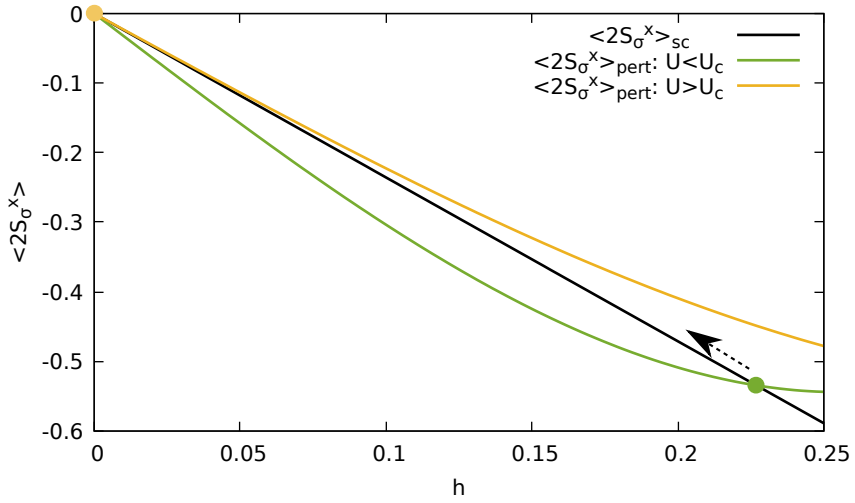

FIGURE 2.3: Graphical representation of Eq.2.51. The crossing of $\langle 2S_\sigma^x\rangle_{sc}$ and $\langle 2S_\sigma^x\rangle_{pert}$ at $U < U_c$ corresponding to a metallic solution, continuously moves towards $h = \langle 2S_\sigma^x\rangle = 0$ for growing U and the transition is second order.

Substituting $h^2 = 2\epsilon_0\langle 2S_\sigma^x\rangle = 4\epsilon_0^2 Z$ we finally obtain:

$$Z = \frac{U^2}{128\epsilon_0^2} + \frac{U^3}{2048\epsilon_0^3}, \tag{2.52}$$

which written in a more compact way becomes:

$$Z = \frac{U^2}{128\epsilon_0^2}\left(1 - \frac{U}{U_c}\right). \tag{2.53}$$

In Fig.2.4 the analytical expression is plotted together with the numerical results.

In Appendix C.2.1 we demonstrate the perturbative derivation of the system's behavior away from half-filling. This perturbative approach to the SSMF equations will

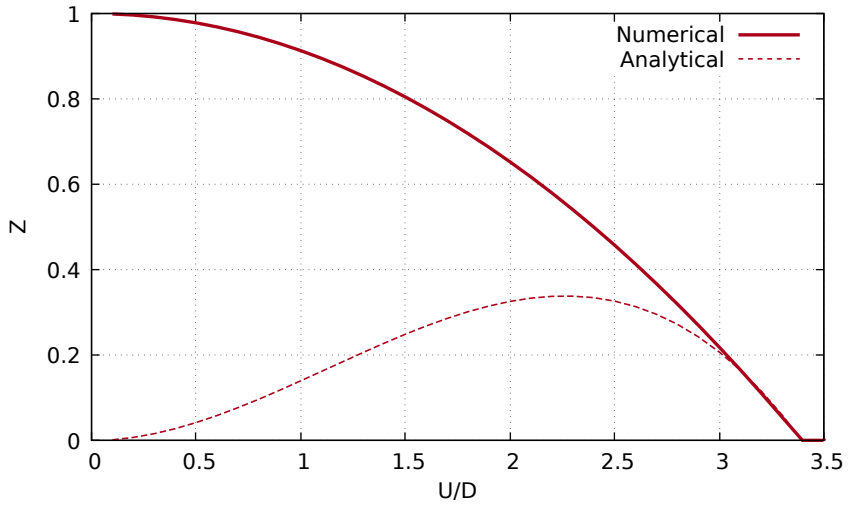

FIGURE 2.4: Quasiparticle weight of a single-orbital system as a function of the interaction strength at half-filling. The numerical results are obtained using SSMF and the analytical ones by applying perturbation theory up to third order in h.

turn out to be very useful in chapter 5 when working on multi-orbital systems. The analytical derivations will complement the numerical results and provide an insight on the physics of the *Hund metal* phase, which will be central in the studies of this manuscript.

2.3 Dynamical Mean Field Theory

Dynamical Mean Field Theory (DMFT) is one of the most widely used methods for describing the electronic properties of strongly correlated systems. The complications in capturing these properties are related to the different energy scales emerging, for instance the atomic exhcitations at high-energy and the appearance of long-lived quasiparticles at low-energy. The technique's success lies in its ability to handle all the energy scales involved in the excitation spectrum of such systems on the same footing, as shown in Fig.2.5 for the paradigmatic single-band Hubbard model. This picture captures at high energy the lower and upper Hubbard bands related to the atomic physics and at low energy a peak corresponding to the quasiparticle excitations [69, 70, 71].

DMFT's goal is to address a lattice problem and its large number of degrees of freedom which make it unsolvable. In order to achieve that, the main idea is to replace the lattice problem by an Anderson impurity embedded into a bath, which effectively describes the environment of an atom in the original lattice and with which the impurity

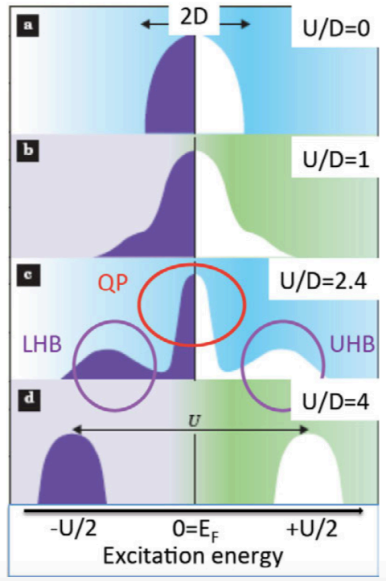

FIGURE 2.5: Sketch of the total density of states of the half-filled Hubbard model as a function of interaction strength U, within DMFT. The high-energy structures are the lower and upper Hubbard bands, while the low-energy peak is due to the quasiparticles [72].

can exchange electrons, Fig.2.6. This approach, first of all, avoids crude approximations often used in other techniques working directly on the lattice. Moreover, the major advantage comes from the fact that the Anderson impurity model has been extensively studied for decades and various methods for solving it are available. In the following sections we will introduce the DMFT method following the formalism of [4] and [73].

2.3.1 Analogy to the Weiss mean field method

The mapping of the problem onto a single impurity in contact with an effective bath, as introduced above, is along the same lines as the well known Weiss mean field applied on an Ising model of classical spins, with the Hamiltonian:

$$\hat{H} = -\sum_{<ij>} J_{ij} S_i S_j - h \sum_i S_i, \tag{2.54}$$

where $< ij >$ implies that neighbouring sites are coupled through J_{ij} and h represents an external magnetic field. The mean-field approximation is applied by mapping the above Hamiltonian to one of single non-interacting spins coupled to an effective field

h^{eff}:

$$\hat{H}^{eff} = -\sum_i h_i^{eff} S_i. \tag{2.55}$$

This effective magnetic field depends on the original external field h as well as on the magnetic field resulting from the interaction of site i with the spins of all the neighbouring sites. The latter is linear in the magnetization $m_i = \langle S_i \rangle$ and the final equation for h^{eff} is:

$$h_i^{eff} = h + \sum_{<ij>} J_{ij} m_j = h + zJm, \tag{2.56}$$

where z is the connectivity (number of neighbouring to i sites) and $J_{ij} = J$ due to translational invariance of the system. It can be shown that the magnetization has the following form:

$$m = tanh[\beta(h + zJm)] \tag{2.57}$$

and therefore the problem can be solved self-consistently.

The DMFT scheme is in the same spirit as the above described Weiss mean field, since a corresponding effective model is introduced, Fig.2.6, allowing us to solve the original lattice problem. The role that h^{eff} plays in the case of the Ising model is played in the Anderson impurity one by the "hybridization" function $\Delta(i\omega)$ between the impurity and the bath, which embodies information of the original lattice problem. The system is then solved self-consistently.

2.3.2 Dynamical Mean Field Theory construction

Before we introduce the DMFT construction, it is important to mention that this mapping of the lattice problem on the Anderson impurity one is exact only in the limits in which the system:

- has infinite dimensions or infinite connectivity z,
- is in the atomic limit, so that there is no electron hopping between the lattice sites,
- is in the non-interacting limit, thus consisting of free electrons.

In the rest of this work when working on realistic materials we will be out of these limits while when studying models we will use the infinite coordination Bethe lattice, which fulfils the first condition.

In the following presentation of the DMFT equations we focus for simplicity on a single-orbital system, however all the calculations can be generalized for the more

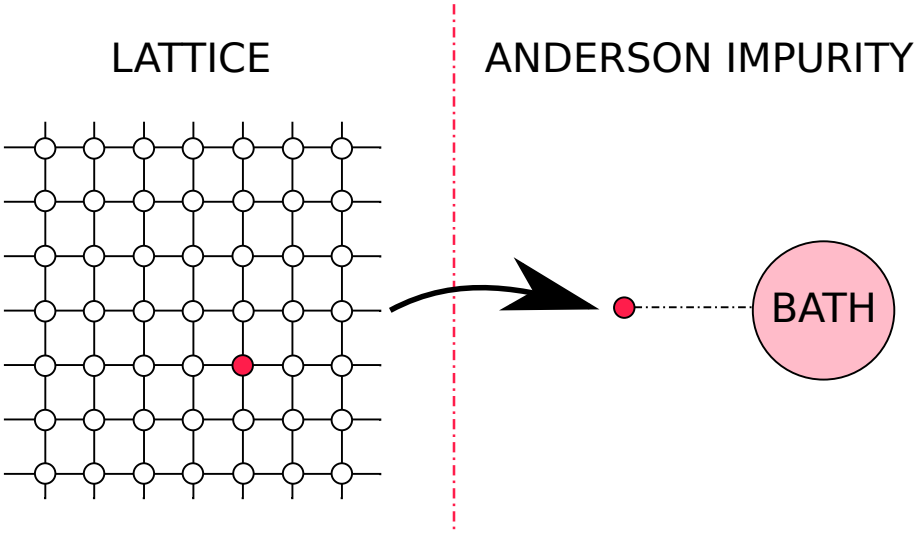

FIGURE 2.6: Mapping of the lattice problem on the Anderson impurity one.

complex multi-orbital case. The single-orbital Hubbard Hamiltonian already introduced in Eq.2.5 and now including the chemical potential and onsite energy terms, describing the lattice problem will be replaced by the Anderson impurity Hamiltonian:

$$\begin{aligned}\hat{H}_{AIM} &= \hat{H}_{impurity} + \hat{H}_{bath} + \hat{H}_{coupling} \\ &= U n^a_\uparrow n^a_\downarrow + (\epsilon_0 - \mu)(n^a_\uparrow + n^a_\downarrow) + \sum_{l,\sigma} \tilde{\epsilon}_l b^\dagger_{l\sigma} b_{l\sigma} + \sum_{l,\sigma} V_l (a^\dagger_\sigma b_{l\sigma} + b^\dagger_{l\sigma} a_\sigma),\end{aligned} \tag{2.58}$$

with the first two local terms corresponding to the impurity $(a_\sigma, a^\dagger_\sigma)$, the third term describing the effective bath $(b_{l,\sigma}, b^\dagger_{l,\sigma})$ and the last term representing the hybridization between them. The parameters $\tilde{\epsilon}_l$ and V_l must be chosen in such a way that the impurity's Green's function coincides with the local Green's function of the lattice problem. If we define the hybridization function:

$$\Delta(i\omega_n) = \sum_l \frac{|V_l|^2}{i\omega_n - \tilde{\epsilon}_l}, \tag{2.59}$$

it can be shown that the action functional formalism gives the following impurity's effective action, with the bath degrees of freedom having been integrated out:

$$S^{eff} = -\int_0^\beta d\tau \int_0^\beta d\tau' \sum_\sigma a^\dagger_\sigma(\tau) \mathcal{G}_0^{-1}(\tau - \tau') a_\sigma(\tau') + U \int_0^\beta d\tau n_\uparrow(\tau) n_\downarrow(\tau), \tag{2.60}$$

where

$$\mathcal{G}_0^{-1}(i\omega_n) = i\omega_n + \mu - \epsilon_0 - \Delta(i\omega_n). \tag{2.61}$$

This $\mathcal{G}_0$ can be viewed as the quantum generalization of the Weiss mean field introduced above, which now is a function of energy and reflects the local quantum fluctuations of the system. It represents the bare Green's function of the impurity and it should not be confused with the local non-interacting Green's function G_0 of the original lattice problem. In analogy with the Weiss mean field process, a self-consistent equation must then be introduced, ensuring that $G_{imp} = G_{loc}$ and allowing us to solve the problem. The local Green's function of the original lattice system is calculated as:

$$G_{loc}(i\omega_n) = \sum_{\mathbf{k}} \frac{1}{i\omega_n + \mu - \epsilon_0 - \epsilon_{\mathbf{k}} - \Sigma(\mathbf{k}, i\omega_n)}. \tag{2.62}$$

The DMFT approximation is made at this stage and the momentum dependence of the self-energy is ignored. $\Sigma(\mathbf{k}, i\omega_n)$ is approximated with the purely local self-energy of the Anderson impurity $\Sigma_{imp}(i\omega_n)$:

$$\Sigma(\mathbf{k}, i\omega_n) \simeq \Sigma_{imp}(i\omega_n), \tag{2.63}$$

where

$$\Sigma_{imp}(i\omega_n) = \mathcal{G}_0^{-1}(i\omega_n) - G_{imp}^{-1}(i\omega_n). \tag{2.64}$$

Using that, the Eq.2.62 becomes:

$$\begin{aligned} G_{loc}(i\omega_n) &= \sum_{\mathbf{k}} \frac{1}{i\omega_n + \mu - \epsilon_0 - \epsilon_{\mathbf{k}} - \Sigma_{imp}(i\omega_n)} \\ &= \sum_{\mathbf{k}} \frac{1}{i\omega_n + \mu - \epsilon_0 - \epsilon_{\mathbf{k}} - (\mathcal{G}_0^{-1}(i\omega_n) - G_{imp}^{-1}(i\omega_n))}, \end{aligned} \tag{2.65}$$

which by making use of Eq.2.61 turns into:

$$\begin{aligned} G_{loc}(i\omega_n) &= \sum_{\mathbf{k}} \frac{1}{i\omega_n + \mu - \epsilon_0 - \epsilon_{\mathbf{k}} - i\omega_n - \mu + \epsilon_0 + \Delta(i\omega_n) + G_{imp}^{-1}(i\omega_n)} \\ &= \sum_{\mathbf{k}} \frac{1}{\Delta(i\omega_n) + G_{imp}^{-1}(i\omega_n) - \epsilon_{\mathbf{k}}}. \end{aligned} \tag{2.66}$$

Since we have assumed that the self-energy of the original lattice problem is purely local and equal to the impurity self-energy, we can take away the subscripts of the two Green's functions and end up with the DMFT self-consistency equation:

$$G(i\omega_n) = \sum_{\mathbf{k}} \frac{1}{\Delta(i\omega_n) + G^{-1}(i\omega_n) - \epsilon_{\mathbf{k}}}, \tag{2.67}$$

which can also be written in the continuum, if one knows the density of states of the system defined as $D(\epsilon) = \sum_k \delta(\epsilon - \epsilon_k)$, as follows:

$$G(i\omega_n) = \int d\epsilon \frac{D(\epsilon)}{\Delta(i\omega_n) + G^{-1}(i\omega_n) - \epsilon}. \tag{2.68}$$

For the DOS of a Bethe lattice $D(\epsilon) = \frac{2}{\pi D}\sqrt{1 - \left(\frac{\epsilon}{D}\right)^2}$ the above integral can be solved analytically and the self-consistency condition takes the simpler form:

$$\Delta(i\omega_n) = t^2 G(i\omega_n), \tag{2.69}$$

where $t = D/2$ (with D the half-bandwidth). In summary, the decisive step shaping the DMFT scheme is the approximation of the original problem's momentum-dependent lattice self-energy with the fully local impurity self-energy. This enforces the local lattice Green's function to be equal to the impurity Green's function, leading to the self-consistency Eq.2.67. All the problem, hence, boils down to solving this equation iteratively, necessitating as sole input the hybridization function Δ of Eq.2.59.

The whole leverage of DMFT lies on the fact that the Anderson impurity embedded in a bath is a well-studied problem, with various techniques available to solve it, which in the DMFT context are called *impurity solvers*. The most widely implemented solvers are the *Continuous-Time Quantum Monte Carlo (CTQMC)* [74, 75, 76, 77, 78], the *Exact Diagonalization (ED)* [79, 80, 81], the *Iterative Perturbation Theory (IPT)* [4, 69, 82, 83], the *Numerical Renormalization Group (NRG)* [84, 85, 86] and the *Density Matrix Renormalization Group (DMRG)* [87, 88]. In this work we have mainly used the Exact Diagonalization impurity solver, which works on a discretized bath. The hybridization function Δ is the problem's input embodying information on the bath and its coupling to the impurity. Δ is given through discretized orbitals labeled l, each of them corresponding to a couple of $\{\tilde{\epsilon}_l, V_l\}$. The number of these orbitals defines the size of the problem's Hilbert space and is, thus, the one controlling the numerical limitations of the approach. We present below the steps followed in the DMFT cycle, specifying the details of the ED solver (the cycle is also plotted schematically in Fig.2.7):

1. The DMFT sef-consistency cycle begins with an initial guess given to the system for the set of values $(\tilde{\epsilon}_l, V_l)$ and Δ is calculated through Eq.2.59. The parameters necessary to build the system's Hamiltonian are provided as input: the dispersion relation of the original lattice's tight-binding (or the density of states $D(\epsilon)$), the chemical potential μ (or the total population of the system n_{tot}) and the interaction strength U (and Hund's coupling J if we are working with a multi-orbital system).

2. Next the Anderson impurity model's Hamiltonian is constructed and making use of the guess the Weiss mean-field $\mathcal{G}_0$ is calculated from Eq.2.61.

3. The following and most resource-consuming step is to utilize the impurity solver and calculate the interacting Green's function of the impurity problem $G_{imp}(i\omega)$, by (in the case of ED) diagonalizing the Hamiltonian. Making use of $G_{imp}(i\omega)$ and $\mathcal{G}_0$ calculated in step 2, one can resort to Dyson's equation and obtain the self-energy of the effective impurity model.

4. At this stage the new Green's function is calculated from the self-consistency Eq.2.67.

5. The Dyson's equation is once again employed in the opposite way, using the earlier calculated self-energy and the new Green's function to obtain the new Weiss mean-field $\mathcal{G}_0^{new}$. It is numerically fitted to Eq.2.61 and $\{\tilde{\epsilon}_l, V_l\}$ are extracted.

6. The last step is the check on convergence, necessary to eventually exit the cycle. A tolerance is set and if two consecutive values of $\mathcal{G}_0$ differ by less than that limit, the system has met convergence and the DMFT loop ends; if not the iterations continue from step 2, with the input now being the result of the current cycle (the convergence check can be equivalently made on $G_{imp}(i\omega)$).

2.3.3 Limitations of Lanczos diagonalization algorithm

In the last section of this methodological chapter we would like to bring attention onto a technical difficulty we encountered during our study with DMFT. As mentioned earlier we have been mainly using ED as the solver in the DMFT cycle, which solves the impurity problem by using a discretized bath to construct the Hamiltonian and evaluate the eigenvalues and eigenvectors. This can be done either by performing what is called a *full diagonalization* or by using the *Lanczos method* [89]. The former is exact but has the problem of imposing a quite low limit on the size of the Hilbert space. On the other hand, Lanczos working on the Krylov space requires less vectors for calculating the ground-state energy and it is computationally much cheaper. To make a comparison we can say that storing a matrix (for a system of N electrons) within the Lanczos approach takes only $\mathcal{O}(N)$ memory and $\mathcal{O}(N)$ time while a full diagonalization needs $\mathcal{O}(N^2)$ for storing the matrix and $\mathcal{O}(N^3)$ diagonalization time [90].This method (together with the similar in spirit *Arpack method* used at finite temperature) has been extensively exploited in the literature of DMFT.

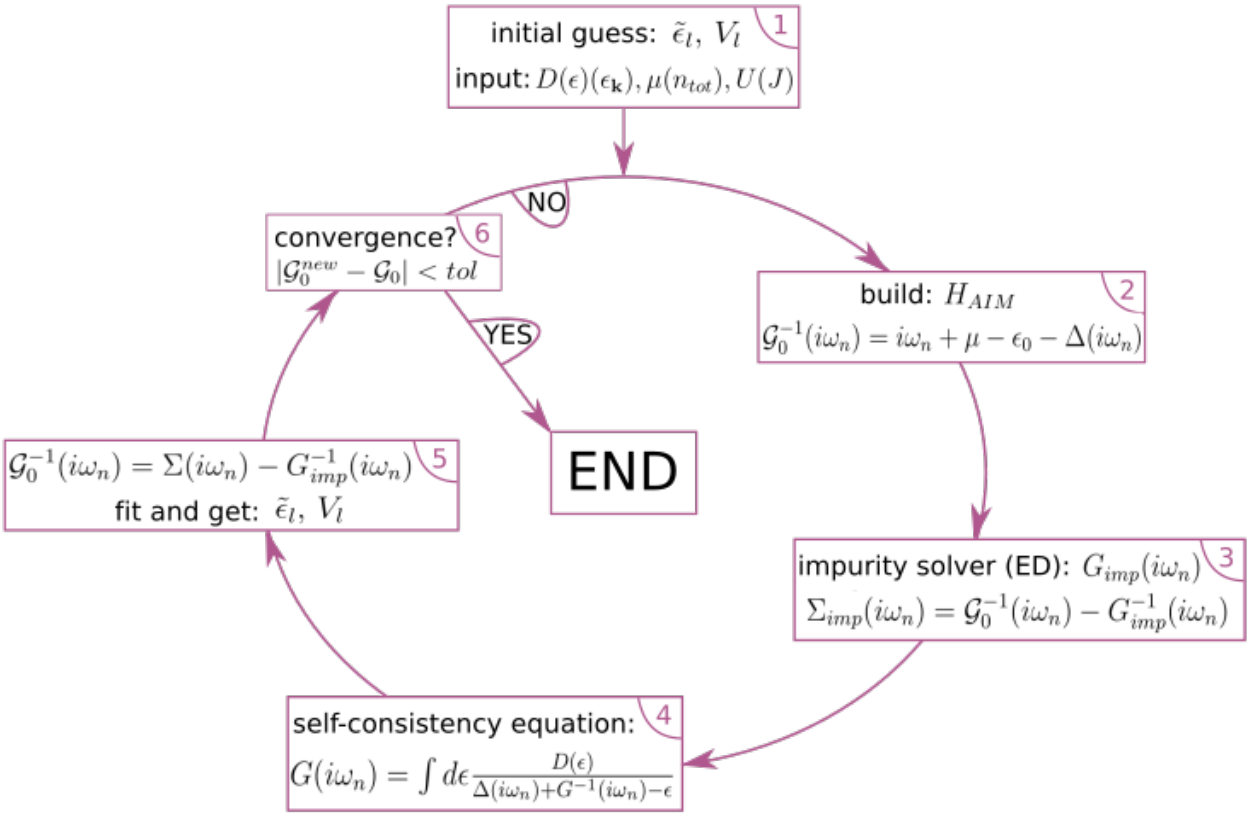

FIGURE 2.7: Schematic representation of the DMFT cycle.

However, it is well known that the algorithm presents some pathologies in resolving degenerate states, which is actually a problem of any Krylov method. The issue is in fact two-fold. On one hand there are spurious degeneracies which are related to the loss of precision in the Krylov basis construction. Essentially there is generation of vectors which have infinitesimal components along some directions they're supposed not to have, i.e. they should be orthogonal. This is generally cured using Block Lanczos and re-orthogonalization. On the other hand and more importantly for the systems of our study, problems are created due to real degeneracies in the spectrum. In this case the iterative construction of the Krylov basis has hard time finding a good basis for the degenerate sub-space. This can in fact be detrimental to the whole procedure because it generates spurious eigensolutions.

In practice, we realized this was causing us severe drawbacks when working in particular regions of the phase space where a high degree of degeneracy is found. We are plotting as an example in Fig.2.8 a direct comparison of the chemical potential as a function of total density calculated with Full ED and Lanczos. We see that for the case of Full ED there is an interesting effect of non monotonicity observed (it will be discussed in detail in chapter 4), which is completely ignored in the Lanczos results. For that reason in most of the work performed in this thesis using ED DMFT we have

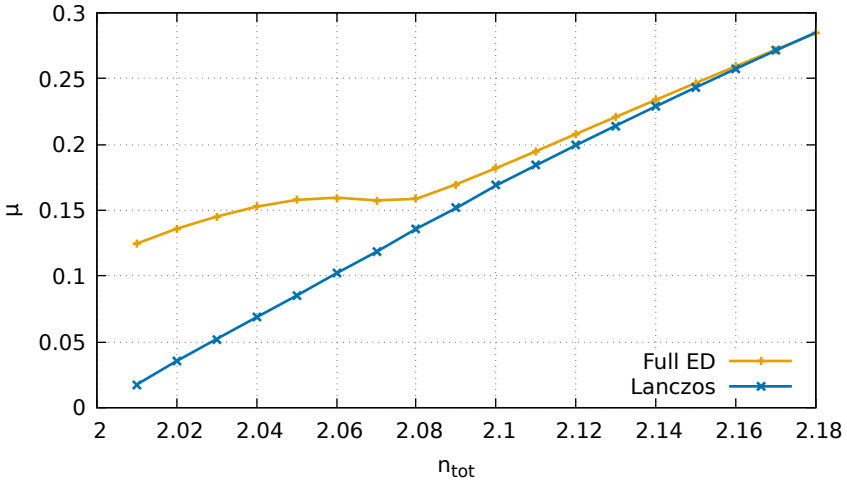

FIGURE 2.8: Chemical potential as a function of total density for a two-band model at $T = 0$ and $U = 1.32, J/U = 0.25$, using $Ns = 6$. We compare the result produced using Full ED and Lanczos and we see that Lanczos fails to reproduce the negative compressibility zone.

applied full diagonalization. When possible, as specified in the text, we still used the Lanczos/Arnoldi algorithm. This choice imposed certain limits on our analysis and we will revisit this issue in the following chapters.

Chapter 3

Hund metals

The *Hund metals* have attracted a lot of attention over the last decade and various different studies have been performed. The precise definition of their properties is the subject of intense ongoing research [91, 92, 93, 94, 95, 96, 97, 98, 99, 100] and somewhat of an open problem. In this chapter we mainly discuss the approach suggested in [1], within which there are three characteristic properties appearing on a frontier between a normal metal and a Hund metal, extending in the interaction-doping plane. The observed properties are (i) strong correlations and mass enhancements, (ii) large local fluctuating magnetic moments and (iii) orbital selectivity based on the degree of correlation. We further present past results of calculations performed on different models as well as on realistic materials considered to be Hund metals, in particular compounds of iron-based superconductors.

3.1 Introduction

In 2011, almost a century after the formulation of Hund's rules by Friedrich Hund [101], the expression *Hund metal* was first introduced in a study of iron-based superconductors (IBSC) [91]. In that context the term referred to a phase in which the metallic properties of a system are highly influenced by *Hund's coupling*[1]. In this thesis we follow the scenario suggested in [1], where a set of emerging properties of Hund metals - listed below - are discussed:

- strong electronic correlations and enhanced electron masses,
- paramagnetic fluctuations controlled by large local magnetic moments,
- orbitally selective electronic correlations.

All the aforementioned features characterising the Hund metal phase emerge beyond a crossover line in the plane of electron doping and interaction strength and they

[1] Hund's coupling refers to the intra-atomic exchange interaction, which favours the electronic spin alignment.

appear enhanced at large interactions and at dopings away from half-filling but close to it. This crossover can be identified (at least near half-filling - as we will discuss more in chapter 5) with the finite temperature "spin freezing" line introduced in [92, 93] within a scenario suggesting that at the frontier a phase transition between a coherent and an incoherent system with frozen local moments and non-Fermi liquid self-energy takes place. In this chapter we show past results indicating that at half-filling Hund's coupling favours the formation of a Mott insulator. We further argue that the proximity of a system to a Mott insulator can play a major role in the properties of the Hund metal phase.

The IBSC are the most widely studied systems called Hund metals [91], however in the last years more materials are considered as such, with most pronounced example the Ruthenates [102, 103]. The characteristic properties of Hund metals exposed above are also met in model studies, as we will extensively present in the rest of this text.

3.2 Experimental evidences

The set of properties suggested to characterize the Hund metals in [1] have been formulated in accordance with experimental findings originally on different compounds of the IBSC. In this section we give distinctive examples of such experimental evidences related to each of the three Hund metal features, accompanied by theoretical calculations.

3.2.1 Mass enhancement signalling strong electronic correlations

There is a long list of experiments performed on IBSC indicating the existence of large electronic masses through ARPES, optical conductivity, specific heat measurements, quantum oscillations and other probes [104, 105, 106, 107, 108, 109]. We show results of specific heat measurements in the normal phase of IBSC compounds. We inquire the evaluation of the *Sommerfeld coefficient*, which in a Fermi liquid is the slope of the specific heat as a function of temperature in the low temperature regime:

$$\frac{c_v}{T} = \gamma + AT^2. \tag{3.1}$$

γ is given by:

$$\gamma = \frac{\pi^2 k_B^2}{3} D^*(\epsilon_F), \tag{3.2}$$

where $D^*(\epsilon_F)$ is the renormalized quasiparticle density of states at the Fermi level. The Sommerfeld coefficient offers a direct estimate of a system's mass enhancement, since the density of states is in turn enhanced by it. In the case of a single-orbital system its

expression is:

$$D^*(\epsilon_F) = \frac{m^*}{m_b} D(\epsilon_F) \tag{3.3}$$

and similarly in a multi-orbital case $D^*(\epsilon_F)$ is proportional to a linear combination of the respective orbital mass enhancements. The experimental data on $BaFeAs_2$, illustrated with blue squares in Fig.3.1, show that decreasing the nominal electronic population from $n_{tot} = 6.25$ (crossing the parent compound at $n_{tot} = 6$) down to KFe_2As_2 (where $n_{tot} = 5.50$) the Sommerfeld coefficient grows largely [110]. Experimentally, below this point in the plot isovalent substitution is applied and indeed the Sommerfeld coefficient continues to increase monotonically up to huge values, typical for the heavy fermion compounds.

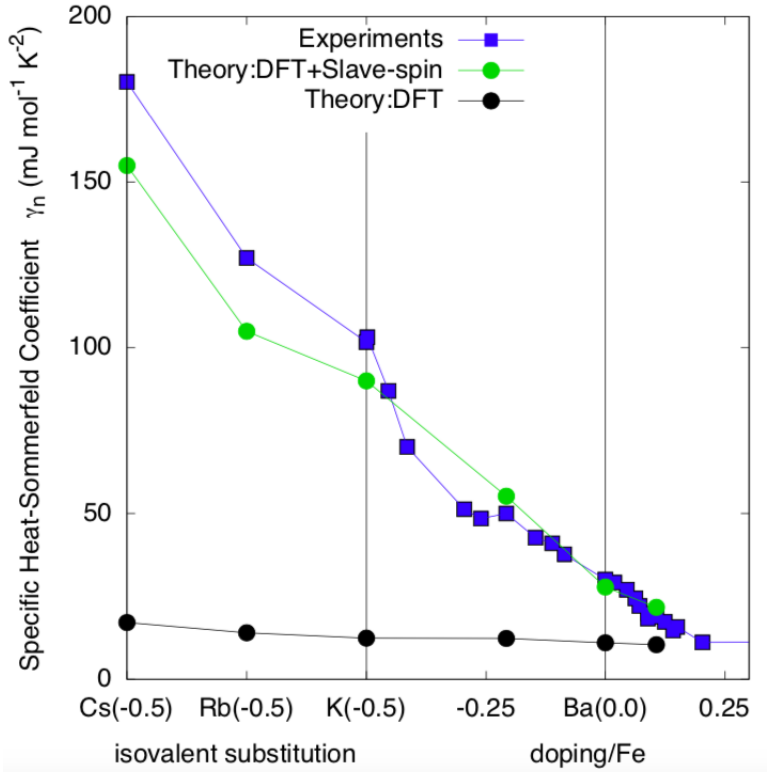

FIGURE 3.1: Measurements of the Sommerfeld coefficient on various IBSC compounds of the 122-family (blue squares). Upon hole doping towards half-filling the system exhibits a large monotonous increase of the Sommerfeld coefficient, signalling an analogous growth of the electronic effective mass. Theoretical calculations using bare DFT band-structures are shown in black circles, with the curve not fitting the experimental data. In green circles DFT+SSMF results with a single choice of $U = 2.7eV$ and $J/U = 0.25$ are plotted, which include explicitly the effect of electronic correlations and they exhibit very good agreement with the experimental measurements [111].

The enormous increase of correlations upon moving towards half-filling implies a purely many-body phenomenon. The enhanced correlations increase the effective

masses of the system's quasiparticles leading to the narrowing of their band-structure, expressed by an amplified $D^*(\epsilon_F)$ and effectively captured by a largely increased Sommerfeld coefficient.

In Fig.3.1 results from theoretical calculations of the Sommerfeld coefficient using DFT (with black points) and DFT+SSMF (with green points) accompany the experimental data. It is evident that DFT in itself fails to reproduce the trend measured in the experiments. However, DFT+SSMF which incorporates explicitly the local many-body correlations exhibits much better agreement with the experiments. It is important to mention that the interaction parameters have been kept unchanged in the calculation of all compounds, therefore the enhanced masses are indeed a product of electronic correlations which should be treated explicitly in the IBSC materials.

3.2.2 High local magnetic moments

As already mentioned in the beginning of this section, another emerging property of the Hund metal zone as proposed in [1] is the formation of large local magnetic moments dominating the paramagnetic fluctuations. Experimentally this phenomenon can be captured by X-ray emission spectroscopy (XES), which estimates the local magnetic moments. In practice, light is shined onto the sample resulting in electrons becoming excited from a core state into a valence one. Typically for such an excitation to take place photons of high energy (in the hard X-ray range) are required and synchrotron radiation is used to produce them. Subsequently, photons are spontaneously emitted as de-excited electrons fill the core holes created earlier and their energy is measured. The emitted line is split into two when a net magnetic moment is present due to an open Fe $3d$ shell with the de-excitation energy depending on the electron's spin character. Therefore, the IAD value [110, 112] which is a measure of this splitting scales with the local magnetic moment. The advantage of this method is that it is a rather fast probe, thus able of capturing these local moments which do not form static long-range orders in the paramagnetic normal phase [110, 112, 113].

In Fig.3.2 data of the IAD value measured on different IBSC compounds are plotted as a function of doping [110]. Upon hole doping the system and approaching half-filling the magnetic moments appear to grow monotonously. In the inset of the figure theoretical calculations of the local magnetic moment using the DFT+SSMF scheme are illustrated as a function of interaction strength U for the compounds KFe_2As_2 and $BaFe_2As_2$. A crossover between a zone of low moments and a zone of high ones appears around the critical interaction of the half-filling Mott transition and in the high moment zone larger values of magnetic moment are exhibited for the compound closer to $n_{tot} = 5$.

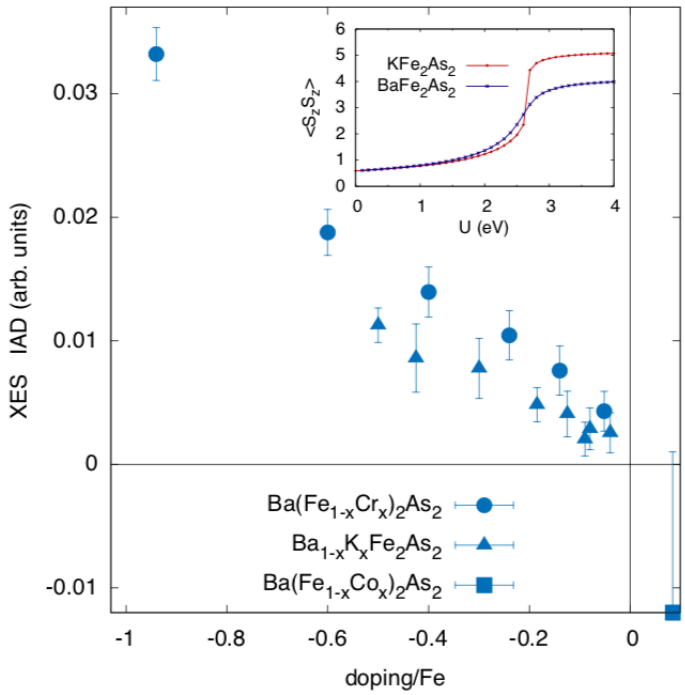

FIGURE 3.2: X-ray emission spectroscopy (XES) measurements on different compounds of $BaFeAs_2$ as a function of hole doping, tracked by the IAD value, a measure of the local magnetic moment, which appears increasing upon approaching half-filling. Inset: theoretical calculations of the local paramagnetic moment on KFe_2As_2 and $BaFe_2As_2$ as a function of interaction strength U, exhibiting a crossover from a low moment zone into a high moment one [110].

This behaviour can be understood considering that Hund's coupling is an interaction favouring the electronic spin alignment. In the vicinity of the Mott insulator the charge fluctuations and ergo the system's metallicity are suppressed and local configurations predominate. Therefore, high local magnetic moments are formed in the Hund metal phase where Hund's coupling holds a dominant role.

3.2.3 Orbitally selective electronic correlations

The third property discussed in [1] as characteristic of Hund metals is the orbital selectivity of the correlation strength. This suggestion emerges from both experimental evidences [114, 115, 116, 104, 105, 106, 107, 117, 118, 108, 119, 109, 120, 121, 122] and theoretical calculations [91, 123, 124, 125, 126, 127, 128, 129, 130, 131, 132] . In Fig.3.3 a collection of different experimental estimates of the mass enhancement on the 122-family of IBSC is illustrated, including data for the specific heat, optical conductivity, ARPES and quantum oscillations. On the electron doped side of the diagram the various experimental probes report very good agreement, however on the hole doped side

they seem to depart from a common line with their differentiation becoming increasingly pronounced by moving towards half-filling.

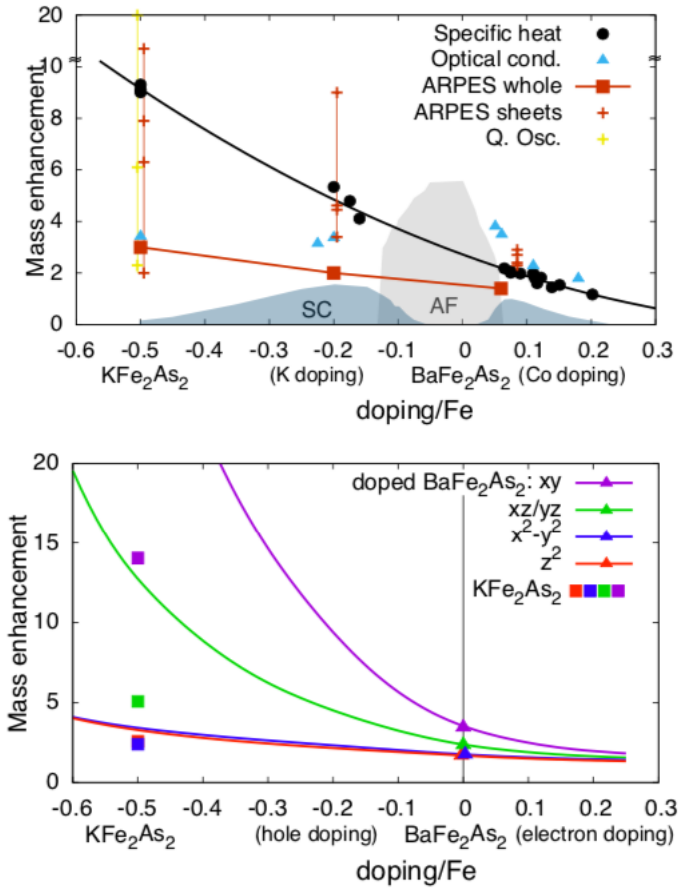

FIGURE 3.3: Upper panel: experimental estimates of the mass enhancement on the 122-family compounds at different doping through specific heat, optical conductivity, two versions of ARPES and quantum oscillations. Certain measurements are sensitive to capturing heavy and others light electrons, while some experiments are orbitally resolved. Lower panel: theoretical calculations of the orbital mass enhancement as a function of doping using DFT+SSMF, confirming the apparent orbital selectivity upon approaching half-filling [123].

The origin of this differentiation is in the way the individual orbital mass renormalizations manifest in each of the plotted experimental measurements. In particular, for the case of specific heat experiments, as it was briefly mentioned in the previous section, the Sommerfeld coefficient in a multi-orbital system is a sum of contributions proportional to the orbital mass enhancements $\left(\frac{m^*}{m_b}\right)_l$. In optical conductivity the low-frequency *Drude spectral weight* is measured, which in a multi-orbital system is a sum of contributions proportional to the inverse electron mass enhancement $\left(\frac{m^*}{m_b}\right)_l^{-1}$. Hence if the orbitals do not exhibit the same degree of correlations, the specific heat measurements will be dominated by the most correlated orbitals, while the optical conductivity by the less correlated ones. For the data points named "ARPES whole" in Fig.3.3 the

mass enhancement is estimated by introducing a global renormalization of the band-structure, determined by the least renormalized of the orbital contributions.

The last two experimental probes reported in Fig.3.3, ARPES (with the data points called "ARPES sheets") and quantum oscillations, evaluate the different orbital mass enhancements individually. These two collections of measurements validate the conclusion suggested by the data of the other probes, by directly showing the renormalized masses of electrons originating from different orbitals to grow apart with decreasing filling.

In the low panel of Fig.3.3 theoretical calculations of the orbitally resolved mass enhancement using DFT+SSMF are shown for the cases of $BaFe_2As_2$ and KFe_2As_2 as a function of doping. The trend of increasing *orbital selectivity* moving towards half-filling is confirmed by these numerical data and in particular the mass enhancement of the xy orbital is always larger and grows faster than the rest of the orbitals. This is interpreted in [123] in terms of "orbital decoupling": a purely many-body effect in which the degree of correlation for electrons in each orbital is mainly set by the proximity of this orbital to individual half-filling. More specifically, the xy orbital in these IBSC compounds is closer to being half-filled ($n_{xy} = 1$) than the others, therefore the mass enhancement of electrons of this orbital character is the largest. Overall, in these systems electrons with different degrees of correlation ("heavier" and "lighter" ones) coexist in most of the phase diagram.

3.3 Model studies of Hund metals

In this section we will review theoretical calculations showing that the aforementioned properties are not specific to the IBSC materials. They are rather general to the models of Hund favoured doped Mott insulating systems. We will be concerned with simplified featureless models of multi-orbital systems including Hund's coupling, eliminating from our analysis realistic band-structures and particularities of the compounds' fermiology.

In these studies the SSMF or DMFT methods have been used to address their zero temperature Fermi liquid phase and evaluate the electron mass enhancements in systems of two, three and five degenerate orbitals, in absence of a crystal-field splitting of the on-site energies between the different orbitals. In the above description of IBSC the non-interacting part of the Hamiltonian embodied properties of each compound through DFT calculations, but these model studies are realized on the *Bethe lattice* [135], which has a featureless semi-circular density of states[2]. Concerning the interacting part

[2]The density of states for the Bethe lattice is given by $D(\epsilon) = \frac{2}{\pi D}\sqrt{1-(\frac{\epsilon}{D})^2}$, where D is the half-bandwidth as described in the methods chapter 2.

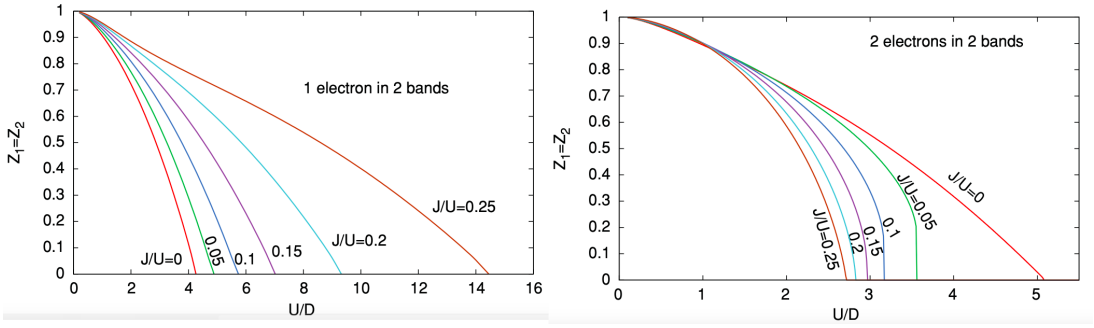

(A)

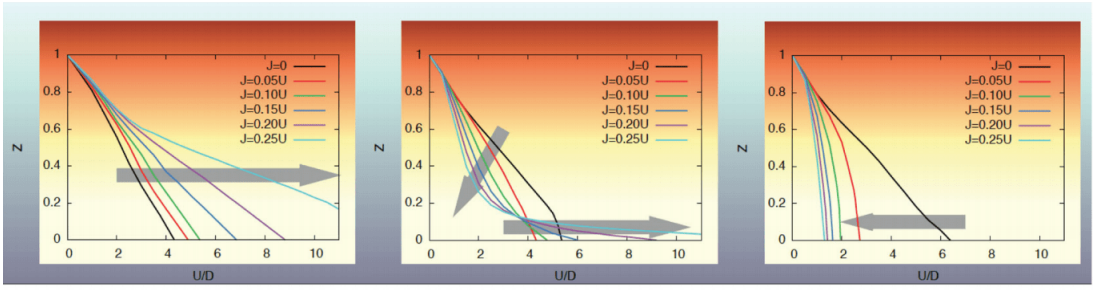

(a) $N = 1$ (b) $N = 2$ (c) $N = 3$

(B)

FIGURE 3.4: **(a)** SSMF calculations of quasiparticle weight in a two-orbital system with Kanamori interactions for different values of J/U, at total electron density $n_{tot} = 1$ (left panel) and $n_{tot} = 2$ (right panel) [133]. **(b)** DMFT calculations for a three-orbital system with Kanamori interactions at total electron density $n_{tot} = 1$ (left panel), $n_{tot} = 2$ (middle panel) and $n_{tot} = 3$ (right panel) [134].

of the Hamiltonian, in some studies the non-rotationally invariant *density-density* form of the Hubbard model Eq.2.9 is used and in others the Kanamori one Eq.2.8. However, the choice between the two does not change qualitatively the conclusions, it only provides some quantitative modifications [57].

In Fig.3.4 the quasiparticle weight Z (measuring the degree of correlation of the system as discussed in section 2.2) as a function of interaction strength U is plotted for a two-orbital system in the upper panel and a three orbital one in the lower panel. Calculations have been performed for the half-filling case ($n_{tot} = 2$ and $n_{tot} = 3$ respectively) as well as for other integer fillings ($n_{tot} = 1$ for the two-orbital case and $n_{tot} = 1$ and 2 for the three orbital one) and for different values of the fixed ratio J/U (J representing Hund's coupling). As observed from the left-most plots of Fig.3.4, when there is one electron in the two or three orbitals respectively, upon increasing the value of J/U the rate of decrease of quasiparticle weight as a function of interaction strength appears more and more diminished. On the contrary, when the systems are at half-filling -as shown on the right-most plots of Fig.3.4- a finite Hund's coupling with increasing value results into a faster disappearance of Z, so a Mott insulator is realized

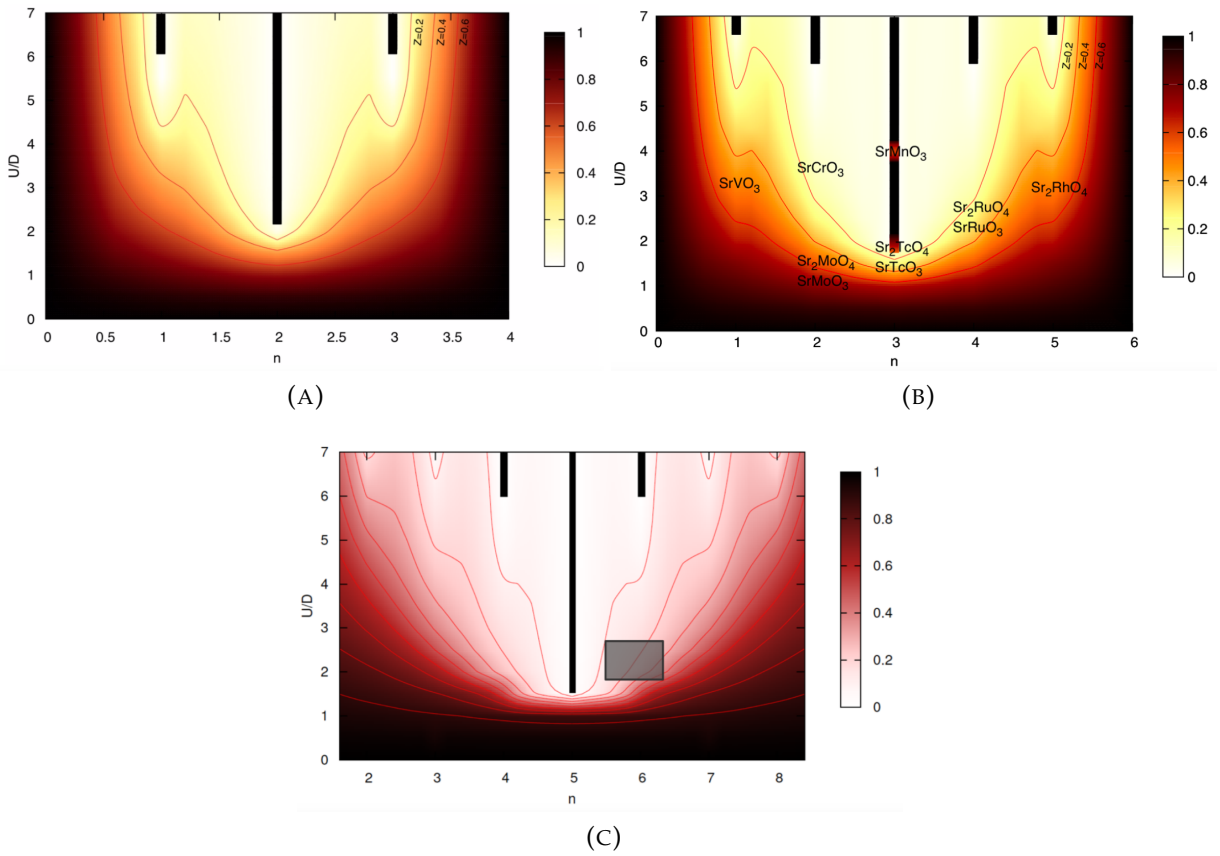

(A) (B)

(C)

FIGURE 3.5: Colour maps of the quasiparticle weight Z on the plane of interaction strength U and total electronic population n_{tot} calculated with DMFT using the Kanamori form of interactions in a system of **(A)** two orbitals with $J/U = 0.15$ [134] and **(B)** three orbitals with $J/U = 0.15$ [134]. Compounds of transition metal oxides are mentioned on the plot at the position (in the $U - n$ plane) where they are estimated to be found. **(C)** Colour maps for a system with five orbitals and $J/U = 0.2$ calculated with SSMF using the density-density form of interactions, where the grey rectangular area is located at the zone where the IBSC compounds are found. In all the plots the black thick lines represent the Mott insulating phases [136].

at smaller U_c. Therefore, a *Hund favoured Mott insulator* is observed at half-filling for both two and three orbital systems, with a significantly reduced critical interaction U_c. A more subtle situation is found in the case of two electrons in three orbitals (middle plot of lower panel in Fig.3.4), where for growing J/U Z is overall suppressed, but above $J/U \simeq 0.1$ the Mott transition is pushed to very large values of interaction strength. This influence of J was called "Janus-faced" because of these two contrasting effects, which thus favor a strongly correlated metallic phase far from a Mott transition.

In Fig.3.5 phase diagrams are plotted in the plane of total electron density and interaction, showing the degree of correlation of the system at each point. These "maps"

are calculated at fixed J/U for two and three orbital systems as well as for the case of five orbitals, further illustrating these trends (in Fig.3.5 $J/U = 0.15$ is chosen for the two- and three- orbital systems and $J/U = 0.2$ for the five-orbital one). The black thick vertical lines at integer fillings represent the Mott insulators and the effect of Hund's coupling is to bring the critical interaction for the transition at smaller values at half-filling, while pushing them at large values at other integer fillings. The colour code is such that the lighter colour represents a smaller Z and thus a larger mass enhancement. There is a region where the system is clearly strongly correlated, which departs at half-filling at the U_c and extends to larger dopings at simultaneously increasing interaction strengths[3]. That is the zone of Hund metals with all the properties defined in the beginning of the chapter, as we detail in the rest of this section.

It is worth mentioning that Hund's coupling, bringing the Mott transition at half-filling to smaller values of U, helps bringing the whole region of Hund metals to interaction strengths where realistic materials are found. In particular for the three orbital case, several $3d$ and $4d$ transition metal oxides are placed around the crossover into the Hund metal region or well inside it, as seen in Fig.3.5b. Similarly for five orbitals, in Fig.3.5c the grey rectangle area around $n_{tot} \simeq 6$ and $U \simeq 2$ represents the zone where the 122 family of the IBSC is located. All the above further supports the view that the many-body physics of the Hund metals is relevant for realistic multi-orbital strongly correlated materials.

The robustness of the Hund metals behavior found in realistic materials is illustrated by the three main characteristics of the phase - as introduced in the beginning of this chapter - being reproduced in the featureless models analyzed in this section. In particular, we focus on the cases of two and three orbital systems and highlight the increase of the (1) mass enhancement, (2) local magnetic moment and (3) orbital selectivity at the Hund metal frontier. In Fig.3.6 results adapted from [2] for the two and three orbitals are plotted side-by-side, with the lower panel exhibiting the mass enhancement, the upper panel the total local moment and the middle one the inter-orbital charge-fluctuation correlation function. All the calculations are shown as a function of interaction strength and for two values of total density n_{tot}, one closer to half-filling than the other, in order to illustrate the boost of the Hund metals properties by the vicinity of the Mott insulator.

In the lower panel referring to the mass enhancement there is a clear crossover from a zone of weak electronic correlations to a zone of strong ones, departing at around $U \simeq 2$ for the two-orbital model and $U \simeq 1.5$ for the three orbital one. Furthermore,

[3]This crossover, as already mentioned, coincides with the finite temperature "spin freezing" line discussed in [92, 93] and in chapter 5 a short discussion is made on this scenario.

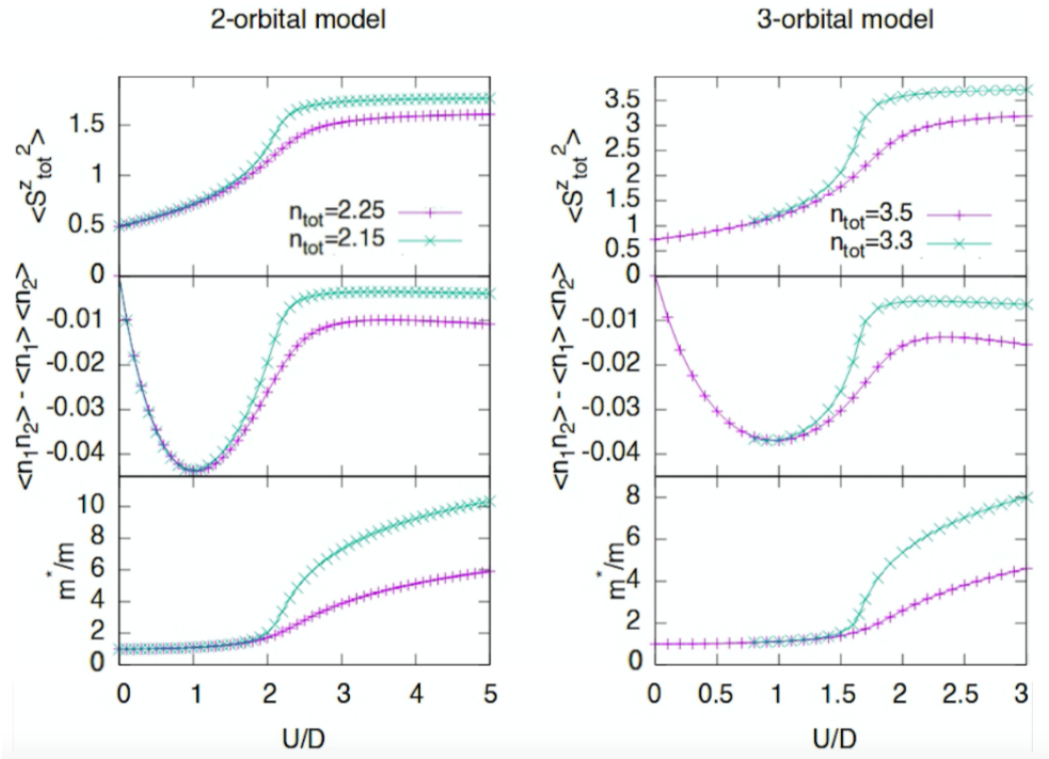

FIGURE 3.6: Calculations using SSMF of the mass enhancement (lowest panels), inter-orbital charge-fluctuation correlation function, employed as a measure of orbital decoupling (middle panels) and total magnetic moment (upper panels) in a two-orbital (left panels) and a three-orbital (right panels) model as a function of interaction strength U. The calculations are done for each case (the two- and three-orbital systems) for two distinct values of the total density, in order to emphasize the increasing intensity of the effects upon approaching half-filling. Adapted from [2].

at the lower doping -so by approaching half-filling- the phenomenon becomes more pronounced, the crossover is more sharp and the value of saturation towards which the system evolves at high U is larger.

The total local moment plotted on the top-most panel of Fig.3.6 enters after $U \simeq 2$ for the two-orbital model and $U \simeq 1.5$ for the three orbital one into a zone of saturation at large values. The curves corresponding to the filling closer to half appear to saturate at higher values and they reach it through a more abrupt evolution.

The last suggested Hund metal property, the orbital selectivity of the electronic correlations, is quite subtle to demonstrate. The reason is that when working with degenerate systems the mass enhancements of the different orbitals are bound to remain identical. Therefore, the inter-orbital charge-fluctuation correlation function has been employed, which can be viewed as an indirect measure of the orbital selectivity. This function, departing from zero at the non-interacting limit, increases (in absolute) its value for a growing interaction strength, since the inter-orbital charge fluctuations are entangled. However, upon approaching the Hund metal crossover the function

becomes suddenly suppressed, due to the emergent "orbital decoupling". The charge fluctuations become independent between the various orbitals and in a way analogous to single-orbital doped Mott insulators the individual filling of each of them turns its specific mass enhancement independently. Indeed orbital selectivity arises if we add to a system - for example of two orbitals - a small crystal-field splitting. In Fig.3.7 such a splitting of the order of $1/40$ of the bandwidth leads to a huge differentiation among the two orbitals' mass enhancements. This counter-intuitive result of a very small orbital energy splitting indicates the many-body nature of the Hund metals' properties.

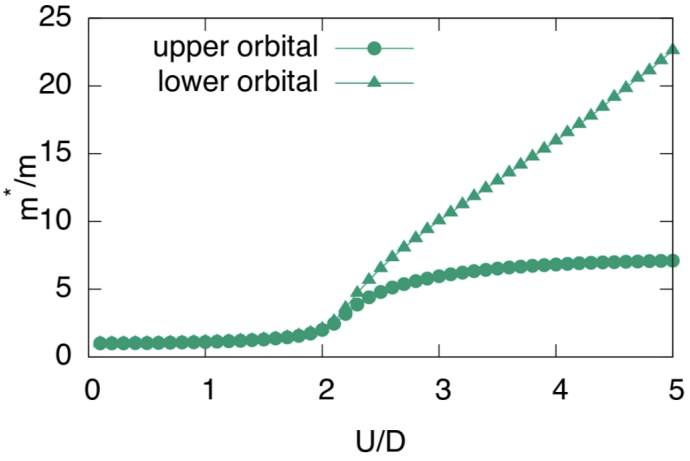

FIGURE 3.7: Mass enhancement as a function of interaction U of the orbitals of a two-orbital system on the Bethe lattice with $n_{tot} = 2.15$, corresponding to the green curves in the left panels of Fig.3.6. A small crystal-field splitting of the on-site orbital energies $\delta\epsilon = 0.05D$ is added lifting the degeneracy and leading to a huge difference in their degree of correlation at large enough U (> 2), as captured by m^*/m [1].

An intuitive insight on the mechanism responsible for this orbital decoupling, is gained considering the atomic spectrum, here of a system of two degenerate orbitals but the analysis holds for a larger number of orbitals. The detailed derivations can be found in [137], where it was shown how Hund's coupling gives rise to Hubbard bands of independent width in two bands with different hopping. Also in [57] it was shown that an analogous mechanism holds at low energy and leads to separate U_c in the two bands. If there is no Hund's coupling in the system, the interactions consist of the intra-orbital and inter-orbital electronic Coulomb repulsion which have the same magnitude U. The spectrum of an isolated atom with zero hopping is plotted in Fig.3.8[4], where the ground state at $N = 2$ (the energy has been arbitrarily put to zero) is six-fold degenerate, since the energy cost of the two electrons occupying the same orbital or different ones is identical and the spin orientation plays no role. The states occupied

[4]For compactness of notation, the slave-spin states are here indicated with the ket of the physical state they represent.

by one or three electrons are the first excitations of the system and the ones occupied by zero or four electrons are higher lying excitations. Adding a finite Hund's coupling J the atomic spectrum changes as shown in Fig.3.9 and the ground state degeneracy is partially lifted, leaving at zero energy the states with maximal total spin.

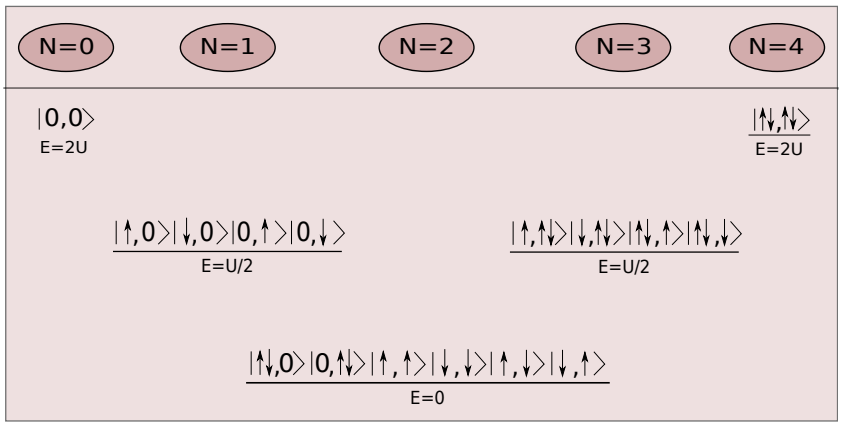

FIGURE 3.8: Atomic spectrum of a degenerate two-orbital model in absence of Hund's coupling, $J = 0$[4].

Adding to the system an extra particle and introducing a small hopping amplitude t allows for charge fluctuations to appear. The difference between the $J = 0$ and the $J \neq 0$ cases is related to the available channels for the particle to hop. When $J = 0$ if an electron is added in let's say orbital 1 then this charge excitation can delocalize through the hopping of an electron of any orbital character. That is exactly due to the ground state degeneracy discussed above, which dictates that all six configurations with two electrons have the same energy. On the contrary, if J is present and hence the degeneracy of the $N = 2$ sector is partially lifted with the ground state consisting of the two high-spin configurations, the only allowed channel for the hopping will be that of the same orbital character than the originally added particle, as visualized in Fig.3.10. This in a simplified picture means that the electron can no longer make use of the multi-orbital character of the system for its delocalization in the lattice, eventually leading to *orbital decoupling*.

We have summed up in a compact way the main properties of Hund metals establishing their generality. In the following chapters we will introduce an additional characteristic feature of those systems and perform numerical and analytical studies exploring the mechanism behind it.

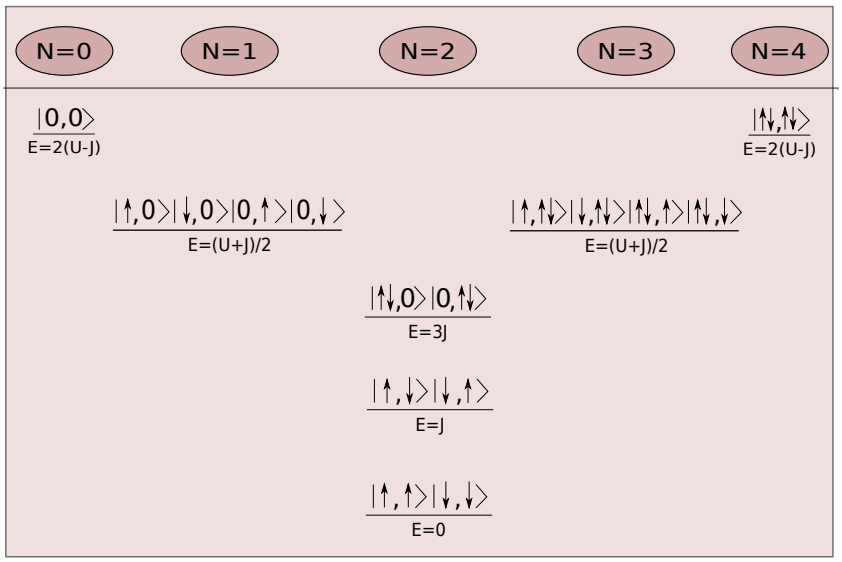

FIGURE 3.9: Atomic spectrum of a degenerate two-orbital model in the presence of Hund's coupling $J \neq 0$[4].

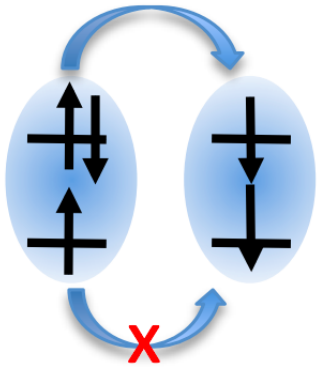

FIGURE 3.10: Schematic representation of hopping processes for a charge excitation in two half-filled bands. The lower process is forbidden for $J \neq 0$ since it leads to a configuration of higher energy.

Chapter 4

Charge instabilities in Hund metals

In this chapter we introduce an additional property emerging at the Hund metal frontier introduced in the previous chapter. Indeed a *zone of charge instability* accompanies the frontier, signalled by a divergent/negative electronic compressibility, which is observed both in models and in realistic simulations of iron-based superconductors in their normal phase. In a new research work, we explore the parameters tuning this zone and we demonstrate that the breaking of rotational invariance enhances the effect, with the instability region getting more extended in the doping plane, reaching the range of densities relevant for IBCS. We provide a description of the mechanism behind this behavior in terms of a rapid change in the electronic kinetic energy, leading to the enhancement and divergence of the compressibility. The main results discussed in this chapter have been published in:

Enhancement of charge instabilities in Hund's metals by breaking of rotational symmetry
Maria Chatzieleftheriou, Maja Berović, Pablo Villar Arribi, Massimo Capone, and Luca de' Medici, Phys. Rev. B **102**, 205127, (2020) [3]

4.1 Enhancement of the electronic compressibility

In the previous chapter we presented three properties characterising the Hund metals zone, namely the:

- electron mass enhancement,
- large local magnetic moments,
- orbital selectivity of electronic correlations.

These aforementioned features emerge from various experimental measurements mainly on iron-based superconductors and are also theoretically calculated using methods accounting both for the realistic structure of the particular materials and for the strong correlations present in them. Moreover, as illustrated in the previous chapter

these characteristics are confirmed in simplified model studies ignoring the details relevant for each compound, and thus proving the generality of the Hund metals phase and its many-body origin. Their onset clearly defines a frontier on the U-density plane.

In [2] it was shown that there is a supplementary property appearing on the same frontier: the enhancement (in some cases divergence) of the electronic compressibility. The electronic compressibility is the uniform and static charge-charge response function given by $\kappa_{el} = dn/d\mu$ and a negative value of it signals a zone where the system is thermodynamically unstable. This charge instability is further related to the emergence of electronic phase separation or the formation of long-range charge density waves.

In the context of isotropic Fermi liquids the derivative of the electron density with respect to the chemical potential, related to κ_{el} is:

$$\begin{aligned} \kappa_{el} = \frac{dn}{d\mu} = \frac{d}{d\mu}\left(\int^{\mu} d\epsilon D^*(\epsilon) \right) = D^*(\mu) + \int^{\mu} d\epsilon \frac{dD^*(\epsilon)}{d\mu} = \\ = D^*(\mu) + \int^{\mu} d\epsilon \frac{dD^*(\epsilon)}{dn}\frac{dn}{d\mu} = D^*(\mu) + \kappa_{el}\int^{\mu} d\epsilon \frac{dD^*(\epsilon)}{dn}, \end{aligned} \tag{4.1}$$

which solving for κ_{el} gives:

$$\kappa_{el} = \frac{D^*(\mu)}{1 - \int^{\mu} d\epsilon \frac{dD^*(\epsilon)}{dn}}. \tag{4.2}$$

In the above expression $D^*(\mu)$ corresponds to the *renormalized* quasiparticle density of states at chemical potential μ, which at zero temperature coincides with the Fermi level. The "correction" in the denominator of κ_{el} is determined by the dependence of the density of states on the electron filling. We can associate this "correction" to the spin symmetric Landau parameter F_0^s, since it can be shown [13] that in an isotropic Fermi liquid:

$$\kappa_{el} = \frac{D^*(\mu)}{1 + F_0^s}. \tag{4.3}$$

The electronic compressibility can hence diverge either due to a diverging $D^*(\mu)$ or a vanishing $1 + F_0^s$. The first possibility can arise if the effective electron mass of the system diverges (the quasiparticle weight goes to zero). The second one comes to play when Z remains finite -although small- as in the Hund metals and F_0^s becomes equal to -1, while when $F_0^s < -1$ the compressibility is negative. Such a negative Landau parameter indicates the presence of attractive forces in the particle-hole channel at $q = 0$, which could give rise to a superconductive pairing mechanism [138].

An alternative scenario which can link the present mechanism to instabilities related to superconductivity refers to the enhancement of interactions between quasiparticles and low-energy bosons. In fact there is a Ward identity relating the density

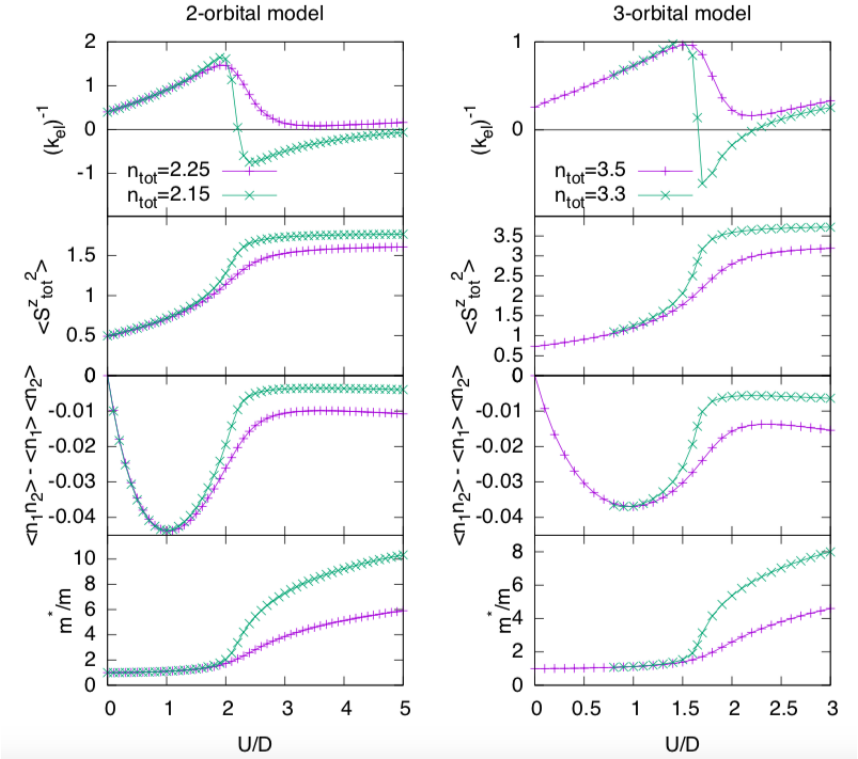

FIGURE 4.1: Calculations using SSMF on a two-orbital system on the left and a three-orbital one on the right, both for two different densities. The three lowest panels (already shown in Fig.3.6) show the mass enhancement, inter-orbital charge-charge correlation function and magnetic moment as a function of interaction, clearly marking a crossover interaction strength for the entrance in the Hund metal phase, as described in the previous section. The upper-most panel reports the inverse electronic compressibility, which in proximity to the same crossover changes sign for the smaller density and is strongly depressed for the larger one, corresponding to a divergence of κ_{el} in the first case and an enhancement of it in the second [2].

vertex $\Lambda(q, \omega)$ to the Landau parameter for the quasiparticles [139] through:

$$Z\Lambda(q \to 0, \omega = 0) = \frac{1}{1 + F_0^s}. \tag{4.4}$$

Therefore, a vanishing $1 + F_0^s$ found in the Hund metals can trigger a symmetry breaking related to the quasiparticle - boson interaction. A more detailed analysis on the way F_0^s becomes negative in simplified models of degenerate bands can be found in Appendix D.

In Fig.4.1 we re-plot the mass enhancement, total magnetic moment and inter-orbital charge-charge correlation function (already shown in Fig.3.6) as a function of

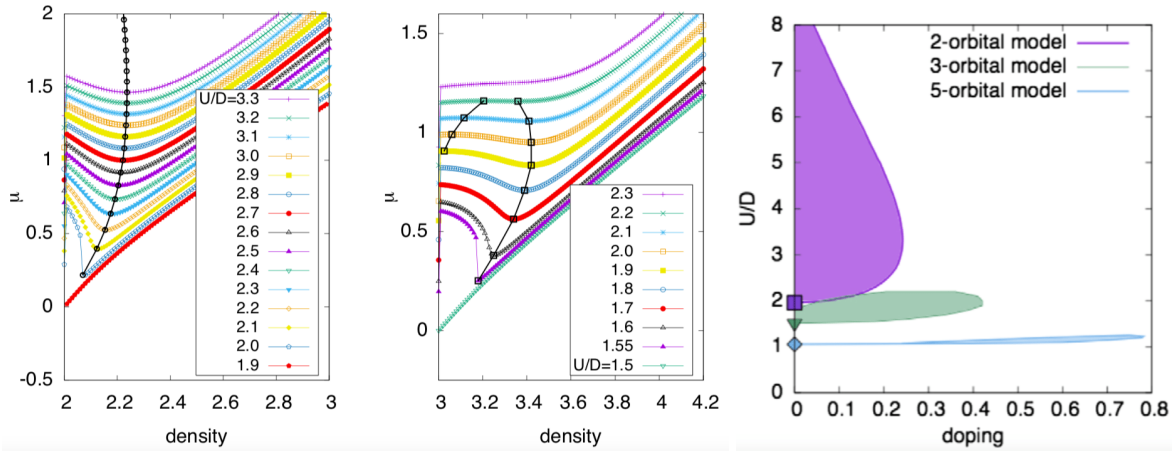

(A) (B)

FIGURE 4.2: **(A)** Chemical potential as a function of total density for different values of interaction strength at fixed $J/U = 0.25$ using the SSMF method for a two-orbital system on the left panel and a three-orbital one on the right. For U right above the U_c of the Mott transition at half-filling and for some range of U a zero and subsequently negative slope is observed. At higher interactions in the three-orbital case the slope remains positive but exhibits a strong suppression[1]. **(B)** Phase diagram illustrating the zone of instability towards phase separation - as defined by the diverging compressibility - in the plane of interaction strength versus doping. The regions for systems of two, three and five orbitals are shown, with the extent of the zone in doping growing with the number of orbitals [2].

interaction strength for the cases of a two- and a three-orbital system and for two different values of total electron density. At the top-most panel we now add the inverse electronic compressibility, which for the lowest reported doping in both systems at a certain value of U becomes zero. This means that κ_{el} diverges and upon raising U it becomes negative, signalling the entrance into an unstable zone. Increasing the total density further away from half-filling we notice that the compressibility does not diverge anymore, however there is a strong enhancement of it still clearly defining two separate regions in U. For both systems the interaction strength around which these four properties emerge is slightly above the critical interaction U_c for the Mott transition at half-filling. Therefore, these four characteristic features as plotted in Fig.4.1 define a frontier between a normal metal at low values of U and a Hund metal at $U > U_c$, as already discussed in the previous chapters.

Graphs of the chemical potential as a function of total density for different values of interaction U (for a two- and a three-orbital system) are shown in Fig.4.2a. Below the U_c of the Mott transition at half-filling, the curves of μ vs n are monotonic, while above U_c and in the vicinity of it they display a flat slope (indicating a diverging compressibility) followed by a negative slope (and a negative compressibility) at smaller densities. At higher values of interaction even though no divergence of κ_{el} is observed,

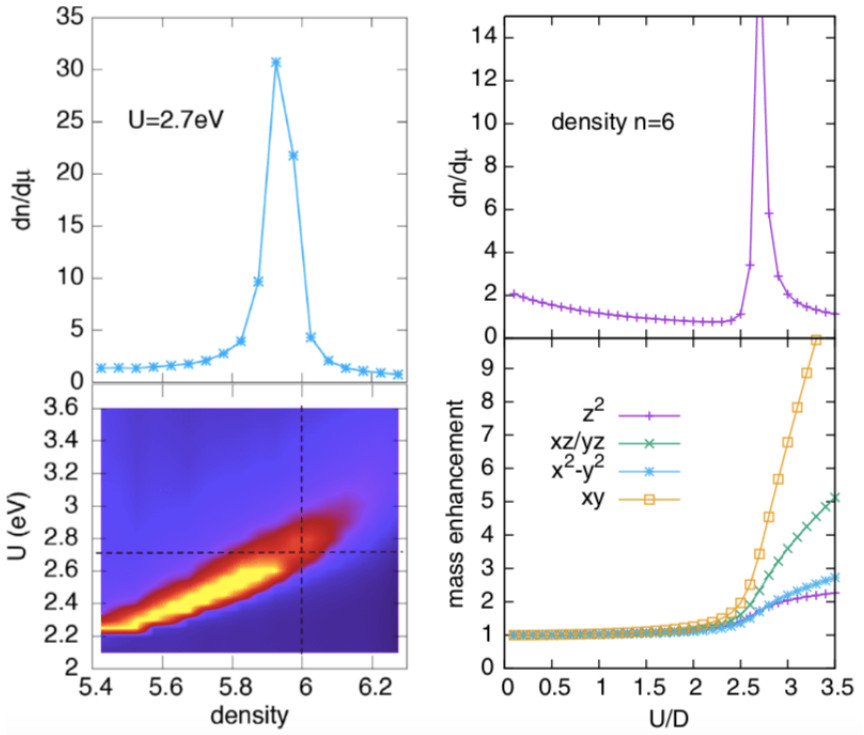

FIGURE 4.3: SSMF calculations using the realistic Hamiltonian of $BaFe_2As_2$ obtained from DFT simulations. **Upper panels:** electronic compressibility as a function of density (left) and U (right), showing a strong enhancement at the values of U and n_{tot} relevant for the compound. **Lower left panel:** zone of charge instability on the density-U plane, extending up to $n_{tot} \simeq 6$. **Lower right panel:** Orbitally resolved mass enhancements vs U, demonstrating that the strong enhancement of κ_{el} appears at the onset of orbital selectivity [2] .

a strong enhancement of it is present.

A similar behaviour is found in the five-orbital case with the regime of diverging/enhanced compressibility reaching larger dopings compared to the systems of less orbitals, but in the meantime exhibiting a smaller extension on the interaction axis. Collecting all those data, phase diagrams of the charge instability zones of two-, three- and five-orbital systems are plotted in Fig.4.2b on the plane of doping versus interaction strength for $J/U = 0.25$. By increasing the number of orbitals, the zone extends to larger dopings and for a two-orbital system the shape of the region differs from those of three and five orbitals. In fact, for the latter cases we observe a "moustache" shaped zone, while for the former the instability seems to persist down to half-filling giving rise to an "onion" shape[1]. In all cases the low-U frontier is quasi-horizontal for a large range of dopings and it can be identified with the finite temperature "spin freezing"

[1]We will see in chapter 5 that this appears to be an artifact of the SSMF method. Indeed DMFT finds a "moustache" shape also in the two-orbital case.

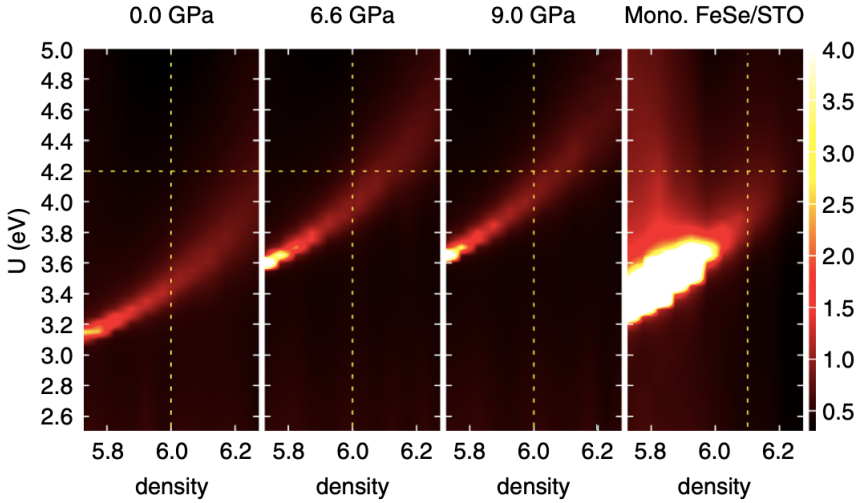

FIGURE 4.4: Color map of the electronic compressibility calculated using SSMF on FeSe under different pressures (three left-most plots) and on monolayer of FeSe ($T_c > 65K$) over a substrate of STO (right-most plot). The crossing of the dashed lines indicates the position on the density-U plane where each stoichiometric compound is estimated to be found. Experimentally T_c is enhanced ($\sim$ 8 to $37K$) by pressure ad culminates around $7 - 9GPa$, correlating positively with the compressibility [140].

crossover [126, 93, 92, 141]. This crossover, related as mentioned above to the other three quantities defining the Hund metal, is sharp the closer the system is to the Mott insulator and it becomes broader and eventually blurred out as the doping is increased.

In [2] the author performed the calculation of the electronic compressibility on a realistic five-orbital Hamiltonian of $BaFe_2As_2$ within SSMF. In Fig.4.3 κ_{el} is plotted on the plane of total density versus interaction. The "moustache" region of instability appears to extend up to density$\simeq$ 6, the value relevant for the stoichiometric compound under study. The compressibility and the orbitally resolved mass enhancements are also plotted, with the second demonstrating that the enhanced κ_{el} manifests at the crossover to the system's orbital selectivity.

Moreover, calculations of the compressibility in different iron-based compounds have been performed [140, 142], with the instability zone of each of them exhibiting a different extent[2]. In particular, for the case of FeSe under different pressures in [140] the authors have shown that the enhancement of electronic compressibility correlates with the critical temperature T_c for superconductivity (Fig.4.4). More recently an analogous correlation was pointed out for the 111 family [144].

The multi-parameter nature of the systems complicates the interpretation of the results and the development of a common explanation for them. In this chapter we try to disentangle the different parameters contributing to each system's complexity and

[2]A phase separation region has been also experimentally observed in another of the IBSC, $RbFe_2As_2$ [143], which has indeed a nominal Fe filling (5.5) closer to half compared to $BaFe_2As_2$ (see Fig.3.1).

we demonstrate the critical role of broken rotational symmetry in the boosting of the mechanism at hand.

4.2 Spin-asymmetric interaction: extension of the instability zone

We first explore the differences in the charge instability zone of a system with interactions in the density-density form and in the Kanamori one. We remind that the interacting part of the Hamiltonian in the particle-hole symmetric form is given by:

$$\begin{aligned}\hat{H}_{int} =& U\sum_{im}\tilde{n}_{im\uparrow}\tilde{n}_{im\downarrow} + U^{'}\sum_{im\neq m'}\tilde{n}_{im\uparrow}\tilde{n}_{im'\downarrow} + (U^{'}-J)\sum_{im<m',\sigma}\tilde{n}_{im\sigma}\tilde{n}_{im'\sigma} \\ &- \alpha J\sum_{im\neq m'} d^{\dagger}_{im\uparrow}d_{im\downarrow}d^{\dagger}_{im'\downarrow}d_{im'\uparrow} + \alpha J\sum_{im\neq m'} d^{\dagger}_{im\uparrow}d^{\dagger}_{im\downarrow}d_{im'\downarrow}d_{im'\uparrow},\end{aligned} \tag{4.5}$$

where $\tilde{n}_{im\sigma} = n_{im\sigma} - 1/2$, $U^{'} = U - 2J$ [31] and α takes the value 0 for a density-density form of the interaction and 1 for a Kanamori one. These two forms are both extensively used in the literature when studying strongly correlated systems. The second one, being rotationally invariant, exhibits a larger ground state degeneracy than the first one and we will present the effect of this on the zone of enhanced compressibility. Given the fact that SSMF cannot treat well the Kanamori interactions - as already mentioned in section 2.2 - we will employ the Rotationally Invariant Slave-Bosons (RISB) method [145], which in the density-density case produces identical to the SSMF results[3].

In Fig.4.5a the two left-most panels illustrate SSMF calculations on a two degenerate orbital model with $\alpha = 0$ (density-density). In the first plot we show the chemical potential as a function of total density for different values of interaction and the compressibility divergence is clearly displayed. In the second plot the zone of instability is drawn on the plane of total density vs interaction for different values of Hund's coupling. By increasing J/U the zone extends to larger and larger values of n_{tot}.

In the two right-most panels of Fig.4.5a the same results are exhibited for the case of $\alpha = 1$ (Kanamori). A non-monotonous behaviour of the maximum density reached for increasing J/U is observed. Moreover, compared to the density-density case for the same value of J/U the extent of the instability region is always smaller. The same trend in comparing the two cases $\alpha = 0$ and $\alpha = 1$ is reproduced in Fig.4.5b and 4.5c, where the instability zones are plotted for systems with three and five orbitals respectively.

[3]The calculations using the RISB method have been performed by our collaborators Maja Berović and Massimo Capone, in SISSA Trieste [146].

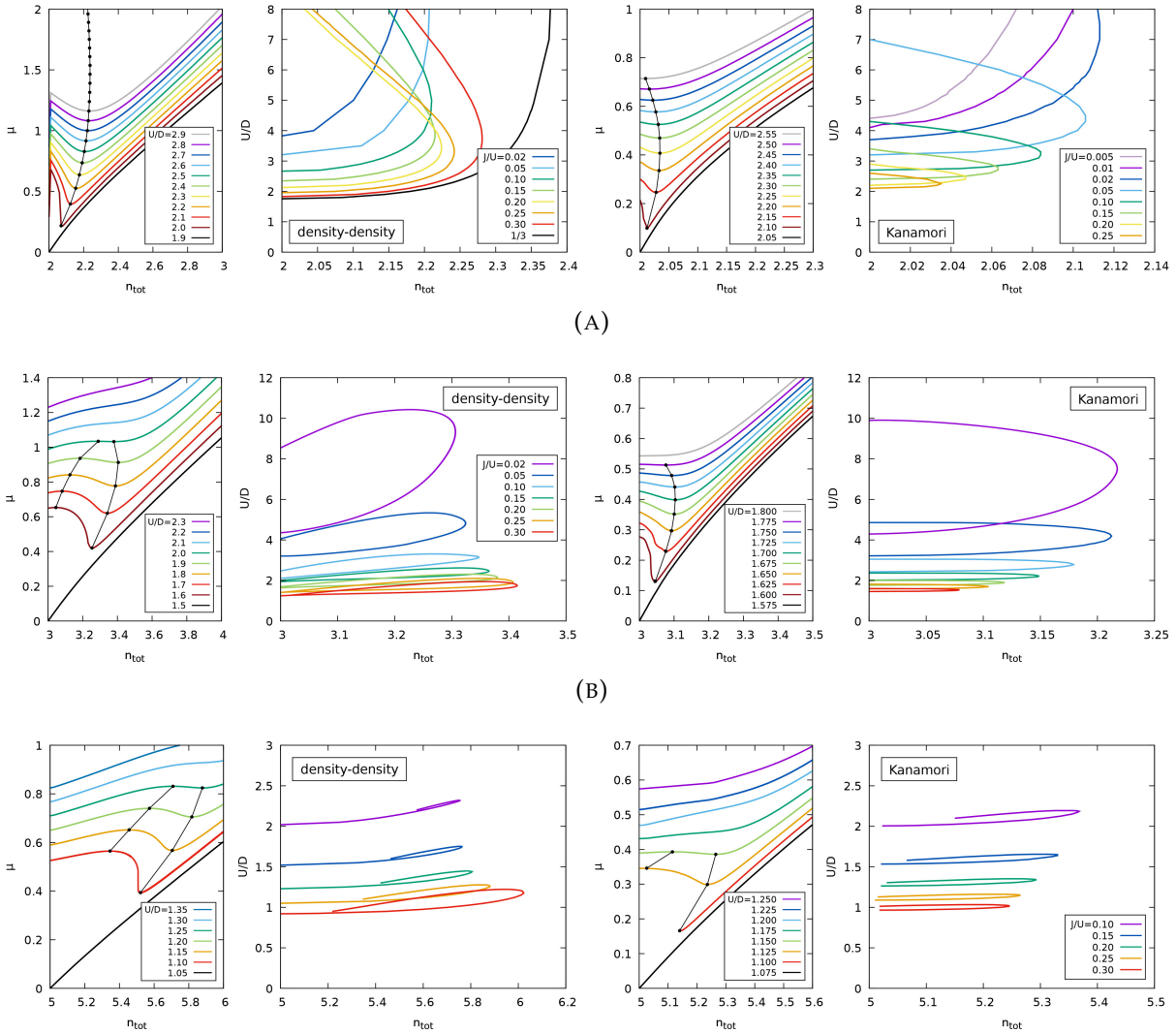

FIGURE 4.5: Comparison of μ vs n_{tot} (for the typical value $J/U = 0.25$) and instability zones (for different values of J/U) in models with density-density (two left-most panels) and Kanamori (two right-most panels) form of interactions. **(A)** two-orbital Hubbard model, the $\alpha = 0$ case is calculated within the SSMF method and the $\alpha = 1$ within the RISB one. **(B), (C)** Three and five-orbital Hubbard models respectively, calculations performed within RISB [3].

As introduced earlier in this chapter, the shape of the zone for $M = 3$ and $M = 5$ differs compared to the one of $M = 2$ and overall by increasing the number of orbitals the extent in doping increases correspondingly for both cases $\alpha = 0$ and $\alpha = 1$.

To conclude, for all values of M we notice two main common features: (1) the lowest border of the frontier (identified here with the Hund metal crossover) departs at half-filling from the U_c of the Mott transition and (2) the $\alpha = 0$ models extend always up to larger densities compared to the $\alpha = 1$ ones of the same J/U. Later in this chapter we will show that the instability region gets widened in the plane of doping when $\alpha = 0$

due to the breaking of spin rotational invariance.

4.3 Breaking of rotational symmetry by crystal-field splitting: extension of the instability zone

Motivated by the results on realistic Hamiltonians of iron-based compounds presented above, we add to our model Hamiltonians the extra complexity of a crystal-field, which reduces the model's symmetry by breaking the orbital degeneracy. This feature is present in the real materials, as discussed in chapter 1, and we will show that it is indeed the decisive parameter extending the instability region to larger dopings.

4.3.1 Two-orbital Hubbard model with finite crystal field

We start from the two-orbital model and splitting the orbital energies is straightforward by introducing $\Delta = \epsilon_1 - \epsilon_2$[4] in Eq.2.32. At half-filling the particle-hole symmetry is preserved by this symmetric crystal-field and the two orbitals have different individual populations, both though at equal distance from individual half-filling. As shown in Fig.4.6a (for the example of $\Delta = 0.2$) increasing the interaction in presence of Hund's coupling the population difference decreases until U_c, where the system becomes a Mott insulator, the two-orbital populations merge and obtain the common value $n_m = 0.5$ [147].

The main effect of a crystal-field splitting at half-filling is to push the critical interaction strength for the transition to slightly larger values, with the two orbitals though still having identical quasiparticle weights between them. In Fig.4.6b we plot Z vs U for models with different values of Δ. U_c increases as a function of Δ and the first-order jump of the transition (which will be discussed in chapter 5) is reduced as Δ is increased.

In a two-orbital model with a finite crystal-field splitting, the local high-spin configurations with a number of particles equal to the number of orbitals ($N = M = 2$) have the same energy than in the $\Delta = 0$ case. On the contrary, the multiplets with $N = 1$ or $N = 3$ are split in energy, half of them appearing lowered by Δ and hence the atomic Mott gap $E_G = E(N = 3) + E(N = 1) - 2E(N = 2)$ becomes reduced compared to the case of degenerate orbitals [57]. In Appendix C.1.4 the detailed derivation of U_c for a system with crystal-field splitting is performed using perturbation theory and one

[4]Throughout this chapter we will be referring to the crystal-field splitting as $\epsilon_{cf} = (\epsilon_1, \epsilon_2, ...)$ depending on the number of orbitals and $\Delta = \epsilon_1 - \epsilon_2$ will be defined by arbitrarily putting one orbital energy to zero.

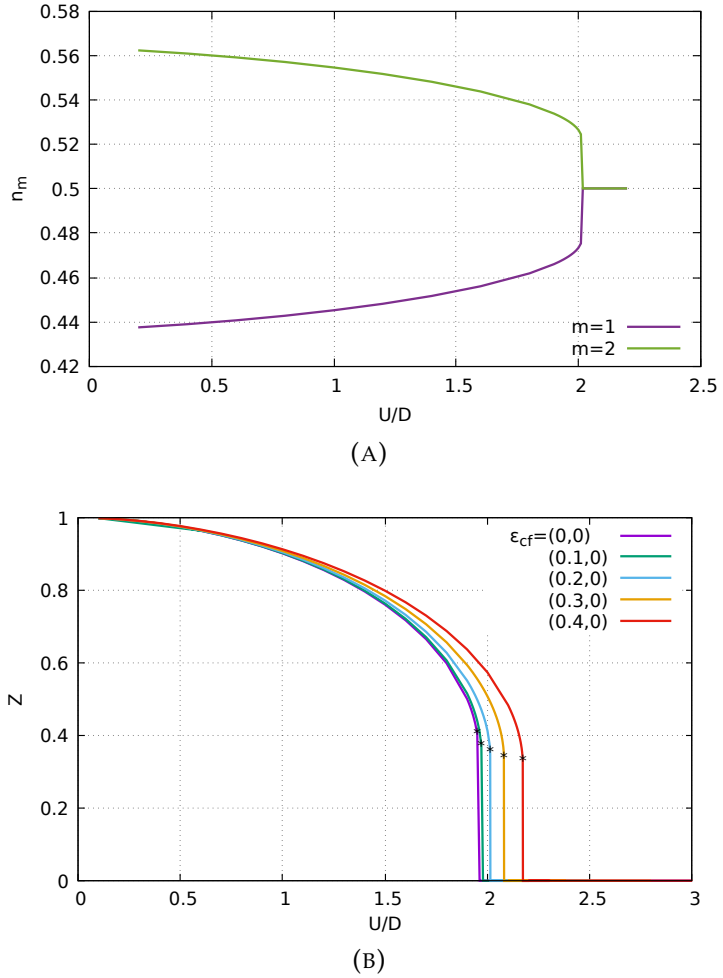

FIGURE 4.6: **(A)** Individual orbital populations as a function of U/D for a two-orbital Hubbard model with density-density interactions $\alpha = 0$, $J/U = 0.25$, $n_{tot} = 2$ and crystal-field splitting $\Delta = 0.2$. The two orbitals undergo a common phase transition turning the system into an unpolarized ($n_m = 0.5$) Mott insulator. **(B)** Quasiparticle weight Z as a function of U/D for the same model with different values of crystal-field splitting. The stars mark the value of Z for which the first-order Mott transition takes place [3]. Both figures are produced using the SSMF method.

obtains:

$$U_c = \frac{4\epsilon_0}{1+\frac{J}{U}}\left(1+\sqrt{1+\left(\frac{\Delta}{4\epsilon_0}\right)^2}\right), \tag{4.6}$$

where ϵ_0 is the bare kinetic energy, as discussed in chapter 2. This calculation is in reality exact when there is a second order transition, which is not the case here as seen in Fig.4.6b. However, the trend is approximately followed as well in the critical interaction for the first-order transition of Z. This result is moreover confirmed by computationally heavier and more accurate Dynamical Mean-Field Theory (DMFT) [147].

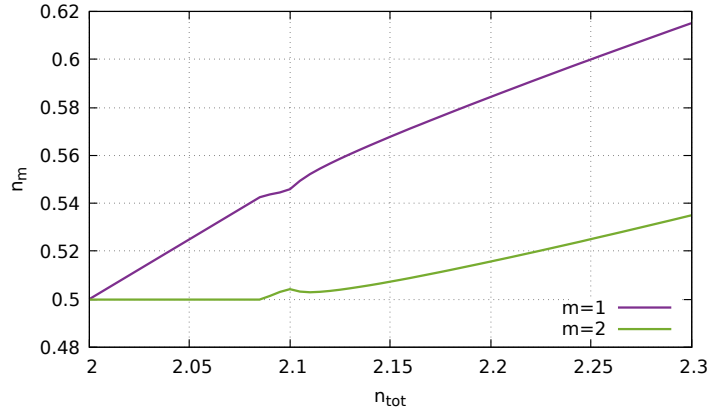

(A)

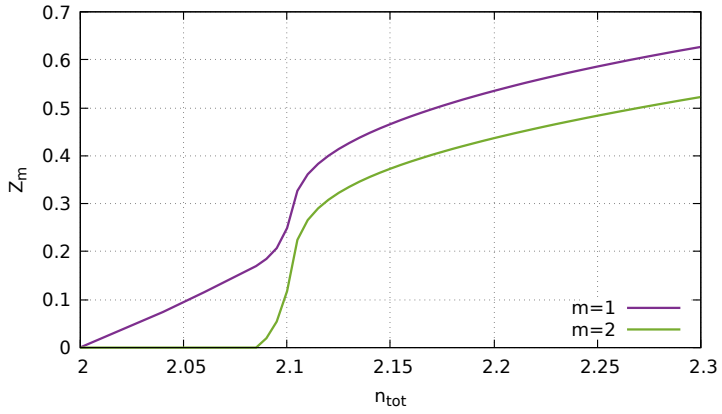

(B)

FIGURE 4.7: Calculations within SSMF on a two-orbital Hubbard model with $\alpha = 0$, $J/U = 0.25$, $\Delta = 0.2$ and at $U = 2.1 > U_c$. **(A)** Individual orbital populations vs total population showing an OSMT localizing one orbital while leaving the other one metallic. **(B)** Orbitally resolved quasi-particle weights vs total density confirming the same findings, an OSMT with one orbital becoming $Z = 0$ and the other one remaining finite. These results are in line with those of [147].

When the system is doped away from half-filling, the two non-degenerate orbitals no longer exhibit a common behaviour. In fact, for $U > U_c$ the orbital which is higher in energy remains insulating for a range of total electron density (keeping its individual filling $n_1 = 0.5$) while the other orbital acquires all the residual density adding up to n_{tot}. As illustrated explicitly in Fig.4.7 for a specific case of $\Delta = 0.2$ and $U = 2.1 > U_c$, the orbital higher in energy remains insulating ($n_1 = 0.5$, $Z_1 = 0$) up to $n_{tot} = 2.085$ and the zone below this density is the *orbitally selective Mott phase (OSMP)*, where one orbital is localized and all the fluctuations originate from the other one [147]. This "orbital decoupling'" mechanism, discussed previously in chapter 3, renders the electronic correlations of each orbital almost independent from the others [133, 123, 148, 136]. At

$n_{tot} > 2.085$ the insulating orbital becomes metallic undergoing thus an *orbitally selective Mott transition (OSMT)*.

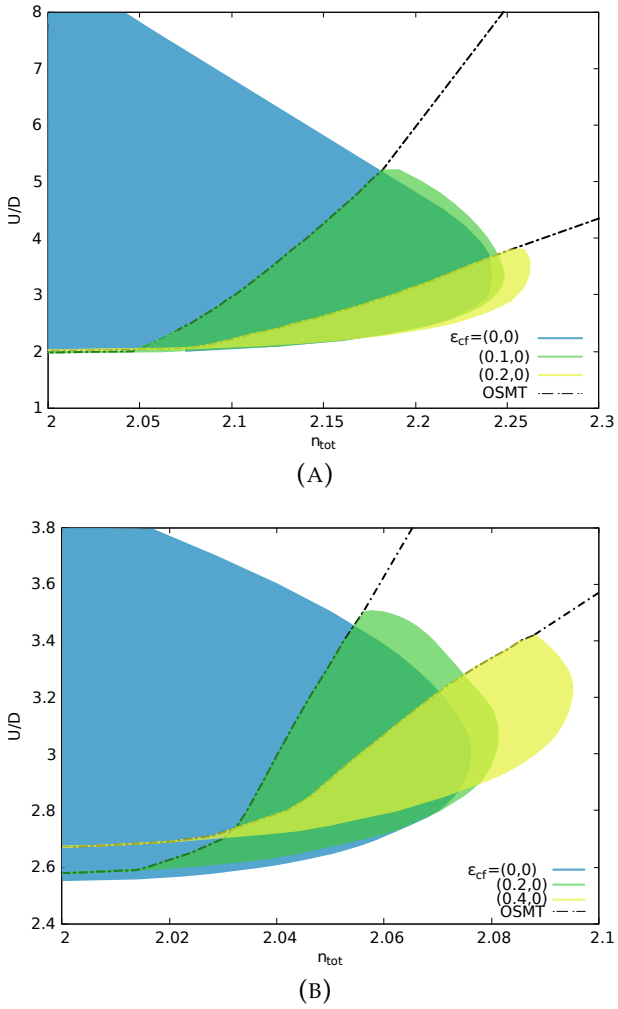

FIGURE 4.8: Phase diagrams of the two-orbital Hubbard model with $J/U = 0.25$ and different values of crystal-field splitting using **(A)** the density-density form of interactions $\alpha = 0$ (calculated within SSMF) and **(B)** the Kanamori form of interactions $\alpha = 1$ (calculated within RISB). The dashed lines correspond to the orbitally-selective Mott transitions (OSMT) which appear to be "chopping" the zones of instability towards phase separation indicated by the coloured regions. By increasing the crystal-field splitting the zone extends to larger densities, with the $\alpha = 0$ case extending always further than the $\alpha = 1$ one [3].

In Fig.4.8 we plot the region of negative electronic compressibility in models with $\epsilon_{cf} = (\epsilon_1, \epsilon_2) = (\Delta, 0)$, for different values of Δ and for both density-density ($\alpha = 0$) and Kanamori ($\alpha = 1$) interactions. Alongside the instability zones for each ϵ_{cf} we plot with black dashes the lines of OSMT, signalling the entrance into the OSMP with one localized orbital. The OSMT appears to be "chopping" the zone and at the same time it "pushes" its extent to larger values in total density. Overall the instability regime

covers a larger range on the doping axis compared to the case of degenerate orbitals but its shape appears to be like a "slice" of the original one, cut by the OSMT line.

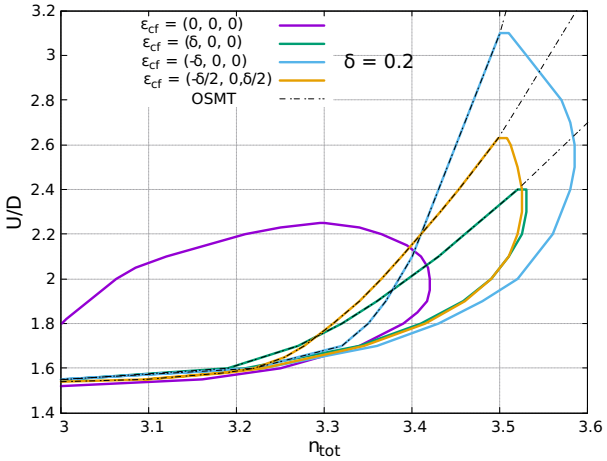

(A)

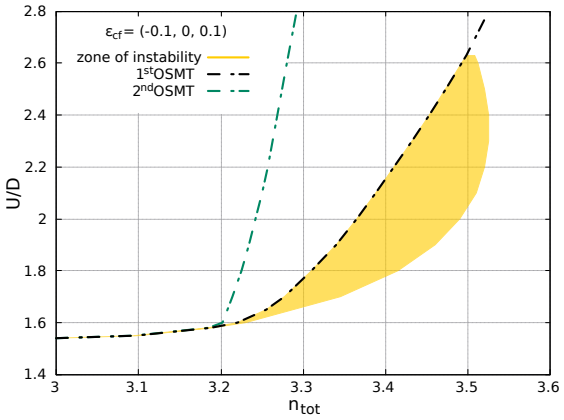

(B)

FIGURE 4.9: Calculations within SSMF of the charge instability zone on a three-orbital Hubbard model (density-density interactions $\alpha = 0$, $J/U = 0.25$) with different crystal-field splittings. **(A)** The three possible versions of splitting the three orbitals with $\Delta = 0.2$, along with their corresponding orbitally-selective Mott transition (OSMT) lines, indicating where the first orbital localizes upon decreasing doping. **(B)** For all these three-orbital models a second OSMT takes place at smaller doping than the first, when the middle orbital localizes, not indicated in the previous plots for clarity. Here we plot explicitly the first and second OSMT lines in the case of $\epsilon_{cf} = (-0.1, 0, 0.1)$.

Comparing the results for density-density and Kanamori form of interactions we observe that in all cases the zone's extent in doping is larger when $\alpha = 0$ compared to $\alpha = 1$ for the same ϵ_{cf}, following the trend observed for degenerate orbitals. Moreover the OSMT emerges closer to half-filling for the case of Kanamori interactions, thus the zone appears less "chopped".

4.3.2 Three-orbital Hubbard model with finite crystal field

In a three-orbital model there are several ways to break the rotational symmetry by introducing a crystal-field splitting. For example, the orbital energies can be distributed equally in the form $\epsilon_{cf} = (-\Delta, 0, \Delta)$ or the energy of one orbital can be lifted or lowered compared to the others through $\epsilon_{cf} = (\Delta, 0, 0)$ or $\epsilon_{cf} = (-\Delta, 0, 0)$. In all cases upon breaking the orbital symmetry the instability zone extends to larger dopings and the OSMT appears to be cutting the region. In Fig.4.9a the region of negative compressibility is presented for models with all these types of ϵ_{cf} for the value $\Delta = 0.2$. In Fig.4.10 we fix instead $\epsilon_{cf} = (-\Delta, 0, \Delta)$ and vary the value of Δ showing that by growing Δ the region extends to increasingly larger dopings, with the maximum n_{tot} reached for $\Delta = 0.2$ being double than the one at $\Delta = 0$.

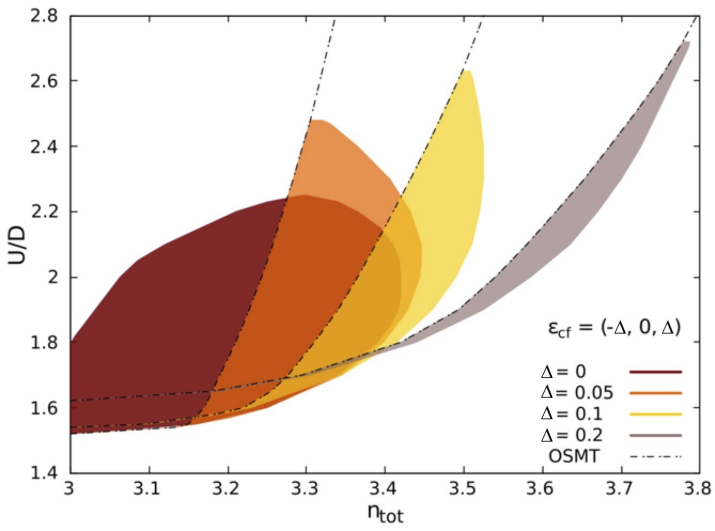

FIGURE 4.10: Calculations within SSMF of the charge instability zone on a three-orbital Hubbard model (density-density interactions $\alpha = 0$, $J/U = 0.25$). Crystal-field splitting of the $\epsilon_{cf} = (-\Delta, 0, \Delta)$ type for different values of Δ, illustrating the correlation of the value of Δ with the extent in doping of the instability zone [3].

For $\epsilon_{cf} = (-\Delta, 0, \Delta)$ once entering the OSMP, by further decreasing the total density, at some point a second OSMT will take place localizing the second higher in energy orbital, as demonstrated in Fig.4.9b for the case of $\Delta = 0.1$.

4.3.3 Five-orbital Hubbard model with finite crystal field

When working on the five-orbital model the possible types of crystal-field splitting increase significantly and one can explore various combinations of orbital energies. However, in all those situations we come across the same physics described above

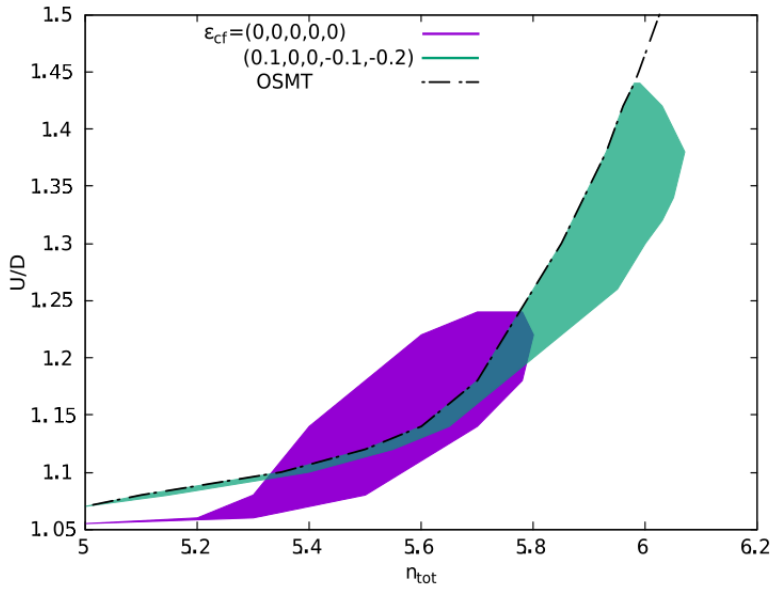

FIGURE 4.11: Phase diagram of the five-orbital Hubbard model demonstrating the zone of charge instability for the case of zero and finite crystal-field splitting (calculated within the SSMF method). The chosen values of ϵ_{cf} in the latter are relevant for the case of IBSC and it is shown that with this choice the region of enhanced/diverging compressibility reaches $n_{tot} = 6$ where the stochiometric compounds are found. As in the case of $M = 3$ there are more OSMT lines at smaller dopings than the first one, but we do not show them here for clarity [3].

for the cases of $M = 2$ and $M = 3$. The broken symmetry phase exhibits a zone of instability which reaches larger regions of total density, with the OSMT "chopping" the regime. We plot in Fig.4.11 the zone of negative compressibility for a five-orbital degenerate model and a crystal-filed split one, the orbital energies of which have been chosen to be relevant for the IBSC compounds, see Fig.1.4 in chapter 1. In particular, we choose ϵ_{cf} so that the two e_g orbitals are split in energy and well below the t_{2g} ones, two of which remain degenerate. The maximum doping reached is indeed strikingly enhanced extending up to $n_{tot} = 6$, the value where the parent compounds of iron-based superconductors are found.

The instability zone reaches larger values in doping for increasing number of orbitals. Therefore, including in a five-orbital system a crystal-field splitting extends the zone even further on the phase diagram, at the ballpark of the iron-based compounds ($n_{tot} = M + 1$).

In the rest of this chapter we will analyze the local ground state configurations and get insight on the mechanism inducing the charge instability, by evaluating the kinetic

energy of the system.

4.4 Charge instabilities and many-body "extra" kinetic energy

In chapter 1 we introduced the physics of strongly correlated systems and we pointed out the importance of the competition between the hopping amplitude t and the interaction strength U on the quasiparticles' itinerancy. In particular, we explained how, when the electron filling is commensurate and U/t is large enough, the quasiparticle weight becomes zero and the system transitions into a Mott insulator.

It has been shown that for systems with M local orbitals, the critical interaction strength necessary for the Mott transition $U_c(M)$ increases linearly with the number of orbitals [149, 5, 150, 151]. The reason behind this effect is related to the local ground state configurations of each model. In a multi-orbital system including Hubbard-U interactions, for an increasing number of orbitals the number of degenerate ground state configurations increases accordingly. These configurations can combine in a linear superposition having an increased hopping amplitude in comparison to the bare atomic states and this was shown to generate wider Hubbard bands compared to the single-band case [152]. This provides also the quasiparticles with a kinetic energy enhanced enough to overcome the repulsion U up to larger values compared to the single-orbital case. Therefore, the critical interaction strength U_c is increased for increasing M, as illustrated in Fig.4.12. Hund's coupling at half-filling has instead the opposite effect: it reduces the available local configurations and thus the width of the Hubbard bands and the itinerancy of the quasiparticles.

In this section we will connect these concepts in the framework of SSMF, giving an analytical and unified perspective. This will provide a description of the charge instability regions as zones of sharp change in the available local configurations and consequently of the kinetic energy of the system, causing a negative curvature of the total energy, i.e. a negative compressibility.

Indeed let's analyze in the context of SSMF perturbation theory a system in proximity to a Mott insulator. As presented in detail in section 2.2.5, the Mott insulating solution, which is defined by $Z_m = 0$, implies $h_m = 0$ for the effective field h_m active in the slave-spin Hamiltonian Eq.2.32, since the self-consistent equation is $h_m = \sqrt{Z_m}\epsilon_0(n_{m\sigma})$, where $Z_m = (1 + c_m)^2\langle S^x_{m\sigma}\rangle^2$ and ϵ_0 is the bare kinetic energy of the electrons. In order to estimate the critical parameters for the Mott transition, the perturbation of Z at linear order in h_m is enough and we do not need to include higher order terms.

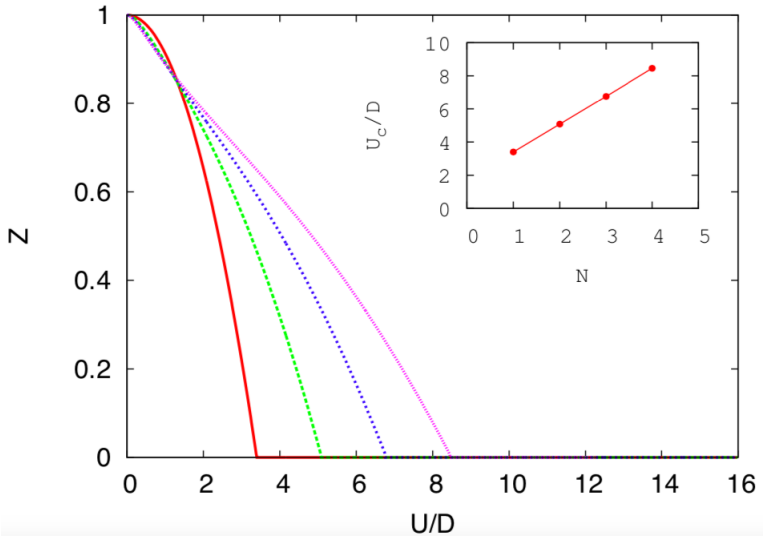

FIGURE 4.12: Quasiparticle weight Z as a function of interaction strength U/D for models with $M = 1, 2, 3, 4$ number of orbitals at half-filling. The critical value U_c for the Mott transition increases for an increasing M. This U_c as a function of orbital number M is shown in the inset [61].

Indeed, h_m determined by the self-consistency equation is a linear function of $\langle S^x_{m\sigma} \rangle$ (in absence of inter-orbital hopping). The latter is calculated from the spin Hamiltonian and is instead a more complicated function of the h_m, that we can calculate explicitly using perturbation theory (as shown in section 5.5). At linear order in h_m the only solution of these equations is trivially in $h_m = 0$, so that higher orders are needed to determine a nontrivial solution yielding a finite h_m. However, for small enough h_m (i.e., close enough to a Mott insulator) the linear term will anyway dominate (and also ultimately determine the critical parameters for the Mott transition. In Appendix C we demonstrate in detail the application of perturbation theory on systems of single or two orbitals and in different cases (at half-filling, away from it, at $J = 0$ or $J \neq 0$, using the density-density or the Kanamori form of interaction), going up to the third order.

The unperturbed Hamiltonian of a multi-orbital system at half-filling, in particle-hole symmetry and with no crystal-field splitting (implying $\mu = \lambda_m = 0$, $h_m = h$ and $c_m = 1$) is the atomic one given by:

$$H_{at} = U \sum_m S^z_{m\uparrow} S^z_{m\downarrow} + (U - 2J) \sum_{m \neq m'} S^z_{m\uparrow} S^z_{m'\downarrow} + (U - 3J) \sum_{m < m', \sigma} S^z_{m\sigma} S^z_{m'\sigma} \tag{4.7}$$

and the perturbing Hamiltonian is:

$$H_{pert} = \sum_{m\sigma} h_m 2 S^x_{m\sigma} = \frac{h}{2} \sum_{m\sigma} \left(S^+_{m\sigma} + S^-_{m\sigma} \right), \tag{4.8}$$

which flips any of the slave-spins. At $T = 0$ we study the ground state of the system

and its degeneracy which plays a key role. As extensively explained in Appendix C.1.2 the corrected ground state ket at linear order reads:

$$|\phi^0_{(1)}\rangle = |\phi^0\rangle + |\phi^0_{(I)}\rangle = |\phi^0\rangle + \sum_{|s\rangle \neq |\phi^0\rangle} \langle s|(E_0 - H_{at})^{-1} H_{pert}|\phi^0\rangle|s\rangle, \tag{4.9}$$

where E_0 is the energy of the ground state $|\phi^0\rangle$ and $|s\rangle$ any excited state connected to $|\phi^0\rangle$ through H_{pert}.

We are interested in the system's kinetic energy per site $E_{kin} = \langle H_0 \rangle$, where H_0 corresponds to the slave-spin Hamiltonian Eq.2.32 without the interaction part and with $\lambda_m = 0$. The kinetic energy of the system per spin in fact coincides with the average value of the perturbation $E_{kin} = \langle H_{pert} \rangle$ and to leading order it becomes:

$$E_{kin} = \langle \phi^0_{(1)}|H_{pert}|\phi^0_{(1)}\rangle = 2\langle \phi^0|H_{pert}(E_0 - H_{at})^{-1} H_{pert}|\phi^0\rangle. \tag{4.10}$$

It represents, starting from the ground state, the number of processes available in order to flip any two slave-spins and return on the ground state itself. These processes practically are the ways in which a particle can hop onto a neighbouring site and back to any of the spin-orbitals still turning the ground state into itself. This can be viewed in analogy to the way the itinerancy of particles in a lattice is described within DMFT, by perturbatively treating the Kondo coupling of an impurity in a bath [4, 153, 154]. The weight $2/(E_0 - E_s)$ in the above expression is twice the inverse of the energy difference between the ground state and the relevant excited state of the particular process.

As we already implied above the ground state degeneracy holds a significant role since it enhances these processes in number. Therefore we will next investigate this degeneracy in the cases of a zero and a finite Hund's coupling J and point out the difference between them. We will keep the number of orbitals M as a free parameter for generality, while in Appendix C.1 a detailed demonstration of the perturbation theory procedure can be found for the case of a two-orbital system. It is enough to know for this demonstration that in order to obtain the unperturbed linear combination giving rise to the ground state $|\phi^0\rangle$, one has to diagonalize the matrix $H^{'} = H_{pert}(E_0 - H_{at})^{-1} H_{pert}$ in the degenerate subspace.

4.4.1 Kinetic energy of a multi-orbital system with $J = 0$, $SU(2M)$ symmetry

When there is no Hund's coupling present, the unperturbed Hamiltonian of Eq.4.7 takes the form:

$$H_{at} = \frac{U}{2}\Big(\sum_{m\sigma} S^z_{m\sigma}\Big)^2 = \frac{U}{2}\Big(S^z_{tot}\Big)^2. \tag{4.11}$$

Given the even number $2M$ of slave-spins on each site, any state with $S^z_{tot} = 0$ will be a ground state, since $(S^z_{tot})^2 \geq 0$. Therefore and due to the $SU(2M)$ symmetry of the problem at hand there are $d_0 = \binom{2M}{M}$ such states ($|S^z = 0\,;\, l\,\rangle$, for $l = 1 \dots d_0$); d_0 representing the ground state degeneracy, which is nothing more than the number of ways available to have half of those $2M$ slave spins up and half down. As explained in chapter 2, in the slave-spin formalism up and down corresponds to the presence or absence of a particle in the system, hence d_0 actually amounts to the possible ways of placing M particles in $2M$ spin-orbitals in order to achieve half-filling.

All the excited states having one spin flipped compared to the ground state differ from it in energy by $U/2$. Thus, one has to diagonalize the matrix $H^{'} = -2H^2_{pert}/U$ in the degenerate subspace in order to obtain the unperturbed ground state manifold:

$$|\phi^0\rangle = \frac{1}{\sqrt{d_0}} \sum_{l=1}^{d_0} |S^z = 0\,;\, l\,\rangle. \tag{4.12}$$

In the above linear combination, all the d_0 degenerate basis states are added with a plus sign in order to ensure the lowest possible energy, since each of them contributes with a $-U/2$. All the "exchange" processes including the d_0 states are present and active. In order to understand this result better one can think of the processes taking place by applying $H^{'}$ on $|\phi^0\rangle$. Starting for example with the first H_{pert} in $H^{'}$ flipping down any one of the M spins pointing up, now the system has $M+1$ spins pointing down and subsequently the second H_{pert} will flip any one of those up. The analogous but opposite process takes place starting with a flip up of any one of the M spins pointing down. Overall, the possible processes are $2M(M+1)$ and they contribute to the kinetic energy giving:

$$E_{kin} = -\frac{32h^2}{U} M(M+1). \tag{4.13}$$

4.4.2 Kinetic energy of a multi-orbital system with $J \neq 0$, Z_2 symmetry (density-density interaction)

We now consider the interaction Eq.2.31 for a finite Hund's coupling $J \neq 0$ and we repeat the steps followed in the previous section of $J = 0$, keeping in mind that now the matrix to be diagonalized in order to evaluate the "correct" unperturbed ground state is $H^{'} = -2H^2_{pert}/U_{eff}$. This results from the fact that the excitation energy is now $U_{eff}/2$, with $U_{eff} = U + (M-1)J$. In fact this is exactly the case only in a two-orbital system ($M = 2$, more detailed derivation in Appendix C.1), since for $M > 2$ the excited multiplets are split by J and using $H^{'} = -2H^2_{pert}/U_{eff}$ is an approximation, however a qualitatively accurate one.

We use the density-density form of interaction and we obtain (see Appendix C.1.2) that the ground state is only two-fold degenerate, since H_{at} splits the manifold with $S^z = 0$ (within the slave-spin formalism, *not to be confused with the real spin* S^z), with these basis states being:

$$|\uparrow,...,\uparrow\rangle, |\downarrow,...,\downarrow\rangle. \tag{4.14}$$

The first state corresponds to a system with M particles (one in each orbital) all with spin up, while the second corresponds to M particles (again one in each orbital) all with spin down (in both cases in the SSMF formalism M slave-spins are pointing up and M are pointing down). The high total spin states are indeed lowered in energy and thus favoured in the presence of Hund's coupling, as expected. In a spirit similar to the one followed in the case of $J = 0$, the "correct" unperturbed ground state is again the linear combination of the above degenerate states with a plus sign, in order to guarantee the lowest eigenenergy. The resulting ground state is thus:

$$|\phi^0\rangle = \frac{1}{\sqrt{2}}(|\uparrow,...,\uparrow\rangle + |\downarrow,...,\downarrow\rangle). \tag{4.15}$$

The leading order in the perturbation is h^2 and to that order the ways to fluctuate and end up back on the ground state are only those flipping twice a given slave-spin. This means that $H^{'}$ acting, for example, on a spin up it flips it down and then subsequently it needs to flip the same spin up again in order to restore the original manifold (the analogous operation holds starting from a spin down). There are $2M$ such processes available and knowing that, we can calculate the kinetic energy for a system with $J \neq 0$:

$$E_{kin} = -\frac{32h^2}{U_{eff}}M = -\frac{32h^2}{U + (M-1)J}M. \tag{4.16}$$

According to Eq.4.13 and Eq.4.16 for any $M \geq 2$ the kinetic energy in the case of a finite Hund's coupling is much smaller than the one of $J = 0$. Therefore, an increased ground state degeneracy, as for a model with $J = 0$, causes the activation of extra hopping channels which subsequently enhances the kinetic energy. In the present formalism of SSMF we cannot address a system with Kanamori form of interaction to the same level of approximation, however in Appendix C.1 calculations are performed for the particular case of a two-orbital model and it is there shown that the ground state degeneracy remains smaller than the one of a $J = 0$ model, confirming thus the conclusions of this section.

In Appendix C.1 the detailed derivation of the critical interaction strength at half-filling for the Mott transition is performed for both cases with $J = 0$ and $J \neq 0$ in a two-orbital system. One can generalize this calculation using the above results for

an undefined number of orbitals M. Using the fact that $\langle 2S^x_{m\sigma}\rangle = \frac{E_{kin}}{4hM}$ and the self-consistency condition $h_m = \sqrt{Z_m}\epsilon_0$ we obtain to a good approximation (exact for $M = 2$):

$$U_c = \begin{cases} -8(M+1)\epsilon_0 & , \quad J = 0 \\ -8\epsilon_0 - (M-1)J & , \quad J \neq 0 \;\; density-density \\ -16\epsilon_0 - (M-1)J & , \quad J \neq 0 \;\; Kanamori \end{cases} \tag{4.17}$$

where $\epsilon_0(n_{m\sigma} = 1/2) \leq 0$. These results prove that introducing Hund's coupling to the system brings the Mott transition at half-filling to a smaller critical interaction, the density-density form of it enhancing even further the reduction of U_c.

4.4.3 Width of the Hubbard bands and Mott gap edge: shrinking of the Hubbard bands due to Hund's coupling

In this section we demonstrate a second effect, resulting from the same mechanism, that reduces the quasiparticle kinetic energy when J is finite: the reduction of the Hubbard band width, which can be estimated by the distance in energy between the Mott gap edge and the lowest lying atomic excited state in the sectors with one more or one less particle [152]. We apply perturbation theory in a system doped away from half-filling but close to it, so that there is a finite $\lambda_m = -\mu$, while we consider $c_m = 1$. Calculating the mean value of $S^x_{m\sigma}$ we obtain:

$$\sqrt{Z_m} = \langle 2S^x_{m\sigma}\rangle = \begin{cases} -\frac{8hU}{U^2 - 4\lambda_m^2}(M+1), & J = 0 \\ -\frac{8h\,U_{eff}}{U_{eff}^2 - 4\lambda_m^2} & , \quad J \neq 0. \end{cases} \tag{4.18}$$

In a similar spirit to the steps followed in previous sections we next insert this relation into the self-consistency equation $h_m = \sqrt{Z_m}\epsilon_0(n_{m\sigma})$ and estimate the condition for $h_m = 0$. We therefore calculate the critical value of the chemical potential μ_c for which the Mott transition takes place by varying the doping. The two expressions obtained for $J = 0$ and $J \neq 0$ are:

$$\mu_c = -\lambda_m = \pm\frac{1}{2}\begin{cases} \sqrt{U^2 + \epsilon_0\, 8U(M+1)}, & J = 0 \\ \sqrt{U_{eff}^2 + \epsilon_0\, 8U_{eff}} & , \quad J \neq 0. \end{cases} \tag{4.19}$$

We are interested in the distance between this μ_c and the lowest lying excitations for $N = M \pm 1$ (N being the number of particles and M the number of orbitals), which for $J = 0$ have energy $U/2$ and for $J \neq 0$ $U_{eff}/2 = \big(U + (M-1)J\big)/2$. If we expand

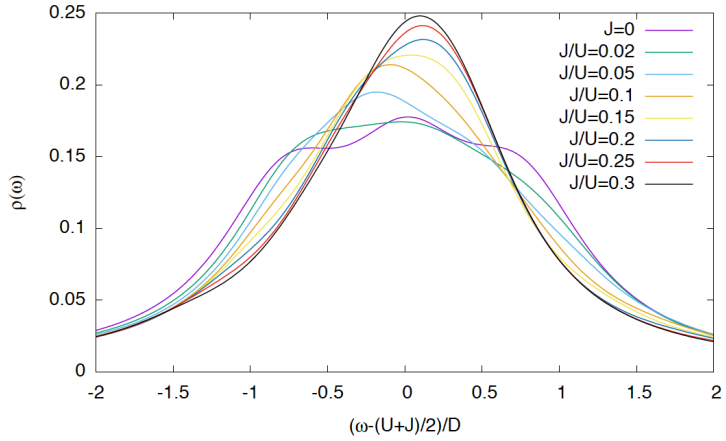

FIGURE 4.13: Hubbard bands in the local spectral function $\rho(\omega)$ calculated with DMFT for a two-orbital Hubbard model at half-filling with the Kanamori Hamiltonian, as a function of Hund's coupling J. The system with $U = 7D$ is a Mott insulator for all values of J. The Hubbard bands (of the addition spectrum plotted here) have a width $\sim W = 2D$ for large J/U, reduced compared to the $J = 0$ value $\sim \sqrt{2}W$ [57].

this distance ΔE_{Hub} at large U we obtain:

$$\Delta E_{Hub} = \begin{cases} 2|\epsilon_0|(M+1), & J = 0 \\ 2|\epsilon_0| \quad , & J \neq 0. \end{cases} \tag{4.20}$$

This distance can be further identified with half the width of the Hubbard band and we see that in absence of Hund's coupling the width increases with the number of orbitals by the same mechanism which enhances the quasiparticle kinetic energy leading to an increased critical interaction for the Mott transition U_c [151], as we showed in the previous section. However, when J is introduced in the system the width of the Hubbard band appears to shrink back to values comparable to the single-orbital case, an effect which was already shown using DMFT in [57], plotted in Fig.4.13. The physical mechanism behind this is here shown to be related to the one reducing the quasiparticle kinetic energy in a system with $J \neq 0$. The explanation, as we introduced above, lies in the fact that J reduces the degeneracy of the ground state (as determined by the degree of symmetry in the model) which in turn further reduces the available hopping channels, yielding both the kinetic energy and the Hubbard band width quenched.

4.4.4 Description in terms of local fluctuations and kinetic energy

In this section we summarize all the results presented above and suggest a unifying principle behind trends of the charge instabilities observed in these systems. In order to have some physical insight it is useful to look at the probability of occurrence of the

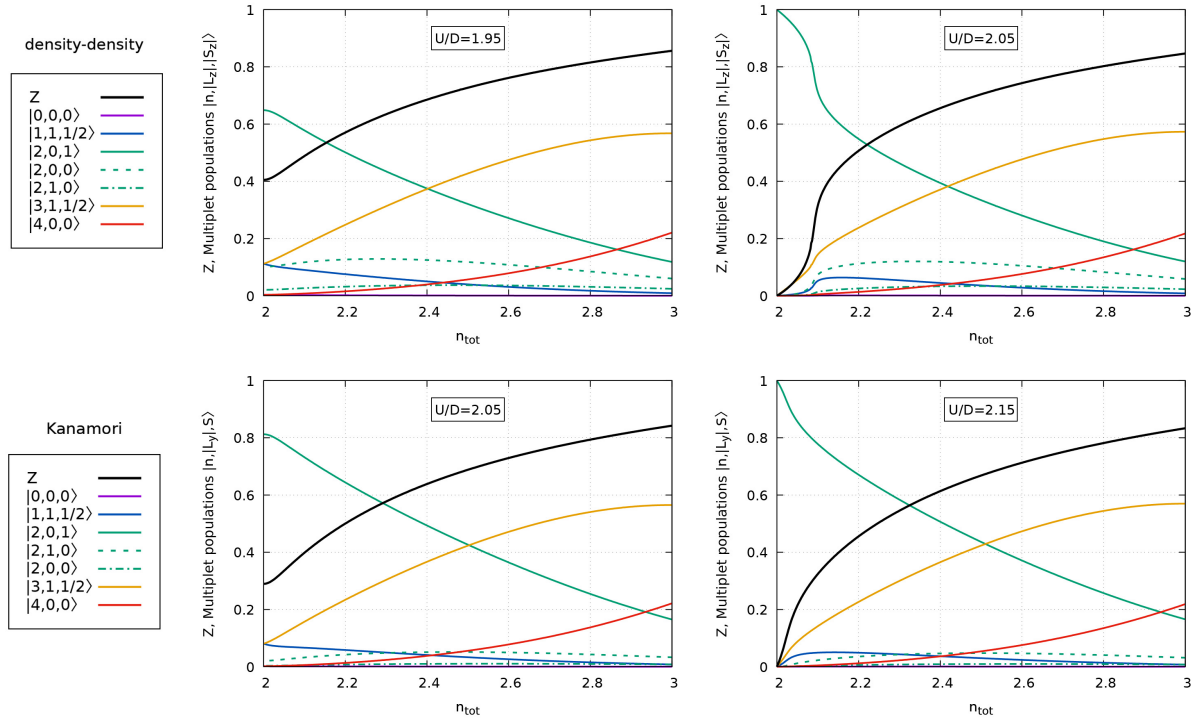

FIGURE 4.14: Atomic multiplet populations (atomic-state amplitudes in the ground state times multiplet degeneracy, color lines) and quasiparticle weight Z (black line) as a function of total electron density for a degenerate two-orbital Hubbard model for density-density ($\alpha = 0$ upper panels) and Kanamori ($\alpha = 1$ lower panels) interactions ($J/U = 0.25$). The left panels are calculated at $U < U_c$ and the right panels at $U > U_c$ [3].

possible local configurations. In the SSMF and RISB methods these are the ground state amplitudes of the respective slave-particle variables corresponding to local configurations. For a system of M degenerate orbitals without Hund's coupling at half-filling we know that in the non-interacting limit all configurations have equal probability of being realized. By increasing the interaction strength the states with a number of particles different than the number of orbitals (so not half-filled) will be less and less occupied compared to those where $N = M$. At the Mott transition all the weight will be carried by those half-filled states of the sector $N = M$ and the rest of the states will have zero weight.

In presence of Hund's coupling, however, not all configurations with number of particles equal to the number of orbitals exhibit the same probability of occupation. That is because, as we have extensively presented earlier, a finite J favours the high-spin configurations, thus lowering their energy compared to the low-spin ones of the same sector with $N = M$. Therefore, at the Mott transition only those high-spin configurations survive with a non-zero weight.

When we dope the system away from half-filling, the metallicity is restored and this is reflected on the low-spin configurations at $N = M$ as well as all those at $N \neq M$

acquiring finite probability of realization. That is the consequence of the release of charge fluctuations by the extra electron density introduced, which were frozen in the Mott insulator and restrained in the metallic regime at half-filling.

In Fig.4.14 we plot for a two degenerate orbital model the atomic multiplet populations together with the quasiparticle weight Z as a function of total electron density for the cases of density-density ($\alpha = 0$) and Kanamori ($\alpha = 1$) interactions and for interaction strengths slightly below and slightly above U_c. There are two distinct regimes in the plots, one close to half-filling and one further away from it. In the region away from half-filling (and even approaching the total population $M+1$) for both $\alpha = 0$ and $\alpha = 1$, being above or below the U_c does not particularly affect the evolution of the multiplet populations (and Z), which appear very similar in both cases of U. However, in the region close to half-filling there is clearly a pronounced difference between $U < U_c$ and $U > U_c$. This is expected since at half-filling in the former case all the configurations with $N = M$ have a finite weight, while in the latter only the high-spin ones do and so, by continuity, doping in the vicinity of half-filling will produce different behaviour for the two cases [145, 155, 94, 156].

The doping where the system switches from one regime to the other is identified with the crossover between a normal metal at large doping and a doped high-spin Mott insulator at small doping, which we identify with the Hund metal. The closer U is to the transition value U_c, the closer to half-filling the crossover into the Hund metal is and the more abrupt it appears. This abruptness transfers correspondingly to the evolution of the quasiparticle weight, which also increases in a steeper manner at the crossover. These effects are the result of the release of the fluctuations frozen by U and J in the Mott insulator.

This release of fluctuations can be shown to connect to the diverging/enhanced electronic compressibility observed in these models. In fact, at low doping the crossover into the Hund metal coincides with the frontier into the zone of instability towards phase separation and we can connect the appearance of such instabilities in our systems to the rapidity by which the crossover between a normal and a Hund metal is realized. Consider the definition of the electronic compressibility as the inverse of the curvature of the system's total energy:

$$\kappa_{el}^{-1} = \frac{\partial^2 E_{tot}}{\partial n^2} = \frac{\partial^2 E_{kin}}{\partial n^2} + \frac{\partial^2 E_{pot}}{\partial n^2}, \tag{4.21}$$

where $E_{tot} = E_{kin} + E_{pot}$ and $E_{pot} = \langle H_{int} \rangle / \mathcal{N}_{sites}$. In SSMF, in the Mott insulator the kinetic energy of the system is zero since the fluctuations are frozen and when we dope it, it takes a finite (negative) value. The curve of E_{kin} at small doping connects to the one at higher doping in the metallic regime continuously and the closer we are to

U_c the more abrupt this release of "extra" kinetic energy appears to be, in agreement with the behaviour of the multiplet populations discussed above. In the Hund metal region the kinetic energy exhibits a negative curvature, replaced by a positive one in the metallic phase. This gives us a hint that if the potential energy exhibits a positive curvature (expected since the two have opposite curvatures), provided it is smaller in absolute value than E_{kin}, then according to Eq.4.21 the total energy will have a negative curvature and hence the compressibility will be negative.

In Fig.4.15a the kinetic, potential and total energies are plotted as a function of total population for two values of interaction ($U < U_c$ and $U > U_c$) in the case of two degenerate orbitals with density-density interactions. The zero of energy has been arbitrarily chosen so that at the half-filled Mott insulator $E_{pot} = 0$. In the large doping regime the curves for the two values of the interaction appear quite similar, while in the Hund metal zone they have a very different behaviour. In particular, for $U < U_c$ the evolution of the curves as a function of doping is monotonous. On the other hand, for $U > U_c$ we identify a crossover when E_{kin} and E_{pot} both change curvature with the negative one of E_{kin} not being compensated by the positive curvature of E_{pot}, resulting in an overall negative curvature in E_{tot}. As shown above this ultimately corresponds to a zone of negative compressibility. With this result we can directly connect the release of "extra" kinetic energy as determined by the available hopping channels (which is related to the ground state degeneracy) with the charge instability.

The differences in the instability zones of the various models we report in this study can be traced back to the differences in the quenching and releasing of the multi-orbital kinetic energy.

Let us first look into the comparison between systems with density-density and Kanamori interactions. We saw earlier that the rotational invariance of the $\alpha = 1$ systems preserves the degeneracy of the whole low-energy multiplet with $S^2 = S_{max}(S_{max} + 1)$, while in the case of $\alpha = 0$ only the degenerate doublet with $|S_z| = S_{max}(n)$ is left forming the ground state. This means that the suppression of available hopping channels and hence of multi-orbital fluctuations is more pronounced in the density-density case, leading to a more abrupt doping-driven release compared to the Kanamori one.

In the same spirit, for the models with crystal-field splitting we must take into account the existence of the orbitally-selective Mott insulating phase. Crossing the OSMT towards a larger doping, the kinetic energy which was suppressed due to the complete localization of one among the orbitals is now released abruptly resulting to a negative compressibility zone. In Fig.4.15b we plot the kinetic, potential and total energies as a function of total population for $U < U_c$ and $U > U_c$ in the case of two orbitals with crystal-field splitting $\Delta = 0.2$ and density-density interactions. Indeed, compared to

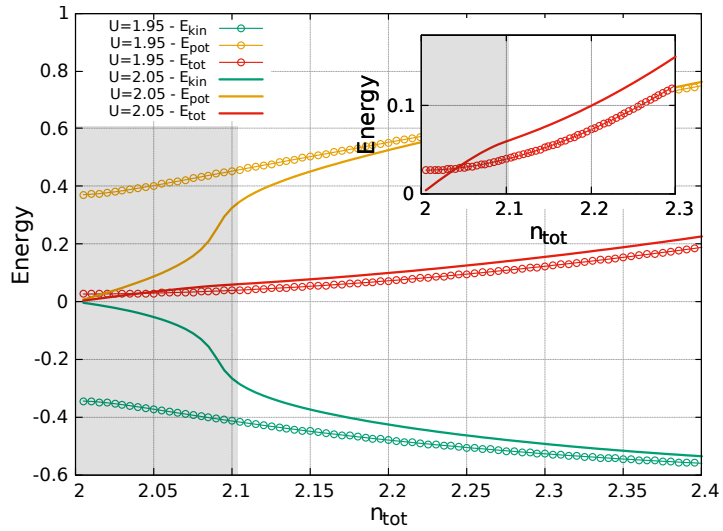

(A)

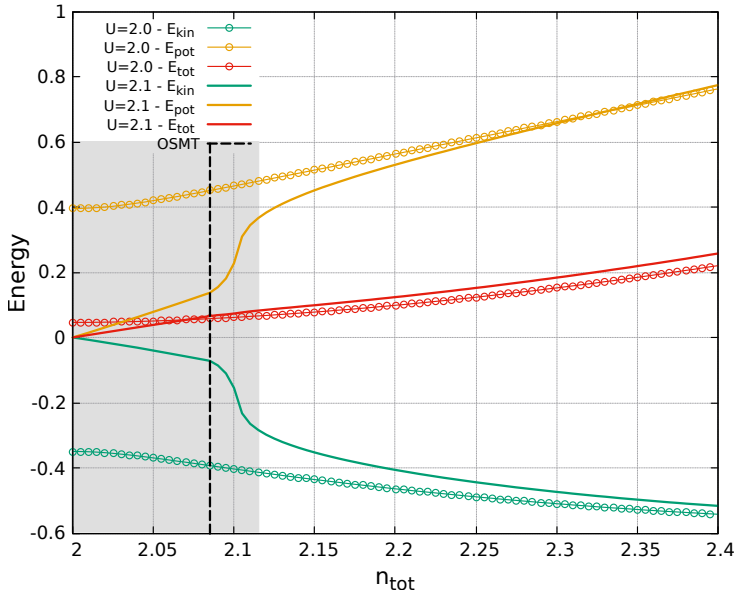

(B)

FIGURE 4.15: **(A)** Total, kinetic and potential energies per site for the two-orbital degenerate Hubbard model with $J/U = 0.25$, density-density interactions $\alpha = 0$, for $U = 1.95 < U_c$ (points) and $U = 2.05 > U_c$ (lines) as a function of total density. The gray zone indicates the zone of charge instability for $U = 2.05$ as defined by a negative compressibility. Inset: blow-up of the total energies highlighting the negative curvature of E_{tot} for $U = 2.05$ at low doping [3]. **(B)** The same calculations performed for a two-orbital system with crystal-field splitting $\Delta = 0.2$, for $U = 2 < U_c$ and $U = 2.1 > U_c$. The crossover into the zone of charge instability appears here more pronounced and extended compared to the degenerate case.

Fig.4.15a the sudden release of kinetic energy takes place at larger dopings. In particular, it happens at the doping of the OSMT, where the orbital higher in energy, being insulating for small n_{tot}, becomes metallic. The release of kinetic energy is more abrupt

compared to the degenerate case, because there is a larger number of hopping channels blocked when an orbital is insulating and hence a stronger increase of kinetic energy when they become available.

When $M > 2$, as we briefly mentioned above, there can be more than one OSMT lines and in reality such an instability zone is present on the side of each OSMT further away from half-filling. However, the largest zone will clearly appear when the last "frozen" orbital becomes metallic and therefore the maximum hopping processes become available. Hence the instability zone extends to larger dopings when there is a crystal-field splitting, since it comes as a result of the finite doping OSMT or of the corresponding strong increase in delocalization of an orbital, relevant for realistic calculations, as shown in the next subsection for FeSe.

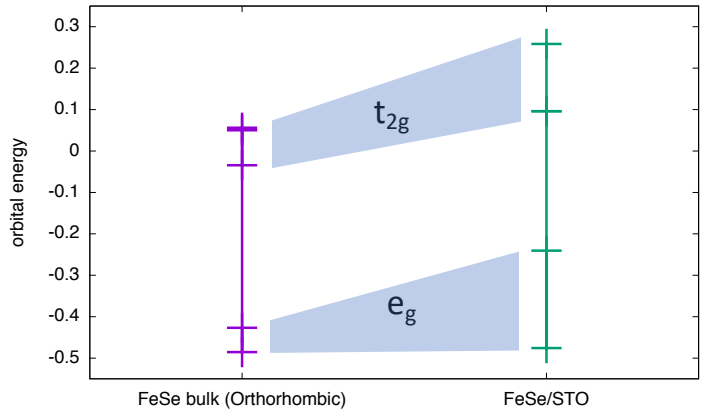

FIGURE 4.16: Values of the Fe 3*d* orbital energies obtained through DFT for the cases of bulk and monolayer FeSe, calculated in [140]. The crystal-field splitting between them is larger in the monolayer system compared to the bulk, resulting to a more extended and pronounced charge instability zone as calculated in [140] and understood on general grounds through our work on simplified models [3].

4.5 Application to the compressibility enhancement in simulations of FeSe bulk and monolayer

In this section we show that the mechanism responsible for the charge instability, as presented above, applies to the realistic cases of FeSe bulk and monolayer. We already mentioned earlier in this chapter that the zone of enhanced/negative compressiblity was found in DFT+SSMF calculations for FeSe in [140] and, in particular, it was there shown that for the case of FeSe monolayer the "moustache" region appears to be more pronounced and extended compared to the bulk [25]. This significant result illustrates

the possible correlation between the compressibility enhancement and the critical temperature T_c for superconductivity, the record value of which is obtained indeed for the monolayer FeSe.

The larger extent and strength of the instability in the monolayer is in agreement with our results on simplified models. The DFT calculations producing the tight-binding bare Hamiltonian used in the DFT+SSMF calculation give us access to the orbital energies of the system and we can make a comparison between those of the bulk and the monolayer. In Fig.4.16 they are plotted for the two cases and the monolayer exhibits a larger crystal-field splitting, therefore according to our description a more extended and pronounced charge instability zone is to be expected.

We should mention that in the realistic cases of iron-based materials (and in particular here in FeSe bulk and monolayer), despite the large crystal-field splittings, there is no orbitally-selective Mott transition observed. Even if a strict OSMT is avoided, nevertheless there is a strong suppression of the quasiparticle weight of the high in energy orbital. This effect defines a clear crossover between an orbitally non-selective regime and a selective one. In the latter, one orbital (or more) is almost localized [123, 157, 158], yielding the weight of certain configurations almost zero and therefore our analysis applicable.

4.6 Summary

In this chapter we showed that the diverging/negative electronic compressibility zone ubiquitously found in the paramagnetic phase diagram of Hund metals is wider in doping:

- for an increasing number of orbitals M,
- for density-density interactions than for the rotational invariant standard Kanamori form,
- when the orbitals are not degenerate; the larger the crystal-field splitting, the larger the doping range.

The series of effects (the first and last in particular) motivates the possible relevance of this instability for iron-based superconductors and other similar materials which are not in the immediate proximity of half-filling, where this instability originates, in agreement with realistic calculations.

We also provided a description of the mechanism behind the effect, by analyzing the kinetic energy of the systems. In the following chapter, we will perform numerical and analytical calculations and show the connection of the charge instability region to the first-order in the Mott-transition at half-filling.

Chapter 5

Phase separation and QCP as a result of first-order Mott transition

In this chapter we connect the appearance of a phase separation region in Hund metals, introduced in the previous chapter, to the first-order of the Mott transition at half-filling at *zero temperature*. Using DMFT we show that, by continuity, the coexisting metallic and insulating solutions at half-filling give rise to a *bistability zone* at finite doping, with two coexisting metals. When this zone closes, a phase separation region with no stable solutions appears, ending at a *quantum critical point (QCP)* (Fig.5.4). Using SSMF we connect the coexisting stable branches through an unstable branch and obtain a continuous sigmoid. We express the mechanism within *Landau theory of phase transitions*. We use the perturbative expansion of SSMF to show that the first-order Mott transition is induced by the lifting of the atomic ground state degeneracy in presence of a small energy scale (in our case J). The results reported in this chapter are the subject of the following article:

First-order in the Mott transition induces a quantum critical point at finite doping
M. Chatzieleftheriou, A. Kowalski, M. Berović, A. Amaricci, M. Capone, L. De Leo, G. Sangiovanni and L. de' Medici, in preparation

5.1 Discussion on the order of the Mott transition

5.1.1 Single-orbital system

Various studies have been carried out on the half-filling Mott transition in a single-orbital system. As shown in Fig.5.1 adapted from [4] where a DMFT analysis was made, there is a zone at low enough temperatures and at a range of interactions, where a metallic and an insulating solution coexist. In fact a metal exists for $0 \leq U < U_{c2}$ while an insulator for $U > U_{c1}$, therefore since $U_{c1} < U_{c2}$ there is overlap of the two

solutions yielding a coexistence (or bistability) zone[1]. The two solutions compete and the solid black line corresponds to the crossing of the two respective energies. On the left of the line the metal is lower in energy and on the right the insulator, so the solid line corresponds to a first-order Mott transition. At zero temperature, though, the solid line merges with the end of the metallic solution, implying that the metal has always a lower energy than the insulator until it vanishes at a second-order transition, since the energy difference between the two solutions behaves as $\Delta E \propto (U - U_{c2})^2$. At $T = 0$ in the range $U_{c1} < U < U_{c2}$ a preformed gap emerges and at zero energy there is a peak in the spectral weight. As the interaction is increased the peak loses weight until it becomes infinitely thin and disappears exactly at U_{c2} [159].

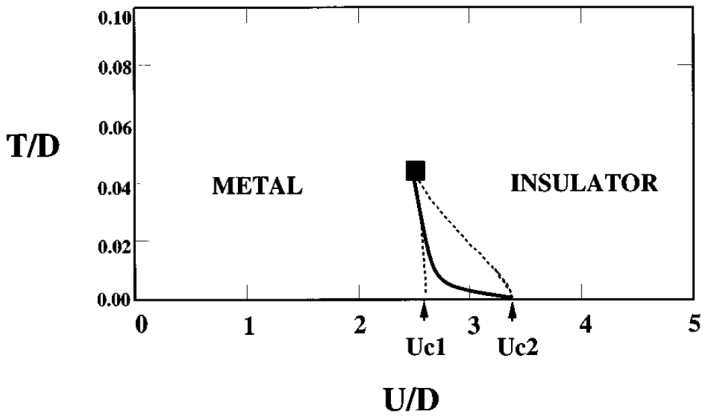

FIGURE 5.1: Phase diagram of a single-orbital system at half-filling. For low enough temperatures there is a zone of interaction strengths $U_{c1} < U < U_{c2}$ where a metallic and an insulating solution coexist. The solid black line corresponds to the first-order transition between the two and at $T = 0$ the transition becomes second-order [4].

5.1.2 Multi-orbital system

In a multi-orbital system in absence of Hund's coupling ($J = 0$) it has been shown that the situation is exactly parallel to the one of single-orbital systems. The Mott transition is first-order for finite temperature, whereas it becomes second-order at $T = 0$ [5, 6]. On the contrary, once a finite Hund's coupling is introduced ($J \neq 0$) the first-order nature of the transition persists down to zero temperature [160, 161, 162]. In the previous chapter 4 we discussed the Mott transition in presence of Hund's coupling within the SSMF framework, for models with both the density-density and the Kanamori form of interactions. Later in this chapter in Fig.5.19 the quasiparticle weight Z is plotted as a function of the interaction U for both models and for different values of J/U. In the

[1] This coexistence exists up to a critical temperature where the two solutions merge, plotted as a solid square in Fig.5.1 and beyond which there is a crossover rather than a transition.

density-density case, an increasing J/U results in a decreasing U_c and a growing first-order jump in the transition. For the model with Kanamori interactions, increasing J/U also leads to a decreasing U_c but the evolution of the jump is non-monotonous. At zero Hund's coupling the Mott transition is second-order [163, 145, 57]. All this analysis within SSMF is done at zero temperature and the method -being computationally light- offers the possibility of producing a number of different results in a short time.

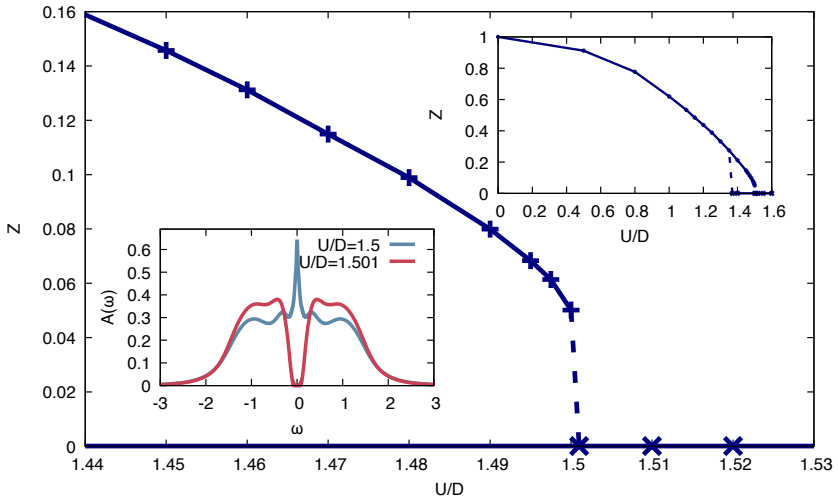

FIGURE 5.2: Quasiparticle weight as a function of interaction strength for a two-orbital system at half-filling and $T = 0$ with $J/U = 0.25$, where the Mott transition is seen to be first order. In the lower inset we see the spectral function's change across the transition. In the upper inset we observe a zone of coexisting solutions, a metallic and an insulating one.

In Fig.5.2 we show the quasiparticle weight Z as a function of the interaction strength U/D for a two-band model with density-density interactions at $T = 0$ (for $J/U = 0.25$), calculated using the more accurate DMFT method. In particular we use NRG for solving the Anderson impurity model. At $U = 1.501$ the system undergoes a first-order Mott transition, confirmed by the spectral function plotted in the lower inset. For $U = 1.5$ there is a clear quasiparticle peak which completely vanishes at $U = 1.501$, without the formation of in-gap states. For a range of interactions, as seen in the upper inset, the metallic solution coexists with an insulating one, the two compete and the metal prevails until the first-order transition takes place.

5.1.3 Comparison of NRG, ED and CTQMC as impurity solvers

In order to further validate the above results on the first order of the Mott transition in presence of Hund's coupling at $T = 0$, we compare it as obtained using different impurity solvers.

We use different impurity solvers for DMFT and in particular the Numerical Renormalization Group (NRG) and the Exact Diagonalization (ED) to address the zero temperature properties and the Continuous-Time Quantum Monte Carlo (CTQMC) for the finite temperature ones[2].

NRG at $T = 0$ describes exactly the low-energy physics, but exhibits a growing inaccuracy in capturing spectral features for an increasing energy. In the DMFT self-consistent procedure the different energy scales are connected, thus the high-energy imprecision can manifest itself through a quantitative inaccuracy in the low-energy results. We use a modified version of the NRG Ljubljana code [86], which implements a QSzTz symmetry (U(1)xU(1)xO(2)). The Full Density Matrix algorithm [164] was used with Λ=4.0, 8000 states kept in every NRG iteration, 8 values for the z-interleaving parameter, and a log-normal broadening of the spectral functions with broadening parameter 0.3. The self-energy was calculated with the so-called Sigma-trick introduced in [165]. The quasiparticle weight is evaluated from the real-axis self-energy $Z = (1 - \partial Re\Sigma(0)/\partial\omega)^{-1}$.

ED describes the Anderson impurity through a discretized bath and it is exact at the limit $N_s \to \infty$, N_s being the bath size. In practice N_s is limited to small values due to the exponential growth of the Hilbert space making the Hamiltonian diagonalization quickly impossible. This truncation results in a limited spectral resolution and an associated systematic error. ED provides a numerically less expensive framework than NRG and at half-filling we were able to work with a large $N_s = 14$ using the Lanczos/Arnoldi algorithm for the diagonalization within the new parallel implementation EDIpack [166]. The self-consistency condition is enforced on a Matsubara frequency grid $\omega_n = (2n + 1)\pi/\beta_{grid}$, with $\beta_{grid} = 200/D$. We fit the discretized variational form of $\Delta(\omega_n)$ on the numerically calculated $G_R(\omega_n)D^2/4$ through a least square fit with weight $1/\omega_n$. The quasiparticle weight is evaluated from the Matsubara axis self-energy as $Z = (1 - Im\Sigma(\omega_0)/\omega_0)^{-1}$. Out of half-filling and especially in the Hund metal regime the Lanzos/Arnoldi algorithm fails (see section 2.3.3 for a discussion on this issue) and we there use instead a full diagonalization numerical routine. This limits to $N_s = 6$ the bath size used in the rest of this chapter for calculations at finite doping[3].

CTQMC is numerically exact albeit limited to finite temperature. The quasiparticle weight is calculated through $Z = (1 - b)^{-1}$, with b being the linear coefficient of a

[2]The CTQMC calculations have been performed by our collaborators Alexander Kowalski and Giorgio Sangiovanni in the University of Würzburg.

[3]We have used $N_s = 6$ and sample benchmarked on $N_s = 8$ finding that they have quantitative but not qualitative differences, so we continued our study with the computationally less expensive choice of $N_s = 6$.

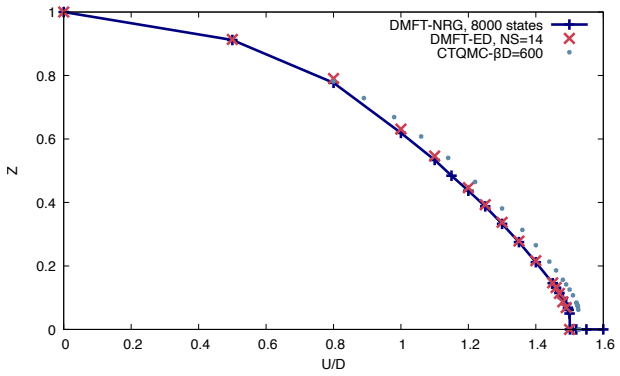

(A)

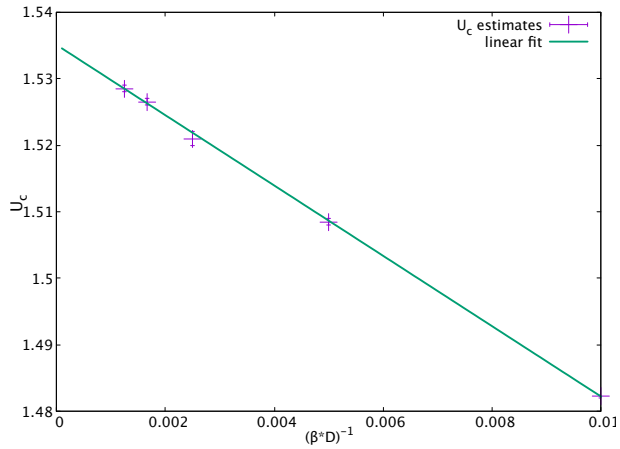

(B)

FIGURE 5.3: **(A)** Quasiparticle weight as a function of interaction for a two-orbital system at half-filling and $T = 0$ (with $J/U = 0.25$) produced with NRG, ED and CTQMC as the DMFT impurity solvers. NRG and ED exhibit very good agreement, while the CTQMC results give a slightly larger value for U_{c2}. **(B)** Calculation of U_{c2} as a function of temperature within CTQMC for extrapolation to $T = 0$.

second-order polynomial best fitted to $Im\Sigma(\omega_n)$ on the five lowest Matsubara frequencies. CTQMC calculations were performed using the CT-HYB solver implemented as part of the w2dynamics package [167]. At all temperatures, a minimum total number of 300000 measurements was performed per iteration, in the last 20 iterations.

In Fig.5.3a we compare the three methods through a combined plot of the quasiparticle weights Z as a function of interaction U/D, for the two-orbital model with $J/U = 0.25$. NRG and ED exhibit a very good agreement and undergo a common first-order Mott transition, whereas Z_{CTQMC} appears to be consistently above the others showing additionally a larger U_{c2}. We use CTQMC in order to obtain low temperature results validating NRG and ED against their systematic inaccuracies. In Fig.5.3b U_c is plotted at different temperatures, calculated with CTQMC and the extrapolation to $T = 0$ shows that the critical interaction is $U_c/D = 1.5351 \pm 0.0004$, indeed larger

than the one found with NRG and ED. Therefore, using this result we can estimate the systematic error of NRG and ED to be approximately $2 \div 3\%$.

The three methods however confirm beyond any possible doubt the first order nature of the Mott transition in the present case.

5.2 Single-orbital doped Mott insulator

In a single-orbital model at zero temperature, upon moving the chemical potential away from the $\mu = 0$ value the evolution of the metallic and the insulating solutions coexisting at $\mu = 0, T = 0, U_{c1} < U < U_{c2}$ differs [4]. Once the chemical potential is moved the metal gets immediately doped. The insulator instead remains at half-filling for the range of μ in the Mott gap and once the chemical potential reaches the gap's edge at $\mu = \mu_{c2}$ the branch vanishes. If μ is moved further the system jumps on the metallic branch. After the second-order Mott transition, for $U > U_{c2}$ the zone of chemical potentials at which there is coexistence of a metallic and an insulating solution gets shifted to larger values. However, it does not vanish, it rather remains finite in range for all values of U, since there is always some gain in forming an in-gap quasiparticle peak for $\mu_{c2} < \mu < \mu_{c1}$ [168]. In conclusion, at finite doping and $T = 0$ only one metallic solution is found and the insulating one is bound to remain at $\delta = 0$ for a range of chemical potentials until completely disappearing (black line in right panel of Fig.5.5).

5.3 Hund metals: bistability, phase separation and QCP at finite doping

In a multi-orbital system with $J = 0$ it has been shown that the situation is - as at half-filling - similar to the single-orbital case [5, 169], with only the metallic solution remaining at finite doping. However, the onset of J qualitatively changes the picture. In the left panel of Fig.5.4 we plot the chemical potential as a function of electron doping for different values of interaction U/D (using NRG). At $U_{c1} < U < U_{c2}$ the metallic solution at half-filling extends continuously to finite doping. The insulating solution though remains at half-filling for a range of chemical potentials until at a given μ it also enters the doping plane becoming a second metallic branch overlapping with the doped metal one. At larger chemical potential this second branch disappears and upon raising further μ the system jumps to the other branch. At $U > U_{c2}$ the doped metal branch does not extend down to half-filling, there is rather a zone at small doping with

only a doped insulator branch. Therefore, at finite doping there is coexistence of two different metallic solutions and a transition from one to the other.

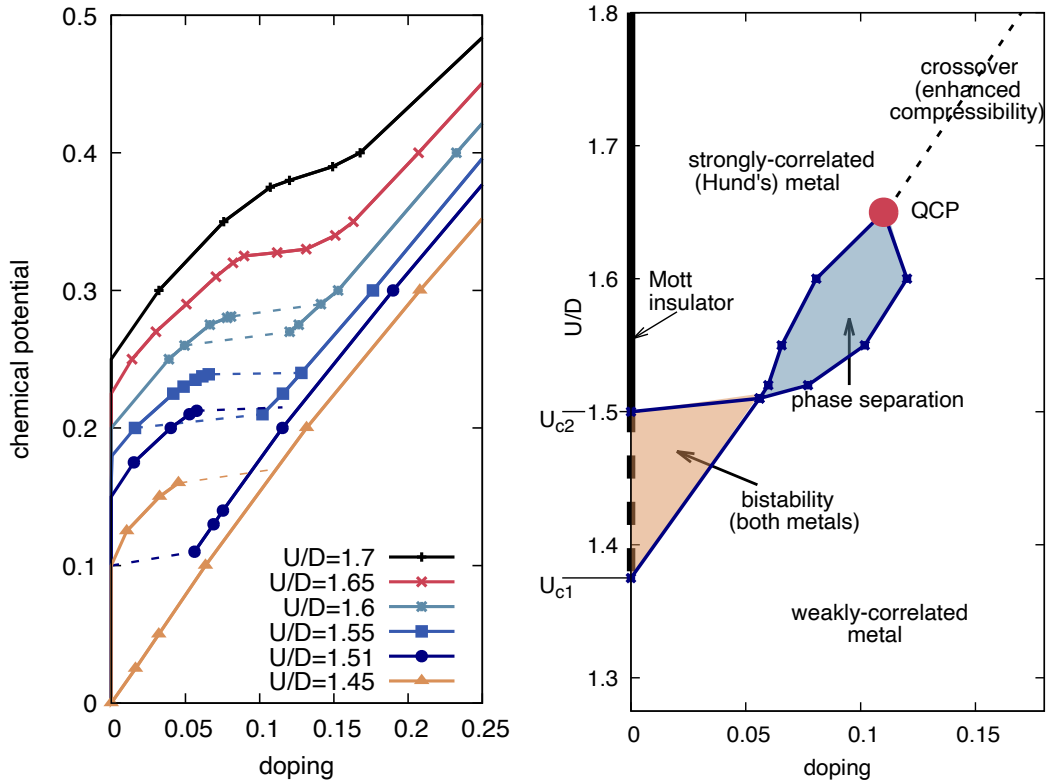

FIGURE 5.4: **Left panel:** Chemical potential as a function of doping for a two-orbital model with $J/U = 0.25$ at $T = 0$, calculated with NRG. Two metallic solutions coexist at finite doping. **Right panel:** Phase diagram on the doping-interaction plane, displaying a bistability zone (in the two branches) followed by a phase separation one, ending at a Quantum Critical Point (QCP).

At fixed doping the two solutions may or may not overlap. They do so at interactions which are above U_{c1} and up to slightly above U_{c2}. That zone is depicted in the right panel of Fig.5.4 as a *bistability zone* in the doping-interaction plane, at which *two metallic solutions* coexist. This zone is followed at larger dopings and interactions by a regime of *phase separation* where there is *no stable solution* for a range of doping. That region ends at a *Quantum Critical Point (QCP)* where the two spinodals of the zero temperature first-order transition merge into *one continuous solution*. Above the QCP there is a crossover in the phase diagram, signalled by an inflection point in the μ vs n curve. Quantum Critical Points (QCP) are a widely studied subject in condensed matter [170, 171], due to the documented occurrence in materials like e.g. heavy fermions [172, 173, 174] and also for being among the most debated explanations of the strange-metallic phase in the cuprates and possibly a key to their superconductivity [175, 176, 177, 178, 179].

Considering that the electronic compressibility is given by $\kappa_{el} = dn/d\mu$, the inflection point at μ vs n corresponds to an enhanced κ_{el}, which eventually diverges at the QCP. The phase separation region where κ_{el} is negative was extensively discussed in the previous chapter 4 based on SSMF results and is now confirmed using DMFT.

As also shown in the previous chapter, the compressibility divergence is found not only at the QCP but also at the two spinodals delimiting the phase separation zone. Indeed in the left panel of Fig.5.5 we plot μ vs n results calculated with ED, which being computationally lighter than NRG allows the possibility of performing more detailed calculations. Moreover, we were able to follow continuously the μ vs n curve by adjusting within the DMFT cycle the chemical potential until convergence was obtained for the desired doping, thus continuously connecting the two branches found with NRG. For each value of $U < U_{QCP}$ at a fixed chemical potential there are three solutions at different dopings, two of them stable since they correspond to a positive κ_{el} and one unstable with negative κ_{el}. A complete color map of compressibility at the doping-interaction plane produced with ED at $T = 0$ is plotted in Fig.5.6 illustrating the phase separation zone[4].

In the right panel of Fig.5.5 we show data adapted from [180] corresponding to a single-orbital Hubbard model at zero temperature and at different values of finite temperature. At $T > 0$ the system exhibits the same behavior found in our study for the Hund metals at $T = 0$, namely there are three solutions for a fixed chemical potential connected through a sigmoid. At $T = 0$, however, there is only one metallic solution at finite doping, while the insulating one remains stuck at half-filling and it actually becomes a double solution, as a limiting case of the finite T sigmoids. An illustration of the equal-area Maxwell construction at $T > 0$ is also shown, connecting the points at which the free energies of the two solutions become equal. At $T = 0$, where two out of the three solutions are collapsed on top of each other on the $\delta = 0$ axis, the Maxwell construction cannot in practice be performed and the transition is bound to take place at the cusp of the collapsed curve in a continuous second-order manner.

Part of this behavior of the Hund metals has been already found at finite temperature in the work presented in [181] and performed using CTQMC as the DMFT impurity solver. There, the authors indeed observed a regime of coexisting solutions in the finite doping plane (see Fig.5.7a) but this result could in principle be attributed to temperature. Indeed for the case of $J = 0$ or a single-orbital system at finite T, as shown in [169] the insulating solution too gets doped, even though it extends to a very small

[4] In the calculations of μ vs n we have used Full ED with $Ns = 6$ sites in the bath discretization, due to problems with the Lanczos algorithm in the Hund metals regime, discussed in section 2.3.3. For that reason the whole zone is shifted in U compared to the NRG data and the U_c is different than the one produced with Lanczos (and $Ns = 14$) plotted in Fig.5.2.

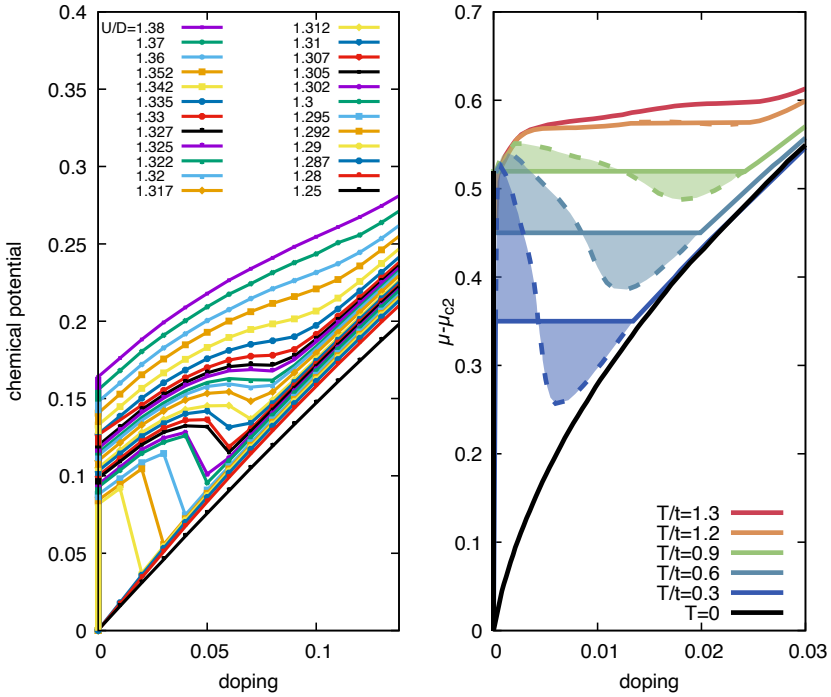

FIGURE 5.5: **Left panel:** Chemical potential as a function of doping for a two-orbital Hund metal system with $J/U = 0.25$ at $T = 0$ calculated using ED as the DMFT solver. For a range of values of U, the curve has a sigmoidal shape connecting continuously the two branches found with NRG. Thus for a fixed μ there are three solutions in doping: two stable and one unstable. **Right panel:** Chemical potential as a function of doping for a single-orbital model at different temperatures, where we see the disappearance of the sigmoid at $T = 0$. Adapted from [180].

doping region. In the present work we performed *zero temperature* NRG and ED calculations, thus explicitly ruling out the explanation of the observed effect in terms of temperature and clearly stating that *in Hund metals at $T = 0$ there is a transition between two doped metallic solutions*.

The occurence of a quantum phase transition in systems with finite Hund's coupling has been already discussed in the past in [92]. There the authors used finite temperature CTQMC as a DMFT impurity solver and calculated for a three-orbital model in presence of J a frontier in the doping-interaction plane departing from the Mott transition at half-filling, across which they observed a quick modification of the metallic properties. At large U and small doping a zone with frozen local magnetic moments was found, named the *spin freezing* zone, considered incoherent, as opposed to the coherent paramagnetic regime on the other side of the frontier (the relevant plot is shown in Fig.5.7b). The authors described it as a quantum phase conherence-incoherence transition, however it was later rather considered to be a continuous crossover between Fermi liquid metals with different coherence temperatures. That was because in fact DMFT is by construction bound to produce Fermi liquid behaviors at $T = 0$ [31, 182].

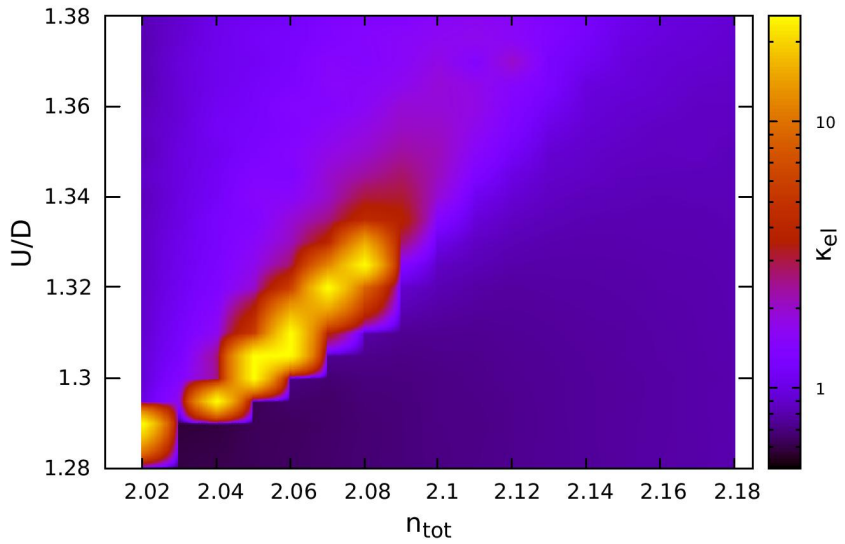

FIGURE 5.6: Color map of the electronic compressibility on the doping-interaction plane of a two-orbital model with $J/U = 0.25$ at $T = 0$, calculated using Full ED with $Ns = 6$.

In this work we show explicitly that for a range of $U < U_{QCP}$ the crossover turns indeed into a zero temperature first-order transition between two distinct Fermi liquids in the doping plane, with very different degree of correlations between them. The coherence temperature in the more correlated one drops exponentially upon approaching the half-filling Mott insulator [183]. Nevertheless, their Fermi liquid character is clearly established since, as shown in Fig.5.8, the quasiparticle peak at zero energy is pinned for both of them at the zero T Fermi liquid value.

5.4 Connection between the first-order of the transitions at finite doping and at half-filling

Even in the ED calculations, that are capable of connecting the two branches across the phase-separation and yield a continuous sigmoid, a discontinuity remains in the bistability region. It is legitimate to ask if another, more complicated multi-valued function connects also these branches. To investigate this point we resort back to SSMF calculations, where we were able to continuously follow the disconnected branches at finite doping and connect them. We did that by applying a modification on our code in order to obtain converged solutions for a fixed quasiparticle weight. In Fig.5.9a Z is plotted as a function of interaction U/D for different dopings close to half-filling. Starting from the $n = 2$ curve related to the one of Fig.5.2 calculated with DMFT, we observe

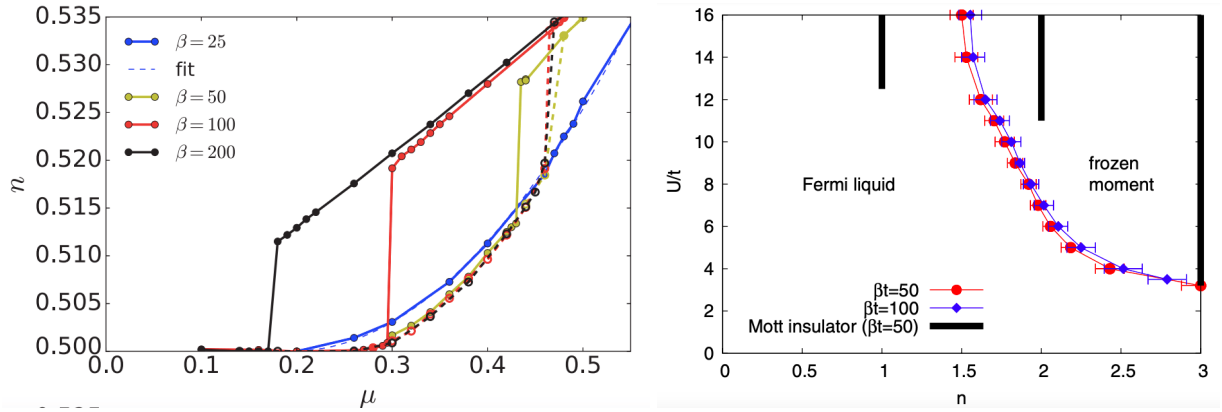

(A) (B)

FIGURE 5.7: **(A)** Coexistence of solutions in the plane of chemical potential and electron doping at finite temperature for different values of β. The calculations have been performed using finite temperature CTQMC and the parameters are expressed in units of $t = D/2$, as opposed to D in our framework. The plot is adapted from [181]. **(B)** Spin-freezing zone of a three-orbital Hubbard model at finite T, calculated again using CTQMC [92].

that the metallic solution connects with the insulating one through an unstable branch where Z grows with increasing U. This behavior is also found in the single-orbital or the two-orbital with $J = 0$ model at finite T, but then vanishes at $T = 0$ since the unstable metallic branch collapses on the insulating one giving rise to a second-order transition. Once the system gets doped the insulating solution of $n = 2$ accepts some doping too and turns into a very strongly correlated metallic branch, which continuously connects to the less correlated metal through another unstable part. Therefore, there is a range of dopings (corresponding to the bistability region) where for each value of U and n there are three coexisting metallic solutions. Upon further doping, this "unfolding" eventually ends marking the closing of the "bistability" zone[5].

In Fig.5.9b the same effect is illustrated from another angle; in the "bistability" zone for any doping there are three solutions, two at low μ connected to the two metallic ones at half-filling (the stable and unstable) and one at high μ connected to the Mott insulator. The evolution of this behavior is such that once the bistablity zone has ended, $\mu(n)$ becomes a univalued function and the very existence of the high μ branch (related to the $n = 2$ insulator) gives rise to the diverging and subsequently negative electronic compressibility.

[5]The doped Mott insulator enters the doping plane with a negative slope as opposed to the positive one observed with DMFT, hence this branch within SSMF is unstable. In the following section we will discuss that this is in fact an artifact of SSMF.

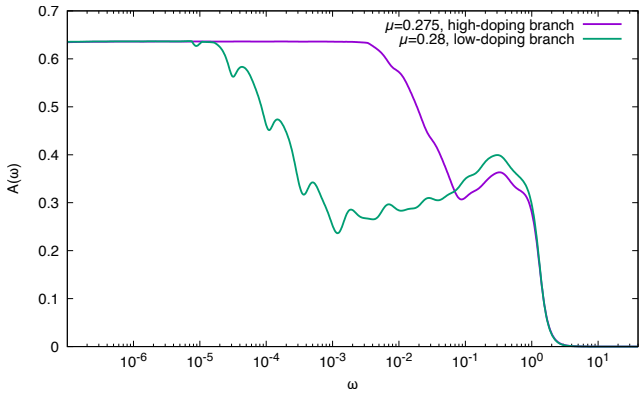

FIGURE 5.8: Local spectral function calculated for $U/D = 1.6$, at energies exponentially approaching zero for two chemical potential values corresponding to the two branches shown in Fig.5.4. They both pin at the same $T = 0$ Fermi liquid value, exhibiting their Fermi liquid character despite their large difference in coherence temperature.

Using this "principle of continuity" [184, 185] we are able to connect the first-order in the doping driven Mott transition to that of the interaction driven one. This connection has been already addressed in [186] where the authors studied a first-order Mott transition, where a metallic and an insulating solution coexist at half-filling, with the second having a lower free energy. They showed that there is a critical chemical potential at which the two energies cross again and that there is hence a first-order doping driven Mott transition. In our work we extend that picture by studying the continuity of the solutions through the existence of spinodal lines, the merging of which into one univalued function leads eventually to a quantum critical point.

5.4.1 Particularities of calculations within the SSMF method

As we have already mentioned multiple times in this manuscript the SSMF method is a computationally not expensive, agile technique which has provided us with a lot of important results and insights. However, one must treat it with caution since it is known that the method is more accurate for a larger number of orbitals [57]. Therefore, in this project where we are working with a two-orbital system there are certain limitations when studying it in the context of SSMF. This issue manifests itself in the fact that the sigmoid of $\mu(n)$ is not captured correctly in the SSMF results shown in Fig.5.9b. The doped insulator branch enters the density plane with a negative slope, even though DMFT calculations show that it initially has a positive slope, becoming negative at larger dopings. The result of this inaccuracy is that there is indeed a sigmoidal line, however here for a given chemical potential there are not three metallic solutions, there is rather: a stable metal, an unstable metal and a stable insulator.

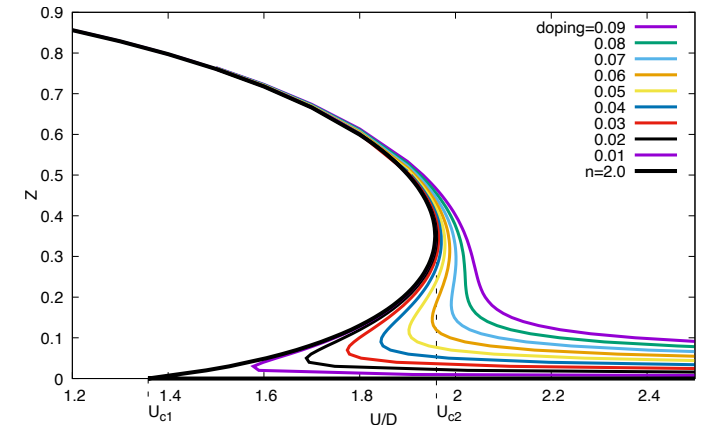

(A)

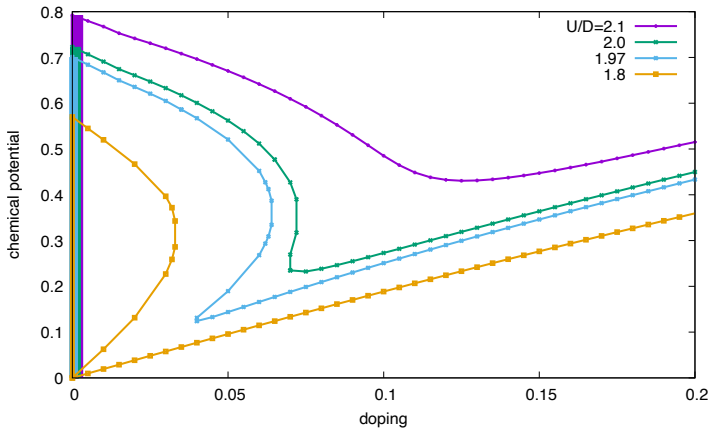

(B)

FIGURE 5.9: **(A)** Quasiparticle weight as a function of interaction strength for a two-orbital model with $J/U = 0.25$ at $T = 0$ for different values of doping. **(B)** Chemical potential as a function of doping for the same model. In these calculations we have used the expression $\lambda_m^0 = \sqrt{Z_m}\frac{2n_{m\sigma}-1}{n_{m\sigma}(1-n_{m\sigma})}h_{m\sigma}$, discussed in section 2.2.4. We observe that there is a range of dopings where the system exhibits coexistence of three metallic solutions. These solutions correspond to doping the three solutions found at each U for $n = 2.0$ in panel (A). The end of this bistability region is marked by $\mu(n)$ becoming a univalued function of n. This "unfolding" results into a sigmoid connecting the larger solution with one adiabatically connected to the half-filled metal and thus into a diverging electronic compressibility. The calculations of both figures are performed using SSMF.

This issue goes back to the discussion made in chapter 4 on the regions of phase separation within SSMF for different number of orbitals M, see Fig.4.2b. It was there shown that the instability zones for $M > 2$ had a "moustache" shape, originating from the fact that the μ vs n curves exhibited a positive slope at large and small dopings, connected through a negative slope in an intermediate doping region. To be exact, this is the case for all relevant values of U in the five-orbital model; in the three-orbital one there is rather a narrow range of U where the negative μ vs n slope persists down to

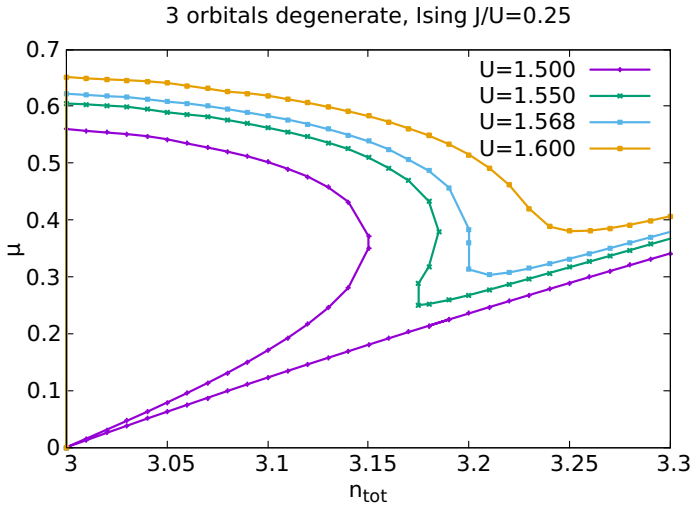

(A)

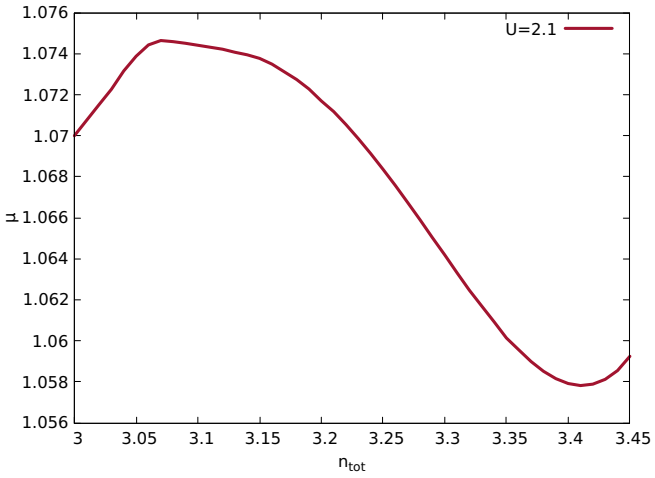

(B)

FIGURE 5.10: **(A)** Chemical potential as a function of density for a three-orbital model with $J/U = 0.25$ calculated within SSMF. We observe the zone of coexistence of three metallic solutions at fixed doping, with $\mu(n)$ evolving at larger interactions to a univalued function exhibiting diverging compressibility. **(B)** Chemical potential as a function of density at a larger value of U, where at small dopings the positive slope of $\mu(n)$ is restored, following a region of negative compressibility.

zero doping. In the two-orbital model, on the other hand, the positive slope is never restored at small dopings and there is an "onion" shape of the phase separation zone.

Performing for a three-orbital system the same calculations we did for the two-orbital one, we obtain for the chemical potential as a function of doping the plot shown in Fig.5.10a. Indeed for a fixed μ there are three solutions (two metallic and one insulating) similar to the two-orbital case and that is because the bistability is found in the U-range where the negative slope in μ vs n persists down to zero doping. However, at larger values of U the positive slope is restored as plotted in Fig.5.10b for $U = 2.1$.

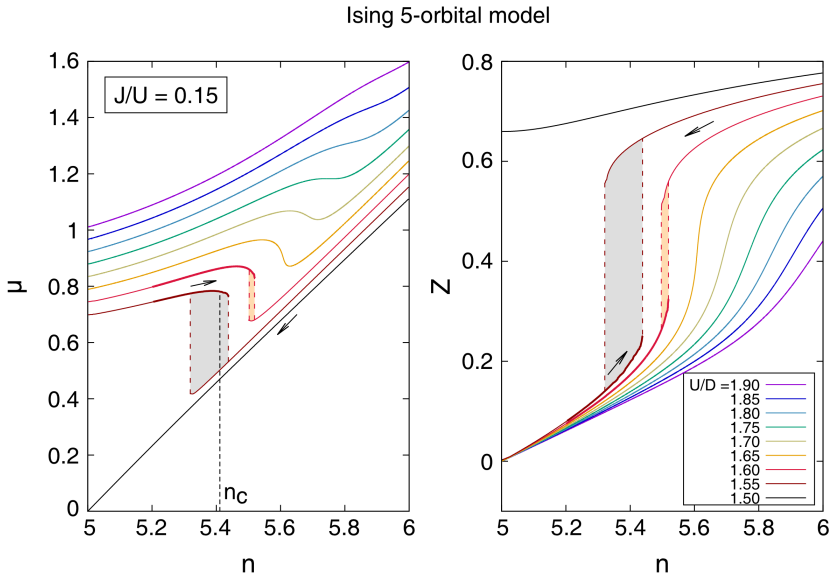

FIGURE 5.11: Coexistence of solutions at finite doping in a five-orbital model with $J/U = 0.15$, as seen both in the chemical potential and in the quasiparticle weight as a function of total density. The calculations have been performed using the Rotationally Invariant Slave Bosons technique by Maja Berović, plot adapted from [146].

In the case of five orbitals the situation resembles more the DMFT one and in the left panel of Fig.5.11 the re-appearance of the positive slope at small dopings is depicted. Moreover, in both the left and right panel the coexistence zone is observed at fixed density.

5.5 Analysis of coexisting solutions at half-filling

In this section we shed light on the mechanism behind the appearance of multiple metallic solutions in the Hund metals, by analyzing the Slave Spin equations. In section 2.2.5 we introduced a perturbative expansion of the SSMF around the Mott insulating solution and showed that it captures both the U_c of the Mott transition and the behavior of $Z(U)$ close to it, in a single-orbital model. This reads:

$$Z = \frac{U^2}{128\epsilon_0^2}\left(1 - \frac{U}{U_c}\right) \tag{5.1}$$

confirming analytically that indeed the Mott transition taking place at $T = 0$ for a single-orbital system is of second order, since Z goes continuously to zero as U grows and approaches U_c. We next extend this analysis to the multi-orbital models and in particular explore the behavior of Hund metals.

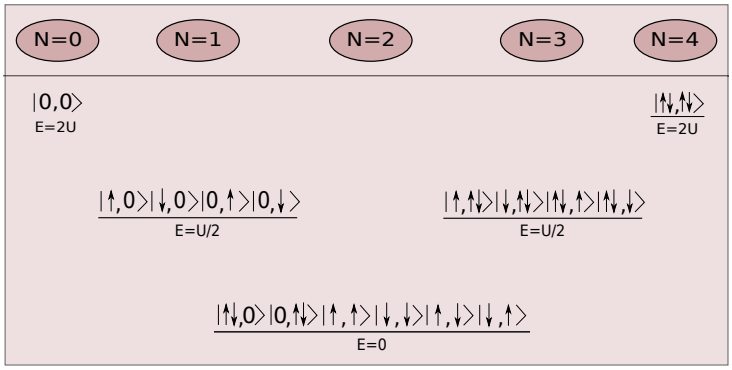

FIGURE 5.12: Atomic spectrum of a degenerate two-orbital Hubbard model at half-filling in absence of Hund's coupling, $J = 0$[6].

A two-band system in absence of Hund's coupling is studied in this section and a finite J will be considered in the following one. We perform perturbation theory around the insulating solution of a system with two degenerate orbitals at half-filling. This procedure allows us to determine at first-order the condition for the Mott transition and at higher orders the behavior of the system before the transition. We start - as done for the single-band model in section 2.2.5 - from a Hamiltonian of interacting slave spins in the SSMF formalism and perturb around the atomic limit $h_m = 0$; the interacting (atomic) Hamiltonian is:

$$H_{at} = U \sum_m S^z_{m\uparrow} S^z_{m\downarrow} + U \sum_{m<m',\sigma,\sigma'} S^z_{m\sigma} S^z_{m'\sigma'}. \tag{5.2}$$

The spectrum of this Hamiltonian is illustrated in Fig.5.12 [6]. We explore the behaviour of the system around this limit by adding the perturbation term:

$$H_{pert} = \sum_{m\sigma} h_m 2 S^x_{m\sigma}, \tag{5.3}$$

related to the kinetic part of the SSMF Hamiltonian (the h_m variable is calculated through the average values of the fermionic operators of SSMF and it constitutes a measure of the system's metallicity - formalism detailed in chapter 2). In Appendix C.1.1 we demonstrate a detailed derivation of the U_c and the $Z(U)$ following the steps presented in section 2.2.5, generalized to the particular system at hand. The result for the critical interaction of the Mott transition is:

$$U_c = -24\epsilon_0 \tag{5.4}$$

[6]For compactness of notation, the slave-spin states are here indicated with the ket of the physical state they represent.

and the dependence of the quasiparticle weight on the interaction around the transition is given - going up to third order in the perturbation - by:

$$Z_m = \frac{U^2}{352\epsilon_0^2}\left(1 - \frac{U}{U_c}\right). \tag{5.5}$$

In Fig.5.13 the numerical results for a two-orbital system with $J = 0$ and a semi-circular DOS are plotted, accompanied by the analytically obtained results of Eq.5.5. The behavior at small $Z_m = Z$ (corresponding to a small $h_m = h$ in the perturbation theory formulation) and the second-order phase transition are reproduced.

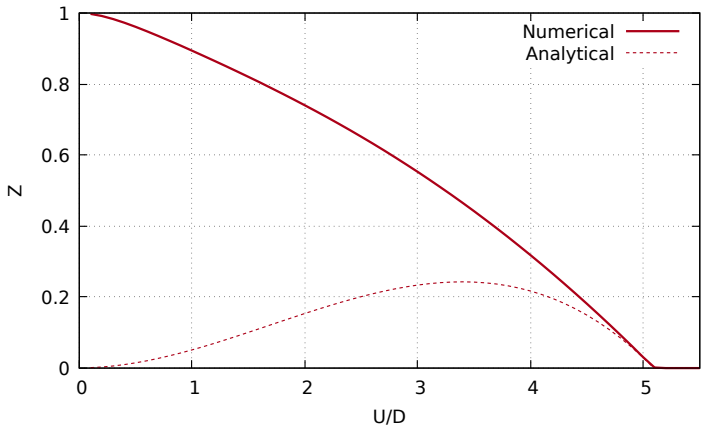

FIGURE 5.13: Quasiparticle weight Z as a function of interaction strength U at half-filling (with Hund's coupling $J = 0$). Numerical results through SSMF and analytical ones by perturbation theory calculations. The transition is second order.

We proceed with the systems of interest to this chapter and we add in the model a finite Hund's coupling in order to investigate its effect on the observables calculated through perturbation theory. Let us first consider the density-density form of interactions:

$$H_{at} = U\sum_m S^z_{m\uparrow}S^z_{m\downarrow} + (U-2J)\sum_{m\neq m'} S^z_{m\uparrow}S^z_{m'\downarrow} + (U-3J)\sum_{m<m',\sigma} S^z_{m\sigma}S^z_{m'\sigma}. \tag{5.6}$$

In Fig.5.14 the atomic spectrum of this Hamiltonian is displayed and it differs from the one of the $J = 0$ system shown in Fig.5.12, due to the breaking of the degeneracy of the ground state in the half-filled sector $N = M = 2$. In particular, the introduction of a finite Hund's coupling raises in energy the low-spin states of this sector and the degenerate ground state manifold now consists of only the two $N = 2$ states with aligned spins. We obtain for the critical interaction of the Mott transition (the detailed

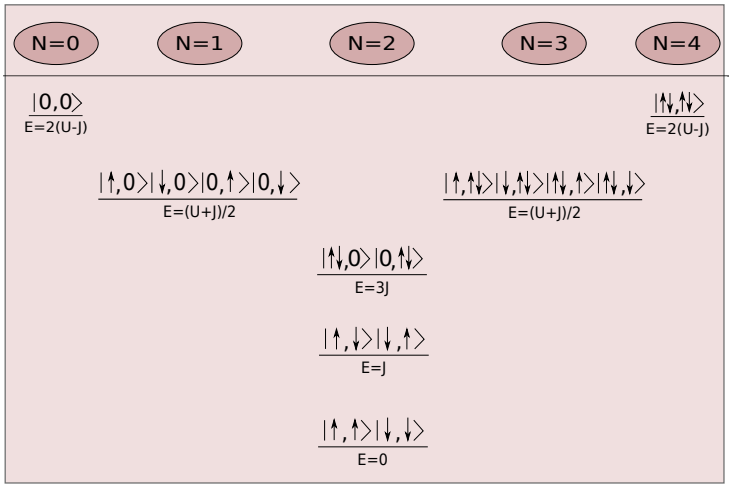

FIGURE 5.14: Atomic spectrum of a degenerate two-orbital Hubbard model at half-filling, in presence of Hund's coupling with density-density interaction[6].

derivation is found in Appendix C.1.2):

$$U_{c1} = -8\epsilon_0 - J. \tag{5.7}$$

The U_{c1} in this case is always smaller than the one corresponding to a system with zero Hund's coupling, regardless of the value of J. This trend is reproduced in the numerical calculations, however the U_{c1} estimated through Eq.5.7 is significantly smaller than the one determined numerically. Indeed - as discussed earlier in this chapter - the Mott transition is first-order. Operatively this means that by raising U, Z does not vanish continuously but there is a limiting $U = U_{c2}$ at which the metallic solution, still with a finite Z, can be found. Raising U further only the insulating solution remains. These two solutions connect through an unstable branch - already introduced in previous sections - and we determine this unstable metallic solution (Fig.5.15) numerically by fixing in our code the desired value of Z and varying U until convergence is met. The interaction $U_{c1} = -8\epsilon_0 - J$ obtained above coincides with the value of U at which this unstable branch connects continuously with the stable insulating $Z = 0$ branch. We will show (Fig. 5.20) that at $U < U_{c1}$ the insulating solution becomes unstable[7] hence $U_{c1} = -8\epsilon_0 - J$ can be identified with the interaction at which in the DMFT description the insulating solution disappears. The key result here is that we can characterize the first- or second-order of the Mott transition in this framework by $Z = \langle 2S_\sigma^x \rangle^2 \to 0$ with a positive or negative slope. This in turn entails the presence of coexisting solutions at a given U.

[7] Within SSMF the insulator ($Z = 0$) is trivially always a solution and this is an artifact of the method. We will see, however, in a following section that below U_{c1} it becomes unstable.

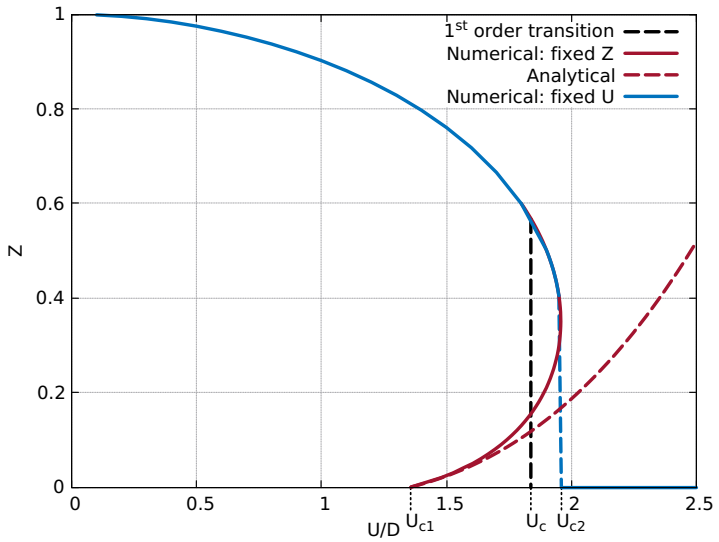

FIGURE 5.15: Quasiparticle weight Z as a function of interaction strength U (with $J/U = 0.25$) at half-filling. Numerical results through SSMF (blue line by fixing U, solid red by fixing Z) and analytical ones (dashed red line) through perturbation theory calculations. The first-order nature of the transition is described analytically in SSMF perturbation theory around the Mott insulator as a $Z(U)$ departing from zero with positive slope at U_{c1}.

In Fig.5.16 we plot the total energy of the system calculated for increasing interactions. There is indeed a U-range where three solutions coexist, two metallic and one insulating. The energies of the stable metal and insulator at some point cross (determining the first-order transition) and there is a "bow"-like continuous connection of the curves, with the edges of the bow defined by the vanishing of the metallic and insulating solution respectively[7].

The arising of multiple metallic solutions is illustrated by the graphic solution (Fig.5.17) of the self-consistency equation $\langle 2S^x_\sigma \rangle = \frac{h}{2\epsilon_0}$[8]. There we have plotted its left term $\langle 2S^x_\sigma \rangle_{pert}$ developed up to third order, while the right term $\langle 2S^x_\sigma \rangle_{sc} = \frac{h}{2\epsilon_0}$ is simply linear. In Fig.2.3 of chapter 2 the same plot was shown for a single-orbital system. In that case the third-order term of $\langle 2S^x_\sigma \rangle$ had positive sign and hence the metallic solution vanished continuously when the slopes of the two plotted functions coincided. In the case of a two-orbital system with finite J instead, due to the third-order term of $\langle 2S^x_\sigma \rangle$ having negative sign, the metallic (large h) solution is given by the fifth-order term and a more complicated picture emerges. At $U < U_{c1}$ there is one metallic solution, at $U_{c1} < U < U_{c2}$ once the slope of $\langle 2S^x_\sigma \rangle$ becomes smaller than the one of $\frac{h}{2\epsilon_0}$, a second metallic solution appears. At U_{c2} the two metallic solutions coalesce and at $U > U_{c2}$ only the insulating one remains. The sign of the third-order term in the perturbative

[8]We have calculated $\langle 2S^x_\sigma \rangle_{pert}$ up to third order in h and in Fig.5.17 we add by hand a fifth order term with the expected sign, in order to visualize more clearly the first-order transition.

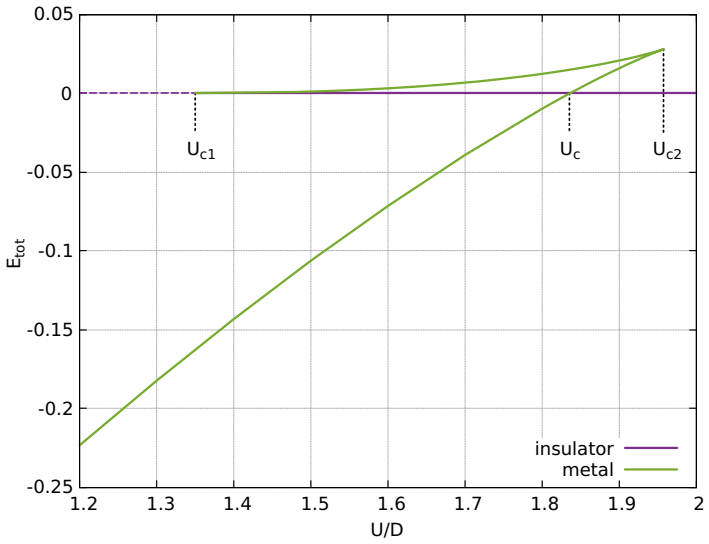

FIGURE 5.16: Total energy as a function of U for a two-orbital system at half-filling. In the range $U_{c1} < U < U_{c2}$ two metallic solutions and one insulating coexist. The first-order transition takes place at the U_c where E_{metal} and $E_{insulator}$ cross[7].

development of $\langle 2S^x_\sigma \rangle$ in h, is then of key importance since it determines the order of the transition. Its physical meaning will be clarified in the analysis of the Landau free energy of section 5.6.

In order to capture the negative slope of Z as a function of U appearing in Fig.5.15, the third order term in perturbation is necessary. Using the expression 2.44 we get the formula (in Appendix C.1.2 all the steps of this process are detailed):

$$Z_m = \frac{(U+J)^2(U-J)3J}{256\epsilon_0^3(8U^2+7J^2-9UJ)}(U_c-U). \tag{5.8}$$

This analytical formula reproduces at small Z the behavior of the quasiparticle weight as a function of interaction at half-filling in the unstable branch (where Z decreases for decreasing U), as depicted in Fig.5.15. In the rest of this chapter we identify the cause behind this behavior and discuss the role of Hund's coupling. The derivative of the above expression at U_{c1} reads:

$$\left.\frac{\partial Z}{\partial U}\right|_{U_{c1}} \simeq \frac{3.555(1-j^2)j}{7j^2-9j+8}. \tag{5.9}$$

In this part we approach the previous model with the addition of the spin-flip and

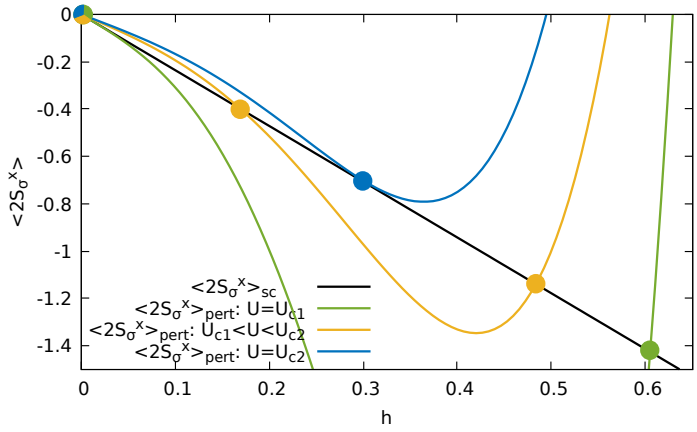

FIGURE 5.17: Graphical solution of the self-consistency equation $\langle 2S^x_\sigma \rangle = \frac{h}{2\epsilon_0}$. The left term is developed up to third order and the right term $\langle 2S^x_\sigma \rangle_{sc} = \frac{h}{2\epsilon_0}$ is linear. At $U < U_{c1}$ one metallic solution is found at large h. At $U_{c1} < U < U_{c2}$ two metallic solutions exist which merge at U_{c2}, above which only the insulating solution remains. For a better graphical illustration we have added by hand the fifth-order term in $\langle 2S^x_\sigma \rangle$[8].

pair-hopping terms in the Hamiltonian (see Appendix C.1.3 for an extensive derivation). This Kanamori form of the Hubbard model in the atomic limit is:

$$\begin{aligned} H_{at} =& U \sum_m S^z_{m\uparrow} S^z_{m\downarrow} + (U-2J) \sum_{m \neq m'} S^z_{m\uparrow} S^z_{m'\downarrow} + (U-3J) \sum_{m<m',\sigma} S^z_{m\sigma} S^z_{m'\sigma} \\ & - J \sum_m \left(S^+_{m\uparrow} S^-_{m\downarrow} S^+_{\bar{m}\downarrow} S^-_{\bar{m}\uparrow} + S^+_{m\uparrow} S^+_{m\downarrow} S^-_{\bar{m}\uparrow} S^-_{\bar{m}\downarrow} + h.c. \right), \end{aligned} \tag{5.10}$$

with the spectrum explicitly drawn in Fig.5.18. Repeating the steps followed in previous sections, we perform the perturbation theory calculations and get for the critical interaction of the Mott transition:

$$U_{c1} = -16\epsilon_0 - J. \tag{5.11}$$

Applying the theory up to third order we obtain the quasiparticle weight as a function of interaction strength, given by:

$$Z_m = \frac{(U+J)^2(U-J)J}{512\epsilon_0^3(U^2+8J^2-7UJ)}(U_c - U) \tag{5.12}$$

and its derivative at U_{c1}:

$$\frac{\partial Z}{\partial U} \simeq \frac{2.312(1-j^2)j}{8j^2-7j+1}. \tag{5.13}$$

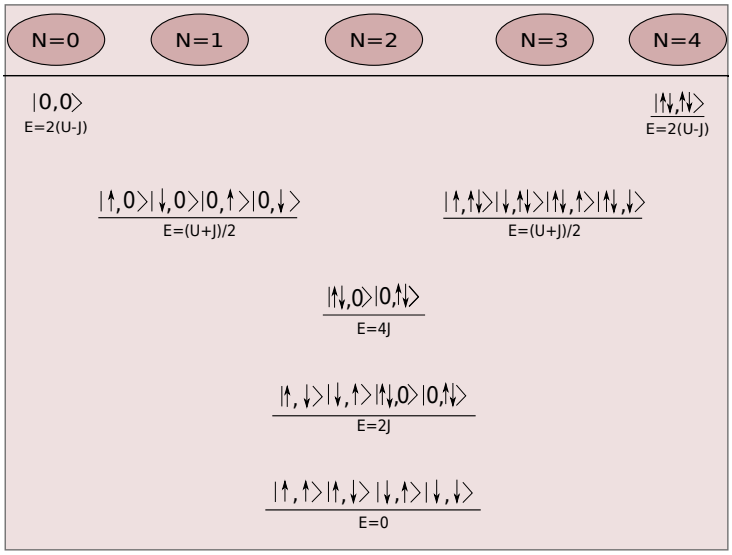

FIGURE 5.18: Atomic spectrum of a degenerate two-orbital Hubbard model with Kanamori interactions, at half-filling[6].

We showed that SSMF reproduces correctly the DMFT result discussed in the beginning of the chapter both for a single-orbital system and a multi-orbital one in absence of Hund's coupling ($J = 0$) exhibiting second-order Mott transitions at a critical interaction U_c. As known from previous studies [57] and already discussed above, in a system with $J \neq 0$ and density-density form of interactions the Mott transition is always discontinuous, with the first-order jump increasing for an increasing ratio $j = J/U$. In the case of a Kanamori Hamiltonian the transition is indeed first-order for small j, with the jump however growing with j until a value after which it starts diminishing with increasing j. The transition becomes then second-order for large values of the ratio, Fig.5.19.

This difference in behaviour can be extracted from our perturbation theory calculations. The results of the previous sections indicate that a first-order transition is linked to a positive slope in Z as a function of U for small Z (around U_{c1}). As it was showed earlier, in a system with zero Hund's coupling the slope of Z vs U is always negative, hence there is a second-order transition. In Eq.5.9 and Eq.5.13 of the derivatives of $Z(U)$ evaluated at U_{c1} for the two models, the denominators depend on the ratio $j = J/U$. For the density-density case the denominator is always positive and the numerator is also positive for all values of $j < 1$. Therefore, in the case of density-density interactions the overall sign of the slope is definite positive and the transition is always first-order as illustrated numerically in Fig.5.19.

The sign of the denominator in the Kanamori case, is positive for $j < 0.1798$ and negative for $j > 0.1798$. The numerator is always positive as in the case of density-density. Thus, the overall sign is opposite in the two regions leading in the final result of a positive slope for $j < 0.1798$ (first-order transition) and a negative one for

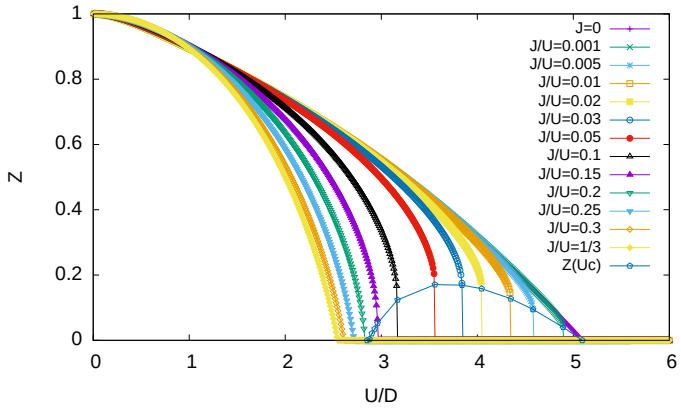

(A)

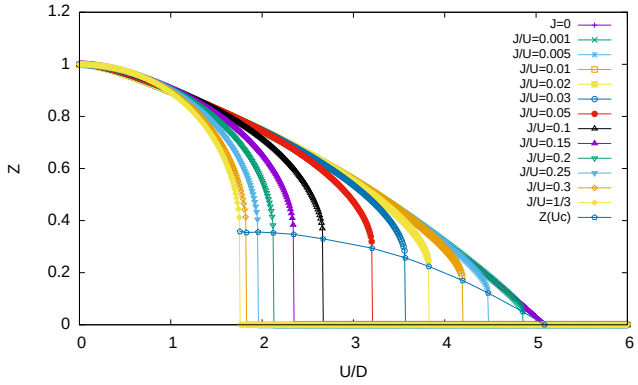

(B)

FIGURE 5.19: Quasiparticle weight as a function of interaction strength for different values of $j = J/U$ for a two-orbital system at half-filling with **(A)** Kanamori form of the interactions and **(B)** density-density one [57].

$j > 0.1798$ (second-order transition). These numbers reproduce the numerical results giving first and second-order transitions for different values of $j = J/U$, as shown in Fig.5.19.

5.6 Origin of the first-order phase transition in the context of Landau theory

In the framework of SSMF, the quasiparticle weight Z is proportional to the square of the total on-site magnetization of the auxiliary quantum spins $\sqrt{Z} = 2\langle S^x_{m\sigma}\rangle = m_x/M$. In the notation of this section the slave spin single-site effective Hamiltonian is written as $\hat{H}_S = h^{sc}\sum_{m\sigma} S^x_{m\sigma} + \hat{H}_{int}[S^z]$, with $h^{sc} = 8\epsilon_0\langle S^x_{m\sigma}\rangle$ the self-consistent Weiss field[9] embodying the effect of hopping through the bare fermionic kinetic energy $\epsilon_0 =$

[9] In this section we change notation with respect to the rest of the manuscript and use $h^{sc} = 2h$, in order to be consistent with a publication related to this work, which is in preparation.

$\int_{-\infty}^{\mu} d\epsilon D(\epsilon)\epsilon < 0$ and $\hat{H}_{int}[S^z]$ is given in Eq.5.6. In this spirit, the Mott transition corresponds to a ferromagnetic-to-paramagnetic transition of the slave spin system, with $\sqrt{Z} \propto m_x$ playing the role of the order parameter.

According to the Landau theory of phase transitions [187], the competing solutions can be analyzed by coupling to the system a *fictitious external magnetic field* conjugated to m_x, adding to the Hamiltonian the term $\hat{H}_{ext} = h_{ext} \sum_{m\sigma} S^x_{m\sigma}$. The corresponding Gibbs free energy per site is:

$$\Gamma(m_x) = E(h_{ext}(m_x)) - h_{ext}(m_x)m_x, \tag{5.14}$$

with $E(h_{ext}) = \langle \hat{H}_S + \hat{H}_{ext} \rangle$ being the ground state energy in presence of the external driving magnetic field. Since the energy due to the external field is subtracted, Γ corresponds to the energy of the system alone, driven out of equilibrium as a function of the order parameter. Therefore, Γ acts as a Landau function [187] and the formula:

$$\frac{\partial \Gamma}{\partial m_x} = -h_{ext} \tag{5.15}$$

indicates that the extrema of $\Gamma(m_x)$ correspond to the equilibrium solutions in absence of the driving field.

Numerically, an external magnetic field h_{ext} is given as input to the SSMF code and we trace $\Gamma(m_x)$, plotted in Fig.5.20. Below $U_c \simeq 1.35$ the system has only one metallic solution. Increasing U a second solution appears (a second minimum in $\Gamma(m_x)$) at $m_x = 0$, an insulator. This is realized through the emergence of an unstable solution (a maximum in $\Gamma(m_x)$) in between the two stable ones. The first-order phase transition takes place when the energy of the insulating solution (at $m_x = 0$) becomes lower than that of the metallic one and is thus favored in the system. This is observed at $U \simeq 1.95$ in agreement with the self-consistent calculations of Z as a function of U, plotted in Fig.5.15. This analysis illustrating the coexistence of a stable metal, a stable insulator and an unstable metal is in complete analogy with the discussion made earlier in this chapter in the context of both DMFT and SSMF.

We can additionally get more physical insight through an analytical calculation of the Gibbs free energy in the context of SSMF perturbation theory. According to the Landau theory, the free energy of a given system undergoing a phase transition can be expressed as a polynomial expansion in powers of the relevant order parameter, enforcing that the expansion respects the system's symmetries [188]. In the cases where the energy does not depend on the direction of the order parameter the expansion includes only the even orders in the polynomial [189] $\Gamma(m_x) = \gamma_2 m_x^2 + \gamma_4 m_x^4 + O(m_x^6)$. A first-order transition is associated with a double minimum structure in $\Gamma(m_x)$ and this

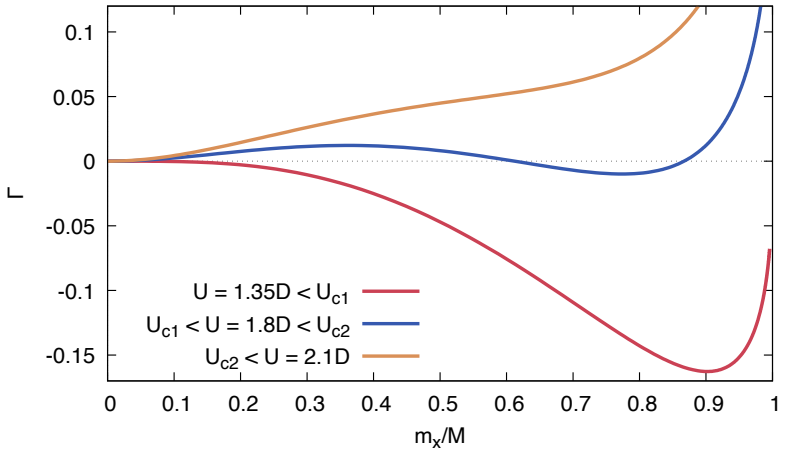

FIGURE 5.20: Landau free energy as a function of the order parameter $m_x/M = \sqrt{Z}$ for different values of interaction U. The minima correspond to stable solutions and for $U_{c1} < U < U_{c2}$ there are two competing solutions, a metallic (large Z) and an insulating one ($Z = 0$). In these calculations we have used the expression $\lambda_m^0 = \sqrt{Z_m}\frac{2n_{m\sigma}-1}{n_{m\sigma}(1-n_{m\sigma})}h_{m\sigma}$, discussed in section 2.2.4, in order to obtain quantitative accuracy.

implies a negative γ_4 when γ_2 changes its sign from negative to positive for a growing U and in fact when $U = U_{c1}$. Using the methodology followed throughout this chapter (and in more detail in Appendix C) we can evaluate the ground state energy of the single-site slave-spin Hamiltonian H_S in the total field $\tilde{h} = h_{ext} + h^{sc}$. The relevant perturbation formulas up to fourth order in the field are [68]:

$$
\begin{aligned}
E_\phi^{(1)} &= V_{\phi\phi}, \\
E_\phi^{(2)} &= \frac{|V_{\phi\kappa_2}|^2}{E_{\phi\kappa_2}}, \\
E_\phi^{(3)} &= \frac{V_{\phi\kappa_3}V_{\kappa_3\kappa_2}V_{\kappa_2\phi}}{E_{\phi\kappa_2}E_{\phi\kappa_3}} - V_{\phi\phi}\frac{|V_{\phi\kappa_3}|^2}{E_{\phi\kappa_3}^2}, \\
E_\phi^{(4)} &= \frac{V_{\phi\kappa_4}V_{\kappa_4\kappa_3}V_{\kappa_3\kappa_2}V_{\kappa_2\phi}}{E_{\phi\kappa_2}E_{\phi\kappa_3}E_{\phi\kappa_4}} - E_\phi^{(2)}\frac{|V_{\phi\kappa_4}|^2}{E_{\phi\kappa_4}^2} - 2V_{\phi\phi}\frac{V_{\phi\kappa_4}V_{\kappa_4\kappa_3}V_{\kappa_3\phi}}{E_{\phi\kappa_3}^2E_{\phi\kappa_4}} + V_{\phi\phi}^2\frac{|V_{\phi\kappa_4}|^2}{E_{\phi\kappa_4}^3},
\end{aligned}
\tag{5.16}
$$

where we remind that $V_{\mu\kappa} = \langle\mu^0|V|\kappa^0\rangle$, $V = \sum_{m\sigma} 2S_{m\sigma}^x$, $E_{\mu\kappa} = E_\mu^0 - E_\kappa^0$ and we sum over all states $|\kappa_l\rangle$ excluding the ground state manifold. As mentioned in chapter 2, $V_{\phi\phi} = 0$ in our case because the basis states are eigenstates of $S_{m\sigma}^z$. Only neighbouring sectors are connected through V, so the terms including $V_{\phi\kappa_3}V_{\kappa_3\kappa_2}V_{\kappa_2\phi}$ vanish as well.

The remaining terms are:

$$E_{\phi}^{(2)} = \frac{|V_{\phi\kappa_2}|^2}{E_{\phi\kappa_2}},$$
$$E_{\phi}^{(4)} = \frac{V_{\phi\kappa_4}V_{\kappa_4\kappa_3}V_{\kappa_3\kappa_2}V_{\kappa_2\phi}}{E_{\phi\kappa_2}E_{\phi\kappa_3}E_{\phi\kappa_4}} - E_{\phi}^{(2)}\frac{|V_{\phi\kappa_4}|^2}{E_{\phi\kappa_4}^2} \tag{5.17}$$

and hence $E(\tilde{h}) = e_2\tilde{h}^2 + e_4\tilde{h}^4 + O(\tilde{h^6})$. Performing all the summations we obtain:

$$E(\tilde{h}) = -\frac{2}{U(1+j)}\tilde{h}_{l,\sigma}^2 - \frac{2(7j^2-9j+8)}{U^3(1+j)^3(1-j)3j}\tilde{h}_{l,\sigma}^4. \tag{5.18}$$

Our goal is to determine $\Gamma(m_x)$ and in particular the sign of the γ_4 coefficient in its polynomial expansion. For both $\Gamma(m_x)$ and $E(\tilde{h})$ the following equations hold:

$$h_{ext} = -\frac{\partial\Gamma}{\partial m_x} = -2\gamma_2 m_x - 4\gamma_4 m_x^3 + O(m_x^5), \tag{5.19}$$

$$m_x = \frac{\partial E}{\partial\tilde{h}} = 2e_2\tilde{h} + 4e_4\tilde{h}^3 + O(\tilde{h}^6). \tag{5.20}$$

We invert the last one[10] and obtain $\tilde{h} = (2e_2)^{-1}m_x - 4e_4(2e_2)^{-4}m_x^3$ which since $\tilde{h} = h_{ext} + h^{sc}$ gives:

$$h_{ext} = \left(\frac{1}{2e_2} - \frac{4\epsilon_0}{M}\right)m_x - \frac{4e_4}{(2e_2)^4}m_x^3. \tag{5.21}$$

The comparison of Eq.5.19 and Eq.5.21 indicates that the sign of γ_4, the fourth order coefficient in $\Gamma(m_x)$, is the same as that of the parameter e_4 in $E(\tilde{h})$, which as shown in Eq.5.18 reads:

$$e_4 = -\frac{2(7j^2-9j+8)}{U^3(1+j)^3(1-j)3j}. \tag{5.22}$$

This parameter is indeed negative for all $j < 1$, since the numerator is always positive. It is interesting to notice that we here confirm what was already suggested in Fig.5.17; the negative sign of the third-order term in $\langle 2S_\sigma^x\rangle$ in Eq.5.20 allows for the coexistence of two metallic and one insulating solutions at $U_{c1} < U < U_{c2}$, leading to a first-order Mott transition.

We can indeed evaluate explicitly $\Gamma(m_x)$. Eq.5.21 using Eq.5.18 becomes:

$$h_{ext} = \left(-\frac{U(1+j)}{4} - 2\epsilon_0\right)m_x + \frac{U(1+j)(7j^2-9j+8)}{32(1-j)3j}m_x^3 \tag{5.23}$$

[10] If $y \simeq a_1x + a_3x^3$ then $x \simeq b_1y + b_3y^3$ with $b_1 = (a_1)^{-1}$ and $b_3 = -\frac{a_3}{a_1^4}$.

and from Eq.5.19 the coefficients of the Gibbs free energy can be extracted, so that $\Gamma(m_x)$ takes the form:

$$\Gamma(m_x) = \left(\frac{U(1+j)}{8} + \epsilon_0\right) m_x^2 - \frac{U(1+j)(7j^2-9j+8)}{128(1-j)3j} m_x^4. \tag{5.24}$$

Indeed, the second-order coefficient is negative below $U_c = -8\epsilon_0 - J$ and positive above and the fourth order one is always negative. For $U < U_c$, with both coefficients of m^2 and m^4 being negative, the function has negative curvature as shown in Fig.5.20. For $U > U_c$, though, with the coefficient of m^2 being positive while the one of m^4 is negative, the necessary condition for a first-order phase transition is fulfilled. In order to calculate analytically the precise value of m_x and Γ at the minimum corresponding to the metallic solution and thus the value of U at which the transition takes place, we would have to calculate higher orders in $\Gamma(m_x)$ and study the competition between the coexisting solutions.

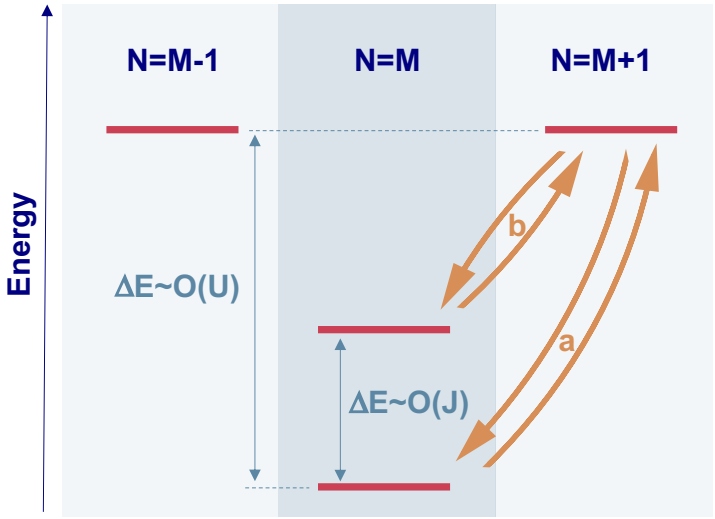

FIGURE 5.21: Schematic plot of generic spectrum, showing the processes involved in the ground state energy corrections in perturbation theory; the "connected" ones following a-b-b-a and the "disconnected" ones being a double product of the a-a path.

We can attribute a physical significance to the sign of e_4 (and thus to the analysis of Fig.5.17) by considering the fourth order formula in Eq.5.17 of the ground state energy. The hopping processes between neighboring sectors, always starting from the ground state and ending back on it, are either *connected* of the form $\frac{V_{nk_4}V_{k_4k_3}V_{k_3k_2}V_{k_2n}}{E_{nk_2}E_{nk_3}E_{nk_4}}$ or *disconnected* of the form $-\frac{|V_{nk_2}|^2}{E_{nk_2}}\frac{|V_{nk_4}|^2}{E_{nk_4}^2}$. The first ones always lower the energy and carry a negative sign and the second ones a positive (since $E_{nk} < 0$). In Fig.5.21 a scheme

of the spectrum is sketched and the connected processes follow the arrows a-b-b-a, while the disconnected ones perform twice the a-a path. As schematically drawn in Fig.5.21 and shown in Appendix C, the first excited states of the $N = M$ central sector are at distance J (in the density-density case) from the ground state, while those of the $N = M \pm 1$ sectors are at distance $(U + J)/2 > J$. Therefore, the connected processes dominate for small enough J and they control the overall negative sign of the fourth order term in energy. Comparing the spectra in Fig.5.14 and 5.18, one notices that in the case of Kanamori interactions the lower-lying excited states of the $N = M$ sector are at distance $2J$ from the ground state, twice as large as the density-density case. For that reason, as discussed in the previous section and shown in Fig.5.19, in a system with Kanamori interactions above a value of $j = J/U$ the disconnected processes dominate and the transition becomes second order again.

Thus we conclude that *the lifting of the ground state degeneracy induced by a finite Hund's coupling* (thus breaking of the $SU(2M)$ symmetry of the Hamiltonian) and the emergence of excited states in the central sector in addition to the ones of other sectors changes drastically the available hopping channels and qualitatively changes the nature of the Mott transition in the system. The competition between hopping involving excited states of the half-filled sector or the doped sectors finally *defines wether the system will undergo a first-order or a second-order transition*. This analysis confirms with solid arguments the empirical rule proposed in [155], stating that "the transition tends to be first-order if the lowest-lying excitations are in the same charge sector as the atomic ground state".

We can extend this analysis in the context of Landau theory into the finite doping plane. In Fig.5.22 the Gibbs free energy is shown as a function of m_x for different values of interaction and at different chemical potentials. Depending on the value of U and μ there can be up to two minima in the energy profile, a metallic and an insulating solution connected through a maximum (corresponding to an unstable metal). This picture is in analogy with the description made earlier in this chapter when discussing the μ vs n behavior both in SSMF - as shown graphically in Fig.5.9b - and in DMFT (where instead there are three metallic solutions coexisting).

5.7 Summary and perspectives

In this chapter we have connected the existence of the charge instability zone systematically found at the frontier of the Hund metals with the first-order nature of the Mott transition at half-filling.

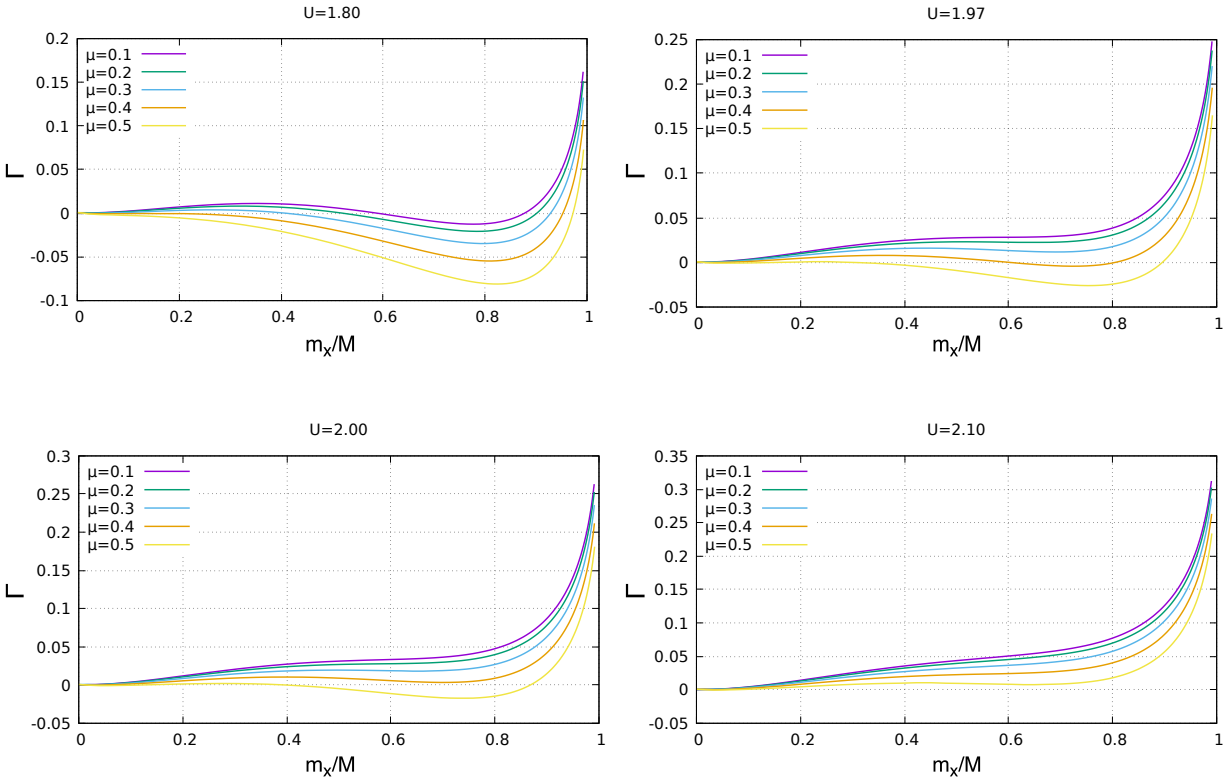

FIGURE 5.22: Landau analysis at finite doping: free energy as a function of order parameter for different values of U and different chemical potentials.

Using NRG as a DMFT impurity solver we could confirm the existence of this finite-doping instability at $T = 0$. With the combined use of ED in DMFT and SSMF we could then continuously connect the compressibility divergence to the coexistence of solutions at half-filling, which due to the first-order nature of the Mott transition extends to finite doping. The ensuing spinodal lines terminate in a QCP at finite doping, which is then a consequence of the first-order Mott transition.

We have moreover analyzed the nature of the transition by building a Landau theory using the magnetization of the auxiliary slave-spins (proportional to the square of the quasiparticle weight) as an order parameter for the Mott transition.

Finally we have backtracked the first-order nature of the Mott transition to the fact that the atomic ground state multiplet is split by a small energy scale, in our case Hund's coupling J. This motivates the negative sign of the quartic coefficient of the expansion of the Landau free energy and in general the non-monotonic energy landscape causing the reported complex interplay of phase transitions.

Among the perspectives supported by this work there is a natural parallel with the

cuprates. Indeed charge instabilities like phase separation and charge-density waves are known to happen there, in proximity of the Mott insulating phase, with the related fluctuations extending in a large part of the phase diagram (see [190] for a recent review), and have been singled out early on as possible factors favoring the high-Tc superconductivity [191, 192].

Several theoretical studies on the single-band bi-dimensional Hubbard model - considered widely as embodying the essential traits of cuprate physics -, treated in a way to include non-local correlations have indeed highlighted a tendency of this model towards phase separation (see [193] respectively for a recent review)[11].

More recently Sordi et al., using cluster dynamical mean-field theory (CDMFT) have shown an enhancement of the compressibility at finite temperature in this model, culminating with an instability zone at low temperature (see Fig.5.23 from [197] and [198]) which marks the entrance into the pseudogap phase [199, 200]. This finite-doping instability causes a first-order transition between two metals across a frontier which can be traced back to the Mott transition at half-filling, in close analogy with the physics presented in this chapter for the Hund metals. It can be speculated, - although this was not yet explicitly shown yet, in the best of the author's knowledge - that this zone ends in a quantum critical point at a critical value of the interaction strength, as it happens for the multi-orbital models we presented.

An exciting perspective is thus a possible common scenario for the physics of cuprates and iron-based superconductors, as already speculated in [2] and [201]. This is an open and fascinating perspective for future work.

[11] This natural tendency is signaled by charge instabilities being triggered in this model quite easily by other extrinsic mechanisms like phonons [194, 195] or competition between antiferromagnetism and superconductivity [196].

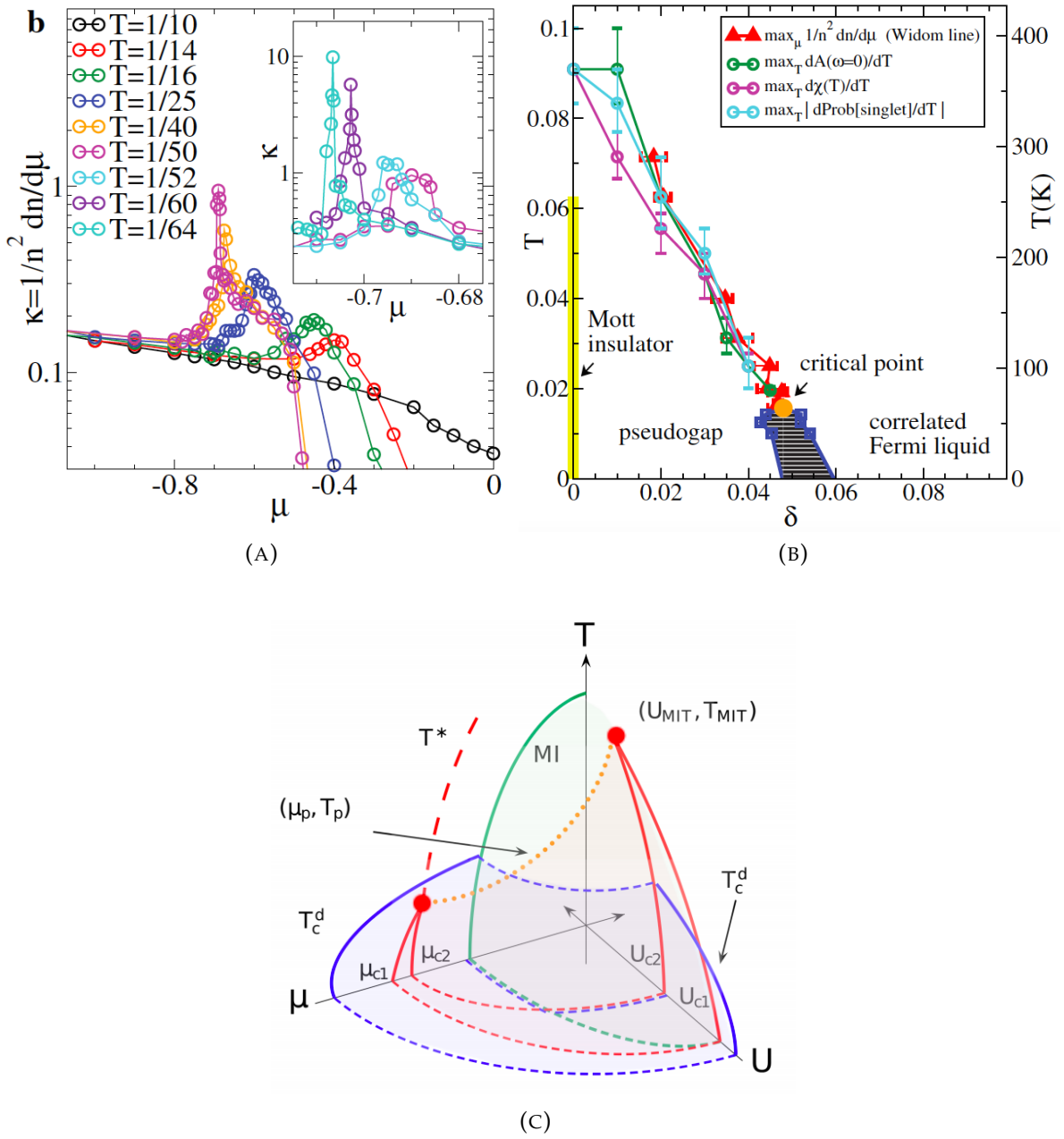

FIGURE 5.23: **(A)** Compressibility as a function of chemical potential for different values of temperature in a single-band Hubbard model, calculated with CDMFT, from [198]. **(B)** Phase diagram of the same model on the plane of temperature vs doping. An instability region (extrapolated down to $T = 0$) marks a transition between two different metals (a Fermi liquid at high doping and a pseudogap phase at low doping), from [198]. **(C)** Temperature - interaction strength - chemical potential phase diagram showing the connection between this transition and the Mott transition at half-filling, from [197].

Chapter 6

Transport calculations using Exact Diagonalization in DMFT

In this chapter we present a *method for performing transport calculations using Exact Diagonalization (ED) as the DMFT impurity solver*. We report a very good agreement with NRG results of resistivity on a single-orbital Hubbard model calculated in [7] (Fig.6.8). We explore the region of validity of the low-temperature expansion of the resistivity and suggest a qualitative signal of the system crossing the *Mott-Ioffe-Regel limit*. We apply the method on a two-orbital Hubbard model and observe the expected drop of the Fermi liquid energy scale due to Hund's coupling, by reporting a quick departure of the resistivity from the Fermi liquid behavior compared to the single-band case. We further perform *transport calculations on the early transition metal oxides* $SrVO_3$ and $SrCrO_3$ and we show that their resistivities largely differ between them, as expected from experimental measurements. This last section is part of our on-going work and the preliminary results we provide will be the subject of a forthcoming article:

Transport calculations with Exact Diagonalization as the impurity solver for DMFT
M. Chatzieleftheriou et al., in preparation

6.1 Introduction

The basics of electronic transport in metals are usually modelled in the framework of the *Drude model* [8]. The electrical resistivity is given by:

$$\rho(T) = \frac{m}{ne^2}\left(\frac{1}{\tau}\right), \tag{6.1}$$

where n is the electron density, e its charge and m the mass, while $1/\tau$ is the scattering rate of the conduction electrons, determining the temperature dependence of the resistivity. Its calculation depends on the particular system at hand. For the correlated

systems of interest to this work the dominant scattering processes are those between electrons (*electron-electron scattering*) and $1/\tau$ is derived by Fermi's golden rule [202] giving:

$$\frac{1}{\tau} \propto (\epsilon - \epsilon_F)^2 + \pi T^2. \tag{6.2}$$

The T^2 dependence of the resistivity is a characteristic property of Fermi liquids and this behavior is observed in the low temperature range. Experiments on different correlated compounds show distinct trends of resistivity depending on temperature and electron filling. The theoretical calculation of transport properties in systems exhibiting strong correlations has been a long-standing challenge within the scientific community.

The DC resistivity is given by the inverse of the $\omega \to 0$ limit of the optical conductivity. The latter is the linear response function connecting the electric field to the induced current through:

$$J_\alpha(\omega) = \sum_\beta \sigma_{\alpha\beta}(\omega) E_\beta(\omega). \tag{6.3}$$

Neglecting vertex corrections, the conductivity parallel to the applied field takes the form:

$$\sigma_{\alpha\alpha} = e^2 \int_{-\infty}^{\infty} d\omega \Big(-\frac{\partial f}{\partial \omega} \Big) \Phi(\omega), \tag{6.4}$$

where $f(\omega)$ is the Fermi function and:

$$\Phi(\omega) = \frac{2\pi\hbar}{V} \sum_{\mathbf{k}} tr\big[v_\alpha(\mathbf{k}) \rho(\mathbf{k},\omega) v_\alpha(\mathbf{k}) \rho(\mathbf{k},\omega) \big] \tag{6.5}$$

is the *transport distribution function*. The prefactor 2 corresponds to the spin degeneracy, V is the total volume of the crystal with periodic boundary conditions, $\rho(\mathbf{k},\omega) = \frac{1}{2i\pi}[G^\dagger(\mathbf{k},\omega) - G(\mathbf{k},\omega)]$ is the spectral function matrix and $v_\alpha(\mathbf{k})$ is that of the electron velocity, which we express in the Peierls approximation as [203]:

$$v_\alpha(\mathbf{k}) = \frac{1}{\hbar} \frac{\partial H(\mathbf{k})}{\partial k_\alpha}, \tag{6.6}$$

where $H(\mathbf{k})$ is the Fourier transform of the tight-binding Hamiltonian matrix in the basis of localized orbitals[1]. In the low temperature regime - where Fermi liquid theory rigorously applies - the conductivity reduces to (a full derivation of the low-T formulas

[1] Actually, in the Peierls approximation, Eq.6.6 there is an additional term $-\frac{i\Delta_R H(\mathbf{k})}{\hbar}$. Δ_R is the matrix of distances between the centres of the localized basis functions within the same unit cell. Hence, this term is nonzero only when more than one atomic site per unit cell is considered [204], which is not our case.

is found in Appendix E):

$$\sigma_{\alpha\alpha} = E_0 e^2 \Phi(\tilde{\mu}), \tag{6.7}$$

where $E_0 \simeq 0.822467$ and the low-T limit of the transport distribution function is:

$$\Phi(\epsilon) = \frac{\hbar}{V\gamma(T)} \sum_{\mathbf{k},n} \delta(\epsilon - \epsilon_{n\mathbf{k}}) \sum_{n'} v_\alpha^{nn'}(\mathbf{k}) v_\alpha^{n'n}(\mathbf{k}). \tag{6.8}$$

In the above n, n' are band indices, $\tilde{\mu} = \mu - Re\Sigma(0)$ is the effective chemical potential and $\gamma = 1/\tau = -Im\Sigma(0)$ is the scattering rate. We express the scattering rate in this form - in contrast to the one introduced in chapter 1 where the inverse lifetime was multiplied by Z - as it is customarily done in transport calculations. In parts of this chapter we will work on the infinite coordination Bethe lattice and in that case the transport function is expressed in terms of the semi-circular density of states in the sum-rule preserving expression [205]:

$$\Phi(\epsilon) = \sum_n \frac{2\hbar}{3\pi D^2 \gamma(T)} \left(D^2 - \epsilon_n^2\right)^{3/2}. \tag{6.9}$$

Methods such as the slave particles mean-fields do not offer direct access to the imaginary part of the system's self-energy, necessary in transport calculations. DMFT on the other hand gives directly the self-energy on the real or the imaginary axis, depending on the impurity solver. In this second case analytical continuation is needed to get $\Sigma(\omega)$ and then $\rho(\mathbf{k}, \omega)$. However, with each solver different limitations emerge.

When one is interested in a system's low frequency regime, Numerical Renormalization Group (NRG) is the most accurate method to be implemented. The advantage of this method lies exactly on its ability to approach with increasingly improved precision an increasingly small energy range, thus being able to describe very well the real axis spectral function at low frequency.

6.2 Resistivity in a single-orbital Hubbard model: NRG vs ED as the DMFT impurity solver

The NRG technique has been naturally exploited in calculating transport properties and for example in [7] the temperature dependence of the resistivity for a single-band strongly correlated system was evaluated. The letter's authors studied theoretically a well-known experimentally observed transport phenomenon in strongly correlated

systems. At high enough T the resistivity is found to acquire very large values, exceeding the *Mott-Ioffe-Regel (MIR) limit*[2], thus signalling the emergence of bad metallic behavior and the breakdown of the quasiparticle picture [206]. An interesting fact is that the two energy scales defined by the end of Fermi liquid behavior (at low-T) and the entrance into the bad metallic zone (at high-T) do not coincide. There is a large intermediate regime where clearly defined quasiparticles still exist but they are not following the $\rho_{FL} \propto T^2$ behaviour.

The authors demonstrated the passage from a Fermi liquid with $\rho_{FL} \propto T^2$ at small T into a region of *resilient quasiparticles (RQP)* at intermediate T which disappear at high T, when the system crosses the MIR limit and enters a bad metallic zone, Fig.6.1. In particular, they worked with a single-orbital system on the Bethe lattice. They used a slightly different notation for the resistivity $\sigma = \frac{2\pi e^2}{\hbar} \int d\epsilon (-\frac{\partial f(\omega)}{\partial \omega}) \Phi(\epsilon) \rho^2(\omega)$, where the spectral function and the constant coefficients are not included in the definition of the transport function, which has the form $\Phi(\epsilon) = \Phi(0)[1 - (\epsilon/D)^2]^{3/2}$, with $\Phi(0) = 2D/3\pi$. In this context the MIR limit is defined through [7]:

$$\frac{1}{\rho_{MIR}} = \frac{e^2 \Phi(0)}{\hbar D} \simeq \frac{1}{4.71}, \tag{6.10}$$

with the half-bandwidth being $D = 1$. In [7] the resistivity is expressed in units of ρ_{MIR}.

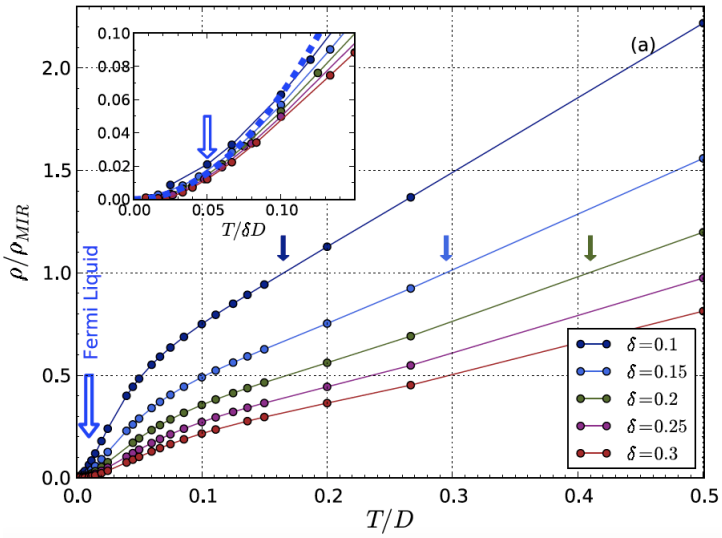

FIGURE 6.1: Resistivity as a function of temperature using NRG for three values of doping at $U = 4$. Three zones are observed: a Fermi liquid region at $T < T_{FL}$, a regime of resilient quasiparticles at $T_{FL} < T < T_{MIR}$ and a zone of bad metallicity at $T > T_{MIR}$ [7].

[2]The MIR limit is crossed when the mean-free path l becomes equal to the lattice spacing.

In the plot of the resistivity as a function temperature of Fig.6.1 there are three distinct zones, as introduced earlier. At $T < T_{FL}$ (T_{FL} designated by the large empty arrow) the curve follows a T^2 behavior, for $T_{FL} < T < T_{MIR}$ (T_{MIR} for each doping corresponding to the smaller full arrows) a linear behaviour in T with negative intercept evolves through a "kink" into a linear curve with positive intercept, crossing T_{MIR}. The authors of [7] demonstrate the existence of resilient quasiparticles in the intermediate region, exhibiting clear peaks close to the Fermi level in the spectral function, which gradually disappear as T is increased, Fig.6.2.

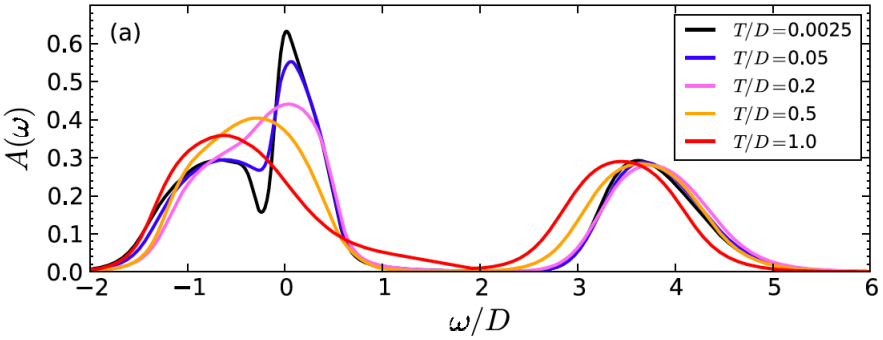

FIGURE 6.2: Local spectral function at different values of temperature T for $\delta = 0.2$. At $T < 0.5$ there is a clear peak due to quasiparticles which disappears for a larger T, adapted from [7].

A disadvantage of the very precise NRG is that it becomes significantly heavy when the number of orbitals is increased. Therefore, the existence of a computationally lighter method able to exhibit similar precision in the resistivity calculations is essential. Another broadly used impurity solver Quantum Monte-Carlo (QMC) treats multi-orbital systems exactly at finite temperatures but it evaluates the Green's function and self-energy on the imaginary axis. In order to calculate the real axis quantities one must perform the analytic continuation and different methods have been developed for this purpose, among which the Padé method [207, 208] and the MaxEnt [209, 210]. Also, arbitrarily low temperatures are not accessible with this method. In our DMFT study we use Exact Diagonalization (ED) as the impurity solver, which yields the retarded Green's function through its Lehmann representation. This can be evaluated close to the real axis directly, by introducing a small broadening parameter $i\delta_{0^+}$ added to the frequency. Likewise the bare Green's function of the impurity, which on the Matsubara axis is given by Eq.2.61, on the real axis is:

$$\mathcal{G}_0^{-1}(\omega) = \omega + i\delta_{0^+} + \mu - \epsilon_0 - \Delta(\omega). \tag{6.11}$$

From these functions, the real axis self-energy is calculated through the Dyson equation. The discretized character of the bath in the context of ED - discussed in chapter 2

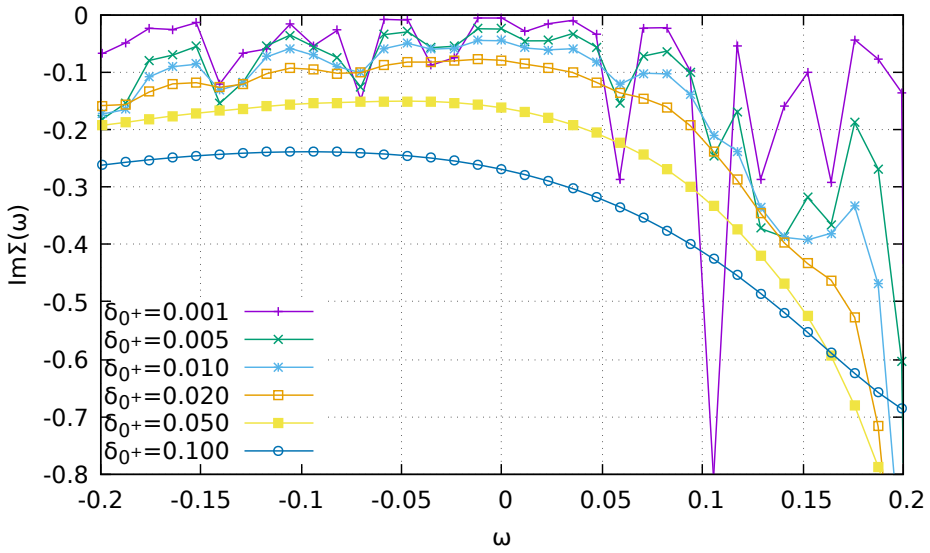

FIGURE 6.3: Imaginary part of the self-energy on the real axis of a single-band model with $U = 4$, $n_{tot} = 1.20$ and $\beta = 100$, calculated using full ED with Ns=6 for different values of the broadening parameter δ_{0^+}.

-, however, gives rise to very spiky functions on the real axis. For an increasing value of δ_{0^+} the curves become smoother, but the distance from the real axis is also larger and the results lose their accuracy.

In the calculations of this chapter with NRG we have used a modified version of the NRG Ljubljana code [86] and in those with ED we have performed full diagonalization using $N_s = 6$ sites (except from the last section of the chapter, where the technical parameters will be specified).

In Fig.6.3 the imaginary part of the self-energy on the real axis evaluated for an increasing value of δ_{0^+} is shown for a single-band system at temperature $\beta = 100$, with parameters $U = 4$ and $n_{tot} = 1.20$ expressed in units of $D = 1$. The very spiky curves at small δ_{0^+} turn into smooth ones at larger δ_{0^+}. However, an increasing δ_{0^+} overall shifts the function to high values (in absolute), smearing the features and leading to unphysical results. These issues render the calculation of transport properties from the real axis functions evaluated directly for $\delta_{0^+} \to 0$ within ED practically impossible.

One can calculate, though, the resistivity directly from the Matsubara axis using the formula [4, 211]:

$$\sigma(i\omega_m) = \frac{1}{i\omega_m \beta} \sum_{\nu_n} \int_{-\infty}^{\infty} d\epsilon \, \Phi(\epsilon) \big(G(\epsilon, i\nu_n) G(\epsilon, i\nu_n + i\omega_m) - G(\epsilon, i\nu_n)^2 \big). \tag{6.12}$$

This formula can only be evaluated on the grid of bosonic Matsubara frequencies $\omega_m = 2\pi m/\beta$ but not directly for $m = 0$. So the result at $\omega_m = 0$ has to be extrapolated from

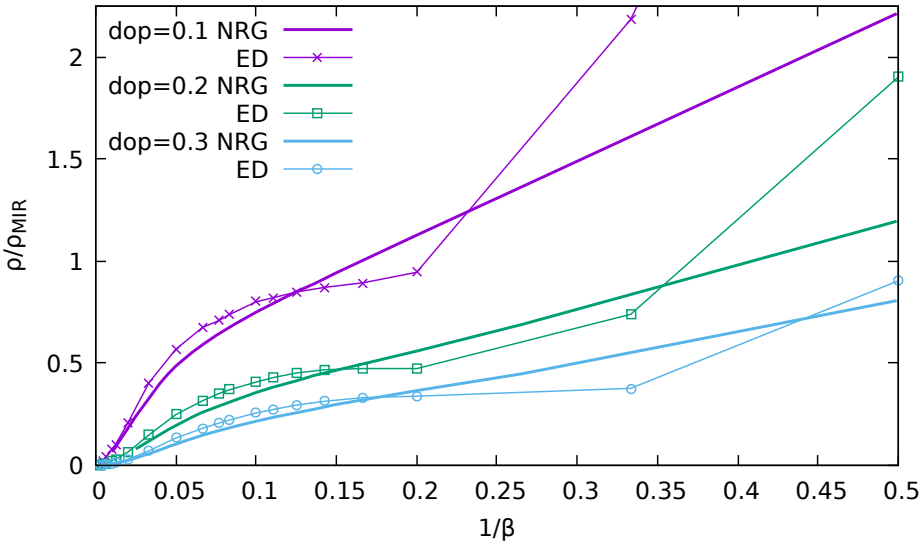

FIGURE 6.4: Resistivity as a function of temperature using NRG and ED for three values of doping ($U = 4$, $\rho_{MIR} = 4.71$). The ED resistivity is calculated from the Matsubara axis using Eq.6.12 and performing an extrapolation to $\omega_n = 0$. The agreement between the two methods is bad away from the very small-T region.

a rather coarse set of points at $m > 0$ and its accuracy worsens quickly with increasing spacing due to temperature. In Fig.6.4 results for three different values of doping are shown and a rather bad agreement with the NRG data is reported. The two methods coincide only at very low temperatures in the Fermi liquid regime, but ED does not reproduce the intermediate and high-T behaviors.

6.3 New method for transport calculations using ED in DMFT

In this section we present a recently developed method for *calculating the resistivity directly from the real axis functions using ED* and we report a drastic improvement of the results. There are two steps involved in the method and they are discussed below.

6.3.1 Disconnect the imaginary axis grid from the system's temperature

DMFT is a two-step procedure where local correlation functions of a lattice problem are calculated by an impurity solver with a given bath $\{V_l, \epsilon_l\}$. The bath in turn is determined by a self-consistency condition involving the Green's function. In practice this self-consistency condition in a numerical code is enforced on a finite set of points. In

ED the common practice is to use the fermionic Matsubara frequencies [79]. For an increasing temperature, however, the Matsubara frequencies $\omega_{Mats} = (2n+1)\pi/\beta$ are at increasing distance between them and the first one for $n = 0$ moves further away from the real axis, hence the resolution of the low frequency features deteriorates. $G(i\omega_n)$ is connected to the retarded Green's function $G^R(\omega)$ through analytic continuation (by performing $i\omega \to \omega + i\delta_{0^+}$). In practice ED gives the common Lehmann representation of these two functions that can be evaluated at all points of the imaginary half-plane [14]. Thus, two distinct scales β and β_{grid} can be introduced, with the first one corresponding to the real temperature of the system and the second one simply defining the imaginary frequency grid. The two parameters have to be equal only for the evaluation of Matsubara sums[3]. It is, after all, common practice in $T = 0$ calculations within ED as the DMFT impurity solver to use an arbitrary β_{grid} for the opposite reason of the Matsubara frequencies accumulating.

In Fig.6.5 we compare the imaginary part of the self-energy calculated with NRG and with ED using $\beta_{grid} = \beta$, $\beta_{grid} = 10\beta$ (where this is *not* a post-process technique and the DFMT scheme is converged separately for each β_{grid}) and $\beta_{grid} = 10\beta$ in one shot (where DMFT is converged for $\beta_{grid} = \beta$ and subsequently the self-energy is evaluated on a more dense grid defined by $\beta_{grid} = 10\beta$, through the Lehmann representation). We show results of $Im\Sigma$ for $U = 3.2$ and two values of doping $\delta = 0.01$ and $\delta = 0.30$ at $\beta = 10$ in the upper panels and at $\beta = 100$ in the lower panels.

For the larger temperature $\beta = 10$ and the larger doping $\delta = 0.30$ (upper right panel) the agreement between NRG and all the three versions of DMFT is good. For the smaller doping $\delta = 0.01$ (upper left panel), however, for ED with $\beta_{grid} = \beta$, in the low energy regime the Matsubara frequencies are at distances larger than those required to resolve the low frequency behavior. The curve of $\beta_{grid} = 10\beta$ though exhibits a very good agreement with the one of NRG, while the one shot calculation using $\beta_{grid} = 10\beta$ appears to have a very small intercept at $\omega_{Mats} = 0$. For $\beta = 100$ (lower panels) a similar behavior is found. For $\delta = 0.30$ (bottom right panel) all three DMFT versions agree well with NRG. For the small doping $\delta = 0.01$ (bottom left panel), the $\beta_{grid} = \beta$ data do not reproduce the NRG ones, since a low frequency minimum in $Im\Sigma$ emerges at a scale smaller than the one accessible. The result for $\beta_{grid} = 10\beta$, albeit being slightly far from the NRG line, captures qualitatively the behaviour of the system at small ω_n, which is of larger importance. As for $\beta = 10$, the one shot calculation with $\beta_{grid} = 10\beta$ extrapolates to a very small value, far from the one of NRG.

[3] We should remind that, as discussed in the previous section, in the calculation of the resistivity from the imaginary axis Eq.6.12 the use of $\beta_{grid} = \beta$ is required.

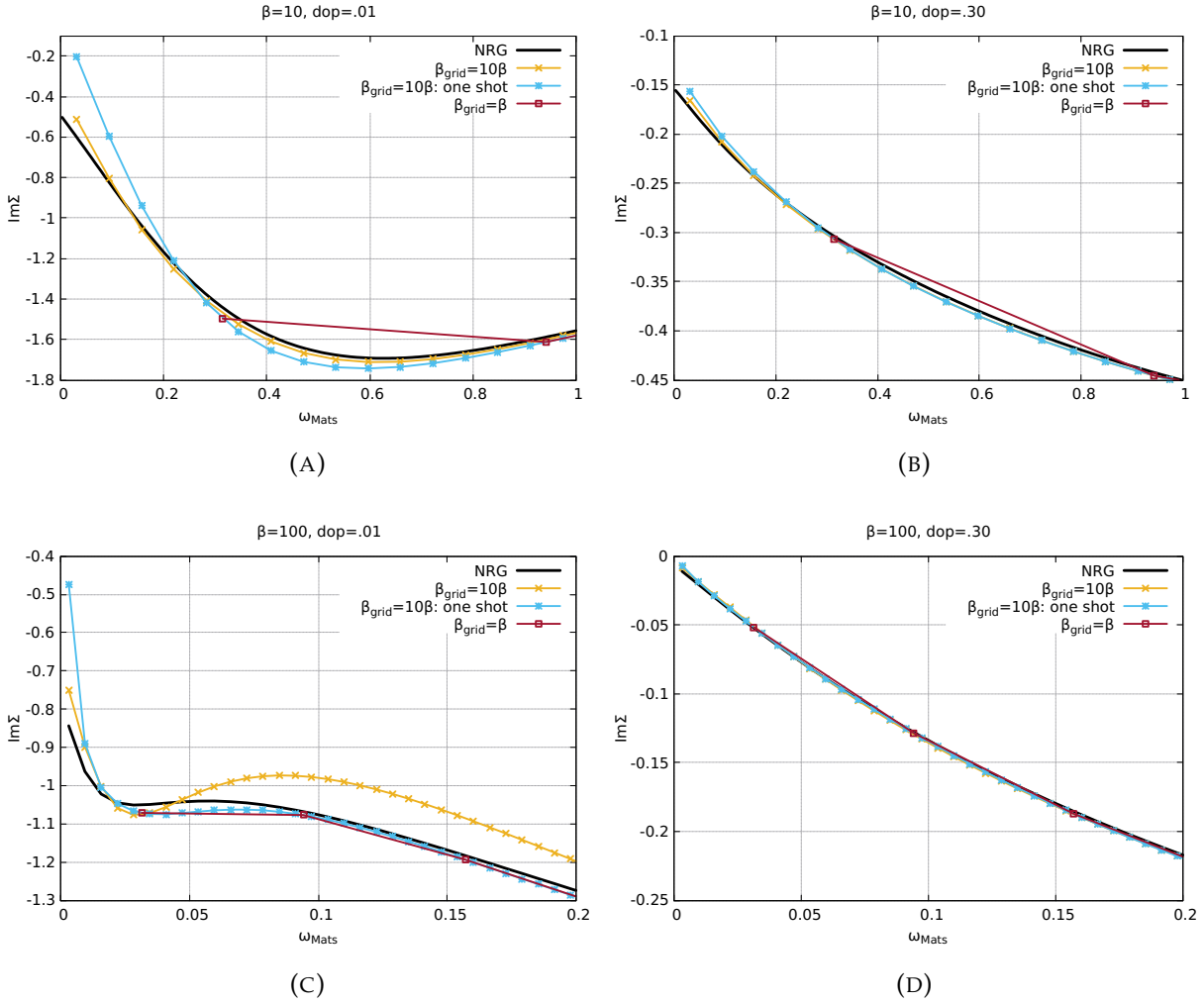

FIGURE 6.5: Imaginary part of the self-energy for $U = 3.2$ and two dopings ($\delta = 0.01$ in the left panels and $\delta = 0.30$ in the right panels) and two temperatures ($\beta = 10$ in the upper panels and $\beta = 100$ in the lower panels) using NRG (the technical parameters for NRG are specified in chapter 5, here however $\Lambda = 2.0$ is used) and ED, the latter in three different versions: $\beta_{grid} = \beta$, $\beta_{grid} = 10\beta$ and $\beta_{grid} = 10\beta$ in a one shot calculation from data converged with $\beta_{grid} = \beta$. At small doping for both temperatures the $\beta_{grid} = \beta$ results fail to reproduce the low-frequency features captured by NRG. The one shot calculations with $\beta_{grid} = 10\beta$ also extrapolate to wrong values, while the $\beta_{grid} = 10\beta$ (converged) curves show a much better agreement with NRG ones.

From the above study we can conclude that *using a β_{grid} larger than β* and applying the self-consistency on frequencies of that grid, allows for a better description of the important low frequency features in the dynamical quantities, especially at small doping. As already discussed, though, this modification cannot be used in the calculation of the resistivity from the Matsubara axis Eq.6.12.

ED as the DMFT impurity solver describes the properties of a system in the thermodynamic limit with a discretized Anderson impurity model. Thus even after optimizing the self-consistency grid a lower frequency unit remains, below which discretization effects appear. Hence quantities depending on the low energy physics have to be extrapolated.

6.3.2 Calculate the resistivity on the real axis for different broadening δ_{0^+} and extrapolate

We introduce a $\beta_{grid} \neq \beta$ following the analysis of the previous section and we can use either a fixed value or one depending on the real temperature. We calculate the real axis self-energy as a function of the broadening parameter δ_{0^+} introduced above and evaluate the resistivity for each $\Sigma[\delta_{0^+}]$. In Fig.6.6 we plot ρ calculated on the real axis from Eq.6.4 using $\beta_{grid} = 10\beta$, extrapolating ρ vs δ_{0^+} to $\delta_{0^+} = 0$. A polynomial fit of seventh order is performed for the extrapolation. The agreement with the NRG data is remarkable for all dopings, even though for the smallest one $\delta = 0.10$ at large temperature there is a departure of the ED results from the NRG ones. Overall, the results are significantly improved compared to the calculations of resistivity from the imaginary axis, presented in Fig.6.4. One can also extrapolate the self-energy on the real axis instead and calculate the resistivity from the extrapolated function. In Appendix F.1 we discuss results using this method. Moreover, in Appendix F.2 we present results of resistivity obtained using a fixed $\beta_{grid} = 100$ and show that the agreement with NRG is comparable to the one of Fig.6.6 for $\beta_{grid} = 10\beta$.

In Fig.6.7 a combined plot illustrating the steps of the method is showed (for the case of $U = 4$, $\delta = 0.20$, $\beta = 50$ and $\beta_{grid} = 10\beta$). (A) DMFT using the ED impurity solver is converged for a given choice of $\beta_{grid} \neq \beta$. (B) The self-energy is calculated on the real axis for different values of the broadening parameter δ_{0^+}. (C) The resistivity is calculated from Eq.6.4 as a function of δ_{0^+} and the region of extrapolation is determined. (D) ρ vs δ_{0^+} is fitted through a polynomial function of chosen order and $\rho(0)$ is evaluated.

6.3.3 Technical parameters of the method

It is natural for the reader to wonder how reliable the method is and wether its performance is subject to fine tuning. We would like to address this ambiguity and discuss all the parameters involved in the procedure, in order to establish the robustness of the

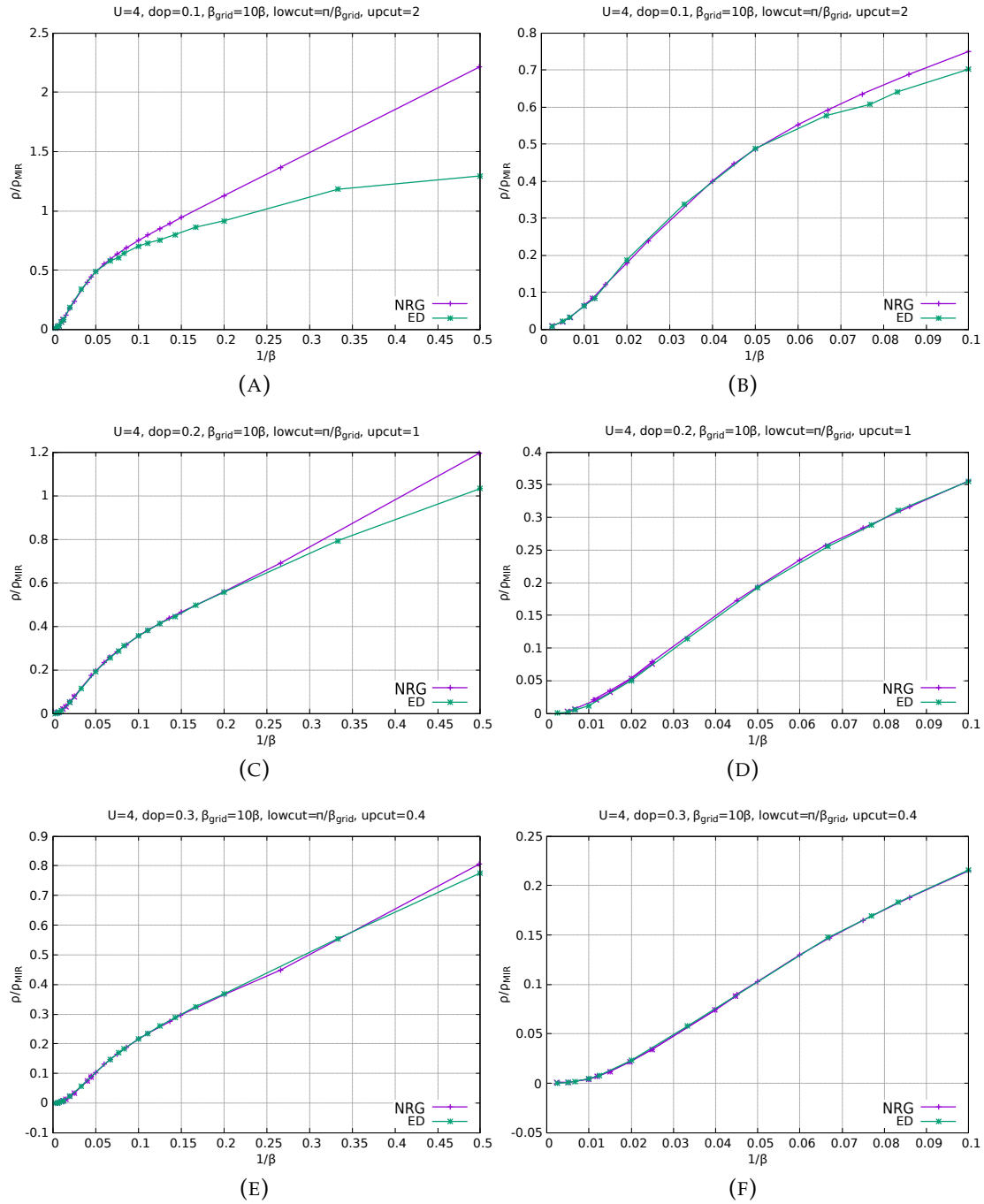

FIGURE 6.6: Resistivity as a function of temperature using NRG and ED for three values of doping. The resistivity is calculated from the real axis at different values of δ_{0^+} and the final result is an extrapolation of ρ vs δ_{0^+} to $\delta_{0^+} = 0$. In the right panels we show for each doping the two curves at the region of small temperatures, which is of more interest to us. The NRG and ED data exhibit very good agreement for all dopings.

method. In the titles of the plots in Fig.6.6 we state two variables, the *lowcut* and the *upcut*. These are the limits of the data used in the extrapolation ($lowcut \leq \delta_{0^+} \leq upcut$). In all cases plotted in Fig.6.6 the lowest value kept is π/β_{grid} (we naturally chose the

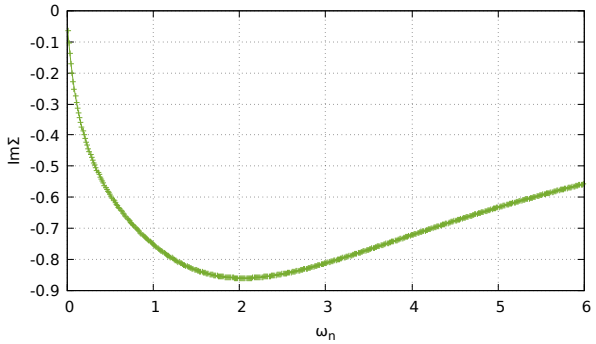

(A) Converge DMFT for β_{grid} of choice.

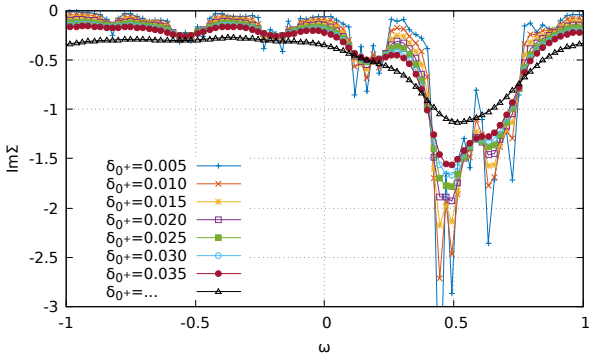

(B) One shot calculation to evaluate the real axis self-energy for different values of δ_{0^+}.

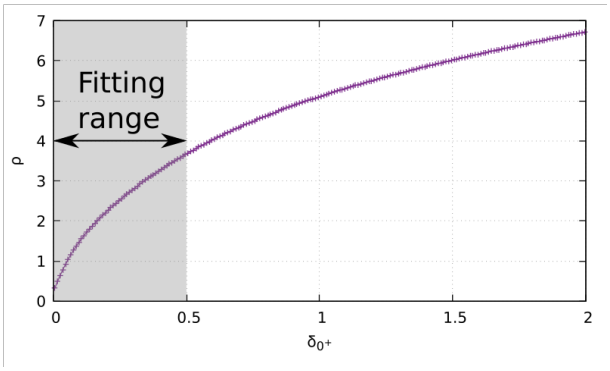

(C) Calculate the resistivity for each δ_{0^+} and define the $\rho(\delta_{0^+})$.

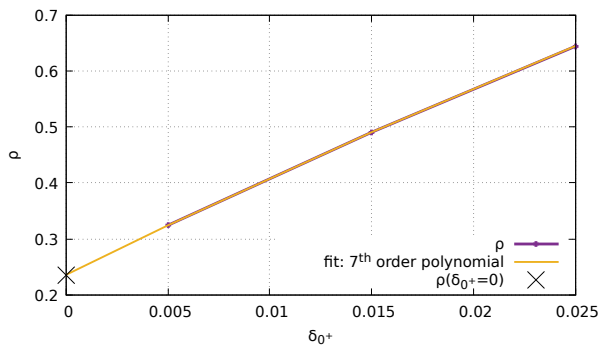

(D) Extrapolate $\rho(\delta_{0^+})$ to $\delta_{0^+} = 0$ with fitting scheme of choice.

FIGURE 6.7: A-B-C-D steps of new method for calculating the resistivity using ED as an impurity solver. The plots are done for $\delta = 0.20$, $\beta = 50$ and $\beta_{grid} = 10\beta$.

first Matsubara frequency) but the highest value differs. We show in Fig.6.6 the results which reported the best agreement with the NRG data in each case. However, a different choice of *upcut* (and also different degree of polynomial fit in the extrapolation) does not alter qualitatively the picture.

In order to visualize the effect of different extrapolation parameters, we plot in Fig.6.8 the NRG and ED data for $\delta = 0.20$ with error bars produced by investigating the various choices of polynomial order (> 4) and *upcut*. At low and intermediate temperatures the error bars are very small and the qualitative picture of a $\sim T^2$ behavior at small T and a linear one at larger T remains robust (see Appendix F.3 for more details).

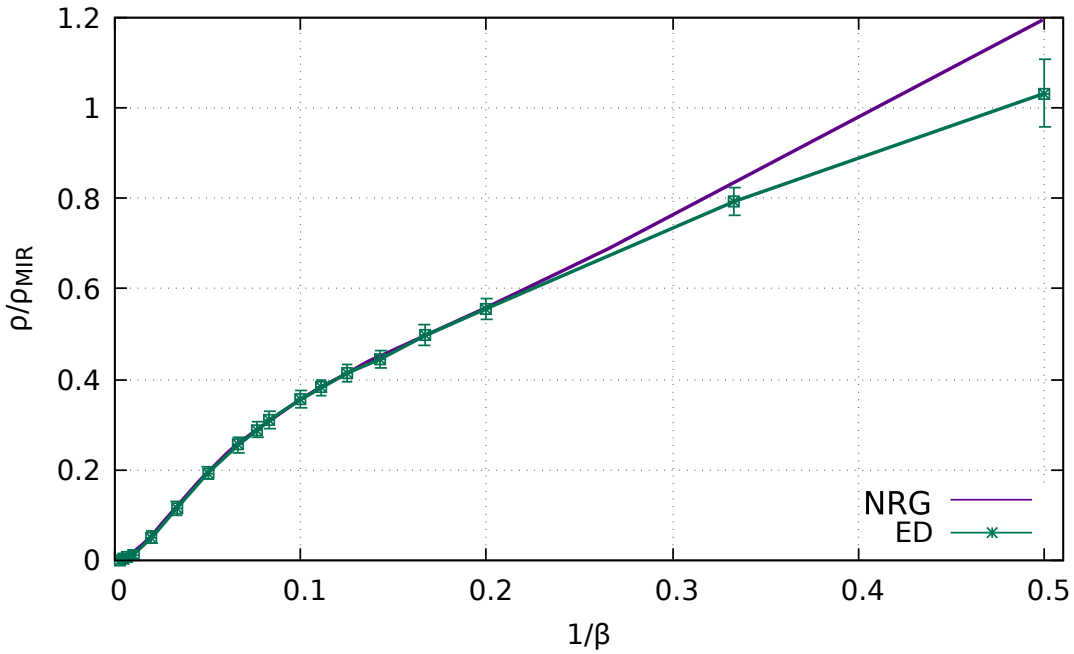

FIGURE 6.8: Resistivity in a single-band Hubbard model as a function of temperature using NRG and ED for $\delta = 0.20$ for $\beta_{grid} = 10\beta$ with error bars produced by investigating the effect of different polynomial fits and different value of *upcut* (larger value kept in the extrapolation). The error bars are very small away from the very large-T regime and the method's robustness is preserved. The low-T regime is shown (without the error bars) in Fig.6.6d and a very good agreement between ED and NRG is observed.

6.4 Extent of the Fermi liquid regime in temperature and doping in a single-orbital Hubbard model

In this section we use our new method to discuss the extent of the Fermi liquid regime both in temperature and in doping through resistivity calculations. It has been shown that in the vicinity to a Mott insulator the coherence temperature below which Fermi liquid behavior is observed is very small and vanishes upon reaching half-filling [212]. In order to study this effect we can compare two quantities: the resistivity (calculated with our newly developed method) and the low temperature Fermi liquid resistivity ρ_{FL}, proportional to the scattering rate as introduced in Eq.6.7. Results for two values of temperature ($\beta = 50$ and $\beta = 100$) at $U = 3.2$ - right above the U_c - are plotted in Fig.6.9. For a range of dopings and for both temperatures, ρ and ρ_{FL} match exactly. Then below a given doping, ρ and ρ_{FL} depart, with the resistivity diverging and the Fermi liquid one exhibiting a maximum and diminishing by approaching half-filling. This disagreement of ρ and ρ_{FL} emerges at larger dopings for the larger temperature, a result expected since the coherence temperature decreases as the doping is decreased.

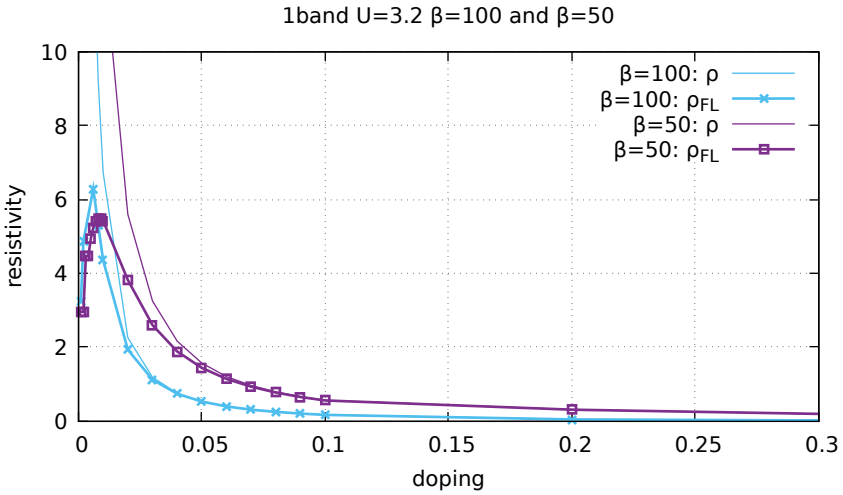

FIGURE 6.9: Resistivity and Fermi liquid resistivity (proportional to the scattering rate $-Im\Sigma(0)$) as a function of doping for two values of temperature $\beta = 100$ and $\beta = 50$. There is a perfect agreement between the two curves at large doping followed by a bifurcation point below which there is a maximum in ρ_{FL}, observed at small dopings. Both the bifurcation and the maximum are found at smaller dopings for the smaller temperature.

We interpret this behavior in the following way: in the region where ρ and ρ_{FL} exhibit perfect matching, the system is a Fermi liquid consisting of well defined quasiparticles. The zone where ρ and ρ_{FL} have detached but they are both growing for decreasing doping corresponds to a phase with resilient quasiparticles, having the properties introduced above. The maximum in ρ_{FL} can be viewed as a signal of crossing the MIR limit, beyond which there is complete loss of coherence in the system.

In Fig.6.10a we plot together ρ and ρ_{FL} as a function of temperature for different values of doping at $U = 4$, the value used in the earlier calculations performed following [7]. We report a bifurcation of the two curves signalling the onset into a region of departure from the Fermi liquid behavior, followed by a maximum in ρ_{FL}. In Fig.6.10b we extract the information of Fig.6.10a and plot the maximum of ρ_{FL} and thus of the scattering rate on the plane of doping and temperature together with the ρ_{MIR} from [7] and the "kink" changing the slope of ρ vs T in the RQP regime. We observe that the maximum of $\gamma = -Im\Sigma(0)$ is at slightly higher T compared to ρ_{MIR}, although following the exact same trend.

The $-Im\Sigma(0)_{max}$ can be thus used as a qualitative signal of the system crossing the MIR limit.

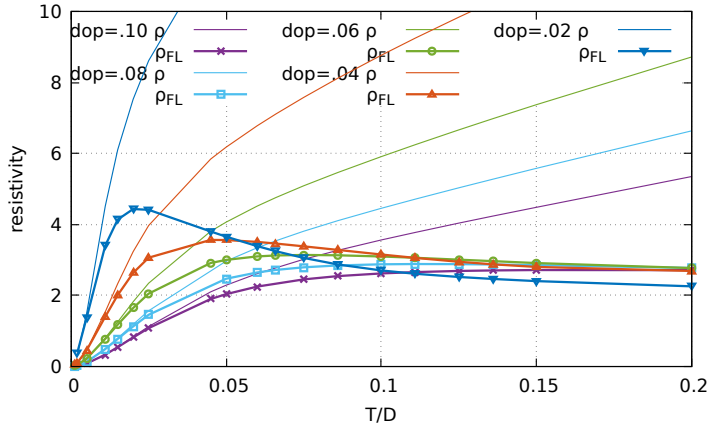

(A)

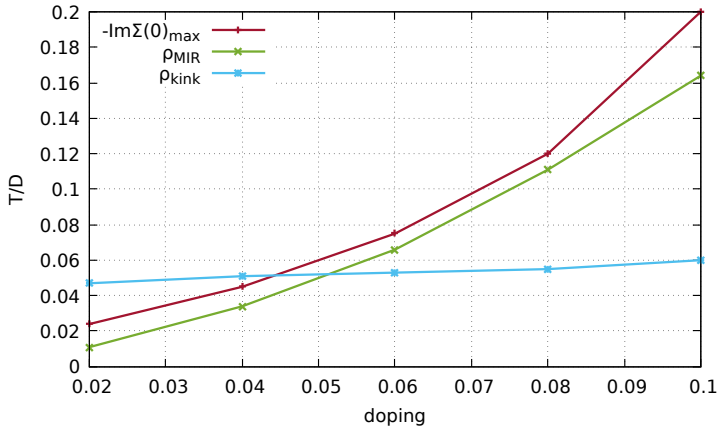

(B)

FIGURE 6.10: **(A)** ρ and ρ_{FL} as a function of temperature for different dopings at $U = 4$. We see both the departure of the two curves at small T and the following maximum in ρ_{FL} signalling the complete loss of coherence. **(B)** Combined plot of maximum in scattering rate, point at which $\rho = \rho_{MIR}$ according to the formalism of section 6.2 and position at which the slope of ρ vs T changes. The $-Im\Sigma(0)_{max}$ can be used as a signal of crossing the MIR limit.

6.5 Resistivity in a two-orbital Hund metal

In this section we apply the newly developed method for resistivity calculations on two-orbital systems with finite Hund's coupling. We have argued in previous chapters that the presence of J in a multi-orbital system enlarges the zone of influence of the half-filled Mott insulator. In the language of this chapter this corresponds to a loss of coherence observed at larger dopings compared to the single-band case.

We are restricted to a full diagonalization with $N_s = 6$ sites, due to the issues of the Lanczos algorithm in the study of Hund metals, discussed in section 2.3.3. We are able to capture certain transport properties of two-orbital Hund metal systems, however we will see in this section the effect of the imposed limitation emerging.

In Fig.6.11 results for ρ and ρ_{FL} as a function of doping are shown, performed on a two-band model with $U = 1.6 > U_c$ and $J/U = 0.25$ for $\beta = 100$ and $\beta = 50$ (using $\beta_{grid} = 5\beta$[4]). We compare the resistivity ρ to the Fermi liquid one ρ_{FL}, proportional to the scattering rate and observe that similarly to Fig.6.9 there is a critical doping for each temperature at which the two curves detach, followed by a second critical doping at which ρ_{FL} exhibits a maximum and below that coherence is totally lost. We must acknowledge the fact that in this case the agreement between the two quantities at large dopings is not as exact as for the single-band model, a result which is expected since we are reaching the limits of the impurity solver by performing a full diagonalization with $Ns = 6$ sites. The bifurcation of the two curves in Fig.6.11 is pushed to larger dopings compared to the single-band case, and the same holds for the $Im\Sigma_{max}(0)$. The region of decreased coherence overall extends to larger dopings.

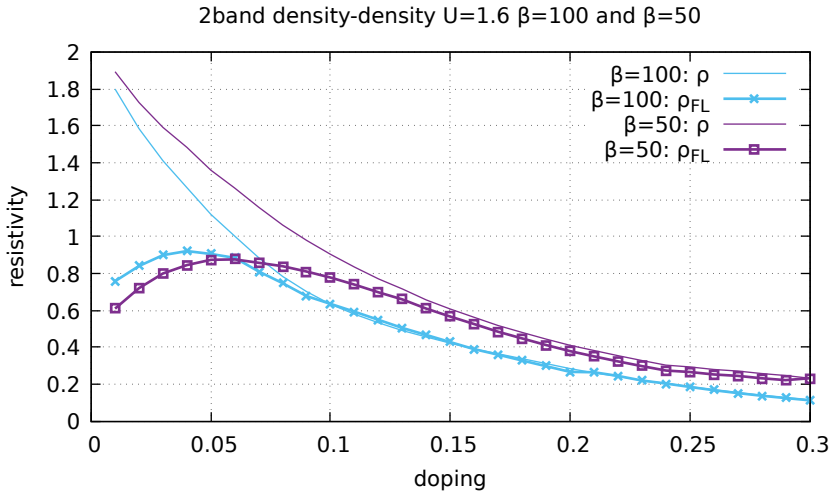

FIGURE 6.11: Resistivity and Fermi liquid resistivity (proportional to the scattering rate) as a function of doping at $U = 1.6$, $J/U = 0.25$, for temperatures of $\beta = 100$ and $\beta = 50$ ($\beta_{grid} = 5\beta$). Both the bifurcation of ρ and ρ_{FL} and the maximum in the latter are at larger dopings compared to the single-band case.

In order to illustrate more clearly the effect and connect it with the properties of Hund metals discussed in earlier chapters, we plot in Fig.6.12b ρ and ρ_{FL} for two values of doping as a function of temperature. In Fig.6.12a we draw a sketch of the bistability and charge instability zones introduced in chapters 4 and 5. We perform a scan in temperature for a doping in the weakly correlated metal region, to the right of the crossover line (red star) and for a doping well inside the Hund metal regime, to the left of the crossover line (blue star), shown in Fig.6.12b. We use $U/D = 1.6$, $\delta = 0.30$,

[4]Using a larger β_{grid} in a two-band model with $Ns = 6$ produces unphysical behaviors. We hence choose $\beta_{grid} = 5\beta$ and consistently ignore the first imaginary axis frequency in the scattering rate extrapolation to avoid any resolution issues at such small scales.

$\delta = 0.10$ and $\beta_{grid} = 5\beta$. The polynomial of seventh order fit is performed in both the real axis resistivity and the scattering rate.

At large doping the system is indeed a well defined Fermi liquid, with ρ and ρ_{FL} matching exactly for all the temperature range plotted. On the contrary, the small doping curves agree only at the smallest temperatures shown and they quickly depart by increasing T, signalling an earlier departure from the Fermi liquid behavior in the system. Hence, in an experimental setup where the resistivity and the scattering rate could be measured separately a disagreement would be found in the Hund metals zone, already at intermediate temperatures and larger dopings. For the single-band case the same effect is observed at quite higher temperatures and much closer to half-filling. For instance, we can compare the results of a single-orbital model with $U = 4$ and a two-orbital one with $U = 1.6$ (values at similar distance from the respective U_c). The bifurcation of ρ and ρ_{FL} for $\delta = 0.10$ in the single-band shown in Fig.6.10a takes place at $T/D \simeq 0.025$. For the same doping in the two-orbital Hund metal the bifurcation emerges at a way smaller $T/D \simeq 0.01$.

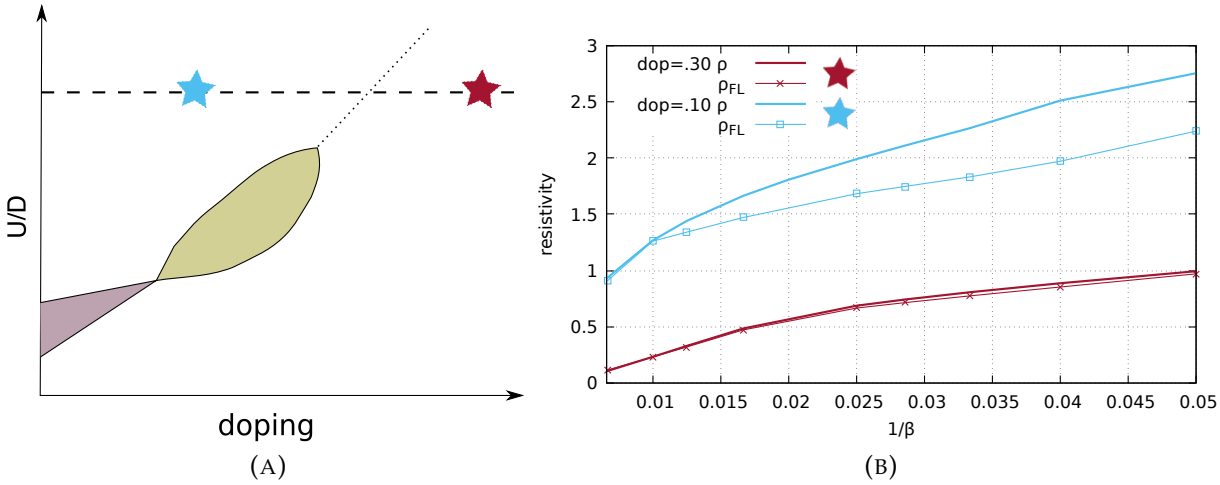

(A) (B)

FIGURE 6.12: (A) Sketch of phase diagram in Hund metals. The two stars correspond to the $U - doping$ choices at which a temperature scan is performed. (B) ρ and ρ_{FL} (corresponding to the scattering rate) as a function of temperature for $U = 1.6$ and $\delta = 0.30$, $\delta = 0.10$. For the large doping Fermi liquid behavior is preserved throughout the temperature range, with ρ and ρ_{FL} matching exactly, while for the small doping they part already around $1/\beta = 0.01$.

We deduce from these transport calculations that when the system crosses the Hund metal crossover line there is a fast drop of the temperature extent of the Fermi liquid behavior, a result expected from the scenario presented throughout this thesis. This result is moreover in line with the analysis made in previous studies, suggesting that in Hund metals at finite temperature a coherent Fermi liquid system is turned into an incoherent non-Fermi liquid one, by increasing J [156] or moving closer to half-filling

[127], as shown in Fig.6.13. And more in general this behavior is predicted by DMFT for a system with a sizeable Hund's coupling moving closer to half-filling, due to the effect of Hund's coupling of lowering the Kondo temperature of the associated impurity model [213, 214, 31, 215]

At large dopings the coherence will also eventually be lost at very high temperatures. The limitation imposed by the use of $Ns = 6$ restricts us from analyzing the high-T and low-doping regions. Introducing a $\beta_{grid} \neq \beta$ improves the low frequency description, however there is a balance between this improvement and a resolution inaccuracy when β_{grid} becomes too large (this additionally creates an issue at the very small temperatures). Therefore, we limited our study to intermediate temperatures which in this case were enough to describe the effect.

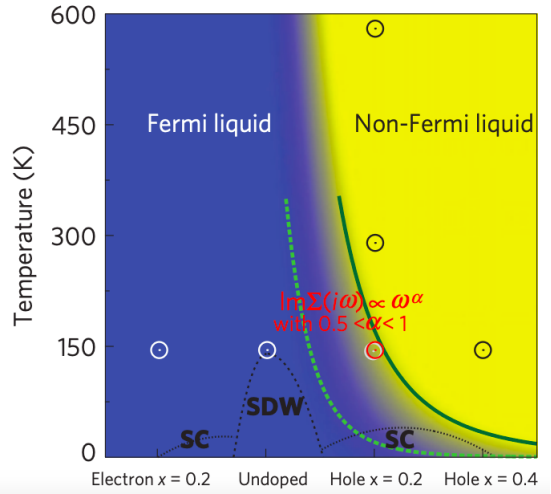

FIGURE 6.13: Sketch of the phase diagram of IBSC, showing a crossover between a coherent Fermi liquid (blue region) and an incoherent non-Fermi liquid (yellow region) closer to half-filling (which in this image would correspond to the position of a hole doping of $x = 1.0$) [127].

6.6 Resistivity of early transition metal oxides

In chapter 1 we introduced the early transition metal oxides and in particular the materials $SrVO_3$, $SrCrO_3$ and $SrMnO_3$. Despite their structural similarities they exhibit very different electronic properties which we attribute to Hund's physics. In particular, the half-filled ($n_{tot} = 3$) $SrMnO_3$ is experimentally found to be an antiferromagnetic Mott insulator, $SrCrO_3$ populated with one electron away from half-filling ($n_{tot} = 2$) exhibits

metallicity with large values of resistivity measured[5] and $SrVO_3$, two electrons away from half-filling ($n_{tot} = 1$), behaves as a good metal. This trend is in line with the theoretical analysis in the context of Hund metals followed throughout this manuscript and originally suggested for these compounds in [31]. Indeed, within this description $SrMnO_3$ is expected to be a half-filled Mott insulator, $SrCrO_3$ a Hund metal and $SrVO_3$ a well-behaved moderately correlated metal.

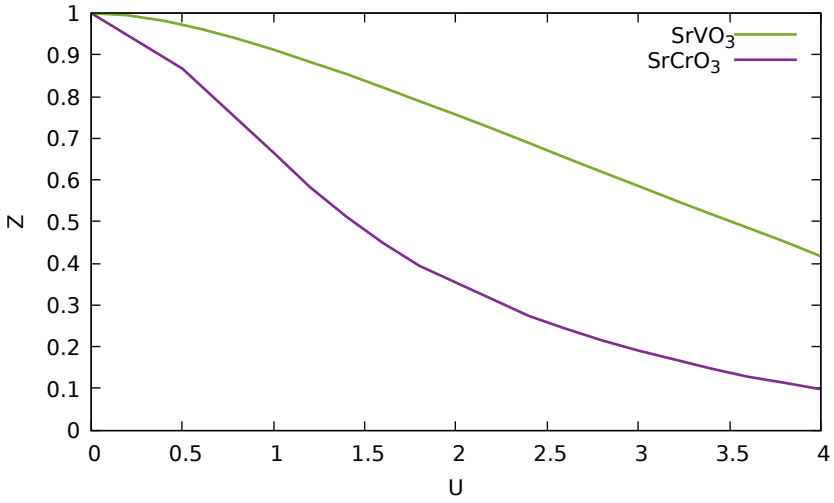

FIGURE 6.14: Quasiparticle weight as a function of interaction for $SrVO_3$ and $SrCrO_3$ at zero temperature for $J/U = 0.15$, calculated with ED as the DMFT impurity solver.

We study $SrVO_3$ and $SrCrO_3$ using the Lanczos/Arnoldi diagonalization algorithm in DMFT within the new parallel implementation EDIpack [166], with $N_s = 14$ bath sites using the Kanamori Hamiltonian. DFT calculations within the PBE approximation for exchange and correlation [216] were performed[6] using Quantum ESPRESSO, a planewave + pseudopotential suite of computer codes [217] and ultrasoft pseudopotentials from the PSlibrary [218]. A cutoff of 80 and 640 Ry was used for the wavefunctions and density, respectively. A 12x12x12 Gamma-centred Monkhorst-Pack grid with gaussian smearing with broadening of 0.01 Ry has been used to converge integrals over the Brillouin Zone. The obtained V (Cr,Mn) t_{2g} manifold was projected over a set of maximally-localized Wannier functions via wannier90 [56, 219], and velocities were computed with the resulting tight-binding Hamiltonian within the Peierls approximation. The experimental lattice parameters used are $a = 3.842500\mathring{A}$ for $SrVO_3$ [45] and $a = 3.819820\mathring{A}$ for $SrCrO_3$ [34].

[5]We remind the reader that - as described in chapter 1 - samples of $SrCrO_3$ are particularly hard to produce at high quality, hence the experiments have been often contradicting. However, the latest experimental measures on high quality thin films suggest that the compound exhibits metallic resistivity with large values.

[6]The DFT calculations are performed by Tommaso Gorni, in ESPCI Paris.

In Fig.6.14 we plot the quasiparticle weight as a function of interaction for the two compounds at zero temperature for $J/U = 0.15$. As expected, $SrVO_3$ exhibits moderate correlations, while $SrCrO_3$ is very strongly correlated at large values of U, relevant for the materials[7].

We perform a temperature scan for the two materials at the interaction $U = 4$. In chapter 1 experimental results of the temperature dependent resistivity for $SrVO_3$ and $SrCrO_3$ were reported and the second was found to be much larger than the first. In our theoretical analysis we treat the resistivity at the low-T Fermi liquid limit using Eq.6.7 and we plot in Fig.6.15 ρ vs T for the two compounds. Both of them exhibit metallic behavior and overall there is a large difference in their resistivities, in agreement with the experimentally found trend.

The preliminary results presented in this section are part of on-going work in progress. However, they clearly boost the description of the early transition metal oxides in terms of Hund's physics. A further investigation of the resistivity dependence on the choice of the U and J/U parameters is in order. A study where the calculation of the resistivity is performed from Eq.6.4 must be also conducted in order to explore the systems' behavior away from the Fermi liquid regime more accurately.

[7] As discussed in chapter 1 all three compounds are considered to have $U \simeq 3 - 4eV$.

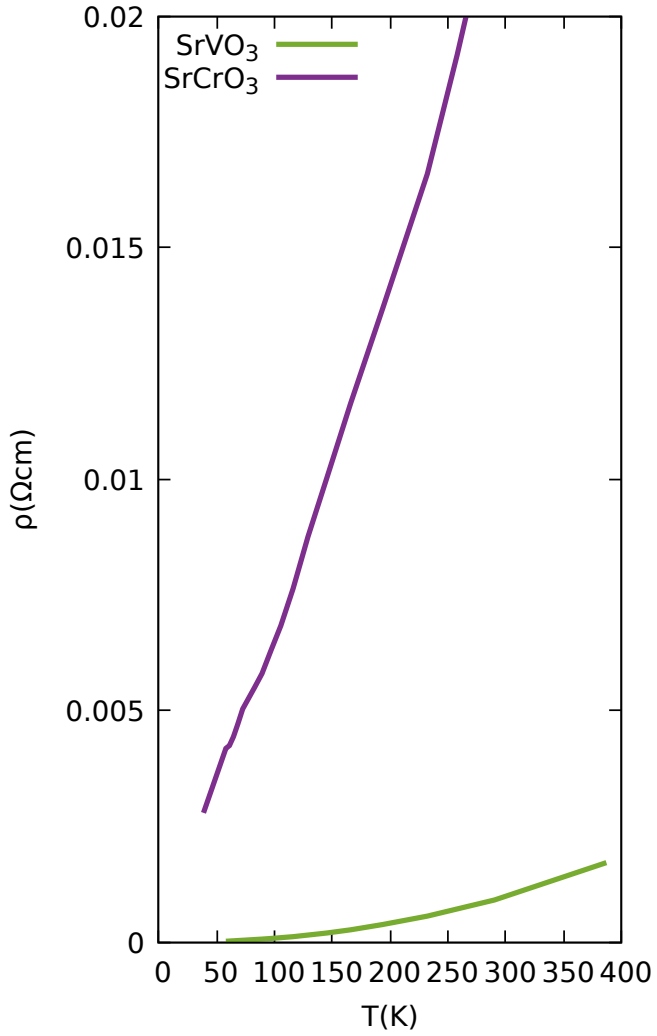

FIGURE 6.15: Fermi liquid resistivity as a function of temperature for $SrVO_3$ and $SrCrO_3$ at $U = 4$, $J/U = 0.15$ using ED as the DMFT impurity solver.

Appendix A

Particle-hole symmetry

A.1 Single-orbital Hubbard model

We want to apply the particle-hole transformation to $\hat{H} - \mu\hat{N}$, with $\hat{H}$ of the single-band Hubbard model given in Eq.2.5. In order to do so we use:

$$\begin{aligned} d^{\dagger}_{i\sigma} &\rightarrow d_{i\bar{\sigma}}, \\ d_{i\sigma} &\rightarrow d^{\dagger}_{i\bar{\sigma}} \end{aligned} \tag{A.1}$$

and obtain:

$$\hat{H} - \mu\hat{N} = -\sum_{ij\sigma} t_{ij} d^{\dagger}_{i\sigma} d_{j\sigma} + U \sum_{i} n_{i\uparrow} n_{i\downarrow} + (\mu - U) \sum_{i\sigma} n_{i\sigma} + U - 2\mu. \tag{A.2}$$

We further consider a bi-partite lattice: the original lattice can be viewed as composed of two sub-lattices A and B, with electrons hopping between them[1]. If we now restrict ourselves to one of the sub-lattices (say A) we can additionally apply a gauge transformation and write:

$$\begin{aligned} d^{\dagger}_{i\sigma} &\rightarrow -d^{\dagger}_{i\sigma}, \\ d_{i\sigma} &\rightarrow -d_{i\sigma}, \end{aligned} \tag{A.3}$$

with $i \in A$ to finally get the expression:

$$\hat{H} - \mu\hat{N} = \sum_{ij\sigma} t_{ij} d^{\dagger}_{i\sigma} d_{j\sigma} + U \sum_{i} n_{i\uparrow} n_{i\downarrow} + (\mu - U) \sum_{i\sigma} n_{i\sigma} + U - 2\mu. \tag{A.4}$$

This form of $\hat{H} - \mu\hat{N}$ is in fact completely identical to the initial Eq.2.5 adding the chemical potential term, if $\mu = U/2$, therefore this value enforces the particle-hole

[1] In the above we used the hermiticity of the Hamiltonian to write $t_{ij} = t_{ji}$.

symmetry in the system and we can thus rewrite the interaction as:

$$U\sum_i (n_{i\uparrow}-\frac{1}{2})(n_{i\downarrow}-\frac{1}{2}) = U\sum_i n_{i\uparrow}n_{i\downarrow} - \frac{U}{2}\sum_{i\sigma} n_{i\sigma} + \frac{U}{4}, \tag{A.5}$$

which is equal to $U\sum_i n_{i\uparrow}n_{i\downarrow} - \frac{U}{2}\sum_{i\sigma} n_{i\sigma}$ plus a constant shift. One might also notice that this is not the only way in which the interaction part can be written as particle-hole symmetric. We could also write it (up to a rescaling constant):

$$\begin{aligned}\sum_i \Big(\sum_\sigma (n_{i\sigma}-\frac{1}{2})\Big)^2 &= \frac{U}{2}\sum_i (n_{i\uparrow}+n_{i\downarrow}-1)^2 = \\ &= \frac{U}{2}\sum_i (n_{i\uparrow}+n_{i\downarrow})^2 - U\sum_i (n_{i\uparrow}+n_{i\downarrow}) + \frac{U}{2} = \\ &= \frac{U}{2}\sum_i (n_{i\uparrow}+n_{i\downarrow}+2n_{i\uparrow}n_{i\downarrow}) - U\sum_i (n_{i\uparrow}+n_{i\downarrow}) + \frac{U}{2} = \\ &= U\sum_i n_{i\uparrow}n_{i\downarrow} - \frac{U}{2}\sum_i (n_{i\uparrow}+n_{i\downarrow}) + \frac{U}{2}\end{aligned} \tag{A.6}$$

and this form turns out to be very convenient for our calculations.

A.2 Multi-orbital Hubbard model

Focusing on the density-density multi-orbital Hamiltonian of Eq.2.9 we have the interaction part together with the chemical potential term:

$$\hat{H} - \mu\hat{N} = U\sum_m n_{m\uparrow}n_{m\downarrow} + U^{'}\sum_{m\neq m'} n_{m\uparrow}n_{m'\downarrow} + (U^{'}-J)\sum_{m<m',\sigma} n_{m\sigma}n_{m'\sigma} - \mu\sum_{m\sigma} n_{m\sigma}. \tag{A.7}$$

We can now introduce the shifted operators $\tilde{n}_{m\sigma} = n_{m\sigma} - 1/2$ and rewrite the interaction as:

$$\hat{\tilde{H}} = U\sum_m \tilde{n}_{m\uparrow}\tilde{n}_{m\downarrow} + U^{'}\sum_{m\neq m'} \tilde{n}_{m\uparrow}\tilde{n}_{m'\downarrow} + (U^{'}-J)\sum_{m<m',\sigma} \tilde{n}_{m\sigma}\tilde{n}_{m'\sigma}, \tag{A.8}$$

so that if now we attempt -in a spirit similar to the one followed for the single-orbital model- to match the two above expressions, using $U^{'} = U - 2J$ we get:

$$\mu_{half-filling} = \frac{U(2M-1) - 5J(M-1)}{2} \tag{A.9}$$

as the condition for particle-hole symmetry, with M the number of orbitals.

Appendix B

SSMF gauge derivation

We calculate the gauge of the SSMF formalism imposing that the non-interacting limit $Z(U=0)=1$ is reproduced. The non-interacting single-site, single-orbital slave-spin Hamiltonian of Eq.2.23 is:

$$\hat{H}_s = hO^\dagger + h^*O + \lambda S^z, \tag{B.1}$$

where $O = S^- + cS^+$. We have dropped the spin index σ, since at the non-interacting limit up-spin and down-spin fermions are decoupled. We diagonalize the above Hamiltonian in the $S^z = \pm\frac{1}{2}$ basis and upon defining $\alpha = h + ch^*$ we get:

$$\begin{aligned} \epsilon_{GS} &= -\sqrt{|\alpha|^2 + \frac{\lambda^2}{4}}, \\ \phi_{GS} &= \begin{pmatrix} \frac{\frac{\lambda}{2}-\epsilon_{GS}}{N} \\ \frac{-\alpha^*}{N} \end{pmatrix}, \end{aligned} \tag{B.2}$$

where $N = \sqrt{-2\epsilon_{GS}(\frac{\lambda}{2}) - \epsilon_{GS}}$. We calculate the expectation values:

$$\begin{aligned} \langle S^z \rangle &= -\frac{\lambda}{4\epsilon_{GS}}, \\ \langle P \rangle &= \frac{c\alpha^* + \alpha}{2\epsilon_{GS}}. \end{aligned} \tag{B.3}$$

From the constraint condition we get:

$$n_\sigma = \langle S^z \rangle + \frac{1}{2} = -\frac{\lambda}{4\epsilon_{GS}} + \frac{1}{2}. \tag{B.4}$$

We impose the non-interacting limit through $Z(U=0) = \langle O \rangle^2 = 1$ and obtain:

$$|c\alpha^* + \alpha|^2 = 4\epsilon_{GS}^2. \tag{B.5}$$

Using the above two equations we end up with:

$$\frac{|\alpha|^2}{|c\alpha^* + \alpha|^2} = n_\sigma - n_\sigma^2. \tag{B.6}$$

Assuming c, h, α to be real the final expression for the gauge is:

$$c = \frac{1}{\sqrt{n_\sigma(1 - n_\sigma)}} - 1. \tag{B.7}$$

Appendix C

SSMF perturbative expansion

C.1 Two-orbital Hubbard model

C.1.1 In absence of Hund's coupling $J = 0$

We apply perturbation theory on a two-orbital system with $J = 0$ at half-filling, where the interacting Hamiltonian is given by:

$$H_{at} = U \sum_{m} S^z_{m\uparrow} S^z_{m\downarrow} + U^{'} \sum_{m<m',\sigma,\sigma'} S^z_{m\sigma} S^z_{m'\sigma'} \tag{C.1}$$

and in fact $U^{'} = U$. We explore the behavior of the system around this atomic limit by including as a perturbation the term:

$$H_{pert} = \sum_{m\sigma} h_m 2 S^x_{m\sigma}, \tag{C.2}$$

which is related to the kinetic part of the SSMF Hamiltonian. Since the ground state of the unperturbed system is two times degenerate and the perturbation does not have non-zero elements in the low energy subspace of the atomic spectrum, we need - as in the single orbital case in section 2.2.5 - to perform second order perturbation theory in order to find the combination of states to which the perturbed state tends for $h_m \to 0$. By doing that one obtains $H^{'} = H_{pert}(E_0 - H_{at})^{-1} H_{pert} = -\frac{2}{U} H^2_{pert}$, leading to:

$$H^{'} = -\frac{4h_m^2}{U} \begin{pmatrix} 1 & 0 \\ 0 & 1 \end{pmatrix}. \tag{C.3}$$

Therefore the ground state of the perturbed system is:

$$|\phi^0\rangle = \frac{1}{\sqrt{6}} \Big(|\uparrow,\uparrow\rangle + |\downarrow,\downarrow\rangle + |\uparrow,\downarrow\rangle + |\downarrow,\uparrow\rangle + |\uparrow\downarrow,0\rangle + |0,\uparrow\downarrow\rangle \Big). \tag{C.4}$$

The first-order term in perturbation is given by Eq.2.44 and one notices that the ground state is connected through H_{pert} only with the degenerate states of sectors $N = 1$ and $N = 3$, so we get:

$$|\phi^0_{(I)}\rangle = -\frac{\sqrt{6}h}{U}\Big(|\uparrow\downarrow,\uparrow\rangle + |\uparrow\downarrow,\downarrow\rangle + |\uparrow,\uparrow\downarrow\rangle + |\downarrow,\uparrow\downarrow\rangle + |0,\uparrow\rangle + |0,\downarrow\rangle + |\uparrow,0\rangle + |\downarrow,0\rangle\Big). \tag{C.5}$$

We calculate $\langle 2S^x_{m\sigma}\rangle$ and make use of the self-consistency equation $h_m = 2\epsilon_0\langle 2S^x_{m\sigma}\rangle$ to estimate the critical U for the transition:

$$\begin{aligned}\langle 2S^x_{m\sigma}\rangle_{(0)} + \langle 2S^x_{m\sigma}\rangle_{(I)} &= 2\cdot\Big(\langle\phi^0|2S^x_{m\sigma}|\phi^0\rangle + \langle\phi^0_{(I)}|2S^x_{m\sigma}|\phi^0_{(I)}\rangle + \langle\phi^0|2S^x_{m\sigma}|\phi^0_{(I)}\rangle\Big) = \\ &= -\frac{12h}{U},\end{aligned} \tag{C.6}$$

$$h_m = 2\epsilon_0\langle 2S^x_{m\sigma}\rangle = -\frac{24h_m\epsilon_0}{U}, \tag{C.7}$$

$$U_c = -24\epsilon_0. \tag{C.8}$$

This result reproduces the numerical one obtained for a system with a semi-circular DOS ($\epsilon_0 \simeq -0.2122$) $U_c \simeq 5.09$.

In order to evaluate the system's behavior close to the Mott transition, we calculate the second order perturbation term using the expression 2.44. We separate the two terms of the expression in A and B respectively:

$$\begin{aligned}A &: -\frac{1}{2}\frac{V_{\phi\kappa_1}V_{\kappa_1\phi}}{E^2_{\kappa_1\phi}}|\phi^0\rangle, \\ B &: \frac{V_{\kappa_1\kappa_2}V_{\kappa_2\phi}}{E_{\phi\kappa_1}E_{\phi\kappa_2}}|\kappa^0_1\rangle.\end{aligned} \tag{C.9}$$

It is easier to understand the processes described in A, B by starting from the rightmost state appearing in the numerator and ending through H_{pert} to the leftmost one. In B, the states involved through $V_{\kappa_2\phi}$ are obviously the ground state and as in the first-order the degenerate states of sectors $N = 1$ and $N = 3$. $V_{\kappa_1\kappa_2}$ connects as a second process these last states with all the other non equal to the ground state ones, meaning those of $N = 0$ and $N = 4$. A includes the processes of the first-order term twice. In Fig.C.1 a visualisation of the processes is shown. Carrying out carefully all the above

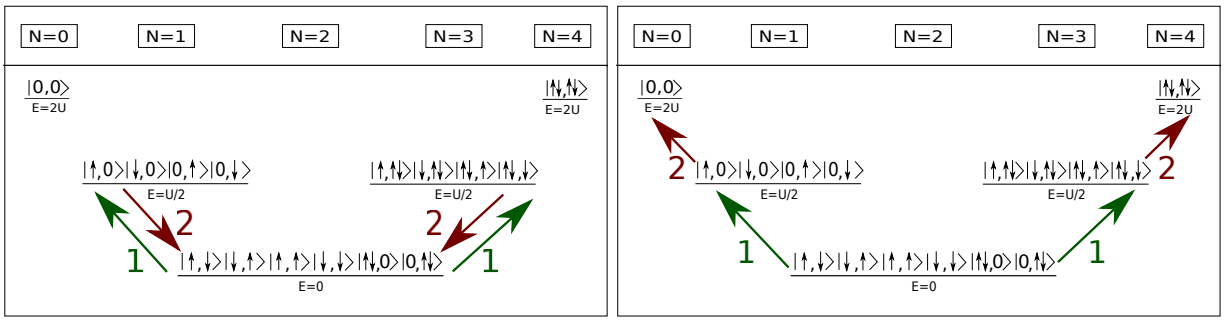

(A) (B)

FIGURE C.1: Visualisation of the processes involved in the second order perturbation term of a two degenerate orbital system. In step (1) the ground state connects to those states for which $\langle\phi^0|H_{pert}|\kappa\rangle \neq 0$. Depending on wether the process is of A or B character, in step (2) these states connect to other available states.

calculations we end up with:

$$|\phi^0_{(II)}\rangle = \frac{12h^2}{\sqrt{6}U^2}\left(|0,0\rangle + |\uparrow\downarrow,\uparrow\downarrow\rangle\right) - \frac{24h^2}{U^2}|\phi^0\rangle. \tag{C.10}$$

As in the single-orbital case the third order term is needed as well because none of the states appearing in $|\phi^0_{(II)}\rangle$ connect with $|\phi^0\rangle$ through H_{pert}. The expression is given in 2.44 and we separate again the terms into A', B' (the processes related to the first order correction and the more complicated ones):

$$\begin{aligned} A' &: \frac{|V_{\phi\kappa_2}|^2 V_{\kappa_1\phi}}{E_{\kappa_1\phi}E_{\phi\kappa_2}}\left(\frac{1}{E_{\phi\kappa_1}} + \frac{1}{2E_{\phi\kappa_2}}\right)|\kappa^0_1\rangle \\ B' &: -\frac{V_{\kappa_1\kappa_2}V_{\kappa_2\kappa_3}V_{\kappa_3\phi}}{E_{\kappa_1\phi}E_{\phi\kappa_2}E_{\phi\kappa_3}}|\kappa^0_1\rangle \end{aligned} \tag{C.11}$$

The processes can be analyzed similarly to the second-order ones and the third order correction is (an illustration of all the processes involved here is shown in Fig.C.2):

$$|\phi^0_{(III)}\rangle = \frac{408h^3}{\sqrt{6}U^3}\Big(|\uparrow\downarrow,\uparrow\rangle + |\uparrow\downarrow,\downarrow\rangle + |\uparrow,\uparrow\downarrow\rangle + |\downarrow,\uparrow\downarrow\rangle + |0,\uparrow\rangle + |0,\downarrow\rangle + |\uparrow,0\rangle + |\downarrow,0\rangle\Big). \tag{C.12}$$

We can estimate $Z(U)$ by calculating $\langle 2S^x_{m\sigma}\rangle$ up to third order.

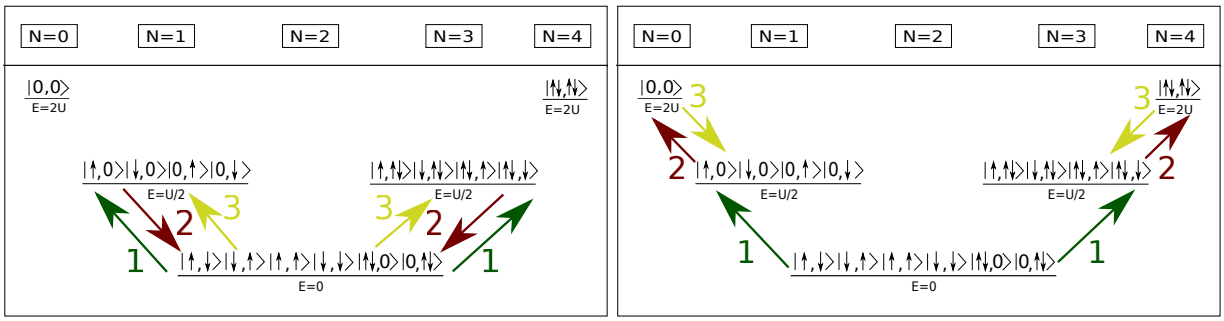

(A) (B)

FIGURE C.2: Visualisation of the processes involved in the third order perturbation term of a two degenerate orbital system. Steps (1) and (2) represent the second order processes.

$$\begin{aligned}
\langle \phi^0 | 2S^x_{m\sigma} | \phi^0_I \rangle &= -\frac{12 h_m}{U} \\
\langle \phi^0_I | 2S^x_{m\sigma} | \phi^0_{II} \rangle &= \frac{240 h_m^3}{U^3} \\
\langle \phi^0 | 2S^x_{m\sigma} | \phi^0_{III} \rangle &= \frac{816 h_m^3}{U^3} \\
\langle 2S^x_{m\sigma} \rangle &= -\frac{12 h_m}{U} + \frac{1056 h_m^3}{U^3} = \frac{h_m}{2\epsilon_0}
\end{aligned} \tag{C.13}$$

Using the self-consistency equation $h_m^2 = 4\epsilon_0^2 Z_m$ we finally obtain:

$$Z_m = \frac{U^3}{8448\epsilon_0^3} + \frac{U^2}{352\epsilon_0^2}, \tag{C.14}$$

which can be re-expressed in terms of U_c as:

$$Z_m = \frac{U^2}{352\epsilon_0^2}\left(1 - \frac{U}{U_c}\right). \tag{C.15}$$

C.1.2 With finite Hund's coupling $J \neq 0$ (density-density form)

A finite Hund's coupling is introduced in the system, considering first the density-density form of the interactions:

$$H_{at} = U \sum_m S^z_{m\uparrow} S^z_{m\downarrow} + (U - 2J) \sum_{m \neq m'} S^z_{m\uparrow} S^z_{m'\downarrow} + (U - 3J) \sum_{m < m', \sigma} S^z_{m\sigma} S^z_{m'\sigma}. \tag{C.16}$$

Following the steps performed in the study of the $J = 0$ case, one obtains the ground state of the perturbed system:

$$|\phi^0\rangle = \frac{1}{\sqrt{2}}\Big(|\uparrow,\uparrow\rangle + |\downarrow,\downarrow\rangle\Big). \tag{C.17}$$

We use the first-order correction to the ground state of Eq.2.44 in order to calculate the critical interaction for the Mott transition. As in section C.1.1, the ground state is connected through H_{pert} only with the degenerate states of sectors $N = 1$ and $N = 3$, so we get:

$$|\phi^0_{(I)}\rangle = -\frac{\sqrt{2}h}{U+J}\Big(|\uparrow\downarrow,\uparrow\rangle + |\uparrow\downarrow,\downarrow\rangle + |\uparrow,\uparrow\downarrow\rangle + |\downarrow,\uparrow\downarrow\rangle + |0,\uparrow\rangle + |0,\downarrow\rangle + |\uparrow,0\rangle + |\downarrow,0\rangle\Big). \tag{C.18}$$

We calculate $\langle 2S^x_{m\sigma}\rangle$ and make use of the self-consistency equation $h_m = 2\epsilon_0\langle 2S^x_{m\sigma}\rangle$ to estimate the critical U for the transition:

$$\begin{aligned}\langle 2S^x_{m\sigma}\rangle_{(0)} + \langle 2S^x_{m\sigma}\rangle_{(I)} &= 2\cdot\Big(\langle\phi^0|2S^x_{m\sigma}|\phi^0\rangle + \langle\phi^0_{(I)}|2S^x_{m\sigma}|\phi^0_{(I)}\rangle + \langle\phi^0|2S^x_{m\sigma}|\phi^0_{(I)}\rangle\Big) = \\ &= -\frac{4h}{U+J},\end{aligned} \tag{C.19}$$

$$h_m = 2\epsilon_0\langle 2S^x_{m\sigma}\rangle = -\frac{8h\epsilon_0}{U+J}, \tag{C.20}$$

$$U_c = -8\epsilon_0 - J. \tag{C.21}$$

In order to capture the negative slope of Z as a function of U appearing in Fig.5.15 we calculate the second-order perturbation term using the expression 2.44, naming again the terms A and B:

$$\begin{aligned}A &: -\frac{1}{2}\frac{V_{\phi\kappa_1}V_{\kappa_1\phi}}{E^2_{\kappa_1\phi}}|\phi^0\rangle \\ B &: \frac{V_{\kappa_1\kappa_2}V_{\kappa_2\phi}}{E_{\phi\kappa_1}E_{\phi\kappa_2}}|\kappa^0_1\rangle\end{aligned} \tag{C.22}$$

Compared to the $J = 0$ case now there are two additional processes arising from the term B, which connect the $N = 1$ and $N = 3$ sectors involving the states of the sector $N = 2$ which are not part of the ground state manifold. In the case of $J = 0$, these low-spin states were forbidden to the second order processes since they belonged to the degenerate ground state. A visualisation of the processes is shown in Fig.C.3.

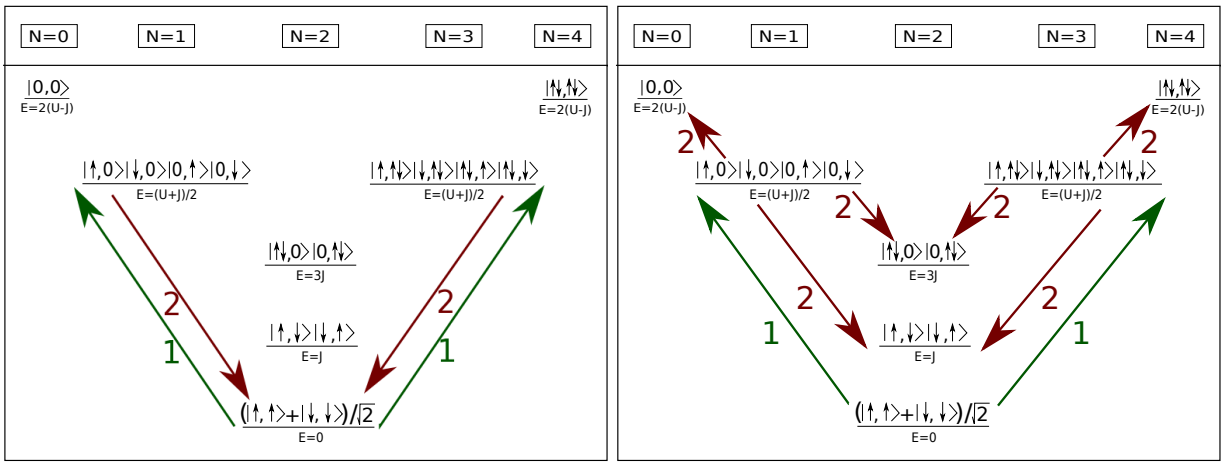

FIGURE C.3: Visualisation of the processes involved in the second order perturbation term of a two degenerate orbital system. In step (1) the ground state connects to those states for which $\langle\phi^0|H_{pert}|\kappa\rangle \neq 0$. Depending on wether the process is of A or B character, in step (2) these states connect to other available states.

Carrying out carefully all the above calculations we end up with:

$$|\phi^0_{(II)}\rangle = \frac{4h^2}{\sqrt{2}(U+J)}\left(\frac{2}{J}\left(|\uparrow,\downarrow\rangle + |\downarrow,\uparrow\rangle\right) + \frac{2}{3J}\left(|\uparrow\downarrow,0\rangle + |0,\downarrow\uparrow\rangle\right) + \frac{1}{U-J}\left(|\uparrow\downarrow,\uparrow\downarrow\rangle + |0,0\rangle\right)\right) - \frac{8h^2}{(U+J)^2}|\phi^0\rangle. \tag{C.23}$$

Once again we calculate the third order term because none of the states appearing in $|\phi^0_{(II)}\rangle$ connect with $|\phi^0\rangle$ through H_{pert}. The expression is given in 2.44 and we separate the terms into A', B':

$$\begin{aligned} A' &: \frac{|V_{\phi\kappa_2}|^2 V_{\kappa_1\phi}}{E_{\kappa_1\phi}E_{\phi\kappa_2}}\left(\frac{1}{E_{\phi\kappa_1}} + \frac{1}{2E_{\phi\kappa_2}}\right)|\kappa^0_1\rangle, \\ B' &: -\frac{V_{\kappa_1\kappa_2}V_{\kappa_2\kappa_3}V_{\kappa_3\phi}}{E_{\kappa_1\phi}E_{\phi\kappa_2}E_{\phi\kappa_3}}|\kappa^0_1\rangle. \end{aligned} \tag{C.24}$$

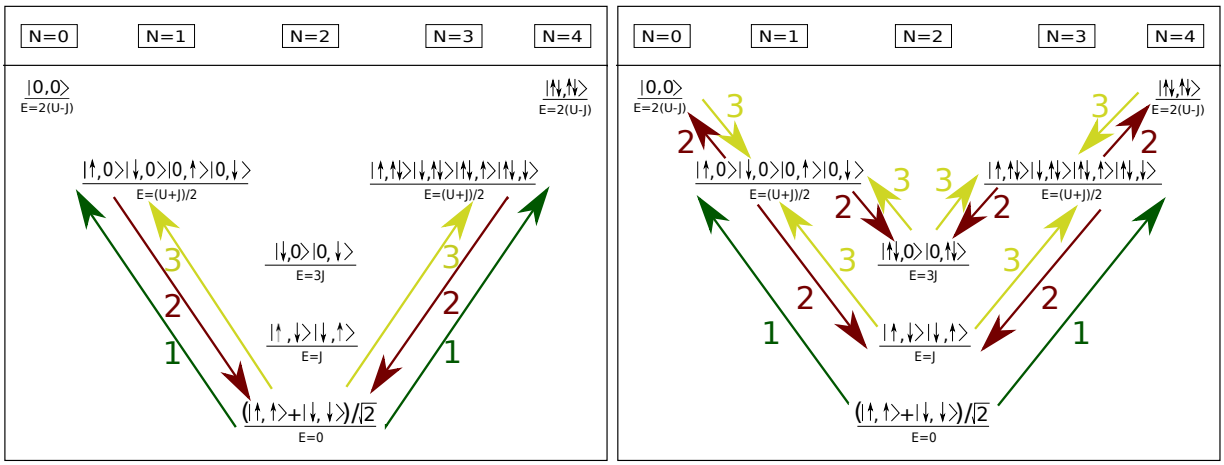

(A) (B)

FIGURE C.4: Visualisation of the processes involved in the third order perturbation term of a two degenerate orbital system. Steps (1) and (2) represent the second order processes.

The third order correction (an illustration of all the processes involved in it is shown in Fig.C.4) is:

$$|\phi^0_{(III)}\rangle = \frac{8h_m^3(-8U^2-13J^2+15UJ)}{\sqrt{2}(U+J)^3(U-J)3J}\cdot \Big(|\uparrow\downarrow,\uparrow\rangle + |\uparrow\downarrow,\downarrow\rangle + |\uparrow,\uparrow\downarrow\rangle + |\downarrow,\uparrow\downarrow\rangle + |0,\uparrow\rangle + |0,\downarrow\rangle + |\uparrow,0\rangle + |\downarrow,0\rangle\Big). \tag{C.25}$$

$Z(U)$ can be calculated by obtaining $\langle 2S^x_{m\sigma}\rangle$ up to third order:

$$\begin{aligned}
\langle\phi^0|2S^x_{m\sigma}|\phi^0_I\rangle &= -\frac{4h_m}{U+J}\\
\langle\phi^0_I|2S^x_{m\sigma}|\phi^0_{II}\rangle &= 16h_m^3\frac{-8U^2-J^2+3UJ}{(U+J)^3(U-J)3J}\\
\langle\phi^0|2S^x_{m\sigma}|\phi^0_{III}\rangle &= 16h_m^3\frac{-8U^2-13J^2+15UJ}{(U+J)^3(U-J)3J}\\
\langle 2S^x_{m\sigma}\rangle &= -\frac{4h_m}{U+J}+16h_m^3\frac{-16U^2-14J^2+18UJ}{(U+J)^3(U-J)3J} = \frac{h_m}{2\epsilon_0}
\end{aligned} \tag{C.26}$$

Using the self-consistency equation $h_m^2 = 4\epsilon_0^2 Z_m$ we obtain:

$$Z_m = \frac{(U+J)^3(U-J)3J}{128\epsilon_0^2(-8U^2-7J^2+9UJ)}\Big(\frac{1}{2\epsilon_0}+\frac{4}{U+J}\Big), \tag{C.27}$$

which can be written in terms of U_c as:

$$Z_m = \frac{(U+J)^2(U-J)3J}{256\epsilon_0^3(8U^2+7J^2-9UJ)}(U_c-U). \tag{C.28}$$

C.1.3 With finite Hund's coupling $J \neq 0$ (Kanamori form)

We use the Kanamori form of interactions in the atomic limit, with the Hamiltonian given by:

$$\begin{aligned} H_{at} =& U\sum_m S^z_{m\uparrow}S^z_{m\downarrow} + (U-2J)\sum_{m\neq m'} S^z_{m\uparrow}S^z_{m'\downarrow} + (U-3J)\sum_{m<m',\sigma} S^z_{m\sigma}S^z_{m'\sigma} \\ & - J\sum_m \left(S^+_{m\uparrow}S^-_{m\downarrow}S^+_{\bar{m}\downarrow}S^-_{\bar{m}\uparrow} + S^+_{m\uparrow}S^+_{m\downarrow}S^-_{\bar{m}\uparrow}S^-_{\bar{m}\downarrow} + h.c.\right). \end{aligned} \tag{C.29}$$

The procedure is identical to the one followed in section C.1.2. First we evaluate the ground state of the perturbed system:

$$|\phi^0\rangle = \frac{1}{2}\Big(|\uparrow,\uparrow\rangle + |\downarrow,\downarrow\rangle + |\uparrow,\downarrow\rangle + |\downarrow,\uparrow\rangle\Big). \tag{C.30}$$

The calculation of the corrections follows the steps of the previous sections and in first order we get:

$$|\phi^0_{(I)}\rangle = -\frac{2h}{U+J}\Big(|\uparrow\downarrow,\uparrow\rangle + |\uparrow\downarrow,\downarrow\rangle + |\uparrow,\uparrow\downarrow\rangle + |\downarrow,\uparrow\downarrow\rangle + |0,\uparrow\rangle + |0,\downarrow\rangle + |\uparrow,0\rangle + |\downarrow,0\rangle\Big). \tag{C.31}$$

We use this expression as in the previous cases and evaluate $\langle 2S^x_{m\sigma}\rangle$ up to first order. Using the self-consistency equation $h_m = 2\epsilon_0\langle 2S^x_{m\sigma}\rangle$ we then estimate the critical U for the Mott transition:

$$\langle 2S^x_{m\sigma}\rangle_{(I)} = -\frac{8h_m}{U+J}, \tag{C.32}$$

$$U_c = -16\epsilon_0 - J. \tag{C.33}$$

We calculate the second- and third-order in the perturbation in order to extract the dependence of Z on U close to the transition.

$$\begin{aligned} |\phi^0_{(II)}\rangle =& \frac{4h_m^2}{(U+J)}\left(\frac{1}{J}(|\uparrow\downarrow,0\rangle + |0,\uparrow\downarrow\rangle) + \frac{2}{U+J}(|\uparrow,\uparrow\rangle + |\uparrow,\downarrow\rangle + |\downarrow,\uparrow\rangle + |\downarrow,\downarrow\rangle) + \right. \\ & \left. + \frac{1}{U-J}(|\uparrow\downarrow,\uparrow\downarrow\rangle + |0,0\rangle)\right), \end{aligned} \tag{C.34}$$

$$|\phi^0_{(III)}\rangle = \frac{8h_m^3(-U^2-12J^2+11UJ)}{(U+J)^3(U-J)J}\cdot \Big(|\uparrow\downarrow,\uparrow\rangle+|\uparrow\downarrow,\downarrow\rangle+|\uparrow,\uparrow\downarrow\rangle+|\downarrow,\uparrow\downarrow\rangle+|0,\uparrow\rangle+|0,\downarrow\rangle+|\uparrow,0\rangle+|\downarrow,0\rangle\Big). \tag{C.35}$$

We calculate $\langle 2S^x_{m\sigma}\rangle$ up to third order and using the self-consistency equation we once again obtain the expression for Z as a function of U:

$$Z_m = \frac{(U+J)^3(U-J)J}{256\epsilon_0^2(-U^2-8J^2+7UJ)}\Big(\frac{1}{2\epsilon_0}+\frac{8}{U+J}\Big), \tag{C.36}$$

which expressed in terms of U_c and making use of Eq.C.33 becomes:

$$Z_m = \frac{(U+J)^2(U-J)J}{512\epsilon_0^3(U^2+8J^2-7UJ)}(U_c-U). \tag{C.37}$$

C.1.4 With a finite crystal-field splitting

We evaluate the critical interaction for the Mott transition in a system with two orbitals in presence of a finite crystal-field splitting. We use the density-density form of interactions in agreement with the calculations shown in the main text. The crystal-field partially lifts the degeneracy of the excited states of sectors $N=1$ and $N=3$ placing half of them higher in energy by a Δ shift and the other half lower by the same amount. Performing the calculations following exactly the steps of the previous sections we get:

$$\langle 2S^x_{m\sigma}\rangle = -2h\left(\frac{1}{U+J+\Delta}+\frac{1}{U+J-\Delta}\right). \tag{C.38}$$

Making use of the self-consistency equation $h = 2\epsilon_m\langle 2S^x_{m\sigma}\rangle$ we obtain:

$$\begin{aligned} -4\epsilon_m\frac{2(U+J)}{(U+J)^2-\Delta^2} &= 1 \Rightarrow \\ (U+J)^2+8\epsilon_m(U+J)-\Delta^2 &= 0 \end{aligned} \tag{C.39}$$

and solving the last equation we get the critical interaction for the transition:

$$U_c = -4\epsilon_m\left(1+\sqrt{1+\left(\frac{\Delta}{4\epsilon_m}\right)^2}\right)-J. \tag{C.40}$$

C.2 Away from half-filling

C.2.1 Single-band system

In this section we shortly explore the behaviour of a single-orbital system (using the Bethe lattice) away from half-filling at small doping around U_c. The Hamiltonian has an additional term $\sum_\sigma \lambda_\sigma(S^z_\sigma + \frac{1}{2})$ compared to the half-filled situation (where $\lambda = 0$) and therefore the spectrum will change into $E_{N=1} = 0$, $E_{N=2} = \frac{U}{2} + \lambda$ and $E_{N=0} = \frac{U}{2} - \lambda$. Following the steps of section 2.2.5, one ends up with the expression:

$$\langle 2S^x_\sigma \rangle = -h(1+c)\frac{4U}{U^2-4\lambda^2} + 32h^3(1+c)^3\frac{U(U^2+4\lambda^2)}{(U^2-4\lambda^2)^3} = \frac{h}{(1+c)\epsilon_0}. \tag{C.41}$$

We also calculate the population $n_\sigma = \langle S^z_\sigma \rangle + \frac{1}{2}$ and get for the doping:

$$\delta = 2n_\sigma - 1 = 2\langle S^z_\sigma \rangle = -h^2(1+c)^2\frac{16U\lambda}{(U^2-4\lambda^2)^2}. \tag{C.42}$$

Using the above equations and assuming $\lambda = \lambda_0 + \lambda'\delta + ...$ we get:

$$\lambda_0 = \pm\sqrt{\frac{U^2}{4} + 4\epsilon_0 U} = \pm\frac{1}{2}\sqrt{U(U-U_c)}, \qquad U_c = -16\epsilon_0. \tag{C.43}$$

In order to evaluate Z as a function of doping we use Eq.C.42,C.43 and keeping only terms linear in δ (so approximating $\lambda \simeq \lambda_0$) we get:

$$h^2(1+c)^2 = -\frac{U_c^2 U}{16\lambda_0}\delta, \tag{C.44}$$

which after some manipulation leads to:

$$Z = \frac{2}{\sqrt{1-\frac{U_c}{U}}}\delta, \tag{C.45}$$

reproducing at small dopings the numerical results, as shown in Fig.C.5.

C.2.2 Two-band system with $J = 0$

The system under study is a two-orbital model in absence of Hund's coupling J away from half-filling, therefore its spectrum will be modified due to the term $\sum_{m,\sigma} \lambda_{m,\sigma}(S^z_{m,\sigma} + \frac{1}{2})$. Following the steps of section C.2.1 in order to capture the behaviour of the quasi-particle weight as a function of doping for interactions larger but close to the critical

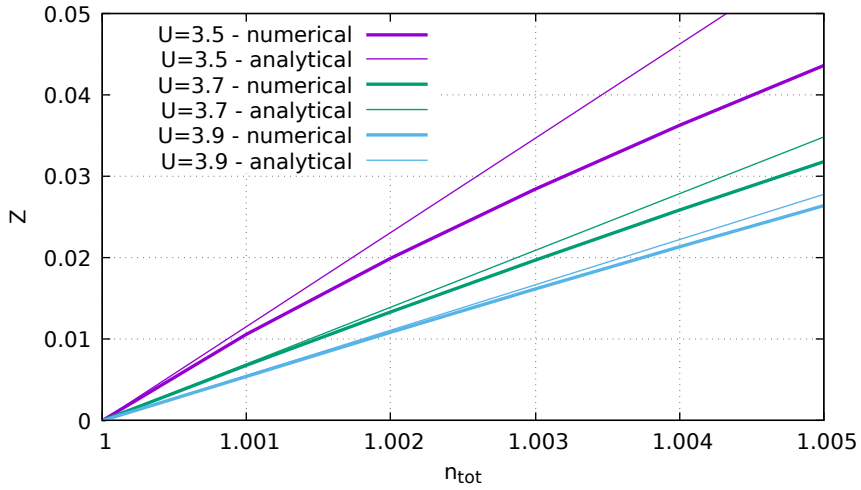

FIGURE C.5: Quasiparticle weight of a single orbital system as a function of total population for $U = 3.5$, $U = 3.7$ and $U = 3.9$, all larger than $U_c \simeq 3.39$ implying that at half-filling we have a Mott insulator. Again the analytical results (through perturbation theory) reproduce the numerical ones (using SSMF) at small dopings, so in the vicinity of the insulator.

one, we first calculate $\langle 2S^x_{m,\sigma} \rangle$ up to first order, which can easily be shown to be:

$$\langle 2S^x_{m,\sigma} \rangle = -\frac{12 h_m U}{U^2 - 4\lambda_m^2}. \tag{C.46}$$

Next we calculate $2\langle S^z_{m,\sigma} \rangle = 2n_{m,\sigma} - 1$ up to second order and approximating for simplicity $c_m + 1 = 2$ we obtain:

$$2\langle S^z_{m,\sigma} \rangle = -48 h_m^2 \frac{\lambda_m U}{(U^2 - 4\lambda_m^2)^2}. \tag{C.47}$$

As in the single-orbital case, we assume $\lambda_m = \lambda_{m,0} + \lambda'_m \delta + ...$ and by solving C.47 we get:

$$\lambda_{m,0} = \pm \frac{1}{2} \sqrt{U(U - U_c)}, \qquad U_c = -24\epsilon_0. \tag{C.48}$$

After some easy manipulations of the above equations we get the expression for Z_m as a function of δ and U:

$$Z_m = \frac{3}{\sqrt{1 - \frac{U_c}{U}}} \delta. \tag{C.49}$$

In Fig.C.6 we see the analytical calculations together with the numerical results.

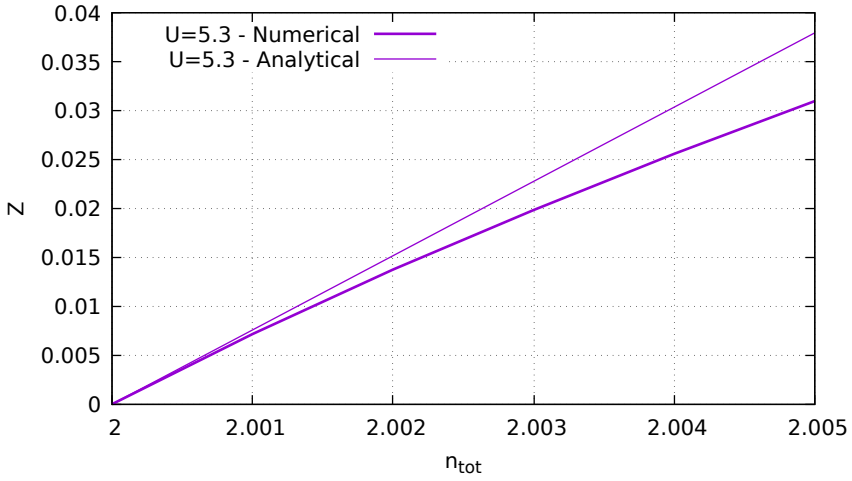

FIGURE C.6: Quasiparticle weight Z as a function of total population n_{tot} for a fixed value of $U = 5.3$, larger than $U_c \simeq 5.09$. Numerical results obtained through SSMF and analytical ones by perturbation theory calculations.

C.2.3 Two-band system with $J \neq 0$

We add a finite Hund's coupling J in a system with density-density form of interactions. We follow the steps of the previous sections and first calculate $\langle 2S^x_{m,\sigma}\rangle$:

$$\langle 2S^x_{m,\sigma}\rangle = -2h_m(1+c_m)\frac{U+J}{(U+J)^2-4\lambda_m^2}. \tag{C.50}$$

We define $U+J = U_{eff}$ and calculate $2\langle S^z_{m,\sigma}\rangle = 2n_{m,\sigma} - 1$ (approximating $c_m + 1 = 2$). We obtain:

$$2\langle S^z_{m,\sigma}\rangle = -64h_m^2\frac{\lambda U_{eff}}{(U_{eff}^2-4\lambda_m^2)^2}. \tag{C.51}$$

As in the cases of a single-orbital and two orbitals with $J = 0$ we assume $\lambda_m = \lambda_{m,0} + \lambda'_m\delta + ...$ and by solving the above equation we get:

$$\lambda_{m,0} = \pm\frac{1}{2}\sqrt{U_{eff}(U_{eff}-U_{eff,c})}, \qquad U_c = -8\epsilon_0. \tag{C.52}$$

We calculate the expression for Z_m as a function of δ and U:

$$Z_m = \frac{1}{2\sqrt{1-\frac{U_{eff,c}}{U_{eff}}}}\delta. \tag{C.53}$$

In Fig.C.7 the analytical calculations of $Z_m(n_{tot})$ are shown together with the numerical results.

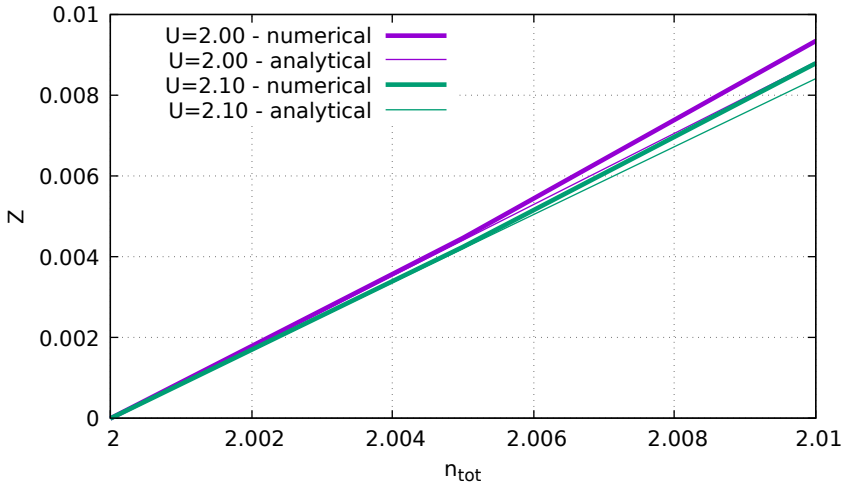

FIGURE C.7: Quasiparticle weight Z as a function of total population n_{tot} for different values of U, larger than $U_c \simeq 1.96$ (for $J/U = 0.25$). Numerical results obtained through SSMF and analytical ones by perturbation theory calculations.

Appendix D

Derivation of electronic compressibility formulas

In the main text we gave a short description of the formulas related to the divergent electronic compressibility. Within SSMF the fermionic Hamiltonian has the form:

$$\hat{H} - \mu\hat{N} = \sum_{\mathbf{k}m\sigma} (Z\epsilon_{\mathbf{k}} - \mu - \lambda) f^{\dagger}_{km\sigma} f_{km\sigma}, \tag{D.1}$$

the total electron density is given by:

$$n = \int^{(\mu+\lambda)/Z} d\epsilon D(\epsilon) \tag{D.2}$$

and thus the electronic compressibility becomes:

$$\begin{aligned} \kappa_{el} = \frac{dn}{d\mu} = D\Big(\frac{\mu+\lambda}{Z}\Big)\frac{d}{d\mu}\Big(\frac{\mu+\lambda}{Z}\Big) = D\Big(\frac{\mu+\lambda}{Z}\Big)\left[\frac{1}{Z} + \frac{1}{Z}\frac{d\lambda}{d\mu} - \frac{\mu+\lambda}{Z^2}\frac{dZ}{d\mu}\right] = \\ = D\Big(\frac{\mu+\lambda}{Z}\Big)\frac{1}{Z}\left[1 + \Big(\frac{d\lambda}{d\mu} - \frac{\mu+\lambda}{Z}\frac{dZ}{d\mu}\Big)\right]. \end{aligned} \tag{D.3}$$

According to the Luttinger theorem the volume of the Fermi surface in an interacting system is proportional to the particle density and hence the chemical potential of that system is related to the one of the non-interacting case (at the same density) through:

$$\mu_0 = \frac{\mu+\lambda}{Z}. \tag{D.4}$$

We can further define the renormalized density of states $D^*(\mu) = D(\mu_0)/Z$. Collecting all the above we write:

$$\frac{dn}{d\mu} = \left[1 - \frac{dn}{d\mu}\Big(\mu_0\frac{dZ}{dn} - \frac{d\lambda}{dn}\Big)\right] D^*(\mu), \tag{D.5}$$

and Eq.D.3 becomes:

$$\kappa_{el} = \frac{1}{D^*(\mu)^{-1} + \left[\mu_0 \frac{dZ}{dn} - \frac{d\lambda}{dn}\right]}. \tag{D.6}$$

As mentioned in the main text the electronic compressibility in Fermi liquid theory is given by:

$$\kappa_{el} = \frac{D^*(\epsilon_f)}{1 + F_0^s} = \frac{1}{D^*(\epsilon_f)^{-1} + f_0^s} \tag{D.7}$$

and comparing it with the previous equation we finally get:

$$\begin{aligned} F_0^s &= D^*(\mu)\left[\mu_0 \frac{dZ}{dn} - \frac{d\lambda}{dn}\right], \\ f_0^s &= \mu_0 \frac{dZ}{dn} - \frac{d\lambda}{dn}. \end{aligned} \tag{D.8}$$

$\mu_0 \frac{dZ}{dn}$ is always positive (since the slope of Z has always the sign of μ_0), therefore in order for the Landau parameter to be negative, $\frac{d\lambda}{dn}$ needs to be positive and indeed is what is found numerically [2].

Appendix E

Resistivity in the low-temperature regime

We calculate the resistivity formula at low-temperature following the derivations performed in [212, 220]. We assume local, orbital independent correlations and a Fermi-liquid form for the self-energy. The latter was expanded up to linear order in frequency in chapter 1 of the main text, Eq.1.3. Including the quadratic order in the expansion, the low-temperature momentum-independent self-energy becomes:

$$\Sigma(\omega) \simeq \mathbb{1}\left[Re\Sigma(0) + \left(1 - \frac{1}{Z}\right)\hbar\omega - i\gamma\left[1 + \left(\frac{\hbar\beta\omega}{\pi}\right)^2\right]\right], \tag{E.1}$$

where $Z = \left(1 - \partial_\omega Re\Sigma(\omega)\big|_{\omega=0}\right)^{-1}$ and $\gamma(T) = \gamma = Im\Sigma(0)$. The self-energy is diagonal in any basis, therefore the retarded Green's function will be diagonal in the band basis with elements:

$$\begin{aligned} G(\mathbf{k},\omega) = G(\epsilon_{n\mathbf{k}},\omega) &= \frac{1}{\hbar\omega + \mu - \epsilon_{n\mathbf{k}} - \Sigma(\omega)} \simeq \\ &\simeq \frac{1}{\hbar\omega + \mu - \epsilon_{n\mathbf{k}} - Re\Sigma(0) - \left(1 - \frac{1}{Z}\right)\hbar\omega + i\gamma\left[1 + \left(\frac{\hbar\beta\omega}{\pi}\right)^2\right]} = \\ &= \frac{1}{\frac{xk_BT}{Z} + \tilde{\mu} - \epsilon_{n\mathbf{k}} + i\gamma\left[1 + \left(\frac{x}{\pi}\right)^2\right]}, \end{aligned} \tag{E.2}$$

where $\tilde{\mu} = \mu - Re\Sigma(0)$ is the effective chemical potential, $\epsilon_{n\mathbf{k}}$ are the eigenvalues of $H(\mathbf{k})$ and $x = \hbar\beta\omega$ has been defined. The spectral function will in turn be:

$$\rho_{nn}(\mathbf{k},\omega) = \rho(\epsilon_{n\mathbf{k}},\omega) = \frac{\gamma\left(1 + (\frac{x}{\pi})^2\right)/\pi}{\left(\frac{xk_BT}{Z} + \tilde{\mu} - \epsilon_{n\mathbf{k}}\right)^2 + \gamma^2\left(1 + (\frac{x}{\pi})^2\right)^2}. \tag{E.3}$$

We can now write explictly Eq.6.4 of the main text as:

$$\sigma_{\alpha\alpha} = \frac{2\pi e^2\hbar}{V}\sum_{\mathbf{k}nn'} v_\alpha^{nn'}(\mathbf{k})v_\alpha^{n'n}(\mathbf{k})\int_{-\infty}^{+\infty} dx \frac{\rho(\epsilon_{n\mathbf{k}},x)\rho(\epsilon_{n'\mathbf{k}},x)}{4cosh^2\frac{x}{2}}. \tag{E.4}$$

The two spectral functions are two lorentzians centred at $\epsilon_{n\mathbf{k}} = \tilde{\mu} + \frac{xk_BT}{Z}$ and $\epsilon_{n'\mathbf{k}} = \tilde{\mu} + \frac{xk_BT}{Z}$ respectively and both have broadening equal to $\gamma^2(1+\left(\frac{x}{\pi}\right)^2)$. The above integral is therefore non-zero only when the two lorentzians overlap within the thermal window defined by γ. We can understand this by defining:

$$\begin{aligned} y &= \gamma\Big(1+\big(\frac{x}{\pi}\big)^2\Big) \\ z &= \frac{xk_BT}{Z} + \tilde{\mu} - \epsilon_{n\mathbf{k}} \end{aligned} \tag{E.5}$$

and noticing that:

$$\int_{-\infty}^{\infty} dz \Big(\frac{y/\pi}{z^2+y^2}\Big)^2 = \frac{1}{2\pi y}, \tag{E.6}$$

so to a good approximation we can replace $\left(\frac{y/\pi}{z^2+y^2}\right)^2 = \frac{\delta(z)}{2\pi y}$ and (since, as we mentioned, at very low temperatures the weight is concentrated around $\epsilon_{n\mathbf{k}} = \tilde{\mu} + \frac{xk_BT}{Z}$) get:

$$\sigma_{\alpha\alpha} = e^2\int_{-\infty}^{+\infty} dx \frac{\Phi\big(\tilde{\mu}+\frac{xk_BT}{Z}\big)}{4cosh^2\big(\frac{x}{2}\big)\big[1+\big(\frac{x}{\pi}\big)^2\big]}, \tag{E.7}$$

where:

$$\Phi(\epsilon) = \frac{\hbar}{V\gamma}\sum_{\mathbf{k}n}\delta(\epsilon-\epsilon_{\mathbf{k}n})\sum_{n'} v_\alpha^{nn'}(\mathbf{k})v_\alpha^{n'n}(\mathbf{k}) \tag{E.8}$$

is the transport distribution function, originally defined in Eq.6.5 of the main text. We further expand the transport function around $\tilde{\mu}$ and obtain:

$$\sigma_{\alpha\alpha} \simeq e^2\int_{-\infty}^{+\infty} dx \frac{1}{4cosh^2(\frac{x}{2})} \frac{\Phi(\tilde{\mu}) + \frac{xk_BT}{Z}\frac{d\Phi(\tilde{\mu})}{d\tilde{\mu}} + \frac{1}{2}\big(\frac{xk_BT}{Z}\big)^2\frac{d^2\Phi(\tilde{\mu})}{d^2\tilde{\mu}}}{\big[1+(\frac{x}{\pi})^2\big]}, \tag{E.9}$$

which for the conductivity at low-T reduces to:

$$\sigma_{\alpha\alpha} = e^2E_0\Phi(\tilde{\mu}), \tag{E.10}$$

where:

$$E_0 = \int_{-\infty}^{\infty} dx \frac{1}{4cosh^2(\frac{x}{2})[1+(\frac{x}{\pi})^2]} \tag{E.11}$$

can be solved numerically and we get $E_0 \simeq 0.822467$.

Appendix F

Details of new method for transport calculations with ED in DMFT

F.1 Self-energy extrapolation on the real axis

In section 6.3.2 of the main text we presented a new method for calculating the resistivity from the real axis self-energy using ED as the DMFT impurity solver (with a $\beta_{grid} \neq \beta$). We showed that after the resistivity is calculated using Eq.6.4 as a function of the broadening parameter δ_{0^+} an extrapolation is performed and the value of ρ on the real axis is evaluated. Within the same spirit one can alternatively calculate the real axis self-energy at different δ_{0^+}, extrapolate it to $\delta_{0^+} = 0$ and then evaluate the resistivity through Eq.6.4 using $\Sigma(\omega)\Big|_{\delta_{0^+}=0}$. This method is in principle advantageous because it can also give access to other transport properties like optical conductivity.

In Fig.F.1 we plot for $U = 4$ and for three dopings ($\delta = 0.30, \delta = 0.20$ and $\delta = 0.10$) NRG and ED results using $\beta_{grid} = 10\beta$. The agreement between the methods is very good, similar to the one obtained within the first approach in Fig.6.6 of the main text. This second technique is computationally more expensive so for the resistivity calculations in the main text we implement the first approach. However, since the study of transport properties is part of our on-going work, this method is under further investigation.

F.2 Resistivity calculated using a fixed $\beta_{grid} > \beta$

In Fig.F.2 we compare for $\delta = 0.20$ the resistivity calculated using $\beta_{grid} = 10\beta$ and $\beta_{grid} = 100$. The results for the two β_{grid} are very similar, especially for small and intermediate values of T. At the right panel of Fig.F.2 only the small temperature region of the left panel is shown. We should note that in the case of $\beta_{grid} = 100$, for $\beta > 100$

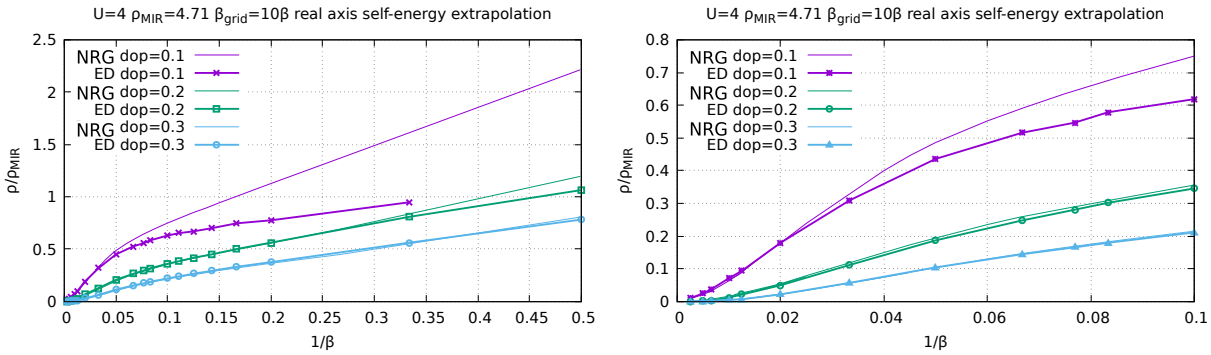

(A) (B)

FIGURE F.1: Resistivity as a function of temperature using NRG and ED for three dopings. The ED data are calculated by extrapolating the real axis self-energy vs δ_{0^+} to $\delta_{0^+} = 0$ and then calculating the resistivity using the extrapolated value of the self-energy. In the right panel we show once again the same plot limited in the temperature range of our interest.

we use $\beta_{grid} = \beta$. We hence deduce that at the very small temperatures of the Fermi liquid regime, $\beta_{grid} = \beta$ is enough to capture the system's behavior.

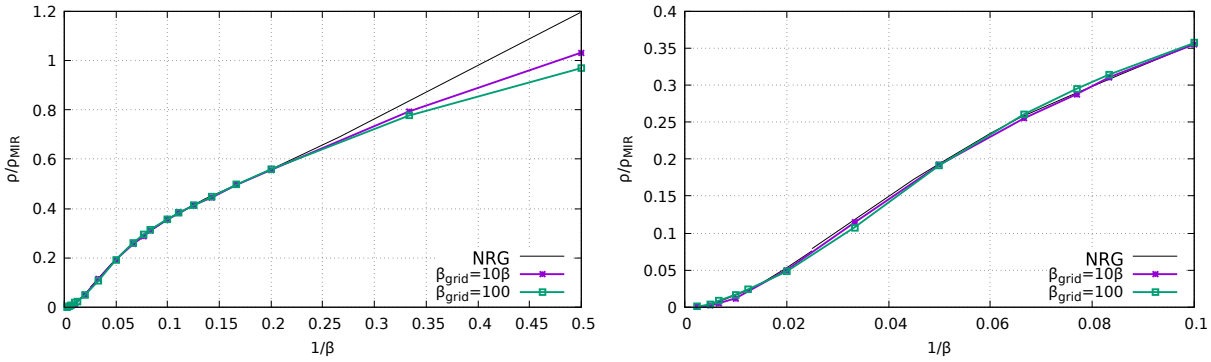

(A) (B)

FIGURE F.2: Resistivity as a function of temperature using NRG and ED for $\delta = 0.20$, for the cases $\beta_{grid} = 10\beta$ and $\beta_{grid} = 100$ (lowcutoff$= \pi/\beta_{grid}$ and uppercutoff$= 1$). In the right panel we plot the same curves for a smaller region of temperatures, in order to verify the agreement at the Fermi liquid regime.

F.3 Effect of technical parameters involved in the resistivity extrapolation

In Fig.6.8 of the main text we showed the comparison between NRG and ED calculations, including for the latter error bars produced by studying the different choices of

polynomial fit. In this part we show results for certain examples of such choices, in order to illustrate that the picture remains qualitatively the same among them.

In Fig.F.3 $\rho(T)$ is shown calculated using different extrapolation schemes for $\delta = 0.20$. We show the results of polynomial order and upper cutoff which produced the most different curves from the NRG ones. We confirm that the trends observed are qualitatively unchanged and the only effect the different schemes have is to relocate the whole curve monotonously higher or lower in the plane.

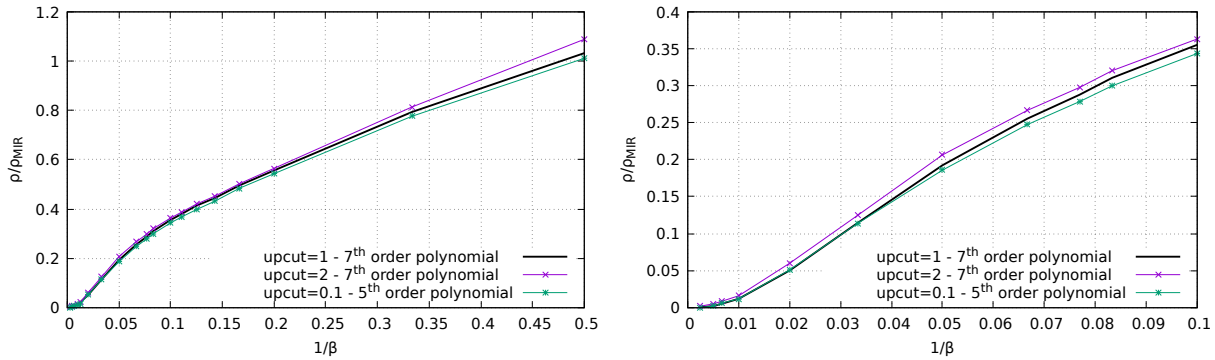

(A) (B)

FIGURE F.3: Resistivity as a function of temperature using ED for $\delta = 0.20$ and for $\beta_{grid} = 10\beta$, plotted for different choices of polynomial order and upper limit in the δ_{0^+} range for the extrapolation. In the right panel we see the same plot only in the region of temperatures relevant for studies of real materials.

Bibliography

[1] Luca de'Medici. Hund's metals explained. *The Physics of Correlated Insulators, Metals, and Superconductors, Forschungszentrum Julich*, 2017.

[2] Luca de'Medici. Hund's induced fermi-liquid instabilities and enhanced quasiparticle interactions. *Physical review letters*, 118(16):167003, 2017. doi:10.1103/PhysRevLett.118.167003.

[3] Maria Chatzieleftheriou, Maja Berović, Pablo Villar Arribi, Massimo Capone, and Luca de'Medici. Enhancement of charge instabilities in Hund's metals by breaking of rotational symmetry. *Physical Review B*, 102(20):205127, 2020. doi:10.1103/PhysRevB.102.205127.

[4] Antoine Georges, Gabriel Kotliar, Werner Krauth, and Marcelo J Rozenberg. Dynamical mean-field theory of strongly correlated fermion systems and the limit of infinite dimensions. *Reviews of Modern Physics*, 68(1):13, 1996. doi:10.1103/RevModPhys.68.13.

[5] Marcelo J Rozenberg. Integer-filling metal-insulator transitions in the degenerate Hubbard model. *Physical Review B*, 55(8):R4855, 1997. doi:10.1103/PhysRevB.55.R4855.

[6] Kensuke Inaba, Akihisa Koga, Sei-ichiro Suga, and Norio Kawakami. Condensed matter: Electronic structure, electrical, magnetic and optical properties-phase diagram of orbital-selective Mott transitions at finite temperatures. *Journal of the Physical Society of Japan*, 74(9):2393–2396, 2005.

[7] Xiaoyu Deng, Jernej Mravlje, Michel Ferrero, Gabriel Kotliar, Antoine Georges, et al. How bad metals turn good: Spectroscopic signatures of resilient quasiparticles. *Physical review letters*, 110(8):086401, 2013. doi:10.1103/PhysRevLett.110.086401.

[8] N. W. Ashcroft and N. D. Mermin. *Solid state physics*, volume 2005. Holt, Rinehart and Winston, 1976.

[9] Masatoshi Imada, Atsushi Fujimori, and Yoshinori Tokura. Metal-insulator transitions. *Rev. Mod. Phys.*, 70:1039–1263, Oct 1998. doi:10.1103/RevModPhys.70.1039.

[10] N. F. Mott. The basis of the electron theory of metals, with special reference to the transition metals. *Proceedings of the Physical Society, Section A*, 62(7):416, 1949.

[11] LD Landau. Kinetic equation approach. *Sov. Phys. JETP*, 3:920, 1957.

[12] LD Landau. On the theory of the fermi liquid. *Sov. Phys. JETP*, 8(1):70, 1959.

[13] P. Nozieres. *Theory of interacting Fermi systems*. Westview Press, 1997.

[14] Henrik Bruus and Karsten Flensberg. *Many-body quantum theory in condensed matter physics: an introduction*. Oxford university press, 2004.

[15] Heike Kamerlingh Onnes. *Through measurement to knowledge: The selected papers of Heike Kamerlingh Onnes 1853–1926*, volume 124. Springer Science & Business Media, 2012.

[16] John Bardeen, Leon N Cooper, and John Robert Schrieffer. Theory of superconductivity. *Physical review*, 108(5):1175, 1957. doi:10.1103/PhysRev.108.1175.

[17] Vitaly L Ginzburg and Lev D Landau. On the theory of superconductivity. In *On Superconductivity and Superfluidity*, pages 113–137. Springer, 2009.

[18] J. George Bednorz and K. Alex Müller. Possible high T_c superconductivity in the Ba-La-Cu-O system. *Zeitschrift für Physik B Condensed Matter*, 64(2):189–193, 1986.

[19] Maw-Kuen Wu, Jo R Ashburn, ClJ Torng, Ph H Hor, Rl L Meng, Lo Gao, Z Jo Huang, YQ Wang, and aCW Chu. Superconductivity at 93 K in a new mixed-phase Y-Ba-Cu-O compound system at ambient pressure. *Physical review letters*, 58(9):908, 1987. doi:10.1103/PhysRevLett.58.908.

[20] Hiroshi Maeda, Yoshiaki Tanaka, Masao Fukutomi, and Toshihisa Asano. A new high-T_c oxide superconductor without a rare earth element. *Japanese Journal of Applied Physics*, 27(2A):L209, 1988. doi:10.1143/jjap.27.l209.

[21] ZZ Sheng and AM Hermann. Bulk superconductivity at 120 K in the Tl–Ca/Ba–Cu–O system. *Nature*, 332(6160):138–139, 1988. doi:10.1038/332138a0.

[22] MA Subramanian, CC Torardi, JC Calabrese, J Gopalakrishnan, KJ Morrissey, TR Askew, RB Flippen, U Chowdhry, and AW Sleight. A new high-temperature superconductor: Bi_2Sr_{3-x} $Ca_xCu_2O_{8+y}$. *Science*, 239(4843):1015–1017, 1988. doi:https://science.sciencemag.org/content/239/4843/1015.

[23] Yoichi Kamihara, Hidenori Hiramatsu, Masahiro Hirano, Ryuto Kawamura, Hiroshi Yanagi, Toshio Kamiya, and Hideo Hosono. Iron-based layered superconductor: LaOFeP. *Journal of the American Chemical Society*, 128(31):10012–10013, 2006. doi:https://doi.org/10.1021/ja063355c.

[24] Yoichi Kamihara, Takumi Watanabe, Masahiro Hirano, and Hideo Hosono. Iron-based layered superconductor La[$O_{1-x}F_x$] FeAs (x= 0.05- 0.12) with T_c= 26 K. *Journal of the American Chemical Society*, 130(11):3296–3297, 2008. doi:https://doi.org/10.1021/ja800073m.

[25] Jian-Feng Ge, Zhi-Long Liu, Canhua Liu, Chun-Lei Gao, Dong Qian, Qi-Kun Xue, Ying Liu, and Jin-Feng Jia. Superconductivity above 100 K in single-layer fese films on doped $SrTiO_3$. *Nature materials*, 14(3):285–289, 2015. doi:10.1038/nmat4153.

[26] Elliot Snider, Nathan Dasenbrock-Gammon, Raymond McBride, Mathew Debessai, Hiranya Vindana, Kevin Vencatasamy, Keith V Lawler, Ashkan Salamat, and Ranga P Dias. Room-temperature superconductivity in a carbonaceous sulfur hydride. *Nature*, 586(7829):373–377, 2020. doi:10.1038/s41586-020-2801-z.

[27] Pia Jensen Ray. Figure 2.4 in master's thesis," structural investigation of $La_{(2-x)}Sr_{(x)}CuO_{(4+y)}$-following staging as a function of temperature". *Niels Bohr Institute, Faculty of Science, University of Copenhagen. Copenhagen, Denmark*, 2015.

[28] Pablo Villar Arribi. *Heavy fermions and Hund's metals in iron-based superconductors*. PhD thesis, Université Grenoble Alpes, 2018.

[29] DN Basov and Andrey V Chubukov. Manifesto for a higher t_c. *Nature Physics*, 7(4):272–276, 2011. doi:10.1038/nphys1975.

[30] Gabriele Sclauzero, Krzysztof Dymkowski, and Claude Ederer. Tuning the metal-insulator transition in d^1 and d^2 perovskites by epitaxial strain: A first-principles-based study. *Physical Review B*, 94(24):245109, 2016. doi:10.1103/PhysRevB.94.245109.

[31] Antoine Georges, Luca de' Medici, and Jernej Mravlje. Strong correlations from hund's coupling. *Annu. Rev. Condens. Matter Phys.*, 4(1):137–178, 2013. doi:10.1146/annurev-conmatphys-020911-125045.

[32] KHL Zhang, Yingge Du, PV Sushko, Mark E Bowden, V Shutthanandan, Liang Qiao, GX Cao, Zheng Gai, Shawn Sallis, LFJ Piper, et al. Electronic and magnetic properties of epitaxial perovskite $SrCrO_3$ (0 0 1). *Journal of Physics: Condensed Matter*, 27(24):245605, 2015. doi:10.1088/0953-8984/27/24/245605.

[33] BL Chamberland. Preparation and properties of $SrCrO_3$. *Solid State Communications*, 5(8):663–666, 1967. doi:10.1016/0038-1098(67)90088-9.

[34] J-S Zhou, C-Q Jin, Y-W Long, L-X Yang, and JB Goodenough. Anomalous electronic state in $CaCrO_3$ and $SrCrO_3$. *Physical review letters*, 96(4):046408, 2006. doi:10.1103/PhysRevLett.96.046408.

[35] Yifan Ding, Lipeng Cao, Weipeng Wang, Boyu Jing, Xi Shen, Yuan Yao, Lifang Xu, Junjie Li, Changqing Jin, and Richeng Yu. Bond length fluctuation in perovskite chromate $SrCrO_3$. *Journal of Applied Physics*, 127(7):075106, 2020. doi:10.1063/1.5131406.

[36] Angel M Arévalo-López, Elizabeth Castillo-Martinez, and Miguel A Alario-Franco. Electron energy loss spectroscopy in $ACrO_3$ (A= Ca, Sr and Pb) perovskites. *Journal of Physics: Condensed Matter*, 20(50):505207, 2008. doi:10.1088/0953-8984/20/50/505207.

[37] Youwen Long, Liuxiang Yang, Yuxi Lv, Qingqing Liu, Changqing Jin, Jianshi Zhou, and John B Goodenough. Crossover from itinerant-electron to localized-electron behavior in $Sr_{1-x}Ca_xCrO_3$ perovskite solid solution. *Journal of Physics: Condensed Matter*, 23(35):355601, 2011. doi:10.1088/0953-8984/23/35/355601.

[38] KHL Zhang, PV Sushko, R Colby, Yingge Du, Mark E Bowden, and Scott A Chambers. Reversible nano-structuring of $SrCrO_3$-δ through oxidation and reduction at low temperature. *Nature communications*, 5(1):1–7, 2014. doi:10.1038/ncomms5669.

[39] AJ Williams, A Gillies, JP Attfield, G Heymann, H Huppertz, MJ Martinez-Lope, and JA Alonso. Charge transfer and antiferromagnetic insulator phase in $SrRu_{1-x}Cr_xO_3$ perovskites: solid solutions between two itinerant electron oxides. *Physical Review B*, 73(10):104409, 2006. doi:10.1103/PhysRevB.73.104409.

[40] K-W Lee and WE Pickett. Orbital-ordering driven structural distortion in metallic $SrCrO_3$. *Physical Review B*, 80(12):125133, 2009. doi:10.1103/PhysRevB.80.125133.

[41] Luis Ortega-San-Martin, Anthony J Williams, Jennifer Rodgers, J Paul Attfield, Gunter Heymann, and Hubert Huppertz. Microstrain sensitivity of orbital and electronic phase separation in $SrCrO_3$. *Physical review letters*, 99(25):255701, 2007. doi:10.1103/PhysRevLett.99.255701.

[42] Yumin Qian, Guangtao Wang, Zhi Li, CQ Jin, and Zhong Fang. The electronic structure of a weakly correlated antiferromagnetic metal, $SrCrO_3$: first-principles

calculations. *New Journal of Physics*, 13(5):053002, 2011. doi:10.1088/1367-2630/13/5/053002.

[43] G Herranz, F Sánchez, J Fontcuberta, Vladimir Laukhin, J Galibert, MV García-Cuenca, C Ferrater, and M Varela. Magnetic field effect on quantum corrections to the low-temperature conductivity in metallic perovskite oxides. *Physical Review B*, 72(1):014457, 2005. doi:10.1103/PhysRevB.72.014457.

[44] Yan Xu, Jincang Zhang, Guixin Cao, Chao Jing, and Shixun Cao. Low-temperature resistivity minimum and weak spin disorder of polycrystalline $La_{2/3}Ca_{1/3}MnO_3$ in a magnetic field. *Physical Review B*, 73(22):224410, 2006. doi:10.1103/PhysRevB.73.224410.

[45] YC Lan, XL Chen, and M He. Structure, magnetic susceptibility and resistivity properties of $SrVO_3$. *Journal of alloys and compounds*, 354(1-2):95–98, 2003. doi:10.1016/S0925-8388(02)01349-X.

[46] IH Inoue, O Goto, H Makino, NE Hussey, and M Ishikawa. Bandwidth control in a perovskite-type 3d correlated metal $Ca_{1-x}Sr_xVO_3$. evolution of the electronic properties and effective mass. *Physical Review B*, 58(8):4372, 1998. doi:10.1103/PhysRevB.58.4372.

[47] MJ Rey, Ph Dehaudt, JC Joubert, B Lambert-Andron, M Cyrot, and F Cyrot-Lackmann. Preparation and structure of the compounds $SrVO_3$ and Sr_2VO_4. *Journal of Solid State Chemistry*, 86(1):101–108, 1990. doi:10.1016/0022-4596(90)90119-I.

[48] M Itoh, M Shikano, H Kawaji, and T Nakamura. Structural aspects on the variations of electric and magnetic properties of the layered compound system $Sr_{n+1}V_nO_{3n+1}$- δ (n= 1, 2, 3,∞). *Solid state communications*, 80(8):545–548, 1991. doi:10.1016/0038-1098(91)90147-N.

[49] Ayumi Nozaki, Hiroshi Yoshikawa, Takahiro Wada, H Yamauchi, and Shoji Tanaka. Layered perovskite compounds $Sr_{n+1}V_nO_{3n+1}$ (n= 1, 2, 3, and ∞). *Physical Review B*, 43(1):181, 1991. doi:10.1103/PhysRevB.43.181.

[50] BL Chamberland and PS Danielson. Alkaline-earth vanadium (IV) oxides having the AVO_3 composition. *Journal of solid state chemistry*, 3(2):243–247, 1971. doi:10.1016/0022-4596(71)90035-1.

[51] Masashige Onoda, Hiroshi Ohta, and Hiroshi Nagasawa. Metallic properties of perovskite oxide $SrVO_3$. *Solid state communications*, 79(4):281–285, 1991. doi:10.1016/0038-1098(91)90546-8.

[52] John Hubbard. Electron correlations in narrow energy bands. *Proceedings of the Royal Society of London. Series A. Mathematical and Physical Sciences*, 276(1365):238–257, 1963. doi:10.1098/rspa.1963.0204.

[53] Martin C Gutzwiller. Effect of correlation on the ferromagnetism of transition metals. *Physical Review Letters*, 10(5):159, 1963. doi:10.1103/PhysRevLett.10.159.

[54] Junjiro Kanamori. Electron correlation and ferromagnetism of transition metals. *Progress of Theoretical Physics*, 30(3):275–289, 1963. doi:10.1143/PTP.30.275.

[55] Gregory H Wannier. The structure of electronic excitation levels in insulating crystals. *Physical Review*, 52(3):191, 1937. doi:10.1103/PhysRev.52.191.

[56] Nicola Marzari, Arash A Mostofi, Jonathan R Yates, Ivo Souza, and David Vanderbilt. Maximally localized wannier functions: Theory and applications. *Reviews of Modern Physics*, 84(4):1419, 2012. doi:10.1103/RevModPhys.84.1419.

[57] Luca de'Medici and Massimo Capone. Modeling many-body physics with slave-spin mean-field: Mott and Hund's physics in fe-superconductors. In *The Iron Pnictide Superconductors*, pages 115–185. Springer, 2017. doi:10.1007/978-3-319-56117-2_4.

[58] Serge Florens and Antoine Georges. Quantum impurity solvers using a slave rotor representation. *Physical Review B*, 66(16):165111, 2002. doi:10.1103/PhysRevB.66.165111.

[59] Serge Florens and Antoine Georges. Slave-rotor mean-field theories of strongly correlated systems and the mott transition in finite dimensions. *Physical Review B*, 70(3):035114, 2004. doi:10.1103/PhysRevB.70.035114.

[60] Gabriel Kotliar and Andrei E Ruckenstein. New functional integral approach to strongly correlated fermi systems: The gutzwiller approximation as a saddle point. *Physical review letters*, 57(11):1362, 1986. doi:10.1103/PhysRevLett.57.1362.

[61] Luca de'Medici, Antoine Georges, and Silke Biermann. Orbital-selective Mott transition in multiband systems: Slave-spin representation and dynamical mean-field theory. *Physical Review B*, 72(20):205124, 2005. doi:10.1103/PhysRevB.72.205124.

[62] Andreas Rüegg, Sebastian D Huber, and Manfred Sigrist. Z2-slave-spin theory for strongly correlated fermions. *Physical Review B*, 81(15):155118, 2010. doi:10.1103/PhysRevB.81.155118.

[63] Alexandru B Georgescu and Sohrab Ismail-Beigi. Generalized slave-particle method for extended hubbard models. *Physical Review B*, 92(23):235117, 2015. doi:10.1103/PhysRevB.92.235117.

[64] SR Hassan and L De'Medici. Slave spins away from half filling: Cluster mean-field theory of the Hubbard and extended Hubbard models. *Physical Review B*, 81(3):035106, 2010. doi:10.1103/PhysRevB.81.035106.

[65] Rong Yu and Qimiao Si. U (1) slave-spin theory and its application to mott transition in a multiorbital model for iron pnictides. *Physical Review B*, 86(8):085104, 2012. doi:10.1103/PhysRevB.86.085104.

[66] José María Pizarro Blanco. Electronic correlations in multiorbital systems. 2019. doi:arXiv:1912.04141.

[67] Jun John Sakurai and Eugene D Commins. Modern quantum mechanics, revised edition. 1995.

[68] Lev Davidovich Landau and Evgenii Mikhailovich Lifshitz. *Quantum mechanics: non-relativistic theory*, volume 3. Elsevier, 2013.

[69] Antoine Georges and Gabriel Kotliar. Hubbard model in infinite dimensions. *Physical Review B*, 45(12):6479, 1992. doi:10.1103/PhysRevB.45.6479.

[70] Walter Metzner and Dieter Vollhardt. Correlated lattice fermions in d=infinite dimensions. *Physical review letters*, 62(3):324, 1989. doi:10.1103/PhysRevLett.62.324.

[71] M Jarrell. Hubbard model in infinite dimensions: A quantum Monte Carlo study. *Physical review letters*, 69(1):168, 1992. doi:10.1103/PhysRevLett.69.168.

[72] Gabriel Kotliar and Dieter Vollhardt. Strongly correlated materials: Insights from dynamical mean-field theory. *Physics today*, 57(3):53–60, 2004. doi:10.1063/1.1712502.

[73] Antoine Georges. Dynamical mean-field theory: materials from an atomic viewpoint beyond the Landau paradigm. *DMFT at*, 25, 2014.

[74] Emanuel Gull, Andrew J Millis, Alexander I Lichtenstein, Alexey N Rubtsov, Matthias Troyer, and Philipp Werner. Continuous-time Monte Carlo methods for quantum impurity models. *Reviews of Modern Physics*, 83(2):349, 2011. doi:10.1103/RevModPhys.83.349.

[75] Alexey N Rubtsov, Vladimir V Savkin, and Alexander I Lichtenstein. Continuous-time quantum Monte Carlo method for fermions. *Physical Review B*, 72(3):035122, 2005. doi:10.1103/PhysRevB.72.035122.

[76] Philipp Werner, Armin Comanac, Luca De'Medici, Matthias Troyer, and Andrew J Millis. Continuous-time solver for quantum impurity models. *Physical Review Letters*, 97(7):076405, 2006. doi:10.1103/PhysRevLett.97.076405.

[77] Emanuel Gull, Philipp Werner, Olivier Parcollet, and Matthias Troyer. Continuous-time auxiliary-field Monte Carlo for quantum impurity models. *EPL (Europhysics Letters)*, 82(5):57003, 2008. doi:10.1209/0295-5075/82/57003.

[78] Markus Wallerberger, Andreas Hausoel, Patrik Gunacker, Alexander Kowalski, Nicolaus Parragh, Florian Goth, Karsten Held, and Giorgio Sangiovanni. w2dynamics: Local one-and two-particle quantities from dynamical mean field theory. *Computer Physics Communications*, 235:388–399, 2019. doi:10.1016/j.cpc.2018.09.007.

[79] Michel Caffarel and Werner Krauth. Exact diagonalization approach to correlated fermions in infinite dimensions: Mott transition and superconductivity. *Physical review letters*, 72(10):1545, 1994. doi:10.1103/PhysRevLett.72.1545.

[80] Qimiao Si, MJ Rozenberg, G Kotliar, and AE Ruckenstein. Correlation induced insulator to metal transitions. *Physical review letters*, 72(17):2761, 1994. doi:10.1103/PhysRevLett.72.2761.

[81] Marcelo J. Rozenberg, Goetz Moeller, and Gabriel Kotliar. The Metal-Insulator Transition in the Hubbard Model at Zero Temperature II. *Modern Physics Letters B*, 8(8-09):535–543, jan 1994. arXiv:cond-mat/9402056, doi:10.1142/S0217984994000571.

[82] MJ Rozenberg, XY Zhang, and G Kotliar. Mott-Hubbard transition in infinite dimensions. *Physical review letters*, 69(8):1236, 1992. doi:10.1103/PhysRevLett.69.1236.

[83] Nagamalleswararao Dasari, Wasim Raja Mondal, Peng Zhang, Juana Moreno, Mark Jarrell, and NS Vidhyadhiraja. A multi-orbital iterated perturbation theory for model hamiltonians and real material-specific calculations of correlated systems. *The European Physical Journal B*, 89(9):1–19, 2016. doi:10.1140/epjb/e2016-70133-4.

[84] Ralf Bulla, Theo A Costi, and Thomas Pruschke. Numerical renormalization group method for quantum impurity systems. *Reviews of Modern Physics*, 80(2):395, 2008. doi:10.1103/RevModPhys.80.395.

[85] Ralf Bulla. Zero temperature metal-insulator transition in the infinite-dimensional Hubbard model. *Physical review letters*, 83(1):136, 1999. doi:10.1103/PhysRevLett.83.136.

[86] Thomas Pruschke et al. Energy resolution and discretization artifacts in the numerical renormalization group. *Physical Review B*, 79(8):085106, 2009. doi:10.1103/PhysRevB.79.085106.

[87] Daniel J García, Karen Hallberg, and Marcelo J Rozenberg. Dynamical mean field theory with the density matrix renormalization group. *Physical review letters*, 93(24):246403, 2004. doi:10.1103/PhysRevLett.93.246403.

[88] Daniel Bauernfeind, Manuel Zingl, Robert Triebl, Markus Aichhorn, and Hans Gerd Evertz. Fork tensor-product states: efficient multiorbital real-time DMFT solver. *Physical Review X*, 7(3):031013, 2017. doi:10.1103/PhysRevX.7.031013.

[89] Cornelius Lanczos. *An iteration method for the solution of the eigenvalue problem of linear differential and integral operators*. United States Governm. Press Office Los Angeles, CA, 1950.

[90] Eva Pavarini, Erik Koch, Dieter Vollhardt, and Alexander Lichtenstein. The LDA+DMFT approach to strongly correlated materials. *Reihe Modeling and Simulation*, 1:2–13, 2011.

[91] ZP Yin, Kristjan Haule, and Gabriel Kotliar. Kinetic frustration and the nature of the magnetic and paramagnetic states in iron pnictides and iron chalcogenides. *Nature materials*, 10(12):932–935, 2011. doi:10.1038/nmat3120.

[92] Philipp Werner, Emanuel Gull, Matthias Troyer, and Andrew J Millis. Spin freezing transition and non-Fermi-liquid self-energy in a three-orbital model. *Physical Review Letters*, 101(16):166405, 2008. doi:10.1103/PhysRevLett.101.16640.

[93] Ansgar Liebsch and Hiroshi Ishida. Correlation-induced spin freezing transition in FeSe: A dynamical mean field study. *Physical Review B*, 82(15):155106, 2010. doi:10.1103/PhysRevB.82.155106.

[94] Laura Fanfarillo and Elena Bascones. Electronic correlations in Hund metals. *Physical Review B*, 92(7):075136, 2015. doi:10.1103/PhysRevB.92.075136.

[95] Katharina M Stadler, Gabriel Kotliar, Andreas Weichselbaum, and Jan von Delft. Hundness versus Mottness in a three-band Hubbard-Hund model: on the origin of strong correlations in Hund metals. *Annals of Physics*, 405:365–409, 2019. doi:10.1016/j.aop.2018.10.017.

[96] Cyrus F. Hirjibehedin. The makings of a hund's metal. *Nature Nanotechnology*, 10(11):914–915, 2015. doi:10.1038/nnano.2015.225.

[97] Aldo Isidori, Maja Berović, Laura Fanfarillo, Luca de' Medici, Michele Fabrizio, and Massimo Capone. Charge disproportionation, mixed valence, and janus effect in multiorbital systems: A tale of two insulators. *Phys. Rev. Lett.*, 122:186401, May 2019. doi:10.1103/PhysRevLett.122.186401.

[98] Manuel Zingl, Jernej Mravlje, Markus Aichhorn, Olivier Parcollet, and Antoine Georges. Hall coefficient signals orbital differentiation in the hund's metal sr2ruo4. *npj Quantum Materials*, 4(1):35, 2019. doi:10.1038/s41535-019-0175-y.

[99] Fabian B. Kugler, Seung-Sup B. Lee, Andreas Weichselbaum, Gabriel Kotliar, and Jan von Delft. Orbital differentiation in hund metals. *Phys. Rev. B*, 100:115159, Sep 2019. doi:10.1103/PhysRevB.100.115159.

[100] Fabian B. Kugler, Manuel Zingl, Hugo U. R. Strand, Seung-Sup B. Lee, Jan von Delft, and Antoine Georges. Strongly correlated materials from a numerical renormalization group perspective: How the fermi-liquid state of sr_2ruo_4 emerges. *Phys. Rev. Lett.*, 124:016401, Jan 2020. doi:10.1103/PhysRevLett.124.016401.

[101] F. C. Hoyt. Review: Linienspektren und periodisches system der elemente, by Friedrich Hund. *Astrophysical Journal*, 65:321, 1927.

[102] Jernej Mravlje, Markus Aichhorn, Takashi Miyake, Kristjan Haule, Gabriel Kotliar, and Antoine Georges. Coherence-incoherence crossover and the mass-renormalization puzzles in Sr_2RuO_4. *Physical review letters*, 106(9):096401, 2011. doi:10.1103/PhysRevLett.106.096401.

[103] Takeshi Kondo, M Ochi, M Nakayama, H Taniguchi, S Akebi, K Kuroda, M Arita, S Sakai, H Namatame, M Taniguchi, et al. Orbital-dependent band narrowing revealed in an extremely correlated Hund's metal emerging on the topmost layer of Sr_2RuO_4. *Physical review letters*, 117(24):247001, 2016. doi:10.1103/PhysRevLett.117.247001.

[104] M Yi, DH Lu, JG Analytis, J-H Chu, S-K Mo, R-H He, RG Moore, XJ Zhou, GF Chen, JL Luo, et al. Electronic structure of the $BaFe_2As_2$ family of iron-pnictide superconductors. *Physical Review B*, 80(2):024515, 2009. doi:10.1103/PhysRevB.80.024515.

[105] F Hardy, P Burger, T Wolf, RA Fisher, P Schweiss, P Adelmann, R Heid, R Fromknecht, R Eder, D Ernst, et al. Doping evolution of superconducting gaps and electronic densities of states in $Ba(Fe_{1-x}Co_x)$ $2As_2$ iron pnictides. *EPL (Europhysics Letters)*, 91(4):47008, 2010. doi:10.1209/0295-5075/91/47008.

[106] P Popovich, AV Boris, OV Dolgov, Alexandre Avraamovitch Golubov, DL Sun, CT Lin, RK Kremer, and B Keimer. Specific heat measurements of $Ba_{0.68}K_{0.32}Fe_2As_2$ single crystals: evidence for a multiband strong-coupling superconducting state. *Physical review letters*, 105(2):027003, 2010. doi:10.1103/PhysRevLett.105.027003.

[107] Taichi Terashima, Motoi Kimata, Nobuyuki Kurita, Hidetaka Satsukawa, Atsushi Harada, Kaori Hazama, Motoharu Imai, Akira Sato, Kunihiro Kihou, Chul-Ho Lee, et al. Fermi surface and mass enhancement in KFe_2As_2 from de Haas-van Alphen effect measurements. *Journal of the Physical Society of Japan*, 79(5):053702, 2010. doi:10.1143/JPSJ.79.053702.

[108] Leonardo Degiorgi. Electronic correlations in iron-pnictide superconductors and beyond: lessons learned from optics. *New Journal of Physics*, 13(2):023011, 2011. doi:10.1088/1367-2630/13/2/023011.

[109] H Ding, K Nakayama, P Richard, S Souma, T Sato, T Takahashi, M Neupane, YM Xu, ZH Pan, AV Fedorov, et al. Electronic structure of optimally doped pnictide $Ba_{0.6}K_{0.4}Fe_2As_2$: a comprehensive angle-resolved photoemission spectroscopy investigation. *Journal of Physics: Condensed Matter*, 23(13):135701, 2011. doi:10.1088/0953-8984/23/13/135701.

[110] S Lafuerza, H Gretarsson, F Hardy, T Wolf, C Meingast, G Giovannetti, M Capone, AS Sefat, Y-J Kim, P Glatzel, et al. Evidence of Mott physics in iron pnictides from x-ray spectroscopy. *Physical Review B*, 96(4):045133, 2017. doi:10.1103/PhysRevB.96.045133.

[111] F Hardy, AE Böhmer, Luca de'Medici, Massimo Capone, G Giovannetti, R Eder, L Wang, M He, T Wolf, P Schweiss, et al. Strong correlations, strong coupling, and s-wave superconductivity in hole-doped $BaFe_2As_2$ single crystals. *Physical Review B*, 94(20):205113, 2016. doi:10.1103/PhysRevB.94.205113.

[112] Hlynur Gretarsson, Andreea Lupascu, Jungho Kim, D Casa, T Gog, W Wu, SR Julian, ZJ Xu, JS Wen, GD Gu, et al. Revealing the dual nature of magnetism in iron pnictides and iron chalcogenides using x-ray emission spectroscopy. *Physical Review B*, 84(10):100509, 2011. doi:10.1103/PhysRevB.84.100509.

[113] Jonathan Pelliciari, Yaobo Huang, Kenji Ishii, Chenglin Zhang, Pengcheng Dai, Gen Fu Chen, Lingyi Xing, Xiancheng Wang, Changqing Jin, Hong Ding, et al. Magnetic moment evolution and spin freezing in doped $BaFe_2As_2$. *Scientific reports*, 7(1):1–8, 2017. doi:10.1038/s41598-017-07286-6.

[114] G Li, WZ Hu, J Dong, Z Li, P Zheng, GF Chen, JL Luo, and NL Wang. Probing the superconducting energy gap from infrared spectroscopy on a $Ba_{0.6}K_{0.4}Fe_2As_2$ single crystal with T_c= 37 K. *Physical review letters*, 101(10):107004, 2008. doi:10.1103/PhysRevLett.101.107004.

[115] Gang Mu, Huiqian Luo, Zhaosheng Wang, Lei Shan, Cong Ren, and Hai-Hu Wen. Low temperature specific heat of the hole-doped $Ba_{0.6}K_{0.4}Fe_2As_2$ single crystals. *Physical Review B*, 79(17):174501, 2009. doi:10.1103/PhysRevB.79.174501.

[116] J Yang, D Hüvonen, U Nagel, T Room, N Ni, PC Canfield, SL Bud'ko, JP Carbotte, and T Timusk. Optical spectroscopy of superconducting $Ba_{0.55}K_{0.45}Fe_2As_2$: Evidence for strong coupling to low-energy bosons. *Physical review letters*, 102(18):187003, 2009. doi:10.1103/PhysRevLett.102.187003.

[117] JS Kim, EG Kim, GR Stewart, XH Chen, and XF Wang. Specific heat in KFe_2As_2 in zero and applied magnetic field. *Physical Review B*, 83(17):172502, 2011. doi:10.1103/PhysRevB.83.172502.

[118] AK Pramanik, M Abdel-Hafiez, S Aswartham, AUB Wolter, S Wurmehl, V Kataev, and B Büchner. Multigap superconductivity in single crystals of $Ba_{0.65}Na_{0.35}Fe_2As_2$: A calorimetric investigation. *Physical Review B*, 84(6):064525, 2011. doi:10.1103/PhysRevB.84.064525.

[119] V Brouet, M Fuglsang Jensen, A Nicolaou, A Taleb-Ibrahimi, P Le Fevre, F Bertran, A Forget, and D Colson. Opening of the superconducting gap in the hole pockets of $ba(fe_{1-x}co_x)_2as_2$ as seen via angle-resolved photoelectron spectroscopy. *Phys. Rev. B*, 2011. doi:10.1103/PhysRevB.85.144508.

[120] M Abdel-Hafiez, S Aswartham, S Wurmehl, V Grinenko, C Hess, S-L Drechsler, S Johnston, AUB Wolter, B Büchner, H Rosner, et al. Specific heat and upper

critical fields in KFe_2As_2 single crystals. *Physical Review B*, 85(13):134533, 2012. doi:10.1103/PhysRevB.85.134533.

[121] NL Wang, WZ Hu, ZG Chen, RH Yuan, G Li, GF Chen, and T Xiang. High energy pseudogap and its evolution with doping in Fe-based superconductors as revealed by optical spectroscopy. *Journal of Physics: Condensed Matter*, 24(29):294202, 2012. doi:10.1088/0953-8984/24/29/294202.

[122] Teppei Yoshida, Shin-ichiro Ideta, Ichiro Nishi, Atsushi Fujimori, Ming Yi, Rob Moore, Sung-Kwan Mo, Donghui Lu, Zhi-Xun Shen, Zahid Hussain, et al. Orbital character and electron correlation effects on two-and three-dimensional Fermi surfaces in KFe_2As_2 revealed by angle-resolved photoemission spectroscopy. *Frontiers in Physics*, 2:17, 2014. doi:10.3389/fphy.2014.00017.

[123] Luca de'Medici, Gianluca Giovannetti, and Massimo Capone. Selective Mott physics as a key to iron superconductors. *Physical review letters*, 112(17):177001, 2014. doi:10.1103/PhysRevLett.112.177001.

[124] AO Shorikov, MA Korotin, SV Streltsov, SL Skornyakov, Dm M Korotin, and VI Anisimov. Coulomb correlation effects in LaFeAsO: An LDA+DMFT (QMC) study. *Journal of Experimental and Theoretical Physics*, 108(1):121–125, 2009. doi:10.1134/S1063776109010154.

[125] Markus Aichhorn, Silke Biermann, Takashi Miyake, Antoine Georges, and Masatoshi Imada. Theoretical evidence for strong correlations and incoherent metallic state in FeSe. *Physical Review B*, 82(6):064504, 2010. doi:10.1103/PhysRevB.82.064504.

[126] Hiroshi Ishida and Ansgar Liebsch. Fermi-liquid, non-Fermi-liquid, and Mott phases in iron pnictides and cuprates. *Physical Review B*, 81(5):054513, 2010. doi:10.1103/PhysRevB.81.054513.

[127] Philipp Werner, Michele Casula, Takashi Miyake, Ferdi Aryasetiawan, Andrew J Millis, and Silke Biermann. Satellites and large doping and temperature dependence of electronic properties in hole-doped $BaFe_2As_2$. *Nature Physics*, 8(4):331–337, 2012. doi:10.1038/nphys2250.

[128] Takahiro Misawa, Kazuma Nakamura, and Masatoshi Imada. Ab initio evidence for strong correlation associated with Mott proximity in iron-based superconductors. *Physical review letters*, 108(17):177007, 2012. doi:10.1103/PhysRevLett.108.177007.

[129] Steffen Backes, Harald O Jeschke, and Roser Valenti. Microscopic nature of correlations in multiorbital AFe_2As_2(A= K, Rb, Cs): Hund's coupling versus Coulomb repulsion. *Physical Review B*, 92(19):195128, 2015. doi:10.1103/PhysRevB.92.195128.

[130] Elena Bascones, Belén Valenzuela, and Maria José Calderón. Magnetic interactions in iron superconductors: A review. *Comptes Rendus Physique*, 17(1-2):36–59, 2016. doi:10.1016/j.crhy.2015.05.004.

[131] Qimiao Si, Rong Yu, and Elihu Abrahams. High-temperature superconductivity in iron pnictides and chalcogenides. *Nature Reviews Materials*, 1(4):1–15, 2016. doi:10.1038/natrevmats.2016.17.

[132] Andreas Kreisel, Brian M Andersen, Peter O Sprau, Andrey Kostin, JC Séamus Davis, and PJ Hirschfeld. Orbital selective pairing and gap structures of iron-based superconductors. *Physical Review B*, 95(17):174504, 2017. doi:10.1103/PhysRevB.95.174504.

[133] Luca de'Medici. Hund's coupling and its key role in tuning multiorbital correlations. *Physical Review B*, 83(20):205112, 2011. doi:10.1103/PhysRevB.83.205112.

[134] Luca De'Medici, Jernej Mravlje, and Antoine Georges. Janus-faced influence of Hund's rule coupling in strongly correlated materials. *Physical review letters*, 107(25):256401, 2011. doi:10.1103/PhysRevLett.107.256401.

[135] Hans A Bethe. Statistical theory of superlattices. *Proceedings of the Royal Society of London. Series A-Mathematical and Physical Sciences*, 150(871):552–575, 1935.

[136] L de'Medici. Weak and strong correlations in iron pnictides. *Iron-based superconductivity, Springer Series in Materials Science*, 211:409–441, 2015.

[137] Akihisa Koga, Norio Kawakami, TM Rice, and Manfred Sigrist. Orbital-selective Mott transitions in the degenerate Hubbard model. *Physical review letters*, 92(21):216402, 2004. doi:10.1103/PhysRevLett.92.216402.

[138] M Grilli, R Raimondi, C Castellani, C Di Castro, and G Kotliar. Phase separation and superconductivity in the U=∞ limit of the extended multiband Hubbard model. *International Journal of Modern Physics B*, 5(01n02):309–321, 1991. doi:10.1142/S0217979291000195.

[139] M Grilli and C Castellani. Electron-phonon interactions in the presence of strong correlations. *Physical Review B*, 50(23):16880, 1994. doi:10.1103/PhysRevB.50.16880.

[140] Pablo Villar Arribi and Luca de'Medici. Hund-enhanced electronic compressibility in FeSe and its correlation with T_c. *Physical review letters*, 121(19):197001, 2018. doi:10.1103/PhysRevLett.121.197001.

[141] Shintaro Hoshino and Philipp Werner. Superconductivity from emerging magnetic moments. *Physical review letters*, 115(24):247001, 2015. doi:10.1103/PhysRevLett.115.247001.

[142] Martin Edelmann, Giorgio Sangiovanni, Massimo Capone, and Luca De'Medici. Chromium analogs of iron-based superconductors. *Physical Review B*, 95(20):205118, 2017. doi:10.1103/PhysRevB.95.205118.

[143] E Civardi, M Moroni, M Babij, Z Bukowski, and P Carretta. Superconductivity emerging from an electronic phase separation in the charge ordered phase of $RbFe_2As_2$. *Physical review letters*, 117(21):217001, 2016. doi:10.1103/PhysRevLett.117.217001.

[144] Pablo Villar Arribi and Luca de' Medici. Hund's metal crossover and superconductivity in the 111 family of iron-based superconductors. *arXiv preprint arXiv:2104.11018*, 2021. doi:arXiv:2104.11018.

[145] Frank Lechermann, Antoine Georges, Gabriel Kotliar, and Olivier Parcollet. Rotationally invariant slave-boson formalism and momentum dependence of the quasiparticle weight. *Physical Review B*, 76(15):155102, 2007. doi:10.1103/PhysRevB.76.155102.

[146] Maja Berovic et al. *Exploring Hund's correlated metals: charge instabilities and effect of selective interactions*. PhD thesis, SISSA, 2018.

[147] Philipp Werner and Andrew J Millis. High-spin to low-spin and orbital polarization transitions in multiorbital Mott systems. *Physical review letters*, 99(12):126405, 2007. doi:10.1103/PhysRevLett.99.126405.

[148] Luca de'Medici, Syed R Hassan, Massimo Capone, and Xi Dai. Orbital-selective Mott transition out of band degeneracy lifting. *Physical review letters*, 102(12):126401, 2009. doi:10.1103/PhysRevLett.102.126401.

[149] Jian Ping Lu. Metal-insulator transitions in degenerate Hubbard models and A_xC_60. *Physical Review B*, 49(8):5687, 1994. doi:10.1103/PhysRevB.49.5687.

[150] JE Han, M Jarrell, and DL Cox. Multiorbital Hubbard model in infinite dimensions: Quantum Monte Carlo calculation. *Physical Review B*, 58(8):R4199, 1998. doi:10.1103/PhysRevB.58.R4199.

[151] Serge Florens, Antoine Georges, Gabriel Kotliar, and Olivier Parcollet. Mott transition at large orbital degeneracy: Dynamical mean-field theory. *Physical Review B*, 66(20):205102, 2002. doi:10.1103/PhysRevB.66.205102.

[152] Olle Gunnarsson, Erik Koch, and Richard M Martin. Mott-Hubbard insulators for systems with orbital degeneracy. *Physical Review B*, 56(3):1146, 1997. doi:10.1103/PhysRevB.56.1146.

[153] John R Schrieffer and Peter A Wolff. Relation between the Anderson and Kondo hamiltonians. *Physical Review*, 149(2):491, 1966. doi:10.1103/PhysRev.149.491.

[154] B Coqblin and JR Schrieffer. Exchange interaction in alloys with cerium impurities. *Physical Review*, 185(2):847, 1969. doi:10.1103/PhysRev.185.847.

[155] Jorge I Facio, V Vildosola, Daniel Julio García, and Pablo S Cornaglia. On the nature of the Mott transition in multiorbital systems. *Physical Review B*, 95(8):085119, 2017. doi:10.1103/PhysRevB.95.085119.

[156] Kristjan Haule and Gabriel Kotliar. Coherence–incoherence crossover in the normal state of iron oxypnictides and importance of Hund's rule coupling. *New journal of physics*, 11(2):025021, 2009. doi:10.1088/1367-2630/11/2/025021.

[157] Ming Yi, ZK Liu, Yan Zhang, Rong Yu, J-X Zhu, JJ Lee, RG Moore, FT Schmitt, Wei Li, SC Riggs, et al. Observation of universal strong orbital-dependent correlation effects in iron chalcogenides. *Nature communications*, 6(1):1–7, 2015. doi:10.1038/ncomms8777.

[158] F Hardy, AE Böhmer, D Aoki, P Burger, T Wolf, P Schweiss, R Heid, P Adelmann, YX Yao, G Kotliar, et al. Evidence of strong correlations and coherence-incoherence crossover in the iron pnictide superconductor KFe_2As_2. *Physical review letters*, 111(2):027002, 2013. doi:10.1103/PhysRevLett.111.027002.

[159] Goetz Moeller, Qimiao Si, Gabriel Kotliar, Marcelo Rozenberg, and Daniel S Fisher. Critical behavior near the Mott transition in the Hubbard model. *Physical review letters*, 74(11):2082, 1995. doi:10.1103/PhysRevLett.74.2082.

[160] Y Ōno, M Potthoff, and R Bulla. Mott transitions in correlated electron systems with orbital degrees of freedom. *Physical Review B*, 67(3):035119, 2003. doi:10.1103/PhysRevB.67.035119.

[161] Th Pruschke and Ralf Bulla. Hund's coupling and the metal-insulator transition in the two-band Hubbard model. *The European Physical Journal B-Condensed Matter and Complex Systems*, 44(2):217–224, 2005. doi:10.1140/epjb/e2005-00117-4.

[162] K Hallberg, Daniel Julio García, Pablo S Cornaglia, Jorge I Facio, and Yuriel Núñez-Fernández. State-of-the-art techniques for calculating spectral functions in models for correlated materials. *EPL (Europhysics Letters)*, 112(1):17001, 2015. doi:10.1209/0295-5075/112/17001.

[163] Andrzej Klejnberg and Jozef Spałek. Simple treatment of the metal-insulator transition: Effects of degeneracy, temperature, and applied magnetic field. *Physical Review B*, 57(19):12041, 1998. doi:10.1103/PhysRevB.57.12041.

[164] Andreas Weichselbaum and Jan von Delft. Sum-rule conserving spectral functions from the numerical renormalization group. *Phys. Rev. Lett.*, 99:076402, 2007. doi:10.1103/PhysRevLett.99.076402.

[165] R Bulla, A C Hewson, and Th Pruschke. Numerical renormalization group calculations for the self-energy of the impurity anderson model. *Journal of Physics: Condensed Matter*, 10(37):8365–8380, 1998. doi:10.1088/0953-8984/10/37/021.

[166] A. Amaricci, L. Crippa, A. Scazzola, G. Mazza, L. de Medici, and M. Capone. Edipack: A parallel exact diagonalization package for quantum impurity problems. 2021. arXiv:2105.06806, doi:arXiv:2105.06806.

[167] Markus Wallerberger, Andreas Hausoel, Patrik Gunacker, Alexander Kowalski, Nicolaus Parragh, Florian Goth, Karsten Held, and Giorgio Sangiovanni. w2dynamics: Local one- and two-particle quantities from dynamical mean field theory. *Computer Physics Communications*, 235:388–399, 2019. doi:10.1016/j.cpc.2018.09.007.

[168] Daniel S Fisher, G Kotliar, and G Moeller. Midgap states in doped Mott insulators in infinite dimensions. *Physical Review B*, 52(24):17112, 1995. doi:10.1103/PhysRevB.52.17112.

[169] G Kotliar, Sahana Murthy, and MJ Rozenberg. Compressibility divergence and the finite temperature Mott transition. *Physical review letters*, 89(4):046401, 2002. doi:10.1103/PhysRevLett.89.046401.

[170] S. Sachdev. *Quantum phase transitions*. Cambridge University Press, Cambridge, second ed. edition, 2011.

[171] L. (Ed.) Carr, editor. *Understanding Quantum Phase Transitions*. CRC Press, (1st ed.) edition, 2010.

[172] P Coleman, C Pépin, Qimiao Si, and R Ramazashvili. How do fermi liquids get heavy and die? *Journal of Physics: Condensed Matter*, 13(35):R723–R738, aug 2001. doi:10.1088/0953-8984/13/35/202.

[173] Philipp Gegenwart, Qimiao Si, and Frank Steglich. Quantum criticality in heavy-fermion metals. *Nature Physics*, 4(3):186–197, 2008. doi:10.1038/nphys892.

[174] Hilbert v. Löhneysen, Achim Rosch, Matthias Vojta, and Peter Wölfle. Fermi-liquid instabilities at magnetic quantum phase transitions. *Rev. Mod. Phys.*, 79:1015–1075, Aug 2007. doi:10.1103/RevModPhys.79.1015.

[175] Alexander Sokol and David Pines. Toward a unified magnetic phase diagram of the cuprate superconductors. *Phys. Rev. Lett.*, 71:2813–2816, Oct 1993. doi:10.1103/PhysRevLett.71.2813.

[176] C. Castellani, C. Di Castro, and M. Grilli. Non-fermi-liquid behavior and d-wave superconductivity near the charge-density-wave quantum critical point. *Zeitschrift für Physik B Condensed Matter*, 103(2):137–144, 1996. doi:10.1007/s002570050347.

[177] C. M. Varma. Non-fermi-liquid states and pairing instability of a general model of copper oxide metals. *Phys. Rev. B*, 55:14554–14580, 1997. doi:10.1103/PhysRevB.55.14554.

[178] K. B. Efetov, H. Meier, and C. Pépin. Pseudogap state near a quantum critical point. *Nature Physics*, 9(7):442–446, 2013. doi:10.1038/nphys2641.

[179] B. Michon, C. Girod, S. Badoux, J. Kačmarčík, Q. Ma, M. Dragomir, H. A. Dabkowska, B. D. Gaulin, J. S. Zhou, S. Pyon, T. Takayama, H. Takagi, S. Verret, N. Doiron-Leyraud, C. Marcenat, L. Taillefer, and T. Klein. Thermodynamic signatures of quantum criticality in cuprate superconductors. *Nature*, 567(7747):218–222, 2019. doi:10.1038/s41586-019-0932-x.

[180] Martin Eckstein, Marcus Kollar, Michael Potthoff, and Dieter Vollhardt. Phase separation in the particle-hole asymmetric Hubbard model. *Physical Review B*, 75(12):125103, 2007. doi:10.1103/PhysRevB.75.125103.

[181] Jakob Steinbauer, Luca de'Medici, and Silke Biermann. Doping-driven metal-insulator transition in correlated electron systems with strong Hund's exchange coupling. *Physical Review B*, 100(8):085104, 2019. doi:10.1103/PhysRevB.100.085104.

[182] Lorenzo De Leo et al. Non-fermi liquid behavior in multi-orbital Anderson impurity models and possible relevance for strongly correlated lattice models. 2004.

[183] Katharina Maria Stadler. *A model study of strong correlations in Hund metals*. PhD thesis, lmu, 2019.

[184] Hugo UR Strand, Andro Sabashvili, Mats Granath, Bo Hellsing, and Stellan Östlund. Dynamical mean field theory phase-space extension and critical properties of the finite temperature Mott transition. *Physical Review B*, 83(20):205136, 2011. doi:10.1103/PhysRevB.83.205136.

[185] Ning-Hua Tong, Shun-Qing Shen, and Fu-Cho Pu. Mott-Hubbard transition in infinite dimensions. *Physical Review B*, 64(23):235109, 2001. doi:10.1103/PhysRevLett.69.1236.

[186] Chuck-Hou Yee and Leon Balents. Phase separation in doped mott insulators. *Phys. Rev. X*, 5:021007, Apr 2015. URL: https://link.aps.org/doi/10.1103/PhysRevX.5.021007, doi:10.1103/PhysRevX.5.021007.

[187] J. W. Negele and H. Orland. *Quantum many-particle systems*. Addison-Wesley, 1988.

[188] Lev Davidovich Landau. On the theory of phase transitions. i. *Zh. Eksp. Teor. Fiz.*, 11:19, 1937.

[189] Lev Davidovich Landau and Evgenii Mikhailovich Lifshitz. *Course of theoretical physics*. Elsevier, 2013.

[190] Riccardo Arpaia and Giacomo Ghiringhelli. Charge order at high temperature in cuprate superconductors, 2021. arXiv:2106.00731.

[191] V. J. Emery, S. A. Kivelson, and H. Q. Lin. Phase separation in the t-j model. *Phys. Rev. Lett.*, 64:475–478, Jan 1990. doi:10.1103/PhysRevLett.64.475.

[192] M. Grilli, R. Raimondi, C. Castellani, C. Di Castro, and G. Kotliar. Phase separation and superconductivity in the $u = \infty$ limit of the extended multiband hubbard model. *International Journal of Modern Physics B*, 05(01n02):309–321, 1991. doi:10.1142/S0217979291000195.

[193] Masatoshi Imada. Charge order and superconductivity as competing brothers in cuprate high-t_c superconductors, 2021. arXiv:2105.07427.

[194] M. Grilli and C. Castellani. Electron-phonon interactions in the presence of strong correlations. *Phys. Rev. B*, 50:16880–16898, Dec 1994. doi:10.1103/PhysRevB.50.16880.

[195] M. Capone, G. Sangiovanni, C. Castellani, C. Di Castro, and M. Grilli. Phase separation close to the density-driven mott transition in the hubbard-holstein model. *Phys. Rev. Lett.*, 92:106401, Mar 2004. doi:10.1103/PhysRevLett.92.106401.

[196] M. Aichhorn, E. Arrigoni, M. Potthoff, and W. Hanke. Antiferromagnetic to superconducting phase transition in the hole- and electron-doped hubbard model at zero temperature. *Phys. Rev. B*, 74:024508, Jul 2006. doi:10.1103/PhysRevB.74.024508.

[197] G. Sordi, P. Sémon, K. Haule, and A.-M. S. Tremblay. Strong coupling superconductivity, pseudogap, and mott transition. *Phys. Rev. Lett.*, 108:216401, May 2012. doi:10.1103/PhysRevLett.108.216401.

[198] G Sordi, P Sémon, Kristjan Haule, and A-MS Tremblay. Pseudogap temperature as a widom line in doped mott insulators. *Scientific reports*, 2(1):1–5, 2012. doi:10.1038/srep00547.

[199] G. Sordi, K. Haule, and A.-M. S. Tremblay. Finite doping signatures of the mott transition in the two-dimensional hubbard model. *Phys. Rev. Lett.*, 104:226402, Jun 2010. doi:10.1103/PhysRevLett.104.226402.

[200] G. Sordi, K. Haule, and A.-M. S. Tremblay. Mott physics and first-order transition between two metals in the normal-state phase diagram of the two-dimensional hubbard model. *Phys. Rev. B*, 84:075161, Aug 2011. doi:10.1103/PhysRevB.84.075161.

[201] Philipp Werner, Shintaro Hoshino, and Hiroshi Shinaoka. Spin-freezing perspective on cuprates. *Phys. Rev. B*, 94:245134, Dec 2016. doi:10.1103/PhysRevB.94.245134.

[202] Piers Coleman. *Introduction to many-body physics*. Cambridge University Press, 2015.

[203] Jan Martin Tomczak. *Propriétés spectrales et optiques des Matériaux corrélés.* PhD thesis, Ecole Polytechnique X, 2007.

[204] Jan M. Tomczak and Silke Biermann. Optical properties of correlated materials: Generalized peierls approach and its application to VO_2. *Phys. Rev. B*, 80:085117, Aug 2009. doi:10.1103/PhysRevB.80.085117.

[205] Nils Blümer. *Mott Hubbard Metal Insulator Transition and Optical Conductivity in High Dimensions*. Citeseer, 2003.

[206] VJ Emery and SA Kivelson. Superconductivity in bad metals. *Physical Review Letters*, 74(16):3253, 1995.

[207] AV Ferris-Prabhu and DH Withers. Numerical analytic continuation using Padé approximants. *Journal of Computational Physics*, 13(1):94–99, 1973. doi:10.1016/0021-9991(73)90127-7.

[208] KSD Beach, RJ Gooding, and F Marsiglio. Reliable padé analytical continuation method based on a high-accuracy symbolic computation algorithm. *Physical Review B*, 61(8):5147, 2000. doi:10.1103/PhysRevB.61.5147.

[209] Richard N Silver, Devinderjit S Sivia, and James E Gubernatis. Maximum-entropy method for analytic continuation of quantum Monte Carlo data. *Physical Review B*, 41(4):2380, 1990. doi:10.1103/PhysRevB.41.2380.

[210] JE Gubernatis, Mark Jarrell, RN Silver, and DS Sivia. Quantum Monte Carlo simulations and maximum entropy: Dynamics from imaginary-time data. *Physical Review B*, 44(12):6011, 1991. doi:10.1103/PhysRevB.44.6011.

[211] AJ Millis. Optical conductivity and correlated electron physics. *Strong interactions in low dimensions*, pages 195–235, 2004.

[212] Gunnar Pálsson and Gabriel Kotliar. Thermoelectric response near the density driven Mott transition. *Physical review letters*, 80(21):4775, 1998. doi:10.1103/PhysRevLett.80.4775.

[213] J. R. Schrieffer. The kondo effect – the link between magnetic and nonmagnetic impurities in metals. *J. Appl. Phys.*, 1967.

[214] I. Okada and K. Yosida. Singlet ground state of the localized d-electrons coupled with conduction electrons in metals. *Prog. Theor. Phys.*, 1973.

[215] K. M. Stadler, Z. P. Yin, J. von Delft, G. Kotliar, and A. Weichselbaum. Dynamical mean-field theory plus numerical renormalization-group study of spin-orbital separation in a three-band hund metal. *Phys. Rev. Lett.*, 115:136401, 2015. doi:10.1103/PhysRevLett.115.136401.

[216] John P Perdew, Kieron Burke, and Matthias Ernzerhof. Generalized gradient approximation made simple. *Physical review letters*, 77(18):3865, 1996. doi:10.1103/PhysRevLett.77.3865.

[217] Paolo Giannozzi, Oliviero Andreussi, Thomas Brumme, Oana Bunau, M Buongiorno Nardelli, Matteo Calandra, Roberto Car, Carlo Cavazzoni, Davide Ceresoli, Matteo Cococcioni, et al. Advanced capabilities for materials modelling with quantum espresso. *Journal of Physics: Condensed Matter*, 29(46):465901, 2017. doi:10.1088/1361-648x/aa8f79.

[218] Andrea Dal Corso. Pseudopotentials periodic table: From h to pu. *Computational Materials Science*, 95:337–350, 2014. doi:10.1016/j.commatsci.2014.07.043.

[219] Giovanni Pizzi, Valerio Vitale, Ryotaro Arita, Stefan Blügel, Frank Freimuth, Guillaume Géranton, Marco Gibertini, Dominik Gresch, Charles Johnson, Takashi Koretsune, et al. Wannier90 as a community code: new features and applications. *Journal of Physics: Condensed Matter*, 32(16):165902, 2020. doi:10.1088/1361-648x/ab51ff.

[220] Gunnar Palsson. *Computational studies of thermoelectricity in strongly correlated electron systems*. Rutgers The State University of New Jersey-New Brunswick, 2001.

RÉSUMÉ

Les systèmes d'électrons fortement corrélès représentent l'un des domaines de recherche les plus actifs en physique de la matière condensée, présentant des phénomènes intrigants tels que la supraconductivité non conventionnelle ou un transport anormal. Dans cette thèse, nous analysons théoriquement *les métaux* à plusieurs orbitales *de Hund*, en utilisant le champ moyen des *Spins Esclaves (SSMF)* et la *Théorie du Champ Moyen Dynamique (DMFT)*.

Nous étudions l'émergence d'une instabilité de charge vers une séparation de phase/onde de densité de charge, signalée par une compressibilité électronique divergente, dans les isolants de Mott à plusieurs orbitales dopés, en présence d'un échange intra-atomique de "Hund" fini. L'effet augmente quand la symétrie locale de spin ou orbitale est rompue, par exemple par un champ cristallin, et est compris en termes énergétiques. Les résultats sont en accord avec des études réalistes des supraconducteurs à base de fer.

Nous connectons également le premier ordre de la transition métal-isolant de Mott des métaux de Hund au démi-remplissage à la coexistence de deux solutions à dopage fini, donnant lieu à la zone d'instabilité de charge qui, à température nulle, se termine en un *point critique quantique (QCP)*. En utilisant la théorie des perturbations, nous décrivons analytiquement cette physique dans la théorie des transitions de phase de Landau. Nous isolons une petite échelle d'énergie (ici le couplage de Hund) levant la dégénérescence de l'état fondamental atomique comme la cause ultime de cette phénoménologie.

Nous adaptons enfin l'algorithme de Diagonalisation Exacte pour la solution des équations de la DMFT au calcul des propriétés de transport, avec une précision comparable dans certains cas au solveur d'impureté à base de Groupe de Renormalisation Numérique, plus précis mais numériquement plus lourd. Nous appliquons ensuite notre méthode sur différents systèmes multi-orbitales et étudions leur résistivité.

MOTS CLÉS

systèmes fortement corrélés - métaux de Hund - transition Mott - séparation de phase - transport - supraconductivité

ABSTRACT

Strongly correlated electron systems represent one of the most active research fields in condensed matter physics, exhibiting intriguing phenomena like unconventional superconductivity and anomalous transport. In this thesis we theoretically analyze the multi-orbital *Hund metals*, using *Slave Spins Mean-Field (SSMF)* and *Dynamical Mean-Field Theory (DMFT)*.

We study the emergence of a charge instability towards phase separation/charge-density wave, signalled by a diverging electronic compressibility, in doped multi-orbital Mott insulators for a finite "Hund's" intra-atomic exchange coupling. The effect is enhanced once the local spin or orbital symmetry is broken by e.g. a crystal field splitting and is understood in terms of energetics. The results are in agreement with realistic studies of iron-based superconductors.

We also connect the first order of the Mott metal-insulator transition found in the Hund metals at half-filling to the coexistence of two metallic solutions away from half-filling, giving rise to the charge instability zone which at zero temperature ends in a *quantum critical point (QCP)*. Using perturbation theory we analytically describe this physics within Landau's theory of phase transitions. We single out a small energy scale (here the Hund's coupling) splitting a degenerate atomic ground state as the ultimate cause of this phenomenology.

We finally adapt the Exact Diagonalization algorithm for solving the DMFT equations to the calculation of transport properties, to an accuracy comparable in some cases to the more accurate but numerically heavier Numerical Renormalization Group solver. We then apply our method on different multi-orbital systems and study their resistivity.

KEYWORDS

strongly correlated systems - Hund metals - Mott transition - phase separation - transport - superconductivity